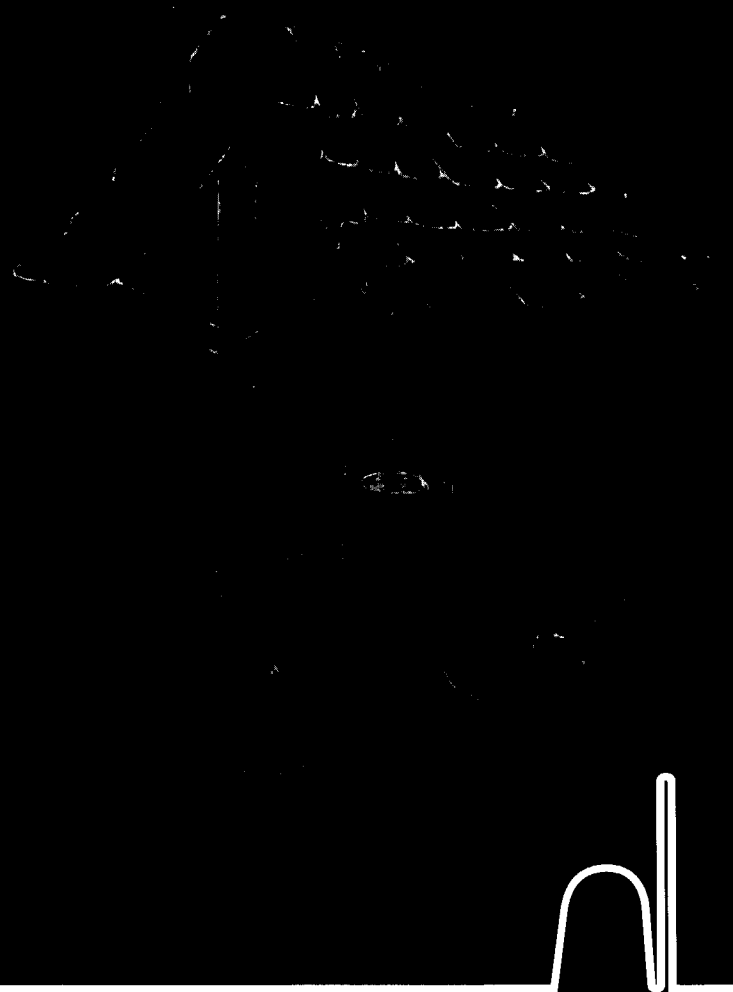


Advanced  $\gamma$ -ray  
spectrometry  
dealing with  
coincidence  
and attenuation  
effects

Sjoerd J.  
Gelsema





3791  
766417  
3-2-67

# Advanced $\gamma$ -ray spectrometry dealing with coincidence and attenuation effects

TR 3791

A three curves approach

Sjoerd J. Gelsema

Cover illustration by Tanya I. Gelsema



Interfacultair Reactor Instituut

The research described in this thesis was conducted within the Physical and Mathematical Radioanalysis group of the Department of Radiochemistry of the Interfaculty Reactor Institute, Delft University of Technology, Mekelweg 15, 2629 JB Delft, The Netherlands

Het in dit proefschrift beschreven onderzoek is uitgevoerd binnen de groep Fysisch Mathematische Radioanalyse van de afdeling Radiochemie van het Interfacultair Reactor Instituut, Technische Universiteit Delft, Mekelweg 15, 2629 JB Delft.

# Advanced $\gamma$ -ray spectrometry dealing with coincidence and attenuation effects

## A three curves approach

Proefschrift

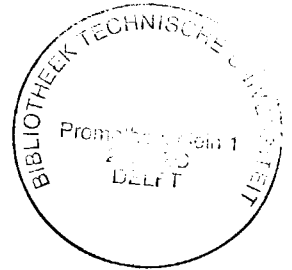
ter verkrijging van de graad van doctor  
aan de Technische Universiteit Delft,  
op gezag van de Rector Magnificus Prof. ir. K.F. Wakker,  
voorzitter van het College voor Promoties,  
in het openbaar te verdedigen

op dinsdag 4 december 2001 te 16.00 uur

door

Sjoerd Jan GELSEMA

Natuurkundig ingenieur  
geboren te Middelburg



Dit proefschrift is goedgekeurd door de promotoren:

Prof. dr. ir. J.J.M. de Goeij

Prof. dr. ir. C.W.E. van Eijk

*Samenstelling Promotiecommissie*

Rector Magnificus,	voorzitter
Prof. dr. ir. J.J.M. de Goeij,	Technische Universiteit Delft, promotor
Prof. dr. ir. C.W.E. van Eijk,	Technische Universiteit Delft, promotor
Prof. dr. ir. M. de Bruin,	Technische Universiteit Delft
Prof. dr. F. de Corte,	Universiteit van Gent
Prof. dr. H. Postma,	Technische Universiteit Delft
Prof. dr. M.J.A. de Voigt,	Technische Universiteit Eindhoven
Dr. K. Debertin,	Physikalisch-Technische Bundesanstalt, Braunschweig
Prof. dr. ir. A.H.M. Verkooijen,	Technische Universiteit Delft, reservelid

Dr. M. Blaauw heeft als begeleider in belangrijke mate aan de totstandkoming van het proefschrift bijgedragen

***Published and distributed by: DUP Science***

DUP Science is an imprint of  
Delft University Press  
P.O. Box 98  
2600 MG Delft  
The Netherlands  
Telephone: +31 15 27 85 678  
Telefax: +31 15 27 85 706  
E-mail: DUP@Library.TUdelft.NL

ISBN 90-407-2253-6

Keywords: radiation detection, gamma-ray spectrometry, coincidence summing

Copyright © 2001 by Sjoerd J. Gelsema.

All rights reserved. No part of the material protected by this copyright notice may be reproduced or utilized in any form or by any means, electronic or mechanical, including photocopying, recording or by any information storage and retrieval system, without written permission from the publisher: Delft University Press.

Printed in the Netherlands

*ter nagedachtenis aan mijn vader*





# Table of contents

---

List of symbols	xi
List of abbreviations	xiii

## **PROLOGUE**

---

<b>Chapter One: General introduction</b>	3
1.1 $\gamma$ -Ray spectrometry	3
1.2 Coincidence summing	5
1.3 This thesis	7

## **PART I: THEORY AND TOOLS**

---

<b>Chapter Two: <math>\gamma</math>-Ray spectrometry</b>	13
2.1 Introduction	13
2.2 Existing theory	16
2.3 Newly developed theory	23
<b>Chapter Three: Monte Carlo calculations</b>	31
3.1 Introduction	31
3.2 Modelling of photon interactions	32
3.3 Determination of full-energy peak efficiency-, PT- and LS-curves, and correlation values	35
3.4 Spectrum simulation	37

## **PART II: WELL-TYPE DETECTION GEOMETRIES**

---

<b>Chapter Four: Geometry effects in well type detectors owing to the introduction of high-Z linings</b>	41
4.1 Introduction	41
4.2 Theoretical considerations	42
4.3 Methods and measurements	45
4.4 Results	47
4.5 Discussion and conclusions	47

---

<b>Chapter Five: The influence of counting geometry and lining on the Compton continuum in well-type detectors</b>	53
5.1 Introduction	53
5.2 Compton continuum in $\gamma$ -ray spectra	54
5.3 Indexes of performance; the peak-to-total ratio and the peak-to-Compton ratio	55
5.4 Measurements	56
5.5 Results and discussion	57
5.6 Conclusions	60
<b>Chapter Six: The missing curve for well-type detection geometries; A Monte Carlo survey</b>	63
6.1 Introduction	63
6.2 Theory	64
6.3 Methods	67
6.4 Point source calibration	70
6.5 Tantalum pentoxide matrix calibration	75
6.6 General discussion and conclusion	81
<b>Chapter Seven: The missing curve for well-type detection geometries; Experimental verification</b>	83
7.1 Introduction	83
7.2 Experimental	84
7.3 Results	87
7.4 General discussion and conclusion	94

---

**PART III: MARINELLI-BEAKER DETECTION GEOMETRIES**

---

<b>Chapter Eight: The missing curve for voluminous source coincidence corrections; A Monte Carlo survey</b>	101
8.1 Introduction	101
8.2 Methods	103
8.3 Validation.	105
8.4 Calibration method	109
8.5 General discussion and conclusion	118
<b>Chapter Nine: The missing curve for voluminous source coincidence corrections; Experimental verification</b>	119
9.1 Introduction	119
9.2 Experimental	120
9.3 Results	124
9.4 Discussion	124
9.5 Concluding remarks	126

**EPILOGUE**

---

<b>Chapter Ten: General discussion</b>	131
10.1 Introduction	131
10.2 Theory aspects	132
10.3 Monte Carlo aspects	133
10.4 Well-type detector aspects	134
10.5 Marinelli beaker aspects	137
10.6 Conclusions	138
<b>Appendix A: A stochastic approach to <math>P_L</math></b>	141
<b>Appendix B: Weighted mean, <math>\bar{x}</math>-scores and <math>\chi^2</math>-values</b>	145
<b>Appendix C: Decay schemes</b>	149
Summary	159
Sammenvatting	165
Dankwoord	169
Curriculum vitae	171
List of publications	173



# List of symbols

---

## Symbols for non-statistical quantities

$A$	activity	[Bq]
$A_E$	area of peak at energy $E$	
$E$	photon energy	[keV, MeV]
$H$	electronic-pulse amplitude	
$N$	number of observed <i>pulses</i> or <i>counts</i> in a $\gamma$ -ray spectrum (Chapter Two)	
$N$	number of disintegrations	
$N_C$	number of photons emitted in a specific cascade	
$N_E$	number of disintegrations determined from peak at energy $E$	
$N_{\text{true}}$	true number of disintegrations	
$M_C$	number of photons constituting the full-energy of a peak	
$P_C$	cascade probability	
$P_E$	probability of observing a count in a $\gamma$ -ray spectrum at energy $E$ owing to the decay of a given nucleus	
$R_m$	mass-radius of spherical source	[kg m <sup>-2</sup> ]
$T$	transmission factor	
$V$	source volume	[m <sup>3</sup> ]
$X_{ij}$	transition probability of a nucleus from its $i$ -th energy level to its $j$ -th level	
$Z$	atomic number	
$a_{0...5}$	polynomial coefficients of Gunninks curve above 200 keV	
$b_{0...2}$	polynomial coefficients of Gunninks curve below 200 keV	
$c$	speed of light	[m s <sup>-1</sup> ]
$c_E$	observed counting rate in the full-energy peak at energy $E$	[s <sup>-1</sup> ]
$d$	thickness of absorber material	[m]
$f_i$	feeding probability of the $i$ -th level	
$g$	photon emission probability given a specific transition	
$g_{0..9}$	parameters describing the full-energy peak efficiency curve	
$h$	height	[m]
$h_{0..2}$	parameters describing the linear-to-squared curve	
$\ell$	source-to-detector distance	[m]
$m_e$	electron rest mass	[kg]
$r$	peak-to-total ratio	
$r, r'$	peak-to-total ratio of a voluminous source	
$n_{0..2}$	parameters describing the peak-to-total curve	

$\gamma_E$	photon-emission rate at energy $E$	[s <sup>-1</sup> ]
$\Sigma_{\text{ext}, E}$	transmission probability through external absorbers for photons of energy $E$	
$\Sigma_{\text{self}, E}$	transmission probability through the source itself for photons of energy $E$	
$\vartheta$	Compton-scattering direction	
$\Omega$	solid angle	[sr]
$\alpha$	internal conversion coefficient (Chapter Two)	
$\alpha$	photon energy as a fraction of the electron's rest energy (Chapter Three)	
$\delta$	mass thickness	[kg m <sup>-2</sup> ]
$\varepsilon$	full-energy peak efficiency	
$\varepsilon_E$	full-energy peak efficiency at energy $E$	
$\varepsilon_{\text{abs}, E}$	absolute detector efficiency at energy $E$	
$\varepsilon_{\text{int}, E}$	intrinsic detector efficiency at energy $E$	
$\varepsilon_t$	total efficiency	
$\lambda$	path length	[m]
$\mu$	linear attenuation coefficient	[m <sup>-1</sup> ]
$\mu/\rho$	mass attenuation coefficient	[m <sup>2</sup> kg <sup>-1</sup> ]
$\mu_E/\rho$	mass attenuation coefficient at energy $E$	[m <sup>2</sup> kg <sup>-1</sup> ]
$\rho$	density	[kg m <sup>-3</sup> ]
$\sigma_c$	Compton collision cross-section	
$\xi$	randomly chosen number from a uniform distribution ranging from 0 to 1	

### Symbols for statistical quantities

$\chi$	$\chi$ -score
$\chi^2$	reduced chi-square value
$\varepsilon$	full-energy peak efficiency regarded as a stochastic variable
$\varepsilon_t$	total efficiency regarded as a stochastic variable
$\eta^2$	scaled variance
$\eta^2_\varepsilon$	scaled variance of $\varepsilon$
$\eta^2_{\varepsilon, t}$	scaled variance of $\varepsilon_t$
$\mu$	mean
$\mu_\varepsilon$	mean of $\varepsilon$ (also referred to as $\bar{\varepsilon}$ )
$\mu_{\varepsilon, t}$	mean of $\varepsilon_t$ (also referred to as $\bar{\varepsilon}_t$ )
$\rho$	correlation coefficient
$\sigma^2$	variance
$\sigma^2_\varepsilon$	variance of $\varepsilon$
$\sigma^2_{\varepsilon, t}$	variance of $\varepsilon_t$

## List of abbreviations

---

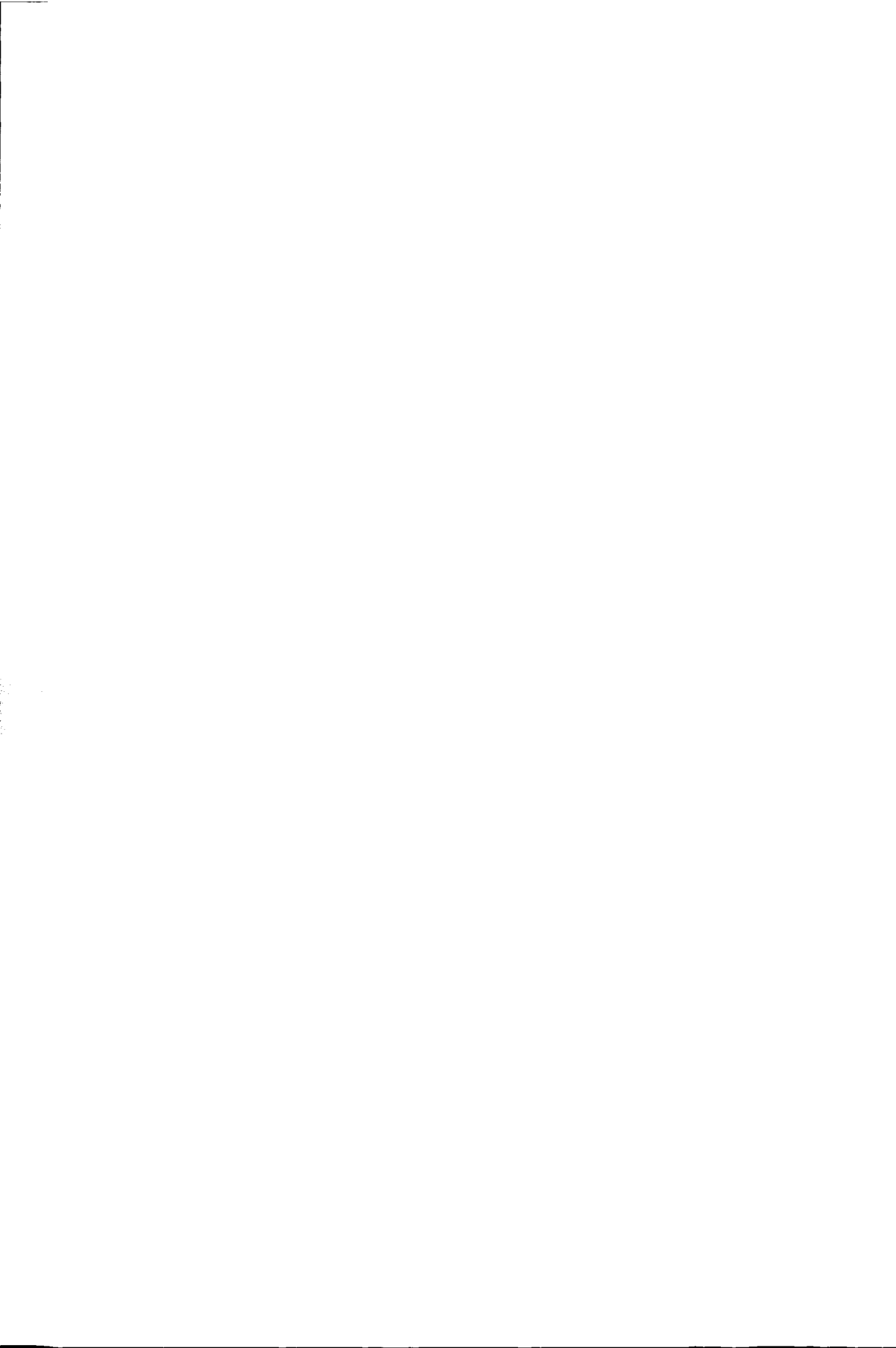
AAS	Atomic Absorption Spectrometry
BISNIS	Big Sample Neutron Irradiation System
EC	Electron Capture
Ge(Li)	Germanium – Lithium doped
HOR	Hoger Onderwijs Reaktor
HPGe	High Purity Germanium
IAEA	International Atomic Energy Agency
ICP/MS	Inductively Coupled Plasma Mass Spectrometry
INAA	Instrumental Neutron Activation Analysis
IRI	Interfaculty Reactor Institute
IT	Internal Transition
IUPAC	International Union of Pure and Applied Chemistry
LLD	Lower Level of Detection
MC	Monte Carlo
NAA	Neutron Activation Analysis
NaI(Tl)	Sodium Iodide – Thallium doped
PC	Peak-to-Compton
PIXE	Proton Induced X-ray Emission
PT	Peak-to-Total
LS	Linear-to-Squared





# Prologue

---



# Chapter One

## General introduction

---

### Abstract

*This chapter discusses shortly the development of radiation measurement techniques since the discovery of radioactivity in 1896. It introduces the problem of coincidence summing resulting from the trend of using more efficient detectors and detection geometries. Finally, based on the literature it specifies the aims of the work described by this thesis.*

### 1.1 $\gamma$ -Ray spectrometry

Since the discovery of radioactivity in 1896 by H. Becquerel, techniques have been developed to identify its source. The earliest measurement devices for individual particles consisted of a thin layer of zinc sulfide crystals; first on film (Sir William Crookes<sup>[1]</sup>, and independently Elster and Geitel in 1903\*) and later in an apparatus called the spinthariscopes (Crookes and Regener in 1908\*). These first devices were only sensitive for alpha and beta radiation. Since they had no energy discrimination capabilities, chemical preparations or separations were necessary to positively identify radionuclides. With the development of ionization chambers, measurement devices became sensitive for  $\gamma$ -radiation as well.

It was not until the late 1940's that devices had enough energy discriminating capabilities to be used as spectrometric devices. By then, sensitive photomultiplier tubes had been developed and were combined with scintillation crystals. In 1948, Hofstadter<sup>[3]</sup> reports the detection of  $\gamma$ -rays using NaI(Tl) crystals. This crystalline material has remained for almost twenty years the most important detector medium for  $\gamma$ -ray spectrometry.

---

\* Information obtained from<sup>[2]</sup>.

At the present, scintillation spectrometers are not considered high-resolution devices anymore. Although they are still widely used for applications that need simplicity of use rather than high energy resolution, Ge(Li) and HPGe detectors have outdated them for use in  $\gamma$ -ray spectrometry. Current developments in  $\gamma$ -ray spectrometry do no longer focus on a high energy resolution of detection systems. Instead they pursue higher throughputs of signals and higher detection efficiency. While the aim of high signal throughput is covered by the improvement of electronic equipment, the aim of higher efficiency is approached by growing larger crystals and improving source-detector configurations. Although  $\gamma$ -ray spectrometry has a much wider applicability, two examples of the need for more efficient detectors are discussed below.

### 1.1.1 $\gamma$ -Ray spectrometry in relation to neutron activation analysis

Neutron activation analysis (NAA) is a technique to measure amounts of chemical elements in a sample, based on the conversion of stable nuclei to other, mostly radioactive nuclei, via irradiation with neutrons. It uses  $\gamma$ -ray spectrometry to identify, qualitatively and quantitatively, either the prompt  $\gamma$ -rays, or the delayed ones of the radioactive irradiation products. Since, for virtually every stable nucleus, the probability of forming its irradiation products is accurately known, the identity of these products indicates which element was activated. Similarly, the activities of specific products indicate the amount of a specific isotope, and therefore of specific element.

Introduced by Georg von Hevesy and Hilde Levi in 1936<sup>[4]</sup>, NAA developed to a powerful technique in the late 50's when nuclear research reactors became available as intense neutron sources and the detection limits of NAA reached the mg/kg and  $\mu$ g/kg levels. Later, its development was accelerated by the introduction of NaI(Tl)  $\gamma$ -ray detectors in 1948, by multichannel pulse-height analysers in the early 60's, by the introduction of Ge(Li) detectors in the late 60's and by programmable minicomputers in the 70's. Nowadays, other trace element analysis techniques such as Atomic Absorption Spectrometry (AAS), Proton Induced X-ray Emission (PIXE) and Inductively Coupled Plasma Mass Spectrometry (ICP/MS) have pretty much caught up in their development with NAA. Especially ICP/MS has become a serious competitor.

Therefore, next to the pursuit of lower detection limits, current developments in NAA emphasize its strong points: (i) The advantages of sample preparation simplicity and of the high penetrating power of both neutrons and  $\gamma$ -rays is exploited by the introduction of a big sample neutron irradiation system (BISNIS) at IRI<sup>[5],[6]</sup>. (ii) The advantage over ICP/MS of very low detection limits for halogens (mainly fluor) is exploited by the recent improvements in an irradiation and measurement facility for short-lived radionuclides<sup>[7]</sup>. (iii) The advantages of NAA being a physically independent technique from ICP/MS are exploited by its use in the certification of reference materials<sup>[8],[9]</sup>.

Lower detection limits in NAA can be realized by using more intense neutron sources, by irradiating more material or by using more efficient  $\gamma$ -ray detectors and

detection geometries. At IRI, detection limits have been lowered mainly owing to the use of efficient detectors. Already in the late 70's, a well-type detector was installed. Another two well-type detectors accompanied this detector in the 80's. By that time, larger germanium detector crystals of over 500 cm<sup>3</sup> became available, and in the early 90's, a 500-cm<sup>3</sup> germanium detector was installed.

The introduction of BISNIS has had its influence on the  $\gamma$ -spectrometry performed at IRI. The large dimensions of the samples cause effects of sample self-attenuation of  $\gamma$ -rays.  $\gamma$ -Spectrometric methods had to be developed to take these effects into account.

### 1.1.2 $\gamma$ -Ray spectrometry in relation to environmental studies

Samples encountered in environmental studies usually contain very low amounts of radioactivity, in the order of 50 Bq/kg. To measure these low amounts, the use of highly efficient detectors alone does not suffice. In addition, samples should consist of large volumes of material. For this purpose, Marinelli beaker type detection geometries are often used. These are optimized to place a large volume of sample material as close to the detector as possible, effectively surrounding the detector. Self-attenuation effects play a large role with these geometries.

## 1.2 Coincidence summing

The tendency of using the newly available, highly efficient detectors and detection geometries calls for an extension of existing spectrometric interpretation methods. Highly efficient detection geometries cause *coincidence summing* effects: Two or more  $\gamma$ -quanta emitted from the same atom can interact with a detector within a very short time (up to 1  $\mu$ s). As a result, the detector cannot distinguish between them and treats them as a single interaction, the energy transfer being the sum of the individual interactions. Such count-rate independent coincidence summing effects can seriously affect a  $\gamma$ -ray spectrum.

Coincidence effects are most prominent when using well-type detectors. They can be corrected for if the source can be considered as a point, i.e. if the detection efficiency does not vary over the source volume. However, in 1978, de Bruin *et al.*<sup>[10]</sup> found that owing to coincidence effects, the areas of high-energy peaks in a  $\gamma$ -ray spectrum were influenced by the attenuation of low-energy photons in the sample, and therefore were matrix dependent. As a consequence, the source cannot be considered as a point, and the correction for coincidence summing is seriously hampered. Coincidence effects therefore necessitate time-consuming radionuclide specific calibrations.

Also when using Marinelli beakers, detection efficiencies generally are high enough to give rise to coincidence summing. Evidently, Marinelli beaker sources cannot be considered as point sources either. Therefore, coincidence summing corrections for Marinelli beaker detection geometries are not trivial. Like well-type geometries, Marinelli

beaker geometries are usually calibrated specifically for each radionuclide and each sample-matrix composition of interest.

### 1.2.1 Coincidence summing corrections for point sources

Point-source coincidence summing effects are in principle well understood. In fact, many authors have reported coincidence summing correction methods for point sources: In 1972, Andreev *et al.*<sup>[11], [12]</sup> have given a general quantitative procedure for the treatment of coincidence effects. In 1975, McCallum and Coote<sup>[13]</sup> have rewritten Andreev's formulas and extended them to include coincidences with annihilation photons. In 1979, Debertain and Schötzig<sup>[14]</sup> have checked Andreev's solution experimentally for cobalt-60, yttrium-88 and europium-152, both for point-source and for beaker geometries close to the detector. In his thesis, Moens<sup>[15]</sup> has generalized Debertain's method and has derived mathematical formulae covering practically all important cases. In 1987, de Corte<sup>[16]</sup> has updated the approach by Moens, has extended it for the cases of  $\gamma$ -KX(EC) and  $\gamma$ -KX(IT) coincidences, and has given practical recommendations for the application of Moens' approach.

In 1993, Blaauw<sup>[17]</sup> published a calibration method for highly efficient point source geometries that uses information implied in a  $\gamma$ -spectrum to determine efficiency curves. Instead of regarding coincidence effects as disturbing, in fact it exploits them. Since the method extracts information to correct for coincidence summing from the effects of coincidence summing, the method can be considered as self-validating; *viz.* the method implicitly corrects for erroneous assumptions or simplifications made in its development.

This analysis of the literature shows that the problem of coincidence corrections for point sources is indeed practically resolved. However, this conclusion is hardly applicable for the case of voluminous sources.

### 1.2.2 Coincidence summing corrections for voluminous sources

Although many authors have described calibration methods for voluminous sources that circumvent the large efforts of radionuclide specific calibration, most authors only address the problem of  $\gamma$ -ray attenuation and neglect coincidence summing corrections. Some authors have developed methods closely related either to the "Effective solid angle" method introduced by Moens *et al.*<sup>[18]</sup>, or to the attenuation correction method introduced by Debertain *et al.*<sup>[19]</sup>. Others have developed methods based on Monte Carlo calculations<sup>[20], [21], [22]</sup>. All authors who use Monte Carlo related calibration methods report the adjustment of some detector dimensions to match the Monte Carlo results with real measurements.

As has been stated by Kolotov *et al.*<sup>[23]</sup>, in spite of the fact that coincidence corrections for small point-like sources are well understood, only few authors have reported coincidence-summing correction methods for voluminous sources<sup>[14], [24], [25], [26]</sup>. This is probably owing to the fact that coincidence correction methods for point sources cannot

simply be applied to voluminous sources. A proper coincidence correction method for voluminous samples should take into account the differential behaviour of both the full-energy peak efficiency and the total efficiency over the source volume. To find this behaviour, the coincidence correction method introduced by Debertin<sup>[14]</sup> uses the information of 40 measurements of a point source located at various positions in a Marinelli beaker filled with inactive material that matches the sample material with respect to  $\gamma$ -ray attenuating properties. A numerical integration then calculates coincidence summing corrections for the whole source. Also de Corte *et al.*<sup>[24]</sup> and Kolotov *et al.*<sup>[23], [25]</sup> use a similar integration for their correction methods.

Although Debertin introduced the concept of “*differential efficiencies*” already in 1979<sup>[14]</sup>, only recently methods have been reported that explicitly use them. In 1995, Korun *et al.*<sup>[26]</sup> introduced an exponential distribution function that describes the variation of the efficiency over the source volume. This function is then added to Semkow’s<sup>[27]</sup> formalism to calculate the detector’s response to a specific source of a given radionuclide. However, Korun does not specify why an exponential function should be used, nor does he provide means to determine the parameters of the function.

In 1996, Wang *et al.*<sup>[28]</sup> introduced “*volume effect factors*” that describe the differential behaviour of the peak and total efficiencies. Volume effect factors have to be calculated for every combination of photon energies that can occur when a given radionuclide decays. This calculation is performed by an adjusted version of Moens’ program SOLANG<sup>[15]</sup>.

The coincidence correction methods described above all require either large calibration efforts or accurate knowledge of detector dimensions, in addition to dedicated computer programs to perform the volume integration. Moreover, the reported results of these correction methods for voluminous sources are far less accurate than correction methods for point sources. For voluminous sources Korun *et al.*<sup>[26]</sup>, for instance, report disagreements between calculated and measured peak areas of up to 15% whereas for point sources Blaauw<sup>[17]</sup> reports no disagreement of statistical significance.

The reason for the high quality of Blaauw’s coincidence calculations may be that Blaauw obtains all information necessary to correct for coincidence effects from measurements that do show these effects. In this way, possible errors or simplifications made in the theory are automatically corrected for. However, Blaauw reports the failure of his method when applied to voluminous source geometries<sup>[29]</sup>.

### 1.3 This thesis

The aim of the work described in this thesis is to extend the theory of coincidence summing effects to be valid for voluminous sources as well. Therefore, it should take into account the variation of the efficiency over the source volume. In addition, it should introduce a calibration method that is based on the extended theory. Like Blaauw’s

method, it should use the theory to provide the general form of efficiency curves. It should, however, obtain the actual curve parameters from measurements showing coincidence effects. This way, the self-validating character of Blaauw's method is preserved.

The newly introduced method should be applicable to point sources as well as to voluminous sources, *i.e.* it should cover well-type geometries as well as Marinelli beaker detection geometries. For the method to be competitive, its inaccuracy and imprecision should be as low as those of the most accurate and precise conventional methods, *i.e.* as low as those of radionuclide specific calibration methods. It should therefore provide both a maximal inaccuracy and imprecision of 1% for its resulting activity values.

### 1.3.1 Part I: Theory and tools

Chapter Two describes the principles of the calibration method. It gives the calculation of full-energy peak detection probabilities in a spectrum based on catalogued decay scheme data. To properly account for coincidence summing effects in voluminous sources, it introduces a new concept of quadratic efficiencies.

Chapter Three describes Monte Carlo simulation techniques for the calculation of efficiency curves and of  $\gamma$ -ray spectra. The subsequent parts will use these calculations to validate the theory and to examine the characteristics of the calibration method.

### 1.3.2 Part II: Well-type detection geometries

Owing to large summation effects encountered with well-type detectors, the attenuation of low-energy photons in the sample can influence high-energy peak areas. In 1979 de Bruin *et al.*<sup>[10]</sup> suggested the use of a high-Z lining inside the well to prevent these low-energy photons from reaching the detector. Chapter Four and Chapter Five discuss the consequences of the application of a high-Z lining. They show that the problems of sample self-attenuation and coincidence summing should be treated analytically rather than by attempts to eliminate them by means of a lining.

Chapter Six describes the analytical treatment of coincidence summing and sample self-attenuation effects for well-type detectors. It describes how the theory developed in Chapter Two provides the general shape of calibration curves. It also describes how actual measurements of a terbium-160 spectrum can provide the parameters of the curves.

Chapter Seven describes the actual use of the calibration method developed in the previous chapter. Whereas the previous chapter used Monte Carlo simulated data, this chapter uses real-life measurements.

### 1.3.3 Part III: Marinelli-beaker detection geometries

Chapter Eight describes the development of a calibration method that includes coincidence effect corrections for Marinelli beaker type detection geometries using Monte Carlo simulation techniques. Like in the well-type case, it describes how the theory developed in Chapter Two provides the general shape of calibration curves. It also shows



how actual measurements of a bromine-82 spectrum in principle can provide the parameters of the curves.

Chapter Nine again describes the use of the of the calibration method with real-life measurements.

### 1.3.4 Epilogue

Finally, Chapter Ten discusses the general aspects of the calibration methods. Based on these aspects, it draws conclusions and gives recommendations for future work.

## References

- [1] W. Crookcs, *Chemical News*, **87** (1903) 241
- [2] C.E. Crouthamel, "*Applied gamma-ray spectrometry*", 2<sup>nd</sup> Ed., Pergamon press, Oxford (1970)
- [3] R. Hofstadter, *Phys. Rev.*, **74** (1948) 100, **75** (1949) 796, **79** (1950) 389
- [4] G. Hevesy, H. Levi, *Det. Kgl. Danske Videnskabernes Selskab, Matematisk fysiske Meddelelser*, **XIV**, **5** (1936) 3
- [5] M. Blaauw, O. Lakmaker, P. van Aller, *Anal.Chem.*, **69** (1997) 2247
- [6] P. Bode, R.M.W. Overwater, J.J.M. De Goeij, *J. Radioanal. Nucl. Chem.*, **216** (1997) 5
- [7] M.J.J. Ammerlaan, P. Bode, S.S. Then, "*CAFIA: Carbonfiber Autonomous Facility for Irradiation and Analysis*", IRI report **IRI-133-90-001**, (1990)
- [8] J.J.M. De Goeij, "*Neutron Activation Analysis: Trends in Developments and Applications*", proceedings of the Intern.Conf. "*Neutrons and their applications*", The international society for optical engineering (1994)
- [9] P. Bode, E.A. De Nadai Fernandes, R.R. Greenberg, *J. Radioanal. Nucl. Chem.*, **245** (2000) 109
- [10] M. de Bruin, P.J.M. Korthoven, P. Bode, *Nucl. Instr. and Meth.*, **159** (1979) 301
- [11] D.S. Andreev, K.I. Erokhina, V.S. Zvonov, I.Kh. Lemberg, *Instr. Expt. Techn.*, **15** (1972) 1358.
- [12] D.S. Andreev, K.I. Erokhina, V.S. Zvonov, I.Kh. Lemberg, *Izv. Akad. Nauk SSSR, Ser. Fiz.*, **37** (1973) 1609.
- [13] G.J. McCallum, G.E. Coote, *Nucl. Instr. and Meth.*, **130** (1975) 189
- [14] K. Debertin, U. Schötzig, *Nucl. Instr. and Meth.*, **158** (1979) 471
- [15] L. Moens, Agrégé thesis, Rijksuniversiteit Gent (1981).
- [16] F. de Corte, "*The  $k_0$ -standardization method, A move to the optimization of neutron activation analysis*", Agrégé thesis, Rijksuniversiteit Gent (1987).
- [17] M. Blaauw, *Nucl. Instr. and Meth.*, **A332** (1993) 493
- [18] L. Moens, J. de Donder, LIN Xi-Lei, F. de Corte, A. de Wispelacre, A. Simonits, J. Hoste, *Nucl. Instr. and Meth.*, **187** (1981) 451
- [19] K. Debertin, R. Jianping, *Nucl. Instr. and Meth.*, **A278** (1989) 541

- 
- [20] F. Sanchez, E. Navarro, J.L. Ferrero, A. Moreno, C. Roldan, *Nucl. Instr. and Meth.*, **B61** (1991) 535
- [21] A. Bertolo, C. Manduchi, G. Manduchi, *Nucl. Instr. and Meth.*, **A314** (1992) 584
- [22] O. Sima, C. Dovlete, *Appl. Radiat. Isot.*, **48** (1997) 59
- [23] V.P. Kolotov, V.V. Atrashkevich, S.J. Gelsema, *J. Radioanal. Nucl. Chem., Articles*, **210** (1996) 183
- [24] F. de Corte, A. de Wispeleare, L. Vancraeynest, P. de Neve, P. van den Haute, *Nucl. Instr. and Meth.*, **A353** (1994) 539
- [25] V.V. Atrashkevich, V.P. Kolotov, *J. Radioanal. Nucl. Chem., Articles*, **169** (1993) 397
- [26] M. Korun, R. Martincic, *Nucl. Instr. and Meth.*, **A355** (1995) 600
- [27] T.M. Semkow, G. Mehmood, P.P. Parekh, M. Virgil, *Nucl. Instr. and Meth.*, **A290** (1990) 437
- [28] Tien-Ko Wang, Tzung-Hua Ying, Wei-Yang Mar, Chia-Lian Tseng, Chi-Hung Liao, Mei-Ya Wang, *Nucl. Instr. and Meth.*, **A376** (1996) 192
- [29] M. Blaauw, M.J.J. Ammerlaan, S.J. Gelsema, *Nucl. Instr. and Meth.*, **A385** (1997) 330

# Part I

## Theory and tools

---



# Chapter Two

## $\gamma$ -Ray spectrometry

---

### Abstract

*This chapter starts with a brief introduction into the principles of  $\gamma$ -ray spectrometry. It then describes the calculation of full-energy peak detection probabilities in the spectra using catalogued decay scheme data. For this purpose, it first describes the full-energy peak efficiency curve. In order to properly account for coincidence summing effects in point source geometries, it then describes the peak-to-total curve. Finally, to properly account for coincidence-summing effects in voluminous source geometries, it introduces the newly developed concept of stochastic efficiencies. In addition it introduces a third curve that relates the conventional linear efficiencies to the quadratic ones: the linear-to-squared curve.*

### 2.1 Introduction

In order to identify radionuclides within a radioactive source and at the same time to determine their absolute activities, it is necessary to be able to discriminate the emitted  $\gamma$ -quanta with respect to their energy. The discrimination is the main property of  $\gamma$ -ray spectrometry.  $\gamma$ -Spectrometry is generally performed with either sodium iodide or germanium detectors. The latter type excels in its high energy resolution of approximately 1%, allowing the separation of many closely spaced  $\gamma$ -ray energies. Since an incident  $\gamma$ -quantum is uncharged and creates no direct ionization or excitation in the detector material, the purpose of the detector is twofold: First it acts as a conversion medium in which incident  $\gamma$ -quanta have reasonable probability of interacting to yield one or more fast electrons. Second, it acts as a conventional detector transferring these fast electrons to electric signals.

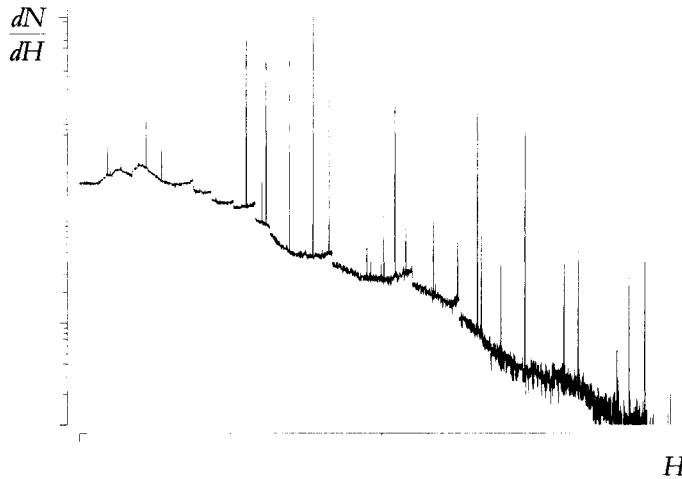


Figure 2.1: Differential pulse-height distribution

### 2.1.1 Pulse-height spectra and $\gamma$ -spectra

Any interaction causes the detector to produce an electronic pulse of which the amplitude is proportional to the energy transferred with the interaction. These pulses are all collected and stored for later interpretation. The most common way of displaying pulse information is through the *differential pulse-height distribution*. Figure 2.1 shows a particular distribution. The abscissa is a linear pulse amplitude scale that covers the range of pulse heights observed from the source. The ordinate is the differential number of pulses  $dN$  observed with an amplitude within the differential amplitude increment  $dH$ , divided by that increment, i.e.  $dN/dH$ . The horizontal scale then has units of pulse amplitude, whereas the vertical scale has units of inverse amplitude. The number of pulses whose amplitude lies between two specific values  $H_1$  and  $H_2$  can be obtained by integrating the area under the distribution between those limits (see Figure 2.1),

$$N_{H_1 < H < H_2} = \int_{H_1}^{H_2} \frac{dN}{dH} dH. \quad (2.1)$$

The proportionality between pulse amplitudes and energy transfer allows for the transformation of the horizontal scale units from units of amplitude to units of energy (keV or MeV are most often used, where  $1 \text{ eV} = 1.6 \cdot 10^{-19} \text{ J}$ ). The vertical scale unit then transforms to units of inverse energy. Equation (2.1) then transforms to

$$N_{E_1 < E < E_2} = \int_{E_1}^{E_2} \frac{dN}{dE} dE, \quad (2.2)$$

representing the number of photon interactions with energy transfer between  $E_1$  and  $E_2$ . The pulse-height spectrum is now called a  $\gamma$ -ray spectrum. The physical interpretation of differential pulse height-spectra or  $\gamma$ -ray spectra always involves areas under the spectrum between two given limits of pulse height or, equivalently, energy. The value of the ordinate itself has no significance until multiplied by an increment of the abscissa<sup>[1]</sup>.

### 2.1.2 Detection efficiency

An incident photon can interact with the detector material via one of three main mechanisms: photoelectric absorption, Compton scattering and pair production. Of these three mechanisms, photoelectric absorption will transfer the full-energy of the photon to the detector. The other two mechanisms transfer only part of the photon-energy to the detector. Though scattering followed by photoelectric absorption can still cause the total energy of the primary photon to be fully transferred, in a considerable number of cases the primary photon is detected only partially (for a detailed and more precise treatment of all three interaction mechanisms, see Chapter Three).

Based on this property of detection, two types of detection efficiency are defined: The first type considers all photon interactions, irrespective of the amount of energy transferred. It is therefore called *total efficiency*  $\epsilon_t$ , and is defined as: *The probability of a photon emitted by the source depositing any non-zero part of its energy in the active volume of the detector.* The other type considers only those interactions that transfer the full amount of photon energy to the detector. This *full-energy peak efficiency*  $\epsilon$  is defined as: *The probability of a photon emitted by the source depositing all its energy in the active volume of the detector.\**

The full-energy peak efficiency and the total efficiency are related by the *peak-to-total* ratio  $r$ ,

$$r = \frac{\epsilon}{\epsilon_t}. \quad (2.3)$$

Because the probability of each interaction mechanism depends on the energy of the incident photon, so do the full-energy peak efficiency and the peak-to-total ratio. In literature, various parameterizations of the efficiency curves have been proposed<sup>[1]</sup>. Section 2.2 discusses the parameterization applied in this work.

---

\* The definition of the full-energy peak efficiency according to the IUPAC yields<sup>[2]</sup>: “*The ratio between the number of ... photons counted with a radiation counter and the number of similar ... photons emitted by the radiation source when only considering the events recorded in the photopeak*”. This definition only equals the definition of this thesis if the *number of photons emitted by the source* goes to infinity. Furthermore, it neglects the influence of some spectrometer settings (I.I.D) and of coincidence summing effects<sup>[3]</sup>.

Highly efficient detection geometries cause *coincidence summing* effects: two or more  $\gamma$ -quanta have interactions with the detector within a time period shorter than the temporal resolution of the detector system, typically 1  $\mu$ s. As a result, the detection system cannot separate them and treats them as a single interaction, the energy transfer being the sum of the transfers of the individual interactions. Two types of coincidence summing can be distinguished. *Random coincidence summing*, or *pile-up* occurs if the  $\gamma$ -quanta originate from more than one decaying nucleus. Its occurrence is therefore dependent on the activity of the source. It can always be reduced by limiting the source activity, even in highly efficient detection geometries. *True coincidence summing* occurs if the  $\gamma$ -quanta originate from the same decaying nucleus. It is therefore not dependent on the activity of the source and cannot be avoided by limiting the source activity.

True coincidence summing effects can only be corrected for if the total efficiency of the detector is known as a function of photon energy, for example by using the peak-to-total ratio,  $r$ , as a function of energy: the peak-to-total curve. Section 2.2.2 describes coincidence summing effects and introduces a parameterization for the peak-to-total curve.

In the case of voluminous sources, the description of coincidence summing effects should also take into account the degree of variation of the efficiency over the source volume. As has been outlined in Chapter One, the description of voluminous source coincidence corrections has been subject of investigations world-wide. However, no adequate and easy-to-use description has been proposed yet\*. Section 2.3 does give an adequate and useful description of coincidence effects for voluminous sources. For this purpose it introduces the novel concept of stochastic efficiency. In addition, it introduces a third curve relating quadratic efficiencies to conventional linear efficiencies, thus taking into account the variation of the efficiency over the source volume.

## 2.2 Existing theory

### 2.2.1 The full-energy peak efficiency curve

The parameterization of the full-energy peak efficiency used in this work is an adaptation of that developed by Gunnink<sup>[5], [6]</sup>. It covers the energy range from 50 keV to 4 MeV with an error less than a few percent. The reason for the choice of Gunnink's parameterization is twofold. First, Gunnink has based his parameterization on data gathered from a large number of coaxial detectors, their active volumes ranging from 30 cm<sup>3</sup> to 350 cm<sup>3</sup>. It therefore represents a wide range of detectors. Second, previous

---

\* In this respect, the reader is referred to a recently published IAEA technical document<sup>[4]</sup> that reads: "... there are two important topics for which there are not yet practical, easy-to-use solutions. They relate to the quantification of activities in samples and involve true-coincidence summing and self-attenuation corrections."



studies performed at IRI have credited its use<sup>[7]</sup>, not only for coaxial detectors, but for well-type detectors as well.

In his papers, Gunnink also introduces a method for detector calibration, i.e. a method to obtain the parameter values for a specific detector set-up. Since his method uses empirical relations between the parameters and detector specifications that are specific for coaxial detectors and point sources, it will be disregarded in this work. Therefore, the adaptation of Gunnink's curve discussed hereafter disregards all relations that are specific for coaxial detectors, thus yielding a more general curve.

Gunnink distinguishes three factors in the definition of the efficiency for a  $\gamma$ -ray of a given energy: (i) the *intrinsic* efficiency  $\epsilon_{\text{int}}$  of the detector, (ii) the source-to-detector distance  $\ell$ , and (iii), the attenuation of  $\gamma$ -rays by the sample or by external absorbers. He defines the intrinsic efficiency as

$$\epsilon_{\text{int},E} = \frac{c_E \ell^2}{y_E \ell_0^2}, \quad (2.4)$$

where  $c_E$  is the observed counting rate in the full-energy peak at energy  $E$  in the absence of attenuation and coincidence effects,  $y_E$  is the known  $\gamma$  emission rate and  $\ell_0$  is a reference source-to-detector distance\*. He determines the true source-to-detector distance by a semi-empirical model<sup>[8], [9], [10]</sup>. The adaptation discussed here will not use the concept of intrinsic efficiency and thus circumvent the use of the source-to-detector distance. Instead it uses the absolute efficiency which is related to the intrinsic efficiency by

$$\epsilon_{\text{abs},E} = \frac{\epsilon_{\text{int},E} \ell_0^2}{\ell^2}. \quad (2.5)$$

Since Gunnink has fitted an efficiency curve using higher-order polynomial equations on a double-log scale, the use of the absolute efficiency instead of intrinsic efficiency will only affect the zeroth-order parameter of the polynomial representation. Originally, Gunnink views the efficiency curve from 50 keV to 4 MeV in three regions: <90 keV, 90 to 200 keV, and >200 keV. This adaptation uses only two regions: respectively <200 keV and >200 keV. In addition, it uses two factors that describe attenuation effects by external absorbers and by the source itself, respectively. Thus, the overall expression for the full-energy peak efficiency of a given source-detector geometry yields

$$\epsilon_E = \sum_{\text{ext},E} \cdot \sum_{\text{self},E} \cdot \epsilon_{\text{abs},E}$$

---

\* Notice that Gunnink's definition of the efficiency resembles the IUPAC definition. The fact that this work uses a different definition of efficiency does not have any influence on the derived parameterization of the efficiency curve. Furthermore, Gunnink's use of source-to-detector distance  $\ell$  is not undisputed. Knoll [1], for instance, uses solid angles instead which yields a more precise definition.

or equivalently

$$\ln \varepsilon_E = \ln \Sigma_{\text{ext}, E} + \ln \Sigma_{\text{self}, E} + \ln \varepsilon_{\text{abs}, E}, \quad (2.6)$$

where  $\Sigma_{\text{ext}, E}$  represents the transmission through external absorbers and  $\Sigma_{\text{self}, E}$  represents the transmission of the source itself.

*Energy region above 200 keV*

The region of the efficiency curve for  $E > 200$  keV has long been known to be nearly linear when the logarithms of the efficiency and the energy are plotted. Because of this, the use of a polynomial function of the following form is convenient,

$$\varepsilon_{\text{abs}, E > 0.2 \text{ MeV}} = \exp \left[ \sum_{j=0}^5 a_j \left( \ln \left[ \frac{E}{E_0} \right] \right)^j \right], \quad (2.7)$$

where  $E_0$  is 1 MeV. However, a fifth-order polynomial like Equation (2.7) over-determines the nearly linear relationship between logarithmic efficiency and energy. The polynomial coefficients are correlated. Based on his experience with a large number of detectors of various dimensions, Gunnink found the following relations.

$$\begin{aligned} a_0 &= g_1, \\ a_1 &= 0.06(1 - g_2) - 1.15 - 0.0778(\ln g_3) + 0.0296(\ln g_3)^2, \\ a_2 &= 0.333 - 0.1154 g_3 + 0.009427 g_3^2, \\ a_3 &= -0.1456 + 0.01592 g_3, \\ a_4 &= -0.015, \\ a_5 &= -0.003 + 0.0092 g_3 - 0.00124 g_3^2. \end{aligned} \quad (2.8)$$

Gunnink also found relations between the  $g_j$  coefficients and detector dimensions and other specifications. The adaptation of this thesis however does not use them. The reason for this is threefold: In the first place,  $g_1$  is affected by the use of absolute efficiency instead of intrinsic efficiency. In the second place, coefficient  $g_3$  is supposed to correspond with the active volume of the detector. Gunnink however, is not clear about the units to be used. Furthermore, Gunnink may very well mean that  $g_3$  corresponds with the logarithm of the active detector volume. Finally: the relations are found using only data from point sources measured on coaxial detectors. Since this adaptation is to be used for voluminous source geometries as well as for well-type geometries, the coefficients are very likely to lose their physical meaning. Later chapters will show that the parameterization itself can be used for voluminous source and well-type geometries.

*Energy region below 200 keV*

The region of the efficiency curve for  $E < 200$  keV is modelled by a simple second order polynomial on double-log scale,

$$\epsilon_{\text{abs}, E < 0.2 \text{ MeV}} = \exp \left[ \sum_{j=0}^2 b_j \left( \ln \left[ \frac{E}{E_0} \right] \right)^j \right]. \quad (2.9)$$

Since at  $E = 200$  keV both the efficiency curve and its first derivative should be continuous, this parameterization of the curve below 200 keV introduces one additional parameter  $g_0$ . Explicitly

$$\begin{aligned} b_2 &= g_0, \\ b_1 &= a_1 + (a_2 - b_2) \ln 0.2 + \sum_{j=3}^5 a_j (\ln 0.2)^{j-1}, \\ b_0 &= a_0 + (a_1 - b_1) \ln 0.2 + (a_2 - b_2) (\ln 0.2)^2 + \sum_{j=3}^5 a_j (\ln 0.2)^j. \end{aligned} \quad (2.10)$$

*External absorbers*

For the modelling of external absorbers, i.e. all layers of material located between the source and the detector, it is assumed that all material is composed of low-Z elements. For these elements, the logarithmic total mass attenuation coefficient  $\mu_E/\rho$  is independent of the material and linearly dependent on logarithmic energy (hence the subscript  $E$ ) as long as  $E$  is larger than the energy of the K-edge and as long as  $\mu_E/\rho$  is larger than  $0.1 \text{ m}^2\text{kg}^{-1}$ . For smaller values of  $\mu_E/\rho$ , deviations from linearity occur, but these will be of minor importance because these smaller value of  $\mu_E/\rho$  implicate only minor attenuation effects. The dependency on logarithmic energy of the logarithmic total mass attenuation coefficient of a mixture or of several layers of low-Z material is linear as well,

$$\ln \left[ \frac{\mu_E/\rho}{\mu_0/\rho_0} \right] = m_0 + m_1 \ln \frac{E}{E_0}, \quad (2.11)$$

with  $\mu_0/\rho_0 = 1 \text{ m}^2\text{kg}^{-1}$ . For the term in Equation (2.6) representing the external absorbers, the following parameterization is derived:

$$\ln \Sigma_{\text{ext}, E} = -\frac{\mu_E}{\rho} \delta = -\delta \frac{\mu_0}{\rho_0} \exp[m_0] \exp \left[ m_1 \ln \frac{E}{E_0} \right] = g_4 \exp \left[ g_5 \ln \frac{E}{E_0} \right], \quad (2.12)$$

where  $\rho$  is the density of the absorber material in  $[\text{kg m}^{-3}]$ ,  $\delta$  is the mass thickness of the material in  $[\text{kg m}^{-2}]$  which is defined as the mass per unit area, and is obtained by

multiplying the thickness of the absorber material,  $d$ , by its density, i.e.,  $\delta = \rho d$ . The parameters  $g_4$  and  $g_5$  are the parameters modelling the absorber.

### Sample self-attenuation

Fleming<sup>[12]</sup> has given an analytical expression for neutron self-shielding factors for e.g. non-scattering spherical samples in a homogeneous, isotropic Maxwellian neutron flux distribution. Since the absorption of neutrons is governed by the same exponential law as the attenuation of  $\gamma$ -rays, Fleming's expression is directly applicable to the latter case. The attenuation of  $\gamma$ -rays in spherical samples thus is described by

$$\Sigma_{\text{self},E} = \frac{3\rho^3}{4\mu_E^3 R_m^3} \left[ \frac{\mu_E^2 R_m^2}{\rho^2} - \frac{1}{2} + \left( \frac{1}{2} + \frac{\mu_E R_m}{\rho} \right) \exp \left[ -2 \frac{\mu_E R_m}{\rho} \right] \right], \quad (2.13)$$

where  $\mu_E/\rho$  is the sample's total mass attenuation coefficient that is modelled by Equation (2.11) and  $R_m$  is the sample mass-radius, in terms of mass per unit area. Expression (2.13) does not account for a variation of the efficiency over the source owing to other causes than self-attenuation, like varying detector distance. Hence, it is only applicable for well-type detectors or if the sample-detector distance is large compared to sample dimensions. In the case of Marinelli beaker samples, this work models the sample self-attenuation as being caused by an external absorber.

### 2.2.2 Coincidence summing calculations; the Peak-to-Total curve

#### Coincidence summing calculations

Let us consider a source of a radionuclide with an arbitrary decay scheme as shown in Figure 2.2. In this general set-up, the decay of a nucleus is described as a set of cascades of transitions, each cascade having its own probability of occurrence  $P_C$ . For the cascade indicated in Figure 2.2,  $P_C$  would be given by

$$P_C = f_{n-1} X_{n-1,2} X_{2,1} X_{1,0}, \quad (2.14)$$

where  $f_i$  denotes the feeding probability to the  $i$ -th level and  $X_{ij}$  denotes the probability of the transition from the  $i$ -th to the  $j$ -th level.

The probability  $P_E$  of detecting a count in the full-energy peak at energy  $E$  owing to the decay of a given nucleus is now obtained by summing, over all cascades, the product of the cascade probability and the probability of the cascade contributing to the peak, i.e.

$$P_E = \sum_{\text{Cascades}} \left[ P_C \cdot \prod_{i=1}^{M_C} g_i \varepsilon_i \prod_{j=M_C+1}^{N_C} (1 - g_j \varepsilon_j) \right], \quad (2.15)$$

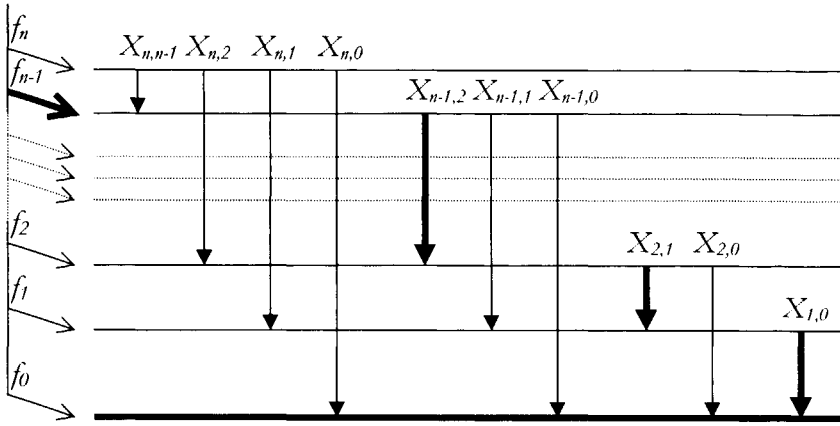


**Figure 2.2:** General decay scheme with one specific cascade indicated bold. Here  $f_i$  denotes the feeding probability to the  $i$ -th level and  $X_{ij}$  denotes the probability of the transition from the  $i$ -th to the  $j$ -th level.

where  $\varepsilon$  denotes the full-energy peak efficiency,  $\varepsilon_t$  denotes the total efficiency, and  $g$  denotes the photon emission probability, more often expressed as  $g=1/(1+\alpha)$  where  $\alpha$  denotes the internal conversion coefficient. In Equation (2.15),  $N_c$  is the number of photons emitted in a specific cascade and  $M_c$  is the number of photons constituting the full-energy of the peak. This means that if  $M_c=1$ , the product over index  $i$  describes simple detection of a photon of energy  $E$ . Else, if  $M_c>1$ , it describes coincidence summing-in of multiple photons with energies adding up to  $E$ . The product over index  $j$  describes summing-out effects by the remaining photons in the cascade. For the sake of simplicity, in the remainder of this chapter, the emission probabilities  $g$  will assumed to be unity. Since, if relevant, all  $\varepsilon$  and  $\varepsilon_t$  can be always replaced by  $g\varepsilon$  and  $g\varepsilon_t$ , this will not alter the generality of the formulas. The formulas can be complicated further by accounting for angular correlations between the photons in the cascade. Angular correlation however are discarded in this work.

*The peak-to-total curve*

Since the full-energy peak efficiency  $\varepsilon$  and the total efficiency  $\varepsilon_t$  are related by the peak-to-total value  $r = \varepsilon/\varepsilon_t$ , Equation (2.15) can be transformed to

$$P_E = \sum_{\text{Cascades}} \left[ P_C \prod_{i=1}^{M_c} \varepsilon_i \prod_{j=M_c+1}^{N_c} \left(1 - \frac{\varepsilon_j}{r_j}\right) \right]. \tag{2.16}$$

The dependency of the peak-to-total ratio  $r$  on energy is commonly described by a linear relation on double-log scale,

$$\ln r = r_0 + r_1 \ln E/E_0. \quad (2.17)$$

Since the total efficiency  $\varepsilon_t$  is always larger than or equal to the peak efficiency  $\varepsilon$ , the peak-to-total ratio should be limited to values  $r < 1$ , thus  $\ln[r] < 0$ . In the parameterization of the peak-to-total curve in this work, this limitation is expressed by a third parameter  $r_2$ . If  $\ln[r] > r_2$  then  $\ln[r]$  is limited by the following function,

$$L(\ln r) = \frac{r_2}{2 - \left( \ln r / r_2 \right)}. \quad (2.18)$$

### *Voluminous sources*

Equation (2.15) or (2.16) is only applicable if the efficiencies can be considered constant throughout the source volume  $V$ . If this condition does not hold, volume averages must be taken and for Equation (2.15) is obtained

$$P_E = \frac{1}{V} \int_V \sum_{\text{Cascades}} \left[ P_C \prod_{i=1}^{M_C} \varepsilon_i \prod_{j=M_C+1}^{N_C} (1 - \varepsilon_j) \right] dV = \sum_{\text{Cascades}} \left[ P_C \prod_{i=1}^{M_C} \overline{\varepsilon_i} \prod_{j=M_C+1}^{N_C} (1 - \overline{\varepsilon_j}) \right]. \quad (2.19)$$

Let us focus on one term in Equation (2.19) that describes one specific cascade. For point-source geometries it was possible to use full-energy-peak efficiency and total efficiency curves describing the complete source-detector geometry. However, for voluminous sources it is not, since those curves would generally yield the volume average efficiencies  $\overline{\varepsilon}$  and  $\overline{\varepsilon_t}$  as a function of photon energy. Equation (2.19) however uses the average product of a set of efficiencies which, in general, is not equal to the product of a set of averaged efficiencies  $\overline{\varepsilon_i}$  and  $\overline{\varepsilon_j}$ . In other words

$$\overline{\prod_{i=1}^{M_C} \varepsilon_i \prod_{j=M_C+1}^{N_C} (1 - \varepsilon_j)} \neq \prod_{i=1}^{M_C} \overline{\varepsilon_i} \prod_{j=M_C+1}^{N_C} (1 - \overline{\varepsilon_j}). \quad (2.20)$$

This inequality was noted and experimentally demonstrated earlier by e.g. Debertin<sup>[13]</sup> and de Corte<sup>[14]</sup>. It is also this inequality that causes Blaauw's method for point sources to fail for voluminous sources<sup>[7]</sup>.

## 2.3 Newly developed theory

### 2.3.1 Coincidence summing calculations for voluminous sources: A Stochastic approach to efficiencies

For voluminous sources, full-energy peak efficiencies  $\varepsilon$  and total efficiencies  $\varepsilon_t$  cannot be considered constant throughout the source volume. Instead, for every single decay, they depend upon the location of the decaying nucleus. Since this location is subject to probabilistic processes, it is natural to view them as stochastic variables  $\varepsilon$  and  $\varepsilon_t$ . In this context, the distribution over the source volume of the full-energy peak efficiency as a function of energy can be described by its moments, of which the first and the second are its mean  $\mu_\varepsilon$  and its variance  $\sigma_\varepsilon^2$ ,

$$\begin{aligned}\mu_\varepsilon(E) &= \mathbf{E} [\varepsilon(E)] \\ \sigma_\varepsilon^2(E) &= \mathbf{E} [(\varepsilon(E) - \mu_\varepsilon(E))^2] \end{aligned} \quad (2.21)$$

Although strictly, these first two moments do not fully describe every possible distribution of the full-energy peak efficiency, in the context of this work, where the source activity is homogeneous, they will prove to suffice.

Similarly, the distribution of the total efficiency is described by

$$\begin{aligned}\mu_{\varepsilon,t}(E) &= \mathbf{E} [\varepsilon_t(E)] \\ \sigma_{\varepsilon,t}^2(E) &= \mathbf{E} [(\varepsilon_t(E) - \mu_{\varepsilon,t}(E))^2] \end{aligned} \quad (2.22)$$

Using these relations, the full-energy peak efficiency curve for voluminous sources is now defined as  $\mu_\varepsilon(E)$ . The peak-to-total value for voluminous sources is defined as  $r_V \equiv \mu_\varepsilon/\mu_{\varepsilon,t}$ , and consequently, the peak-to-total curve is defined as  $r_V(E) \equiv \mu_\varepsilon(E)/\mu_{\varepsilon,t}(E)$ . Notice that, since  $\mu_\varepsilon$  and  $\mu_{\varepsilon,t}$  are both constants for a given detector, a given source and for a given energy, so is  $r_V$ . In other words: By *definition*,  $r_V$  is not a stochastic variable. Furthermore, for non-voluminous sources  $r_V$  reduces to  $r$  as defined by (2.3).

At this point, it is convenient to relate the variance of a stochastic variable to its mean by introducing  $\eta_\varepsilon$  and  $\eta_{\varepsilon,t}$ , defined by

$$\eta_\varepsilon^2 \equiv \frac{\sigma_\varepsilon^2}{\mu_\varepsilon^2} \quad \text{and} \quad \eta_{\varepsilon,t}^2 \equiv \frac{\sigma_{\varepsilon,t}^2}{\mu_{\varepsilon,t}^2}.$$

Since it can safely be assumed that the distributions of the full-energy peak efficiency  $\epsilon$  and the total efficiency  $\epsilon_t$  are fairly similar\*, we can write

$$\eta^2(E) \equiv \frac{\sigma_\epsilon^2(E)}{\mu_\epsilon^2(E)} \cong \frac{\sigma_{\epsilon_t}^2(E)}{\mu_{\epsilon_t}^2(E)}, \quad (2.23)$$

additionally expressing that  $\eta$  is a function of energy. Instead of being characterized by its mean  $\mu_\epsilon$  (or  $\mu_{\epsilon_t}$ ) and variance  $\sigma_\epsilon^2$  (or  $\sigma_{\epsilon_t}^2$ ), a stochastic variable  $\epsilon$  (or  $\epsilon_t$ ) can equally well be characterized by  $\mu_\epsilon$  (or  $\mu_{\epsilon_t}$ ) and  $\eta$ .

To be able to use these efficiency curves, equivalently to the point source case, it is necessary to write the average product on the right-hand term of Equation (2.19) in terms of  $\mu_\epsilon$  and  $\mu_{\epsilon_t}$ . The approach chosen by this work regards every factor of two stochastic variables as a new stochastic variable having its own mean  $\mu$  and scaled variance  $\eta$ . The next paragraph subsequently considers the occurring factors.

First, consider the factors in Equation (2.19), describing summing out effects. The mean and variances of these factors can be written as

$$\begin{aligned} E[1 - \epsilon_t] &= 1 - \mu_{\epsilon_t}, \\ \text{var}[1 - \epsilon_t] &= \sigma_{\epsilon_t}^2 \quad \text{and thus} \\ \eta_{1-\epsilon_t}^2 &= \eta_{\epsilon_t}^2 \frac{\mu_{\epsilon_t}^2}{1 - \mu_{\epsilon_t}^2}. \end{aligned} \quad (2.24)$$

Next, consider a product of two stochastic variables  $\epsilon_1$  and  $\epsilon_2$ , having means  $\mu_1$  and  $\mu_2$ , variances  $\sigma_1$  and  $\sigma_2$ , and cross-correlation  $\rho_{1,2}$ . Since the correlation between  $\epsilon_1$  and  $\epsilon_2$  can be written as

$$\rho_{1,2} = \frac{E[(\epsilon_1 - \mu_1)(\epsilon_2 - \mu_2)]}{\sigma_1 \sigma_2} = \frac{E[\epsilon_1 \epsilon_2] - \mu_1 \mu_2}{\sigma_1 \sigma_2},$$

we can write for the mean product  $\mu_{1,2}$  of the two stochastic variables

$$\begin{aligned} \mu_{1,2} &\equiv E[\epsilon_1 \epsilon_2] = \mu_1 \mu_2 + \rho_{1,2} \sigma_1 \sigma_2 \\ &= (1 + \rho_{1,2} \eta_1 \eta_2) \mu_1 \mu_2. \end{aligned} \quad (2.25)$$

---

\* This assumption is justified by T.-K. Wang et al.<sup>[15]</sup>, who write: "According to the work done by (1) Erten et al.<sup>[16]</sup> [...],  $\epsilon$  and  $\epsilon_t$  have similar variation with distance to [a] detector and by (2) Lin and Heydorn<sup>[17]</sup>, the uncertainty in the  $\epsilon_t$  value is of minor importance to the COI factor", where COI denotes the coincidence correction factor.



To be able to express the variance  $\sigma_{1,2}$  of the product of  $\epsilon_1$  and  $\epsilon_2$  in terms of their means, their variances and their cross-correlation, we need to linearize the product using a Taylor expansion about the point  $(\mu_1, \mu_2)$ ,

$$\begin{aligned} \epsilon_1 \epsilon_2 &= \mu_1 \mu_2 + (\epsilon_1 - \mu_1) \left. \frac{\partial \epsilon_1 \epsilon_2}{\partial \epsilon_1} \right|_{(\epsilon_1, \epsilon_2) = (\mu_1, \mu_2)} + (\epsilon_2 - \mu_2) \left. \frac{\partial \epsilon_1 \epsilon_2}{\partial \epsilon_2} \right|_{(\epsilon_1, \epsilon_2) = (\mu_1, \mu_2)} + O^2, \\ &\approx \mu_2 \epsilon_1 + \mu_1 \epsilon_2 - \mu_1 \mu_2 \end{aligned} \quad (2.26)$$

yielding a variance of

$$\sigma_{1,2}^2 \equiv \text{var} [\epsilon_1 \epsilon_2] \approx \text{var} [\mu_2 \epsilon_1 + \mu_1 \epsilon_2 - \mu_1 \mu_2] = \mu_2^2 \sigma_1^2 + \mu_1^2 \sigma_2^2 + 2\rho_{1,2} \mu_1 \mu_2 \sigma_1 \sigma_2,$$

and a scaled variance of

$$\eta_{1,2}^2 \cong \frac{\text{var} [\mu_2 \epsilon_1 + \mu_1 \epsilon_2 - \mu_1 \mu_2]}{\text{E} [\mu_2 \epsilon_1 + \mu_1 \epsilon_2 - \mu_1 \mu_2]^2} = \eta_1^2 + \eta_2^2 + 2\rho_{1,2} \eta_1 \eta_2 \quad (2.27)$$

We have now developed the necessary expression to calculate the mean and (scaled) variance of a product of two stochastic variables.

Let us now discuss the implementation of this stochastic approach. Firstly, let us focus on the cross-correlation coefficients. They express the correlation between, on the one hand, the efficiency for a certain energy, say,  $\epsilon_1$  at a random position within the source volume and, on the other hand, the efficiency for a different energy, say  $\epsilon_2$ , but for exactly that same position. Since the efficiency values are related by position, it is clear that the correlation between the two is large and positive. Also, since efficiency values are positive by definition, it is safe to say that the correlation between a product of two efficiencies,  $\epsilon_1 \epsilon_2$ , and a third,  $\epsilon_3$ , is also large and positive. Therefore, the practical implementation of the stochastic approach considers all correlations between efficiencies or products of efficiencies large and positive, i.e. it replaces them by a single parameter  $\rho$  near 1. The actual value of  $\rho$  is to be determined by calibration methods.

Secondly, notice that Equation (2.19) contains products of more than two stochastic variables. In principle, these can be calculated by first calculating mean and (scaled) variance of two variables using Equation (2.25) and then subsequently adding extra factors, each time considering the outcome of (2.25) as a single factor. This requires keeping track of the mean and (scaled) variance of the intermediate products.

The final point of discussion concerns the order in which to calculate the constituting factors of Equation (2.19). This point is closely related to the cross-correlation issue. Equation (2.19) distinguishes two main factors, namely that of consisting of factors  $\epsilon_i$ ;  $\prod \epsilon_i$ , and that consisting of factors  $(1-\epsilon_{i,j})$ ;  $\prod (1-\epsilon_{i,j})$ . It is clear that, while the correlation between two factors of  $\epsilon_i$  or between two factors of  $(1-\epsilon_{i,j})$  is positive, the correlation

between a factor  $\varepsilon_i$  and a factor  $(1-\varepsilon_{t,j})$  is negative. Therefore, in order to maintain the *fuzzy* argumentation for replacing all correlations by a single large and positive parameter  $\rho$ , the first steps in the evaluation of (2.19) will be to calculate the two main factors separately. The last step then calculates the mean final product by (2.25), only this time taking the correlation large and *negative*:  $-\rho$ . The systematic application of this approach to expression (2.19) yields

$$\begin{aligned}
 P_E &= \frac{1}{V} \int_V \sum_{\text{Cascades}} \left[ P_C \prod_{i=1}^{M_C} \varepsilon_i \prod_{k=M_C+1}^{N_C} (1-\varepsilon_{t,k}) \right] dV \\
 &\approx \sum_{\text{Cascades}} \left[ P_C \cdot \left\{ 1 - \rho \left( \sum_{i=1}^{M_C} \eta_i \right) \left( \sum_{k=M_C+1}^{N_C} \eta_k \sqrt{\frac{\mu_{\varepsilon,k}^2}{r_k^2 - \mu_{\varepsilon,k}^2}} \right) \right\} \cdot \right. \\
 &\quad \left. \left\{ 1 + \rho \sum_{i=1}^{M_C} \sum_{j=i}^{M_C} \eta_i \eta_j \right\} \cdot \left\{ 1 + \rho \sum_{k=M_C+1}^{N_C} \sum_{l=k}^{N_C} \eta_k \eta_l \right\} \cdot \prod_{i=1}^{M_C} \mu_{\varepsilon,i} \prod_{k=M_C+1}^{N_C} \left( 1 - \frac{\mu_{\varepsilon,k}}{r_k} \right) \right]
 \end{aligned} \tag{2.28}$$

as can be verified in Appendix A. The validity of (2.28) is limited by a constraint on  $\eta$ ,  $\eta < 1$ , set by (A 1). Recalling the definition of  $\eta$  this means that the standard deviation of the distribution of the efficiency over the source volume should not exceed the mean value. Since efficiencies are positive valued by definition, the constraint is met by the majority of sources.

The application of this expression requires knowledge of the mean peak efficiency values  $\mu_\varepsilon$  and the peak-to-total ratios  $r$ , which relate the mean peak efficiency values  $\mu_\varepsilon$  to the mean total efficiency values  $\mu_{\varepsilon,t}$ , both as a function of energy. Both the mean full-energy peak efficiency curve and the peak-to-total curve can be described using the same parameterizations as in the non-voluminous case. In fact, by defining them as mean curves, they are identically defined as the non-voluminous ones. The voluminous nature of the source is described by the scaled variance,  $\eta$ , also as a function of energy, and by the constant  $\rho$ . The only thing that we need yet is a parameterization of the scaled variance

### 2.3.2 Parameterization of the stochastic approach: The Linear-to-squared curve

For practical reasons, it is beneficial to write

$$\eta^2 + 1 \equiv \frac{\text{var}[\varepsilon]}{E[\varepsilon]^2} + 1 = \frac{E[\varepsilon^2] - E[\varepsilon]^2}{E[\varepsilon]^2} + 1 = \frac{E[\varepsilon^2]}{E[\varepsilon]^2}. \tag{2.29}$$

This way, we notice that  $\sqrt{\eta^2 + 1}$ -values directly relate the volume-averaged linear efficiency  $\varepsilon$  to the volume-averaged squared efficiency  $\varepsilon^2$ . Therefore, instead of using the term *scaled variance*, and in accordance with calling the  $r$ -values “*peak-to-total*” or “*PT-ratios*”, the  $\sqrt{\eta^2 + 1}$ -values are referred to as “*linear-to-squared*” or “*LS-ratios*”. Since the LS-ratios depend on energy (see Eq. (2.23)), similarly,  $\sqrt{\eta^2 + 1}$ -curves are referred to as “*LS-curves*”. The reason for using LS-values instead of scaled variances is the possibility of calculating them by Monte Carlo simulation methods, which play an important part in the validation of the stochastic approach. The exact Monte Carlo method is described in the next Chapter.

To arrive at a sensible parameterization of the LS-curve, consider the following. The scaled variance,  $\eta$ , was introduced to take into account the variation of efficiency over the volume of a source. On the one hand, the variation can occur for geometrical reasons: the distance to the detector, or rather the solid angle varies over the volume of the source. On the other hand, it can vary because of  $\gamma$ -ray attenuation in the source volume. At high photon energies, where attenuation in the source is negligible, the variation is mainly determined by the source-detector geometry only (i.e. the solid angle), which is independent of energy. The linear-to-squared curve is therefore expected to have a horizontal asymptote for high energies, defined by one parameter,  $b_0$ . At lower energies, attenuation comes into play and the efficiencies will vary more strongly over the sample volume. The LS-ratio will be larger than at high energies. Since the probability of the photons interacting in the sample depends both on the sample density and on the average atomic number of the elements in the sample through exponential relations, two more parameters,  $b_1^2$  and  $b_2^2$  will be required. These considerations are reflected by the following functional form:

$$\sqrt{\eta^2 + 1} = b_0^2 + b_1^2 \left( \ln \frac{E}{E_0} \right)^{-b_2^2} \quad (2.30)$$

where  $b_0^2$  is the horizontal asymptote and  $b_1^2$  and  $b_2^2$  are related to the sample density and to the average atomic number. In this parameterization, all parameters are squared to ascertain that it yields only physically possible values for  $\sqrt{\eta^2 + 1}$ . The constraint  $\eta < 1$  implies that the LS-ratio should be smaller than  $\sqrt{2}$ . Since this constraint does not originate from the definition of  $\eta$  itself, but rather from its use in Equation (2.28), this constraint is not reflected in the parameterization of the LS-curve.

Figure 2.3 shows Monte Carlo simulated LS-ratios and a corresponding LS curve for a typical Marinelli beaker geometry. Indeed, for high energies, the LS-ratio approaches an asymptote of approximately 1.1. This value is determined from the varying detector distance over the source volume: photons originating from inner layers of the Marinelli beaker are detected more efficiently than those from outer layers because the effective

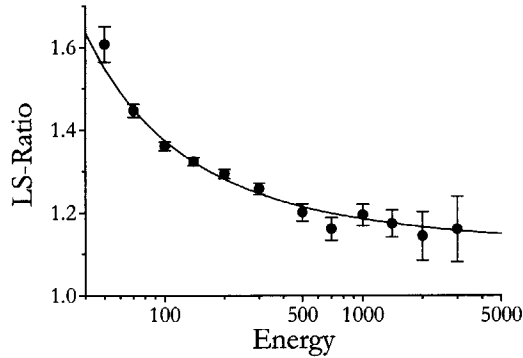


**Figure 2.3:** Example of simulated LS-values and a corresponding LS-curve for a typical Marinelli-beaker geometry.

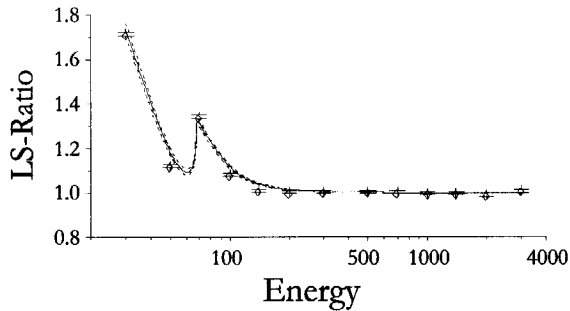


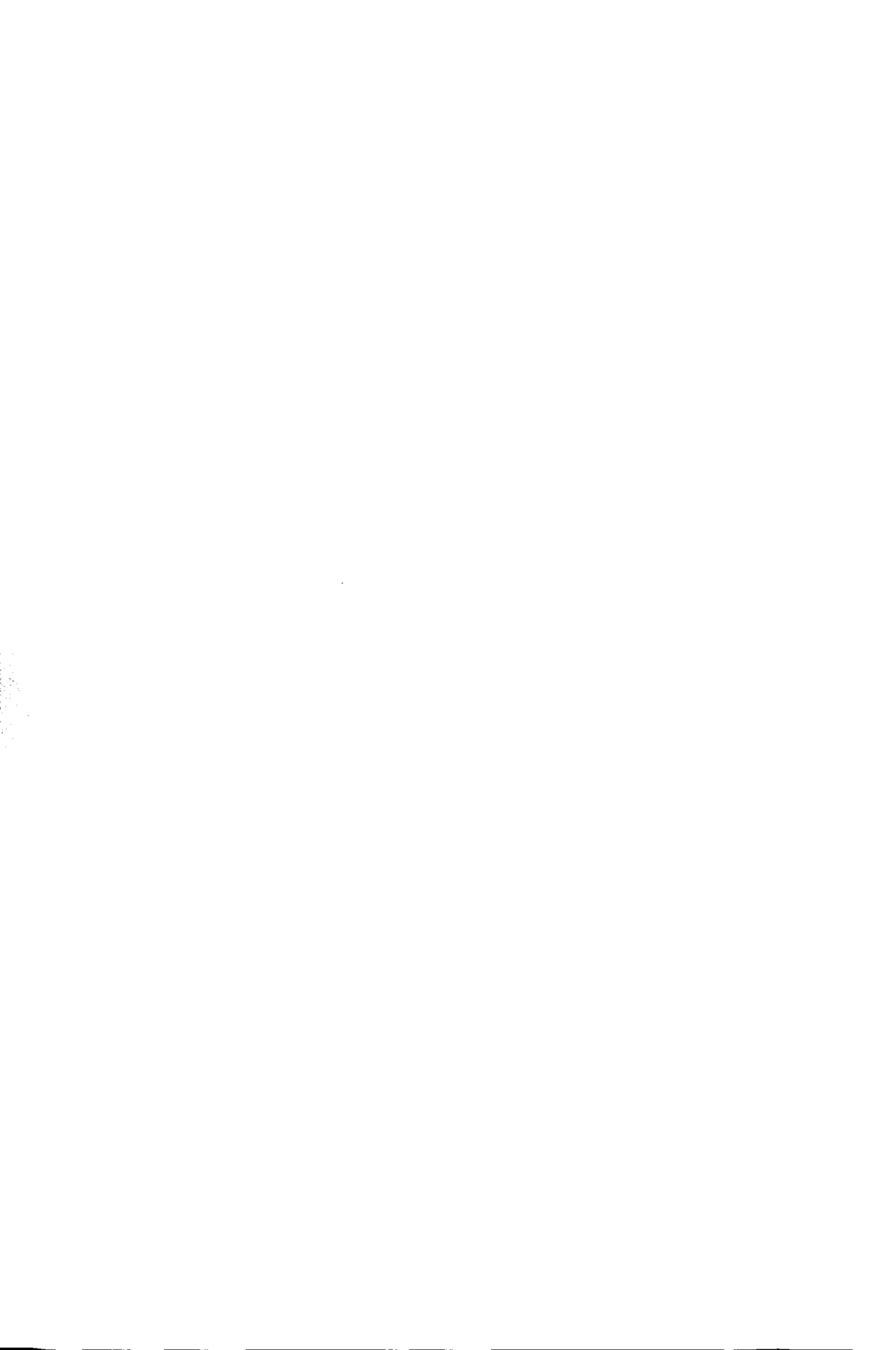
**Figure 2.4:** Example of simulated LS-values and a corresponding LS-curve for a high-Z source in a well-type geometry.

solid angle is larger. The lower the photon energies, the more the attenuation of  $\gamma$ -rays by the source matrix becomes important. Photons originating from the inner layers are detected yet more efficiently, resulting in higher LS-values. The figure shows that the parametrization of the LS curve allows it to follow the individual LS-ratios. For details about the simulation the reader is referred to section 3.3 of the next Chapter.

Figure 2.4 shows simulated LS-ratios and a corresponding LS-curve for a high-Z source in a well-type detector. The high energy asymptote has a value of 1.0. This means that for high energies, the source can be considered as a point source. For energies below approximately 100 keV, the attenuation by the high-Z matrix becomes important and the LS-ratio increases. Again, the parametrization of the LS-curve allows it to follow the simulated LS-values. Notice also the discontinuity owing to the K-edge of the matrix material. The parametrisation of this discontinuity is discussed in Chapter Six.

## References

- [1] G.F. Knoll, "Radiation detection and measurements", 3<sup>rd</sup> Ed., John Wiley & Sons, Inc., New York (2000)
- [2] M. de Bruin, *Pure Appl. Chem.*, **54** (1982) 1534
- [3] M. Blaauw, "The holistic analysis of gamma-ray spectra in instrumental neutron activation analysis", Ph.D. thesis, Delft University of Technology (1993)
- [4] IAEA Technical document 1049
- [5] R. Gunnink, *Nucl. Instr. and Meth.*, **A299** (1990) 372-376
- [6] R. Gunnink, A.L. Prindle, *J. Radioanal. Nucl. Chem., Articles*, **160** (1992) 305
- [7] M. Blaauw, M.J.J. Ammerlaan, S.J. Gelsema, *Nucl. Instr. and Meth.*, **A385** (1997) 330
- [8] R. Gunnink and J.B. Niday, *Proc. ERDA Symp. on X- and Gamma-Ray Source and Applications*, (Ann Arbor Science Publishers, Ann Arbor, MI, 1979) p55
- [9] R. Gunnink and J.B. Niday, *UCRL-51061*, Lawrence Livermore National Laboratory, Livermore, CA (1972)
- [10] R. Gunnink, W.D. Ruther and J.B. Niday, *UCRL-53861 vol.1*, Lawrence Livermore National Laboratory, Livermore, CA (1988)
- [11] F. de Corte, "The  $k_0$ -standardization method, A move to the optimization of neutron activation analysis", Agrégé thesis, Rijksuniversiteit Gent, (1987)
- [12] R.F. Fleming, *Int. J. Appl. Radiat. Isot.* **33** (1982) 1263.
- [13] K. Debertin, R. Jianping, *Nucl. Instr. and Meth.*, **A278** (1989) 541
- [14] F. de Corte, A. de Wispelare, L. Vancraeynest, P. de Neve, P. van den Haute, *Nucl. Instr. and Meth.*, **A353** (1994) 539
- [15] T.-K. Wang, T.-H. Ying, W.-Y. Mar, C.-L. Tseng, C.-H. Liao, M.-Y. Wang, *Nucl. Instr. and Meth.*, **A376** (1996) 192
- [16] H.N. Erten *et al.*, *J. Radioanal. Nucl. Chem., Articles*, **125** (1988) 3
- [17] X. Lin and K. Heydorn, *J. Radioanal. Nucl. Chem., Articles*, **169** (1993) 419



# Chapter Three

## Monte Carlo calculations

---

### Abstract

*This chapter describes the use of Monte Carlo simulation techniques for the calculation of efficiency curves and of  $\gamma$ -ray spectra. First, it describes the modelling of  $\gamma$ -interactions with matter in general. Then it focuses on each of the three main interaction types specifically: photoelectric absorption, incoherent “Compton” scattering and pair production. It is ascertained that the Monte Carlo code described here yields results identical to the widely available and evaluated code EGS4 when electron histories are disregarded. Since later chapters will use Monte Carlo calculations only to compare results with other Monte Carlo calculations, disregarding electron histories will not degrade the usefulness of the code.*

### 3.1 Introduction

The theory described in the previous chapter is validated for well-type detection geometries in Part II of this thesis and for Marinelli beaker type detection geometries in Part III of this thesis. For both, the validation is performed using simulation techniques as well as experimental techniques.

The validation of the theory using Monte Carlo methods requires several programs: for the calculation of both full-energy peak efficiency and total efficiency, for the calculation of I.S.-ratios and for spectrum simulations. All programs use the same Monte Carlo code that simulates the history of a single photon. This code is based on a code originally written by Overwater<sup>[1]</sup>. Initially, Overwater’s code took into account scattering processes only inside the active volume of the detector. The code has been modified to take into account scattering processes in all other materials as well. The code accounts for the three major types of photon interaction with matter, viz. photoelectric effect, Compton effect and pair production. It does not account for the history of electrons to which energy has been transferred during a photon interaction. It assumes that the energy from the photon is absorbed by the matter at the exact location of the interaction. In the

case of pair production, additionally it assumes two photons of  $m_e c^2$  to be created at that same location. For a simple geometry of a point source and a germanium crystal, it has been ascertained that the code yields results identical to the widely used Monte Carlo code EGS4<sup>[2]</sup>, EGS4 used with the option of simulating electron histories disabled. Since the results of the Monte Carlo calculations are only compared with each other, and are not used for calculation of real-life spectra, neglecting electron histories will not degrade the quality of tests.

The use of simulation techniques has several advantages over real-life measurements. First, with these techniques, all the curves needed to test the developed theory can be determined explicitly; in a real-life situation, it can be hard or even impossible to measure these curves directly. Second, possible errors in the decay-scheme data of the test radionuclides are circumvented, since both the procedure to simulate a test spectrum and the procedure that uses the theory to reproduce this spectrum use the same decay-scheme data. Deviations between the two procedures are therefore solely the results of errors, assumptions or simplifications of the theory.

### 3.2 Modelling of photon interactions

The most important interaction process at low  $\gamma$ - or X-ray-energies is the photoelectric effect (3.2.1), defined as the absorption of a photon with subsequent ejection of an atomic electron. For higher energies, the dominant interaction process is incoherent scattering, also known as Compton scattering (3.2.2): A photon is deflected with a reduction in energy, and an electron recoils out of the atom. For photon-energies higher than  $2m_e c^2$ , pair-production (3.2.3) becomes rapidly important: A photon is absorbed to produce an electron-positron pair. After transferring its kinetic energy to the scattering material, the positron annihilates with an electron, producing two secondary quanta each with an energy of  $m_e c^2$  and with opposite directions. A fourth interaction process is coherent or Rayleigh scattering: A photon is deflected with hardly any loss in energy, and the atom recoils as a whole under the impact. Its probability is largest in the low-energy region, but still an order of magnitude lower than that of the photoelectric effect. Therefore, and because there is practically no energy loss involved, Rayleigh scattering is disregarded in the modelling.

The Monte Carlo program characterizes a photon by its energy  $E$ , its origin and its direction. It characterizes the sample-detector environment by a list of objects, each object by its location, its dimensions and its composition in terms of density and atomic mass numbers  $Z_i$  of its constituting elements combined with their relative occurrence. When the program simulates the history of a photon, it first determines the geometrical path length  $\lambda$  for the object the photon travels through. It then decides where and if an interaction within that object occurs by evaluating the following condition,



$$\lambda_i = \frac{-\ln \xi}{\mu_{\text{total},E}} < \lambda, \quad (3.1)$$

where  $\lambda_i$  is the location of the interaction along the photon path,  $\xi = \mathbf{U}(0..1)$ , *i.e.* a randomly chosen number from a uniform distribution ranging from 0 to 1, and  $\mu_{\text{total},E}$  is the linear attenuation coefficient of the object material depending on the photon-energy. The linear attenuation coefficient is a summation of the linear attenuation coefficients for the different possible interactions,

$$\mu_{\text{total},E} = \mu_{\text{photo},E} + (\mu_{\text{coherent},E} \cong 0) + \mu_{\text{Compton},E} + \mu_{\text{pair},E}. \quad (3.2)$$

The Monte Carlo program calculates the various coefficients by logarithmic interpolation using tabulated nuclear scattering data from the XCOM program by Berger/Hubbel<sup>[3]</sup>.

If condition (3.1) holds, then the program decides that interaction indeed takes place and it determines the nature of the interaction according to:

$$\begin{array}{lll} 0 < \xi < \frac{\mu_{\text{photo}}}{\mu_{\text{total}}} & : \text{photo effect,} \\ \frac{\mu_{\text{photo}}}{\mu_{\text{total}}} < \xi < \frac{\mu_{\text{photo}} + \mu_{\text{Compton}}}{\mu_{\text{total}}} & : \text{Compton scattering,} \\ \frac{\mu_{\text{photo}} + \mu_{\text{Compton}}}{\mu_{\text{total}}} < \xi < 1 & : \text{pair production,} \end{array} \quad (3.3)$$

where, again,  $\xi = \mathbf{U}(0..1)$ . The program then calls the appropriate subroutine. Depending on the subroutine, one or two secondary  $\gamma$ -quanta can be returned, which are followed through the scattering environment identically to the primary quantum. If no interaction takes place, it shifts the origin of the  $\gamma$ -quantum to the point where it enters the next object, and the procedure is performed again.

One of the objects in the list that characterizes the sample-detector environment is labelled as being the detector. All energy-loss owing to scattering events in this object is recorded. By coupling the energy-loss to the energy of the primary  $\gamma$ -quantum, it becomes possible to calculate the various efficiency curves and even complete spectra.

### 3.2.1 Photoelectric absorption

Photoelectric absorption is modelled by simply eliminating the primary photon. The energy of the photon is fully transferred to the scattering medium. The history of the atomic ejected electron is not modelled. This means that the electron is supposed to lose its kinetic energy instantaneously. Also the X-rays following the ejection of the atomic electron are supposed to be absorbed completely by the crystal.

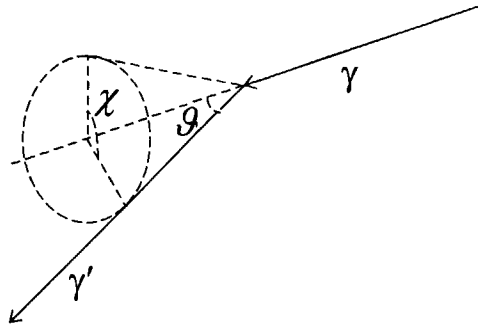


Figure 3.1: Compton scattering

### 3.2.2 Incoherent "Compton" scattering

The subroutine that models Compton scattering returns a secondary photon. The energy  $E'$  of this secondary photon is determined by sampling from the Klein-Nishina collision cross-section distribution and depends on the primary photon-energy. However, the Klein-Nishina differential collision cross-section  $d\sigma_c$  gives the probability of finding the secondary photon in a unit solid angle  $d\Omega = 2\pi \sin \theta d\theta^*$ ,

$$\frac{d\sigma_c}{d\Omega} \propto \left[ \frac{1}{1 + \alpha(1 - \cos \theta)} \right]^2 \left[ \frac{1 + \cos^2 \theta}{2} \right] \left[ 1 + \frac{\alpha^2 (1 - \cos \theta)^2}{(1 + \cos^2 \theta)[1 + \alpha(1 - \cos \theta)]} \right], \quad (3.4)$$

where  $\alpha = E/m_e c^2$  and  $\theta$  is the scattering direction (see Figure 3.1). Since the energy of the primary photon and the energy of the secondary photon are related by the scattering angle by\*

$$\alpha' = \frac{\alpha}{1 + \alpha(1 - \cos \theta)}, \quad (3.5)$$

Equation (3.4) can be written as

$$\frac{d\sigma_c}{d\Omega} \propto \frac{1}{2} \left( \frac{\alpha'}{\alpha} \right)^2 \left( \frac{\alpha}{\alpha'} + \frac{\alpha'}{\alpha} - \sin^2 \theta \right). \quad (3.6)$$

\* Equation obtained from [4]

The probability of finding the secondary  $\gamma$ -quantum with energy between  $\alpha'$  and  $\alpha'+d\alpha'$  is calculated with the aid of Equations (3.4) through (3.6) by

$$P_{\alpha,\alpha'} = \frac{d\sigma_c}{d\alpha'} = \frac{d\sigma_c}{d\Omega} \frac{d\Omega}{d\vartheta} \frac{d\vartheta}{d\alpha'} \propto \frac{1}{\alpha^2} \left( \frac{\alpha}{\alpha'} + \frac{\alpha'}{\alpha} - \frac{2}{\alpha'} + \frac{2}{\alpha} - \frac{2}{\alpha\alpha'} + \frac{1}{\alpha^2} - \frac{1}{\alpha'^2} \right). \quad (3.7)$$

Since at this point the Monte Carlo program already has established that Compton scattering indeed takes place, it can determine the energy of the secondary  $\gamma$ -quantum by solving the following integral equation numerically for  $\alpha'$ ,

$$\frac{\int_0^{\alpha'} P_{\alpha,\alpha'} d\alpha'}{\int_0^{\infty} P_{\alpha,\alpha'} d\alpha'} = \frac{\int_{\alpha'/1+2\alpha}^{\alpha'} P_{\alpha,\alpha'} d\alpha'}{\int_{\alpha'/1+2\alpha}^{\alpha} P_{\alpha,\alpha'} d\alpha'} = \xi, \quad (3.8)$$

where the boundaries of the integration are determined by physical limits and  $\xi = \mathbf{U}(0..1)$ . The corresponding scattering angle is determined using Equation (3.5). To fully determine the direction of the secondary  $\gamma$ -quantum, an azimuth angle  $\chi = \mathbf{U}(0..2\pi)$  is selected.

### 3.2.3 Pair production

Like photoelectric absorption, pair production is modelled by simply eliminating the primary  $\gamma$ -quantum. Two secondary  $\gamma$ -quanta are created, each with energy  $m_e c^2$  and in random directions relative to the direction of the primary  $\gamma$ -quantum, but in opposite directions relative to each other. The energy of the  $\gamma$ -quantum minus  $2m_e c^2$  is transferred to the scattering medium. Again, the history of the positron and the electron is not modelled, i.e. the secondary  $\gamma$ -quanta are created at the exact location of the interaction.

## 3.3 Determination of full-energy peak efficiency-, PT- and LS-curves, and correlation values

To determine a volume-averaged full-energy peak efficiency curve, for the detection geometries described in later chapters, volume-averaged full-energy peak efficiency values  $\varepsilon$  are calculated for twelve energies in the range of 50...3000 keV, approximately equally spaced on a logarithmic scale. For each of the energies, a large number of photons is created randomly in the source volume and followed through the detection geometry. The number of times is counted that the total energy of the photon is deposited in the active volume of the detector. Dividing this number by the total number of generated photons

yields the efficiency value  $\bar{\varepsilon}$ . The total number of photons is to be taken large enough to obtain an imprecision for  $\bar{\varepsilon}$  lower than 0.5%. A full-energy peak efficiency curve  $\varepsilon(E)$  can then be fitted to the twelve  $\bar{\varepsilon}$ -values using Gunnink's efficiency curve (Section 2.2.1). Typically, the fit is accurate within 1% for any detection geometry for all energies up to 1000 keV and within 3% for energies up to 3000 keV.

Similarly, to determine PT-curves, volume-averaged total efficiency values  $\bar{\varepsilon}_t$  can be calculated by counting the number of times that any part of the original photon energy is deposited in the active volume of the detector, and dividing this number by the total number of generated photons. Again, the imprecision of the total efficiency values should be lower than 0.5%. Peak-to-total ratios  $r$  can then be calculated from the  $\bar{\varepsilon}$  and  $\bar{\varepsilon}_t$ -values. A peak-to-total curve  $r(E)$  can be fitted to the PT-ratios, using a straight line on double-log scale. Thus, in essence, two parameters were used to describe the peak-to-total curve. A third peak-to-total parameter limits the curve to physical values (Section 2.2.2).

To determine LS-curves, squared efficiency values  $\bar{\varepsilon}^2$  can be calculated essentially in the same manner as the  $\bar{\varepsilon}$ -values. However, now two photons of the same energy are followed simultaneously through the detection geometry. The number of times is counted that the total energy of both photons was deposited in the active volume of the detector. The imprecision for the squared efficiency values should typically be lower than 1% for energies between 70 and 700 keV and lower than 5% for all energies. Linear-to-squared ratios are calculated from these values using Equation (2.29). A Linear-to-squared curve can then be fitted to the individual LS-ratios using the empirical relation (2.30) given in Chapter Two:

$$\sqrt{\eta^2 + 1} = h_0^2 + h_1^2 \left( \ln E/E_0 \right)^{-h_2} \quad (3.9)$$

Finally, the determination of correlation coefficients  $\rho$ , for the detection geometries described in later chapters is somewhat less straightforward. This is owing to the fuzzy approach of replacing all correlations by a single parameter (see 2.3.2). Equation (2.25) forms the basis for this determination. This equation is rewritten as

$$\rho_{i,j} = \frac{\mu_{i,j} / \mu_i \mu_j - 1}{\eta_i \eta_j} \quad (3.10)$$

First,  $\mu_{ij}$  are estimated by  $\overline{\varepsilon_i \varepsilon_j}$ -values, which can be calculated for any combination of energies, by following two photons of different energy and, again, counting the number of times the total energy of the two photons was detected. The imprecision obtained for

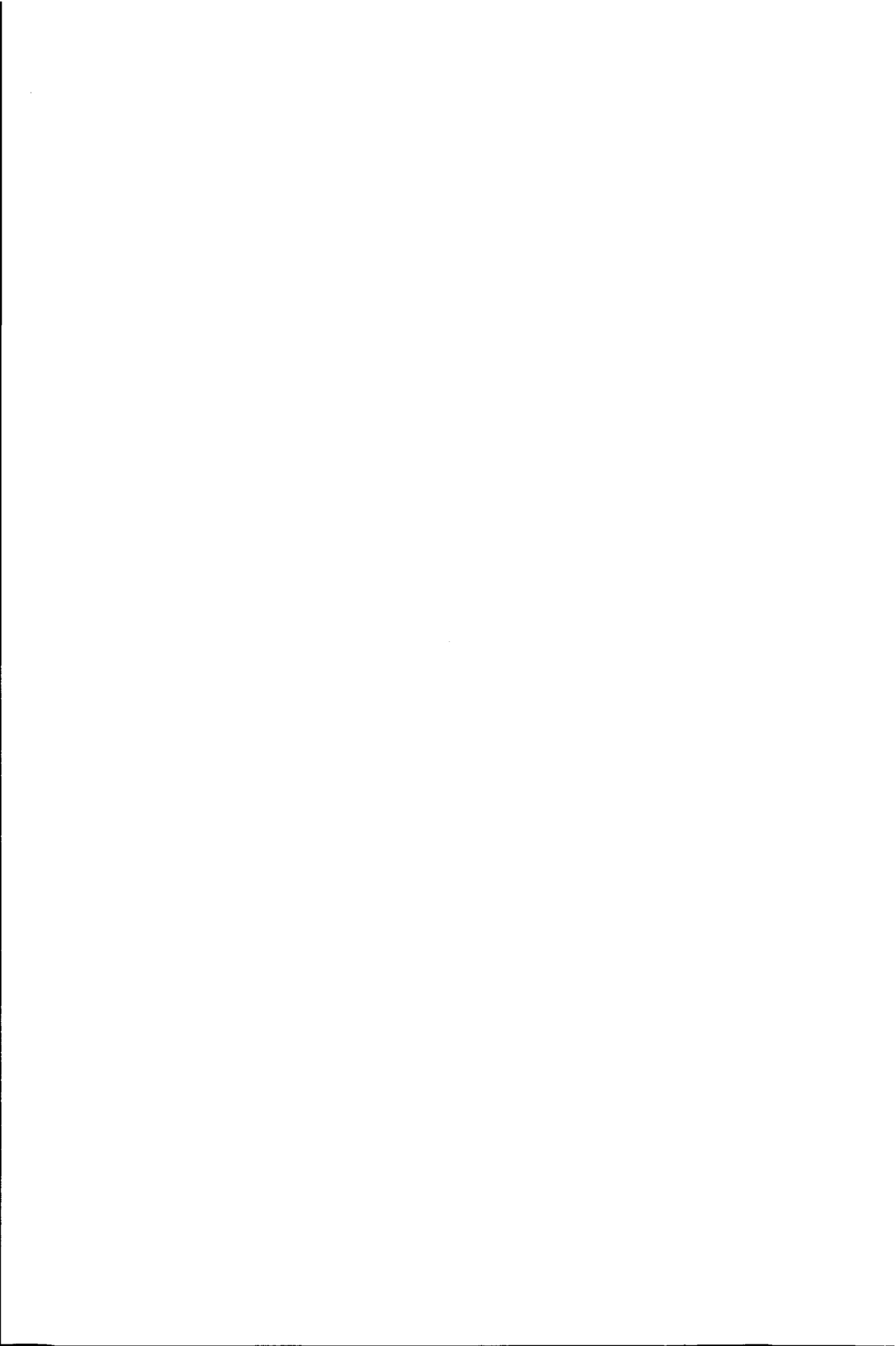
the  $\overline{\varepsilon_i \varepsilon_j}$ -values is typically lower than 3% for energies between 100 and 700 keV and 5% for energies outside this range.  $\mu_i$ , estimated by volume-averaged full-energy peak efficiency values  $\overline{\varepsilon_i}$ , and  $\eta_i$  are determined as described above. Thus, for any combination of energies, a correlation coefficient can be calculated. The final correlation coefficient  $\rho$  simply is the average value of all  $\rho_{ij}$ .

### 3.4 Spectrum simulation

For any geometry, the spectrum of any radionuclide can be simulated by following a large number of batches of photons through the detection geometry. Each batch then contains the photons from a possible cascade from the decay-scheme of the daughter from a fed level to the ground state. Thus, each batch simulates the disintegration of one single nucleus. The specific cascade is determined by Monte Carlo methods too, using the decay-scheme data from Firestone<sup>[5]</sup>. The spectrum is then reconstructed by calculating the energy that was deposited in the active volume of the detector by all photons in the batch. If the deposited energy is equal to the energy of a (sum)peak, a count is added to that peak. The number of disintegrations, effectively the number of batches, determines the imprecision for the areas of the peaks in the spectrum.

### References

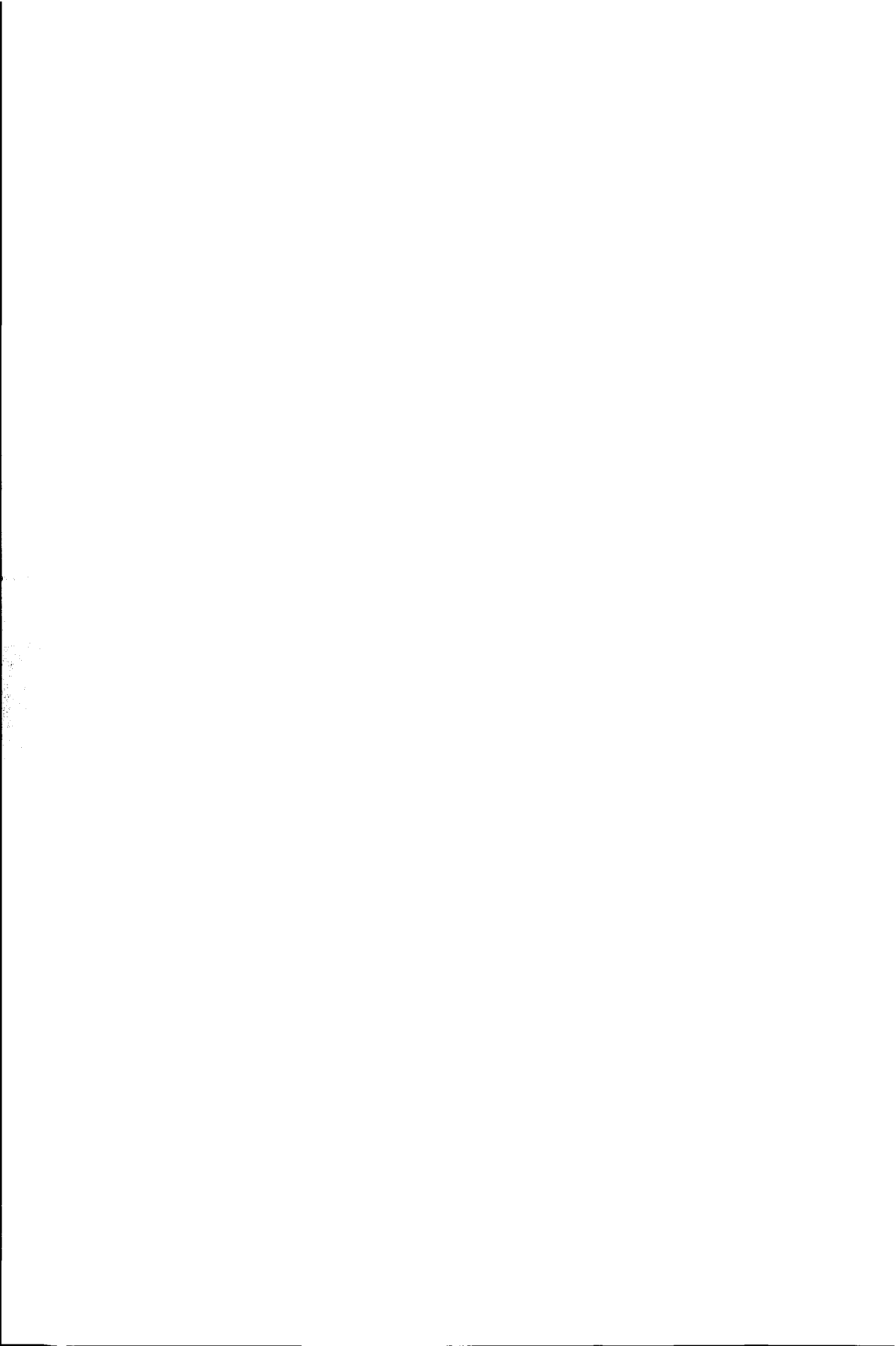
- [1] R.M.W. Overwater, P. Bode, J.J.M. de Goeij, *Nucl. Instr. and Meth.*, **A324** (1993) 209
- [2] W.R. Nelson, H. Hirayama, D.W.O. Rogers, "*The EGS4 code system*", SLAC-Report-265 (1985)
- [3] M.J. Berger, J.H. Hubbell, "*XCOM: Photon cross sections on a personal computer*", NBSIR 87- 3597.(1987)
- [4] R.D. Evans, PhD., "*The atomic nucleus*", McGraw-Hill book company, Inc., New York (1955) p.672
- [5] R.B. Firestone, V.S. Shirley, C.M. Baylin, S.Y.F. Chu, J. Zipkin, "*Table of Isotopes*", CD-ROM Edition 1.0, John Wiley & Sons inc., New York (1996)



# Part II

## Well-type detection geometries

---





# Chapter Four

## Geometry effects in well type detectors owing to the introduction of high- $Z$ linings

---

### Abstract

*In well-type detectors and other highly efficient geometries, the combined effects of sample self-attenuation involving low-energy photons and coincidence summing of a low- and a high-energy photon often influence the entire  $\gamma$ -spectrum of a radionuclide. For well-type detectors, these effects are well understood and it should be possible to correct for these effects analytically. Another possibility to deal with these effects is to prevent the low-energy photons from reaching the detector by lining the well with a high- $Z$  material, as was suggested in the past.*

*This chapter presents a series of measurements which indicates that the problems resulting from sample self-attenuation and coincidence summing should be treated analytically rather than by attempts to eliminate the effects by means of a lining.*

### 4.1 Introduction

In  $\gamma$ -ray spectroscopy, Ge(Li)- and HPGe-detectors are most commonly used. Compared with NaI scintillation detectors they have a very high-energy resolution but a lower detection efficiency. To increase detection efficiency, efficient counting geometries, such as the well-type geometry, are applied.

A major advantage of well-type detectors is the detection efficiency being nearly constant within a range of source positions near the bottom of the well and therefore, when not considering sample self-attenuation effects, being nearly independent of sample dimensions within this range. Although the increased detection efficiencies may give rise to considerable cascade summing effects, these effects can be corrected for, mainly because the detection efficiency often can be considered independent of sample geometry.

In 1978, de Bruin *et al.*<sup>[11]</sup> found that owing to the large summation effects, peak areas of high-energy peaks of a  $\gamma$ -ray spectrum were influenced by the attenuation of low-energy photons in the sample, and therefore were matrix-dependent. The authors suggested the use of a high-Z lining inside the detector well, which absorbs the low-energy photons to such an extent that summation with these photons could be neglected or at least could be considered matrix-independent.

More recent measurements indicated that, although the introduction of the lining in the well indeed reduces the matrix-dependency of the  $\gamma$ -ray spectra, a geometry-dependency is introduced. As a consequence coincidence effects cannot be treated separately from sample dimensions. To investigate the geometry-dependency of spectra from lined well-type detectors more extensively we performed calculations on the attenuation of the lining and we performed a series of measurements on radionuclides emitting several photons in cascade, in a well-type geometry with and without a lining and at varying source positions.

#### 4.2 Theoretical considerations

Consider a radionuclide with a decay scheme as shown in Figure 4.1. The count-rates of the three full-energy peaks can be calculated from the detection efficiencies for the specific combination of detector and sample for the three energies.

When assuming that internal conversion is absent, and with  $X_{ij}$  representing the probability of transition from the  $i$ -th to the  $j$ -th level, thereby emitting  $\gamma_{ij}$ ,  $\varepsilon_{\text{tot},ij}$  the total detection efficiency for  $\gamma_{ij}$ ,  $\varepsilon_{ij}$  the full-energy peak efficiency for  $\gamma_{ij}$ ,  $c_{ij}$  the full-energy count-rate for  $\gamma_{ij}$  [ $\text{s}^{-1}$ ], and  $A$  the disintegration rate [ $\text{Bq}$ ], then  $c_{10}$ ,  $c_{20}$  and  $c_{21}$  are given by

$$\begin{aligned} c_{10} &= A X_{21} \varepsilon_{10} (1 - \varepsilon_{\text{tot},21}), \\ c_{20} &= A (X_{20} \varepsilon_{20} + X_{21} \varepsilon_{21} \varepsilon_{10}), \\ c_{21} &= A X_{21} \varepsilon_{21} (1 - \varepsilon_{\text{tot},10}). \end{aligned} \quad (4.1)$$

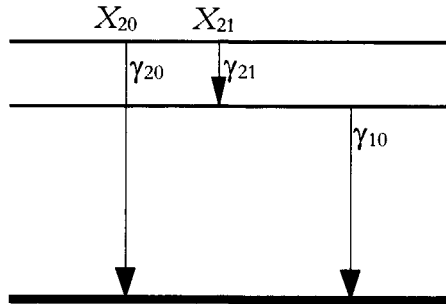


Figure 4.1: Hypothetical decay scheme

For  $\gamma_{21}$  lower than approximately 120 keV, and both  $\gamma_{10}$  and  $\gamma_{20}$  much higher than  $\gamma_{21}$ , only  $\gamma_{21}$  will be subject to substantial self-attenuation effects for samples normally measured in well-type detectors. Since self-attenuation of  $\gamma_{21}$  reduces both  $\epsilon_{21}$  and  $\epsilon_{\text{tot},21}$ ,  $\gamma_{21}$  will not only have a decreasing effect on  $\epsilon_{21}$ , but it will also have a decreasing effect on  $\epsilon_{20}$ , and an increasing effect on  $\epsilon_{10}$ .

As mentioned above, a solution to this problem of matrix-dependent distortion of the  $\gamma$ -ray spectrum is to prevent the low-energy photons from reaching the detector, by applying a high-Z absorber inside the well, between the source and the Ge-crystal<sup>[1]</sup>. A typical lining consists of a tube of gold with wall- and bottom-thickness between 0.5 and 1 mm (Figure 4.2) which tightly fits inside the well of the detector.

Let us consider again the radionuclide from Figure 4.1, positioned as a point source at the two different positions in the well indicated by Figure 4.2. As can be seen, the

average distance a photon travels through the absorber lining is much larger for a photon generated by a source at the bottom of the well than for a photon generated by a source located higher in the well. As a result, the transmission through the absorber of  $\gamma$ -rays of low-energy emitted by the two sources will differ, as will the detection efficiency.

To describe the influence of the lining on the detection efficiencies we should introduce a transmission-factor of the lining as a function of energy and position, which we define as the fraction of photons of energy  $E$  emitted by a source in the well which do not lose any part of their energy in the absorber. This factor  $T(E, h)$  can be calculated by first calculating the transmission for a photon of energy  $E$ , emitted at height  $h$ , in the direction characterized by  $\varphi$  and  $\theta$ , and then averaging over all possible angles  $\varphi$  and  $\theta$ ,

$$T(E, h) = \frac{\int_0^{2\pi} \int_0^\pi \exp\left(-\frac{\mu_{Z,E}}{\rho} \rho \lambda_{h,\theta}\right) \sin(\theta) d\theta d\varphi}{\int_0^{2\pi} \int_0^\pi \sin(\theta) d\theta d\varphi}, \quad (4.2)$$

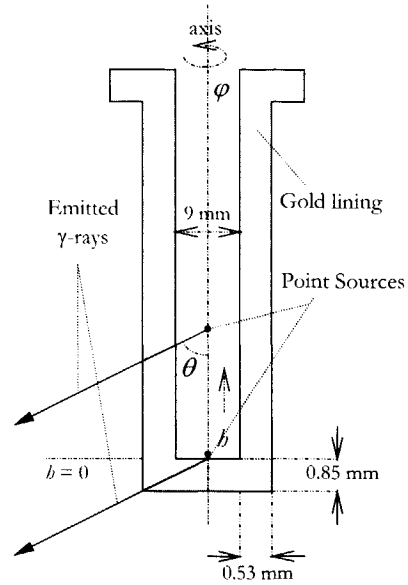


Figure 4.2:  $\gamma$ 's emitted from different positions have different travel lengths through the lining.

where  $\varphi$  is the azimuth integration angle (azimuth direction of an emitted photon),  $\theta$  is the polar integration angle (polar direction of an emitted photon),  $Z$  is the atomic number of lining material,  $\mu_{Z,E}/\rho$  is the total mass attenuation coefficient as a function of  $Z$  and  $E$  [keV] in [ $\text{m}^2\cdot\text{kg}^{-1}$ ],  $\rho$  is the density of the lining material in [ $\text{kg}\cdot\text{m}^{-3}$ ],  $b$  is the distance from the bottom of the well to the position of photon emission in [m], and  $\lambda(b,\theta)$  is the distance a photon travels through the lining, as a function of  $b$  and  $\theta$  in [m]. It should be noted that this expression only gives the transmission coefficient for a source located at height  $b$  along the axis of the well.

In addition we also introduce an average total transmission factor  $T_{\text{tot}}(E,b)$  of the lining, defined as the fraction of photons emitted by a source in the well which is not absorbed totally by the absorber lining. A precise analytical expression for  $T_{\text{tot}}$  is difficult to give because of the possibility of photons being Compton-scattered once or several times before being absorbed totally. The photons resulting from these scattering events will not have the same energy as the incoming photon, which means that the attenuation coefficient  $\mu/\rho$  will differ between scattering events.

Very low-energy photons will be absorbed by the lining and as a result both  $T$  and  $T_{\text{tot}}$  will be 0 for all positions in the well. This was of course the reason for introducing the lining. For high-energy  $\gamma$ -rays, almost all photons will pass through the lining without any energy loss, resulting in a value of  $\sim 1$  for both  $T$  and  $T_{\text{tot}}$ , for all positions. For intermediate energies  $T$  and  $T_{\text{tot}}$  will have (different) values between 0 and 1, and depend on the position  $b$  of the source in the well.

If we consider the lining as an integral part of the detector, the full-energy peak efficiency  $\varepsilon$  of this detector will be proportional to  $T$ , and the total efficiency  $\varepsilon_{\text{tot}}$  will be dependent on  $T_{\text{tot}}$ . Because in some energy range, both transmission coefficients are dependent on  $b$ , both efficiencies are as well. Thus, from theoretical considerations we can expect that one of the main advantages of a well-type detector, namely the aforementioned geometry-independency of the efficiency, will be impaired when using a high- $Z$  lining.

Moreover, this geometry dependency is not only restricted to 'intermediate' energies. By applying the same arguments from the beginning of this section to these position-dependent efficiencies we can see that owing to coincidence summing effects, the lining causes position-dependent distortions of the whole  $\gamma$ -ray spectrum of radionuclides emitting several photons in cascade.

Calculations of the transmission  $T$  of the lining, by numerically solving the integrals in Equation (4.2) for different energies and for infinite height of the lining, show that the position-dependency of the transmission is largest for photon energies in the order of 120 keV. Figure 4.3 shows the theoretical variation with height of  $T$  for energies in the range of 50 keV to 1 MeV. The curves are normalized to 1 for infinite heights so that the relative variation of the transmission for the different energies can be compared.

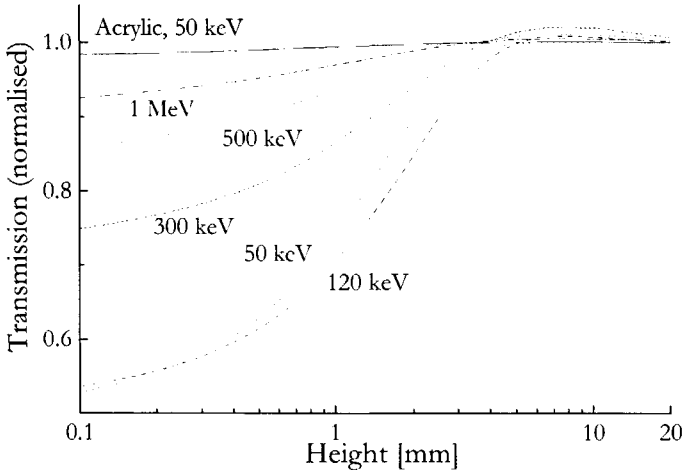


**Figure 4.3:** Theoretical transmission through a gold lining of typical dimensions (Figure 4.2) for photons of different energies, and through an acrylic lining for photons of 50 keV as a function of height. Curves are normalized to 1 for infinite heights. The bottom of the well is at  $b = 0.0$  mm.

### 4.3 Methods and measurements

To investigate the extent of spectrum variations owing to the high-Z lining in the well, we measured a europium-152 point source, a tantalum-182 point source and a selenium-75 point source, each with two different linings and at varying heights in a well-type detector. In the decay scheme of europium-152 and tantalum-182, high-energy  $\gamma$ -transitions are preceded or followed by a low-energy transition (for example 1408 and 122 keV respectively for europium-152). The selenium-75-spectrum has a 401 keV peak mainly owing to summation of a 136 keV and a 265 keV peak in the spectrum.

For our measurements we used a Philips well-type Ge(Li)-detector with absolute full-energy peak efficiencies of 0.5 and 0.05 at 122 keV and 1115 keV respectively, for sources positioned at or near the bottom of the well. The well lining consisted of a tube of either acrylic or gold with a wall thickness of 0.53 mm, and a flat bottom with a thickness of 0.85 mm. To position the sources in the well several solid acrylic cylinders were made with heights varying in the range of 0.25 to 15 mm. The geometry used is shown in Figure 4.4

With a value of  $0.2 \text{ cm}^{-1}$  for  $(\mu/\rho)\cdot\rho$  at 50 keV, it can be asserted that photons with energies greater than 50 keV are absorbed by the acrylic lining only to a very limited extent. In addition to the transmission curves for a typical gold lining, Figure 4.3 also shows the transmission through an acrylic lining for 50 keV photons. The nominal value

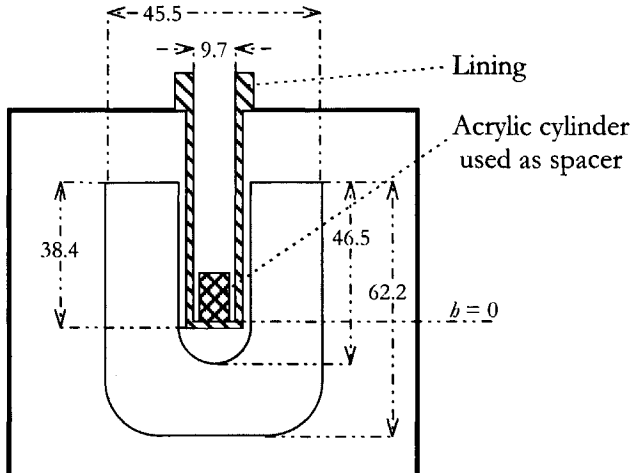


Figure 4.4: Geometry used. The lining consisted of either acrylic or gold.

for infinite height of this  $T$ , as calculated with Equation (4.2) is 0.98. Therefore, we state that the acrylic lining only has negligible influence on the detection efficiency of the well. Other effects on counting efficiencies, such as varying solid angle and varying attenuation of photons in the spacers, are eliminated by dividing the count-rates measured in the gold-lined geometry by those measured in the acrylic-lined geometry.

In addition to the europium-152-, the tantalum-182- and the selenium-75-spectra, we also measured the spectrum of sodium-22. The decay scheme of sodium-22 consists of one transition of 1275 keV. The photon emitted with this transition does only coincide with two 511 keV gammas, produced with the annihilation of the  $\beta^+$ -particle emitted with the decay of sodium-22 to neon-22. Because both photon energies lie outside the region where the variation of detection efficiency is large (Figure 4.3), the well behaves nearly ideally for these energies. This means that although the 1275 keV and the two 511 keV gammas do not originate from the same point, because of the range of the  $\beta^+$ -particle, one should expect a negligible variation of the 1275 keV full-energy peak efficiency. Measuring the spectrum of sodium-22 thus gives the possibility to check if auxiliary effects on detection efficiencies indeed are eliminated by the division method mentioned in the previous paragraph. This does not mean, however, that the 1275 keV peak areas of sodium-22 measured in the two geometries are the same. Since 20% of the 511 keV photons and only 8% of the 1275 keV photons are absorbed by the gold lining, one expects greater summing-out effects in the acrylic-lined case. Therefore, the ratio of the 1275 keV peak area measured in gold-lined to that measured in the acrylic-lined geometry can be expected to be somewhat greater than 1.

**Table 4.1:** Ratio of tantalum-182 peak areas measured with gold lining to those measured with acrylic lining. The difference is given relative to the lowest ratio.

<sup>182</sup> Ta	lowest ratio	highest ratio	difference [%]	<sup>182</sup> Ta	lowest ratio	highest ratio	difference [%]
68 keV	0.19	0.27	42	1189 keV	1.06	1.09	2.8
100 keV	0.060	0.095	58	1221 keV	1.34	1.44	7.5
152 keV	0.35	0.46	31	1231 keV	1.80	1.81	0.6
156 keV	0.38	0.50	32	1274 keV	0.51	0.61	20
179 keV	0.79	1.03	30	1289 keV	0.30	0.34	13
198 keV	0.73	0.94	29	1374 keV	0.33	0.42	27
264 keV	0.85	0.96	13	1387 keV	0.55	0.73	33
1002 keV	2.61	2.82	8.0	1474 keV	0.58	0.72	24
1121 keV	1.80	1.93	7.2				

#### 4.4 Results

The results of the measurements are summarized in Table 4.1 and Figure 4.5 to Figure 4.9. Figure 4.5a-b show the general shape of the peak area curve as a function of height for selenium-75, for the acrylic-lined- and the gold-lined geometry respectively. The ratios of the selenium-75-peak areas measured with gold lining to those measured with acrylic lining are given in Figure 4.6. Figure 4.7 and Figure 4.8 show the general shape of a 'peak area-ratio curve' as a function of height, for one particular set of transitions for europium-152 and tantalum-182, respectively. Figure 4.9 shows the result for sodium-22. This figure indicates that there is no significant variation in the detection efficiency for this radionuclide. The degree of variation of the full-energy peak efficiency for tantalum-182-lines is given in the table. For each characteristic gamma energy, the highest and lowest peak area-ratios in the series of measurements for different heights are given, together with the difference between the two, relative to the lowest ratio.

#### 4.5 Discussion and conclusions

Section 4.3 has asserted that counting efficiencies of gammas with energies greater than 50 keV are not noticeably influenced by the acrylic lining. Figure 4.5a (acrylic-lined geometry) therefore shows the behaviour of a well without a lining. One notices that for source-positions lower than 10 mm from the bottom of the well, the peak areas of selenium-75 do not depend on the position, so the well behaves ideally for these heights. When the source is moved from this position towards the entrance of the well, the effect of a smaller solid angle starts playing a role in the detection efficiency of the well, resulting in less summation of the 136 keV and 265 keV gammas. As the figure shows, the 401 keV peak area becomes smaller. For the 136 and 256 keV peaks there are two competitive effects resulting from a decreasing full-energy-peak efficiency namely, first, a decreasing peak area owing to less efficient detection, and second, summing-out effects becoming

smaller resulting in an increasing peak area. It can be shown that for relatively high detection efficiencies the latter effect plays the most important role as is illustrated in the figure. This result shows that this well-type detector (without lining) should be operated with sample positions in the range of 0 to 10 mm.

However, if a high-Z lining is introduced (Figure 4.5b), then there is no range of possible sample-positions where the peak areas of selenium-75 are constant. In the first 10 mm the transmission of the lining varies as can be expected from the theory. Notice that the reduction of the 136 keV and the 265 keV full-energy peak efficiency as compared to the acrylic-lined geometry reduces both the 136 keV and the 401 keV peak areas, but increases the 256 keV peak area. Notice too that for sample positions higher than 10 mm the peak areas all drop owing to the smaller solid angle. Apparently the lining

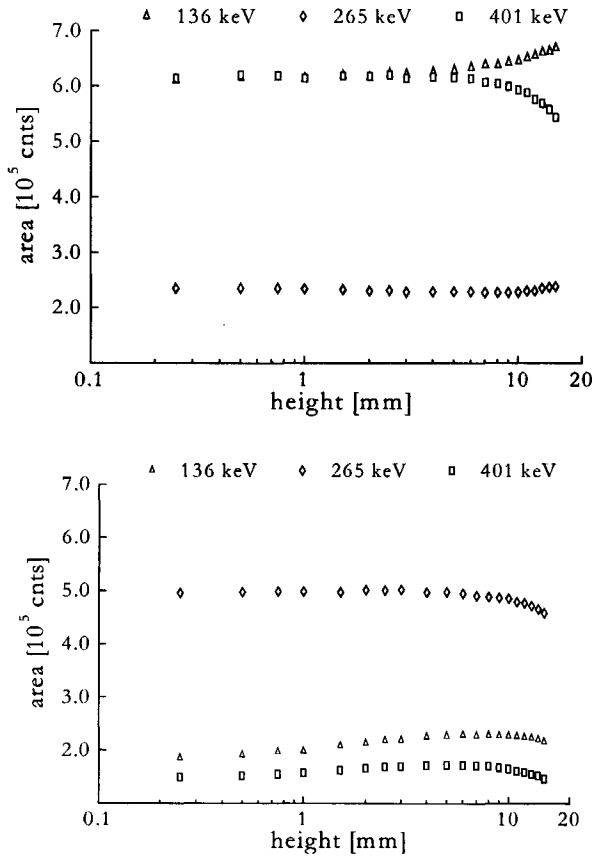


**Figure 4.5:** Peak areas of selenium-75 measured in the acrylic-lined geometry (top) and in the gold-lined geometry (bottom). One-sigma error bars are drawn.



has decreased the 136 keV and 265 keV full-energy peak efficiency to such an extent that the summing out effects play a less important role than the detection efficiency itself, thus resulting in decreasing peak areas.

By dividing the results, we eliminated all effects on counting efficiencies which lie beyond the scope of this study. Thus, the ratios presented in Table 4.1 and Figure 4.6 to Figure 4.9 only depend on the effect of the gold lining. As one should expect, the ratio of counting efficiencies for the 1275 keV peak of sodium-22 does not change as the position of the source changes, which proves that our method is valid.

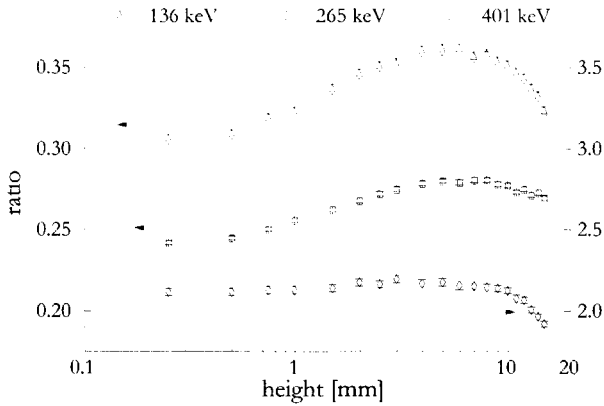


Figure 4.6: Ratio of peak areas of selenium-75 measured in the gold-lined geometry to those measured in the acrylic-lined geometry. One-sigma error bars are drawn

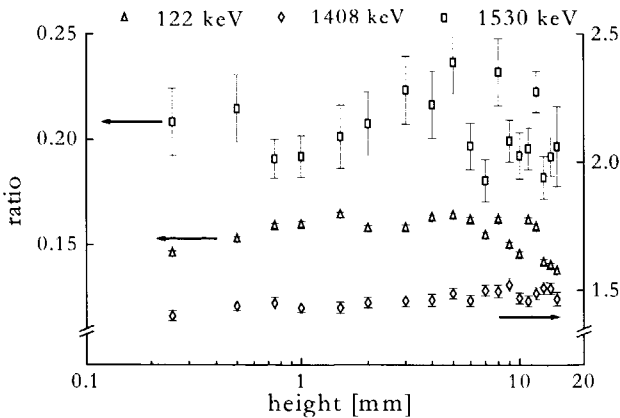
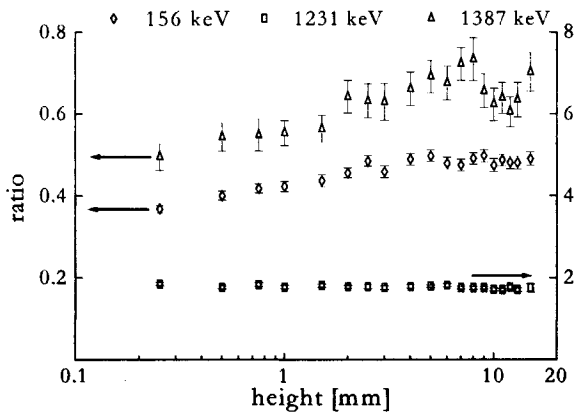
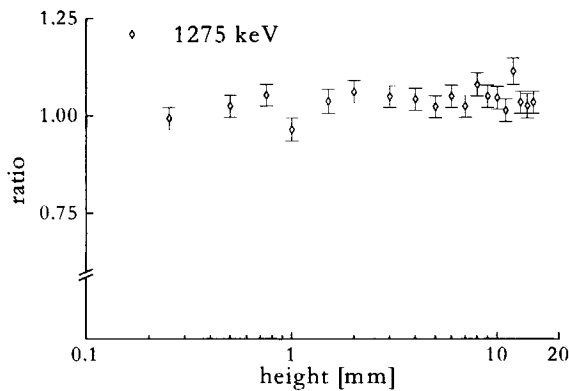


Figure 4.7: Ratio of peak areas of europium-152 measured in the gold-lined geometry to those measured in the acrylic-lined geometry. One-sigma error bars are drawn

The results of our measurements show that owing to the introduction of the gold lining, the counting efficiencies for  $\gamma$ -rays with energies around 100 keV become dependent on the position of the source in the well. This means that lined well-type detectors do not have the major advantage of normal well-type detectors, namely the efficiency being independent of source position or dimensions. This fact itself could be considered as a disadvantage of a high- $Z$  lining. Owing to the high detection efficiency of well-type geometries, resulting in large summation effects, the position- and sample dimension-dependent efficiency for low-energy  $\gamma$ -rays can cause variations in the detection efficiency for high-energy  $\gamma$ -rays. In the case of tantalum-182 we found variations of over 25 percent



**Figure 4.8:** Ratio of peak areas of tantalum-182 measured in the gold-lined geometry to those measured in the acrylic-lined geometry. One-sigma error bars are drawn



**Figure 4.9:** Ratio of peak areas of sodium-22 measured in the gold-lined geometry to those measured in the acrylic-lined geometry. One-sigma error bars are drawn

for  $\gamma$ -rays with energies higher than 1 MeV, when varying the position of the source by several millimetres. These variations can cause serious problems in quantitatively interpreting measured spectra. In general this means that coincidence summing effects occurring in high-Z lined well-type detectors cannot be treated separately from sample dimensions and position.

It is clear that the geometric form of the lining plays an important role in the occurrence of geometry effects in the well-type detector. One might be tempted to think of some form for which the transmission coefficient does not change with height. However, looking at Equation (4.2), one should realize that this form would in general only give good results for one single energy, and only for either  $T$  or  $T_{\text{tot}}$ .

Thus, sample self-attenuation problems cannot be solved by applying a high-Z lining inside the well, and the solution should be searched for in other areas. For coaxial Ge-detectors it is proven to be possible to calculate the amount of sample self-attenuation from a measured spectrum itself<sup>[2]</sup>. M. Blaauw<sup>[3]</sup> showed the possibility of determining efficiencies from a spectrum in the presence of coincidences. Based on these considerations we are exploring methods to calculate the amount of sample self-attenuation from a spectrum, measured in a well-type detector.

## References

- [1] M. de Bruin, P.J.M. Korthoven, P. Bode, *Nucl. Instr. and Meth.*, **A159** (1979) 301
- [2] P. Bode, M. de Bruin, P.J.M. Korthoven, *J. Radioanal. Chem.*, **64** (1981) 153
- [3] M. Blaauw, *Nucl. Instr. and Meth.*, **A332** (1993) 493



# Chapter Five

## The influence of counting geometry and lining on the Compton continuum in well-type detectors

---

### Abstract

*To demonstrate the influence of counting geometry on the performance of a well-type detector, as represented by the PC- and PT-ratio, caesium-137 and cobalt-60 sources were measured at 30 cm distance from the well and in the well; the latter both with and without a gold lining. Observed differences in the Compton continua are discussed. A significant increase in PC- and PT-ratios for caesium-137 is found when repositioning the source from 30 cm distance to a position in the well. For cobalt-60, only the PT-ratio shows a similar behaviour. It is concluded that the detector performs best when counting the source in the well without a lining. It is also concluded that, even though the PT-ratio is preferred as an index of performance, only mono-gamma emitting radionuclides should be used when measuring PC-ratios of a well-type detector.*

### 5.1 Introduction

To increase the detection efficiency of germanium detectors, efficient counting geometries such as the well-type geometry are applied. The increased detection efficiencies may give rise to considerable cascade summing effects which, however, can be corrected for. Apart from a higher efficiency of well-type detectors, an increase in peak-to-Compton ratio was reported<sup>[1]</sup>, but no explanation was given.

At IRI, it was found that owing to the summation effects, peak areas of high-energy peaks were influenced by the attenuation of low-energy photons in the sample, and therefore were matrix-dependent<sup>[2]</sup>. To avoid summation, our well-type detectors were lined with a high-Z material. The lining absorbs low-energy photons to such an extent that summation with these photons now can be neglected or at least can be considered matrix-

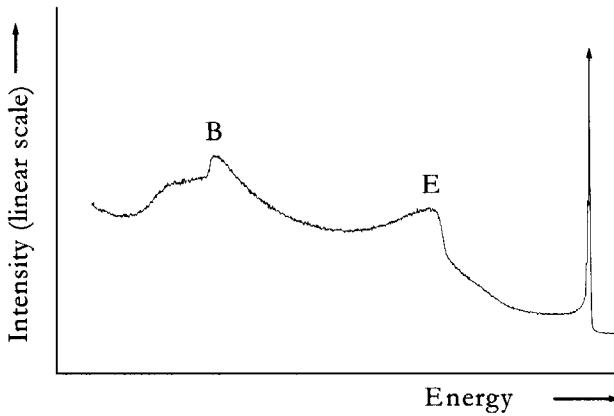


**Figure 5.1:**  $\gamma$ -Ray spectrum from a Ge(Li)-detector (Well-type). B denotes the backscatter peak; E denotes the Compton edge.

independent<sup>[2]</sup>. Since it was observed in Chapter Four that the lining introduces a geometry dependency of the spectra<sup>[3]</sup>, methods are explored to correct for the combined effects of sample self-attenuation and coincidence summing by using information obtained from the spectra themselves.

This study uses spectra of cobalt-60 and caesium-137 measured with a well-type detector, at positions outside the well without lining, and inside the well, both with and without a lining. It compares the spectra with respect to differences in the Compton continuum and we provide a theoretical explanation for the differences. It also compares detector performances as represented by the peak-to-Compton- and the peak-to-total ratios.

## 5.2 Compton continuum in $\gamma$ -ray spectra

Pulse height spectra measured with germanium detectors show various characteristic features, of which a few will be discussed here. In germanium, photons with energy higher than 140 keV have a higher probability for Compton interaction than for photoelectric interaction. Therefore, the Compton continuum is a prominent part of the spectra. Figure 5.1 shows a schematic germanium detector spectrum. The relation between the scattering angle  $\vartheta$  and the energy  $E'$  of the secondary photon after Compton interaction is given by

$$E' = \frac{E}{1 + \alpha[1 - \cos(\vartheta)]}, \quad (5.1)$$

where  $E$  is the energy of the incident photon and  $\alpha \equiv E/m_e c^2$ .

It follows that for  $\mathcal{G} = \pi$ , the minimum in the energy distribution of the scattered photon is reached and consequently a maximum in the energy deposit in the detector is obtained. This maximum can be found in the spectrum as a sharp edge on the right of the Compton continuum (marked 'E' in Figure 5.1). Counts in the spectrum between the Compton edge and the full-energy peak are owing to multiple Compton interactions. The full-energy peak results from any number of scattering events followed by a photoelectric interaction.

The presence of a broad peak at approximately 200 keV (marked 'B' in Figure 5.1) reflects the influence of material surrounding the detector. This so-called backscatter peak is the result of the detection of secondary photons which are produced by Compton interaction, with  $\mathcal{G} \approx \pi$  rad, with the material surrounding the detector.

### 5.3 Indexes of performance; the peak-to-total ratio and the peak-to-Compton ratio

As an index of detector performance, the peak-to-Compton (PC-) ratio is often quoted. It is officially defined as the ratio of the count in the highest full-energy peak channel to the count in a typical channel of the Compton continuum associated with that peak. This sample of the continuum is to be taken in the interval from 358 to 382 keV for the 662 keV  $\gamma$ -ray from caesium-137 and from 1040 to 1096 keV for the 1332 keV  $\gamma$ -ray from cobalt-60<sup>[4]</sup>.

Thus, the PC-ratio only takes into account the registration of Compton-scattering events in a limited range of the scattering-angle. The Compton-edge and the backscatter peak lie outside this region. It should be noted that this ratio is associated with the spectrum of a radionuclide and therefore can be dependent on the radionuclide.

In addition to the PC-ratio this work uses the peak-to-total ratio which is commonly used in coincidence-correction computations and which is associated with one photon of a particular energy  $E$ . This index can be defined as the ratio of the probability of a photon of energy  $E$  depositing all its energy in the detector to the probability of the photon depositing any non-zero fraction of its energy in the detector. This ratio is a characteristic of the detection geometry, and depends only on photon energy, as opposed to the PC-ratio, which can depend on the emitting radionuclide as well. The following sections will refer to this definition when the term '*PT-ratio*' is used. Both the PC-ratios and the PT-ratios are evaluated from the spectrum of caesium-137 and from the spectrum of cobalt-60.

The PC-ratios can be calculated by simply applying the definition. Because the decay product of caesium-137, barium-137m, is a mono gamma-emitter, the PT-ratio for 662 keV can be calculated by dividing the area of the 662 keV peak by the total number of counts in the spectrum, after subtracting the background. Cobalt-60, however, emits two coincident gammas per disintegration and evaluation of the PT-ratio from the cobalt-60 spectra directly is not possible, unless we approximate the PT-ratios for 1173 keV and for

1332 keV to be equal. Since the PT-ratio as a function of energy can be described by a relatively flat linear relation on log-log scale, and because on a log scale the energies of the cobalt-60 peaks are near to equal, this is a valid approximation. For low-efficient geometries, i.e. where coincidence effects can be neglected, the PT-ratio for these energies can now be calculated by dividing the sum of the areas of the two full-energy peaks of cobalt-60 by the total number of counts in the spectrum, again after subtracting background.

For highly efficient geometries another approach has to be followed. In the presence of coincident summing, and when neglecting the weak transition of 2505 keV, the counting rates in the respective peaks,  $c_1$  (1173 keV),  $c_2$  (1332 keV) and  $c_{12}$  (the 2505 keV sumpeak of cobalt-60) can be described by

$$\begin{aligned}c_1 &= A\varepsilon_1(1 - r^{-1}\varepsilon_2), \\c_2 &= A\varepsilon_2(1 - r^{-1}\varepsilon_1), \\c_{12} &= A\varepsilon_1\varepsilon_2,\end{aligned}\tag{5.2}$$

where  $A$  is the activity of the source during the measurement,  $\varepsilon_1$  and  $\varepsilon_2$  are the peak efficiencies for 1173 keV and 1332 keV photons respectively and  $r$  is the PT-ratio for these energies. The PT-ratio can now be evaluated by solving this set of equations with respect to  $r$ , i.e. solving the following quadratic equation with respect to  $r$ ,

$$r^2(c_1c_2 - Ac_{12}) + r(c_1c_{12} + c_2c_{12}) + c_{12}^2 = 0.\tag{5.3}$$

## 5.4 Measurements

The PT-ratio for the system used was evaluated by measuring a cobalt-60 source and a caesium-137 source at a position of 30 cm above the detector without a high-Z lining ("30-cm" geometry). This position was chosen because many manufacturers specify the PC-ratio of a detector for this position. Measurements in the well were performed both with and without a lining (referred to as the "lined" and "non-lined" geometry respectively). The detector used was a Philips well-type Ge(Li)-detector with a specified PC-ratio of 26.5 (1332 keV of cobalt-60, 30 cm) and absolute full-energy peak efficiencies of 0.5 and 0.05 at 122 keV and 1115 keV respectively, measured in the non-lined geometry. The lining consisted of a tube of gold with a wall-thickness of 0.53 mm and a bottom-thickness of 0.85 mm. Figure 5.2 shows the detection geometries used.

After background-subtraction from the spectra, peak areas were obtained by integration. To determine the total number of counts in the spectra, the spectra were cut off at 25 keV to eliminate electronic noise and then were linearly extrapolated towards 0 keV.



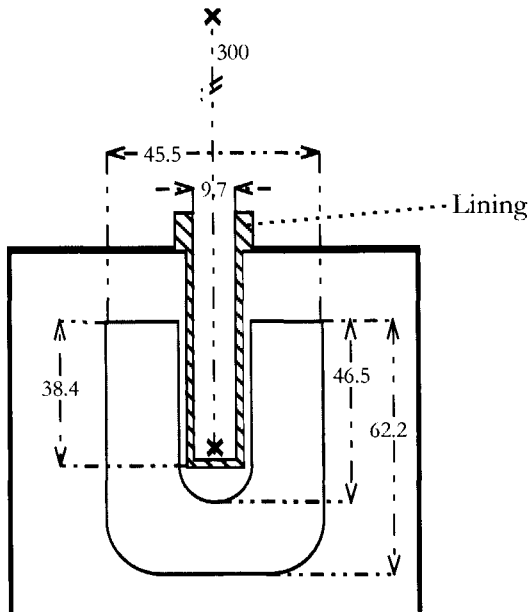


Figure 5.2: Detection geometry. Dimensions are in mm. x denotes the source position

## 5.5 Results and discussion

Figure 5.3 and Figure 5.4 show the spectra of caesium-137 and cobalt-60 measured in the three geometries. Table 5.1 shows the values of the conventional PC-ratio and of the PT-ratio for all six measurements.

### 5.5.1 PT-ratio

From the measurements, two comparisons can be made. First, the measurements from the 30 cm geometry can be compared to the measurements from the non-lined geometry. Second, the measurements from the lined geometry can be compared to the measurements from the non-lined geometry. In both cases the increase of the PT-ratio is evident. The main reason for the high PT-ratio in the non-lined geometry is the higher probability of detecting photons which are scattered (nearly)  $180^\circ$  in the detector.

Figure 5.5 explains this effect: In the 30 cm geometry the probability of the secondary photon leaving the detector is relatively high, whereas in the lined geometry this photon is likely to be absorbed by the lining because of its low energy of approximately 200 keV. In

**Table 5.1:** Peak-to-total ratios (PT) and peak-to-Compton ratios (PC) for 662 keV  $\gamma$ -rays from caesium-137 and for 1332 keV  $\gamma$ -rays from cobalt-60 measured with a well-type detector at 30 cm without a lining, in the well with a lining and in the well without a lining.

Geometry	662 keV from $^{137}\text{Cs}$		1332 keV from $^{60}\text{Co}$	
	PT	PC	PT	PC
30-cm	0.12	34	0.07	24
In-well, lined	0.17	61	0.11	22
In-well, non-lined	0.19	68	0.12	24

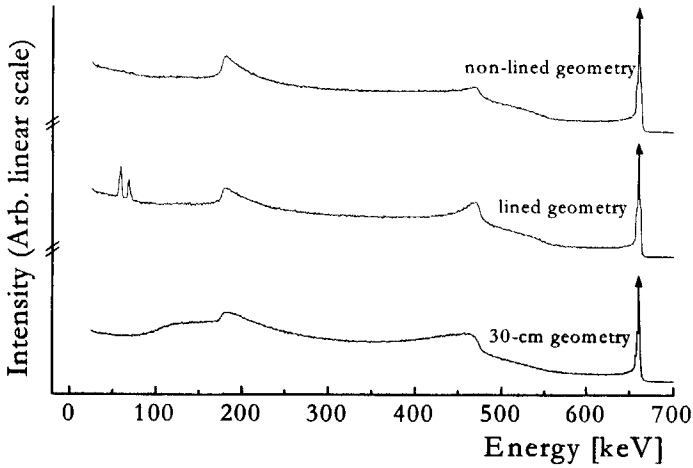


**Figure 5.3:** Spectra of caesium-137 from three geometries

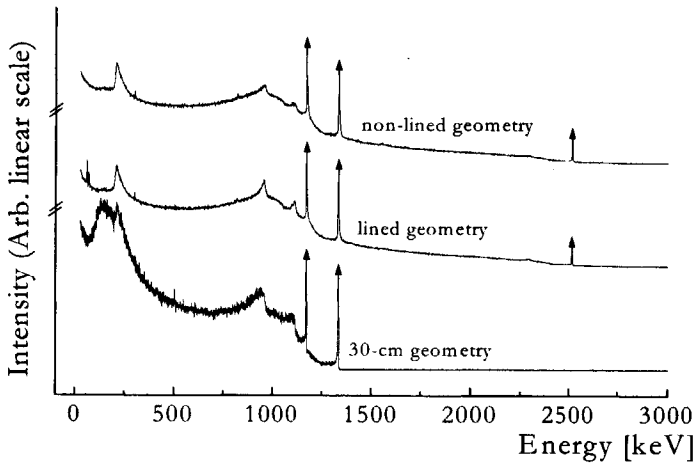


**Figure 5.4:** Spectra of cobalt-60 from three geometries

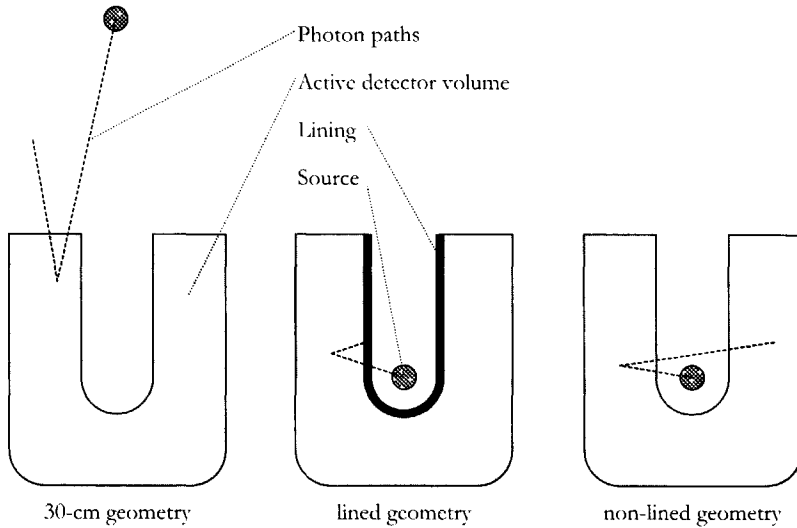


**Figure 5.5:** Backscattering of a primary photon in the three different geometries

the non-lined geometry,  $180^\circ$  scattered photons can reach the detector at the other side of the well. Owing to the more efficient detection of these photons in the non-lined geometry, the full-energy of the primary photon is more likely to be absorbed totally by the detector resulting in a higher full-energy peak and a less prominent Compton-edge. The spectra in Figure 5.3 and Figure 5.4 clearly show the decreased Compton-edge in the non-lined geometry as opposed to the higher edges in the 30 cm and the lined geometries. The difference is particularly clear when comparing the lined geometry with the non-lined geometry, because in this case the only difference in the detection of photons concerns those which are scattered  $180^\circ$  or nearly  $180^\circ$ . The difference in photon-detection between the 30 cm geometry and the non-lined geometry on the other hand concerns photons in a much wider scattering range namely, in the range between  $90^\circ$  and  $180^\circ$ .

The spectra of cobalt-60 also show the occurrence of coincidence summing, not only by the occurrence of a sum peak at 2505 keV, but also by the following. When comparing the spectrum of cobalt-60 in the 30 cm geometry to those measured inside the well, the low-energy part of the "30cm-spectrum" is relatively higher than the spectra from the lined and non-lined geometries. Coincidence summing involving an event of particular energy shifts the resulting count in the spectrum towards a higher energy. This, of course, also holds for Compton events. Therefore, the whole continuum of the spectrum is spread towards higher energies.

A final remark regarding the spectra can be made about the presence of the two peaks in the low energy region of the lined-geometry spectrum. These peaks are owing to the gold-X-rays which are emitted when a gamma is absorbed by the lining.

### 5.5.2 PC-ratio

In the case of caesium-137, when repositioning the source from a position of 30 cm outside the well to a position in the well without lining, the PC-ratio increases from 34 to 68, which behaviour is similar to that of the PT-ratio of caesium-137. For cobalt-60, however, the PC-ratio does not change significantly, while its PT-ratio displays the same behaviour as the caesium-137 ratios. For both nuclides, the difference between the PT-ratio of the lined geometry and the non-lined geometry is similar to the equivalent difference in PC-ratio. However both PC-ratios in the cobalt-60 case are nearly three times lower than in the caesium-137 case, while the PT-ratio only shows a decrease by a factor of 1.5.

The reason for the deviant behaviour of the PC-ratio of cobalt-60 is the occurrence of coincidence summing effects in the well. Apparently, the reduction owing to coincidence summing of the 1332 keV peak area is relatively larger than the corresponding reduction of the defined region of the Compton continuum.

## 5.6 Conclusions

From the measurements, two conclusions can be drawn. Specifying the PC-ratio of cobalt-60 for a well-type detector using measurements at 30 cm distances, as is common practice, may prejudice potential users. Only measurements of the PC-ratio using mono-gamma emitting radionuclides measured in the well will give a well-type detector full credit. As an alternative for the cobalt-60-PC-ratio, the PT-ratio for approx. 1332 keV is suggested which, as the PC-ratio, is energy dependent, but which does not depend on the radionuclide used. This introduces slightly more calculation which, however, is considered only as a minor drawback.

In addition to the geometry effects in well-type detectors introduced by a high-Z lining<sup>[3]</sup>, the lining also deteriorates detector performance with respect to the Compton continuum, most notably in the region of the Compton edge. For these reasons, instead of using a lining to absorb low energy photons from the sample, the problems of summation with these photons, which are subject to attenuation in the sample, should be dealt with in another way. The next chapter describes the appliance to well-type detection geometries of the methods developed in Chapter Two.

## References

- [1] F.P. Brauer, W.A. Mitzlaff, *IEEE Transactions on Nuclear Science*, **Vol.NS-25 No 1** (1978)
- [2] M. de Bruin, P.J.M. Korthoven, P. Bode, *Nucl. Instr. and Meth.*, **A159** (1979) 301
- [3] S.J. Gelsema, M. Blaauw, *Nucl. Instr. and Meth.*, **A379** (1996) 289
- [4] ANSI/IEEE Standard 325-1986, *Test Procedures for Germanium Gamma Ray Detectors* (1986)



# Chapter Six

## The missing curve for well-type detection geometries; A Monte Carlo survey

---

### Abstract

*This chapter describes an efficiency calibration method that includes coincidence, as well as attenuation effect corrections for well-type detection geometries. The method requires knowledge of the variation of the full-energy peak efficiency and the total efficiency over the source volume. Therefore, in addition to a peak efficiency curve and a peak-to-total curve, it uses a third curve that accounts for this variation. Since samples encountered in well-type detectors may have high-Z matrices, this chapter gives special attention to the parameterization of K-edges.*

*This chapter describes two variants of the calibration method and their verification using Monte Carlo simulated data. It is concluded that either variant applied to a terbium-160-spectrum produces accurate values for the parameters describing the well-type detector. Compared to radionuclide specific calibration, potentially the method greatly reduces calibration efforts without compromising calibration quality.*

### 6.1 Introduction

The quantitative analysis of small radioactive samples with low specific activity such as environmental samples, or INAA samples after a long decay time, requires the use of a sample-detection geometry that places the sample as close to a radiation detector as possible. Preferably, the detector should even enclose the sample. Well-type detection geometries are frequently used for this purpose. The small sample volume does only give rise to photon-attenuation at  $\gamma$ -ray or X-ray energies below approximately 100 keV, depending on the matrix composition of the source. Well-type detectors typically have no dead layer between sample and active crystal and are therefore sensitive to these low-

energy  $\gamma$ - and X-rays. In addition, detection efficiencies are usually high enough to give rise to considerable coincidence summing effects. Therefore, the calibration of a well-type detection geometry deserves critical attention.

Chapter Four and Chapter Five showed that even though the effects of attenuation of low-energy  $\gamma$ -rays and X-rays within the sample can be mitigated by the insertion of a high-Z lining, this lining deteriorates the peak-to-total ratio as well as the geometry insensitivity of the detection efficiency. This chapter explores the possibility of modelling the sample and detector together with three efficiency curves as described in Chapter Two through Monte Carlo methods.

In addition to a full-energy peak efficiency curve combined with a peak-to-total curve, the model uses a third curve, the linear-to-squared curve that accounts for the variation of the efficiency over the source. The corresponding calibration method enables simultaneous determination of all three curves. It is based on the philosophy that the curves, that are used to accurately describe coincidence effects, should be obtained from coincidence effects observed in practice. In principle, it only needs one measurement of a radionuclide of known activity that shows considerable coincidence effects (Variant I). This way, it produces curves that are accurate for the energy range limited by the lowest and highest energy in the spectrum. A second variant of the method allows for an extended energy range if the full-energy peak efficiency curve is obtained from a supplementary measurement (Variant II).

## 6.2 Theory

### 6.2.1 High-Z source matrix; parameterization of K-edges

In addition to the general theory developed in Chapter Two, this section presents additional expressions required to deal with the specific well-type detector phenomenon of efficiency curve discontinuities stemming from the discontinuous probability of photoelectric interaction near the so-called K-edge of an absorber. Chapter Two gave a general expression for the full-energy peak efficiency of a given source-detector geometry (see Equation (2.6)), namely

$$\ln \varepsilon_E = \ln \Sigma_{\text{ext}, E} + \ln \Sigma_{\text{self}, E} + \ln \varepsilon_{\text{abs}, E}, \quad (6.1)$$

where  $\varepsilon_{\text{abs}, E}$  represents the absolute efficiency defined by (2.5),  $\Sigma_{\text{ext}, E}$  represents the transmission through external absorbers and  $\Sigma_{\text{self}, E}$  represents the transmission through the source itself. The parameterization described in Chapter Two uses four parameters for the absolute efficiency curve  $\varepsilon_{\text{abs}, E}$ , namely  $g_0 \dots g_3$ , and two parameters for the transmission through an external absorber  $\Sigma_{\text{ext}, E}$ , namely  $g_4$  and  $g_5$ .

In well-type detectors, the transmission through the source can be approximated by Fleming's<sup>[1]</sup> expression for spherical samples (see Equation (2.13)),



$$\Sigma_{\text{self},E} = \frac{3\rho^3}{4\mu_E^3 R_m^3} \left\{ \frac{\mu_E^2 R_m^2}{\rho^2} - \frac{1}{2} + \left( \frac{1}{2} + \frac{\mu_E R_m}{\rho} \right) \exp \left[ -2 \frac{\mu_E R_m}{\rho} \right] \right\}. \quad (6.2)$$

If, like in the case of an external absorber,  $\mu_E/\rho$  as a function of energy is described by a linear relation on double-log scale,

$$\ln \left[ \frac{\mu_E/\rho}{\mu_0/\rho_0} \right] = m_0 + m_1 \ln E/E_0, \quad (6.3)$$

with  $\mu_0/\rho_0 = 1 \text{ m}^2\text{kg}^{-1}$  and  $L_0 = 1 \text{ McV}$ , then the factor  $\mu_E R_m/\rho$  can be described by

$$\frac{\mu_E R_m}{\rho} = R_m \frac{\mu_0}{\rho_0} \exp[m_0] \cdot \exp \left[ m_1 \ln E/E_0 \right] = g_6 \exp \left[ g_7 \ln E/E_0 \right], \quad (6.4)$$

where  $g_6$  and  $g_7$  are the extra parameters modelling the sources transmission.

Strictly, if the sample consists of high- $Z$  material, then the applicability of parameterization (6.4) is limited by two facts. First, the assumption of a linear relation on a double log scale for  $\mu_E/\rho$  is only valid for energies for which  $\mu_E/\rho$  does not exceed  $0.1 \text{ m}^2\text{kg}^{-1}$ . However, since in well-type detectors self-attenuation effects are important only in this energy region, this fact does not limit the use of (6.4) in practice. Secondly, *K-edges\** occur at energies that can be higher than the lowest energy of interest. Therefore *K-edges* have to be modelled.

In this work, *K-edges* are modelled by two additional parameters,  $g_8$  and  $g_9$ . If  $E_K$  represents the *K-edge* energy and  $\Delta m$  represents the discontinuity in  $\mu_E/\rho$ , then (6.3) can be written as

$$\ln \left[ \frac{\mu_E/\rho}{\mu_0/\rho_0} \right] = \begin{cases} m_0 - \Delta m + m_1 \ln \left[ E/E_0 \right] & \text{if } E < E_K \\ m_0 + m_1 \ln \left[ E/E_0 \right] & \text{if } E \geq E_K \end{cases} \quad (6.5)$$

and (6.4) as

---

\* A *K-edge* (or *L*, *M*, ...) is the occurrence of a series of discontinuities in the (mass) attenuation coefficient  $\mu_E$  (or  $\mu_E/\rho$ ) of a specific material at the binding energies of this materials *K* atomic shell(s) (or *L*, *M*, ...). Just above the *K-edge* energy, a photon has enough energy to remove a *K*-electron, whereas just below this energy it has not. This causes a sudden change in the photoelectric absorption probability, resulting in the discontinuity in  $\mu_E$  ( $\mu_E/\rho$ ).

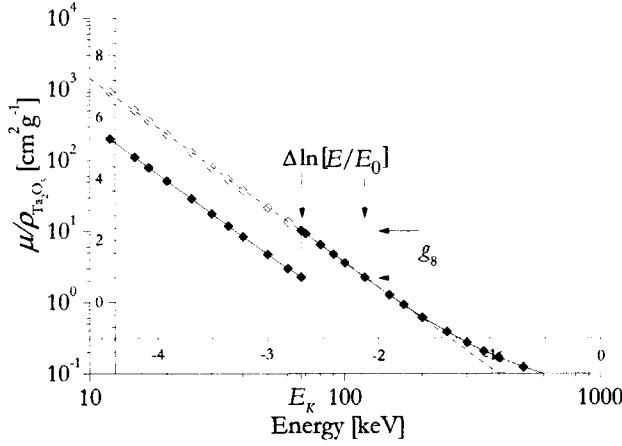


**Figure 6.1:** Modelling of K-edges; Transformation of the attenuation coefficient step to an energy step for  $\text{Ta}_2\text{O}_5$  (inside axes show logarithmic values).

$$\frac{\mu_E R_m}{\rho} = \begin{cases} R_m \frac{\mu_0}{\rho_0} \exp[m_0 - \Delta m] \cdot \exp\left[m_1 \ln E/E_0\right] = g_6 \exp\left[g_7 \ln E/E_0\right] / g_8 & \text{if } E < g_8 \\ R_m \frac{\mu_0}{\rho_0} \exp[m_0] \cdot \exp\left[m_1 \ln E/E_0\right] = g_6 \exp\left[g_7 \ln E/E_0\right] & \text{if } E \geq g_8 \end{cases} \quad (6.6)$$

Thus,  $g_8$  represents  $\exp[\Delta m]$  and  $g_9$  represents the energy of the K-edge. For the case of a tantalum pentaoxide matrix ( $\text{Ta}_2\text{O}_5$ ), the previous is summarized by Figure 6.1.

The LS-curve for a high-Z matrix source is also influenced by the occurrence of K-edges. Therefore, its parameterization has to be modified. For this purpose, the step in the attenuation coefficient  $\mu_E/\rho$  is transformed to a step in energy  $\Delta \ln[E/E_0]$ . Since  $\mu_E/\rho$  is described by a linear relation on double-log scale, this transformation is straightforward (see Figure 6.1).  $\Delta \ln[E/E_0]$  is given by

$$\Delta \ln E/E_0 = -\frac{\ln g_8}{g_7} \quad (6.7)$$

and the resulting parameterization of the LS-curve is (cf. Equation (2.30))

$$\sqrt{\eta^2 + 1} = \begin{cases} h_0^2 + h_1^2 \left( \ln \left[ \frac{E}{E_0} \right] + \Delta \ln \left[ \frac{E}{E_0} \right] \right)^{-h_2} & \text{if } E < E_K \\ h_0^2 + h_1^2 \left( \ln \left[ \frac{E}{E_0} \right] \right)^{-h_2} & \text{if } E > E_K \end{cases} \quad (6.8)$$

Thus, the modified parameterization for the LS-curve does not introduce extra parameters. Moreover, since the variation of efficiency over the source volume for well-type geometries is caused only by the sample-self-attenuation, the asymptote of the LS-curve is 1.0. Thus parameter  $b_0^2$  can be set to 1.0 and the LS-curve for a well-type detector source is described by two parameters.

In order to obtain enough information on the other LS-parameters,  $b_1^2$  and  $b_2^2$ , the calibration radionuclide must be carefully chosen. Bringing in memory its use in Equation (2.25), we see that only if two low-energy photons coincide, the LS-curve, or rather the scaled variance  $\eta$ , is effective. Only then, both associated efficiencies show variation over the over the source volume. If, however, only one of them varies, we are merely faced with the task to determine the mean product of a constant and a stochastic variable, which simply amounts to the product of the constant and the mean value of the variable. Since in well-type detectors, the source volume is rather small, the coinciding photons should both have energies below 100 keV typically.

## 6.3 Methods

### 6.3.1 Detection geometries

The well-type detector modelled by the simulation program bears close resemblance to an actual well-type detector as used for the experiments in Chapter Seven. Figure 6.2 shows the geometry in detail. Two different source types are considered. The first is a point source located at 3.5 mm above the bottom of the well. The second consists of a cylindrical Ta<sub>2</sub>O<sub>5</sub> matrix with dimensions of ( $\varnothing 8.0 \times 9.0$ ) mm, its base located at 3.5 mm above the bottom of the well. The latter type is depicted in the figure.

### 6.3.2 Determination of efficiency-, PT- and LS-curves, and correlation coefficients

Volume-averaged full-energy peak efficiency curves, PT-curves, LS-curves and correlation coefficients for each detection geometries were determined by Monte Carlo calculations as described in Chapter Three.

For the full-energy peak efficiency values  $\bar{\varepsilon}$ , the total number of photons was taken large enough to obtain an imprecision for  $\bar{\varepsilon}$  lower than 0.5%. A full-energy peak efficiency curve  $\varepsilon(E)$  was then fitted to the  $\bar{\varepsilon}$ -values using Gunnink's efficiency curve<sup>[2],[3]</sup> (see Section 2.2).

The imprecision of the total efficiency values  $\bar{\varepsilon}_t$ , was also lower than 0.5%. Peak-to-total ratios  $r$  were calculated from the  $\bar{\varepsilon}$  and  $\bar{\varepsilon}_t$ -values. The peak-to-total curve  $r(E)$  was then fitted to the  $r$ -ratios, using a straight line on a double-log scale. (Subsection 2.2.2)

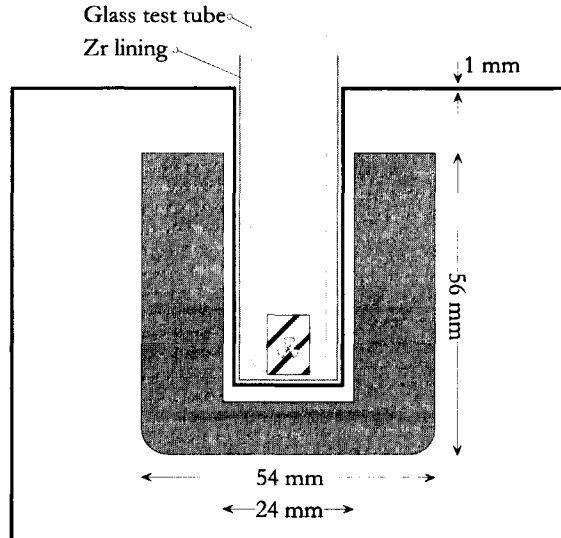


**Figure 6.2:** Well-type geometry. The lining consists of a zirconium tube with wall and bottom thickness of 0.92 mm and 0.70 mm respectively. Sources are placed on the bottom of a glass test tube that acts as a sample holder.

The imprecision for the squared efficiency values was lower than 1% for energies below 2000 keV and lower than 1.5% for all energies. Linear-to-squared ratios  $\sqrt{(\eta^2+1)}$  were calculated from these values using Equation (2.29). A Linear-to-squared curve was then fitted to the LS-ratios using relation (6.8), where parameter  $b_0$  was kept fixed at 1.0.

Finally, the imprecision obtained for the  $\varepsilon_i \varepsilon_j$ -values, needed to calculate the correlation parameter according to Equation (3.10), was lower than 3% for energies between 100 and 700 keV and typically 5% for energies outside this range. The resulting correlation coefficients did not significantly deviate from unity.

### 6.3.3 Spectrum simulation

For both geometries, the spectra of terbium-160 and erbium-171 were simulated by following a large number of batches of photons through the detection geometry, as described in Chapter Three. Each batch contained the photons from a possible cascade from the decay-scheme of the daughter from a fed level to the ground state. The number of disintegrations, effectively the number of batches, was taken large enough to obtain an imprecision lower than 0.5% for the areas of the most important peaks in the spectra.

### 6.3.4 Spectrum interpretation

The theory presented Chapter Two was validated by interpreting the simulated spectra with respect to the number of disintegrations,  $N$ . This number was obtained by first

calculating a separate number of disintegrations,  $N_E$ , associated with each peak in the spectrum, i.e., by dividing peak areas by their corresponding  $P_T$ -values (Equation (2.28)). The reported number of disintegrations,  $N$ , is the weighted average of all the numbers of disintegrations associated with each peak. This calculation of  $N$  also produced a  $\chi^2$ -value. The number of disintegrations,  $N$ , was then compared to the real number,  $N_{true}$ , used in the simulation. The exact procedure is described in Appendix B.

### 6.3.5 Principles of the calibration method

The theory developed in Chapter Two allows for the calculation of all peak areas of a spectrum if the full-energy peak efficiency curve including external and internal  $\gamma$ -attenuation, the PT-curve and the LS-curve are known. For a well-type detector, in principle four parameters are used to describe the full-energy peak efficiency curve, two parameters for external absorbers, four parameters for the sample self-attenuation, three parameters for the PT-curve and two for the LS-curve. Together with two additional parameters representing the correlation coefficient and the number of disintegrations, the total number of parameters used to predict a spectrum is seventeen.

The calibration method described here inverts the problem of calculating peak areas from seventeen parameters: it calculates the parameters from measured peak areas. In the case of terbium-160, over fifty peaks can easily be observed with a well-type detector set-up. This means that over fifty equations can be solved for these parameters. In principle, all seventeen parameters can be obtained by non-linear least squares methods, where the  $\chi^2$ -value of the measured full-energy peaks areas as compared to the computed areas is minimized.

A computer program was written to perform the fitting. As all non-linear least squares fitting algorithms, the program requires a reasonable initial estimate of the parameter values. An estimate for the number of disintegrations is usually available and must be supplied to the program by the user. An initial estimate for the other parameters can either be supplied by the user or by the program itself. If the program is to supply a first estimate for the full-energy peak efficiency parameters, it calculates efficiency values for all main peaks in the spectrum disregarding all coincidence losses or gains. It then fits a Gunnink curve<sup>[2],[3]</sup> to the individual values. As a first estimate for the PT-parameters and the LS-parameters, the program takes a predefined set of parameters for a typical well-type detection geometry. Once the program has obtained estimated values for all parameters it can fit all parameters at once, or one or more sets at a time, three sets consisting of the parameters associated with a specific curve, two sets consisting of the parameters associated with external and internal  $\gamma$ -attenuation, and the fourth consisting of the parameter used for the number of disintegrations.

## 6.4 Point source calibration

The previous section stated that in principle seventeen parameters are needed to predict a well-type spectrum. However, for point-sources, self-attenuation effects are absent. Therefore, the parameters  $g_6 \dots g_9$  can be excluded from the total set of parameters. Also, the LS-curve can be set to 1.0 for all energies, reflecting no efficiency variation over the source volume and obviating the need for a correlation parameter. The total number of parameters thus is limited to ten, including the number of disintegrations.

### 6.4.1 Spectrum interpretation using calculated curves

Figure 6.3(a,b) shows calculated efficiency and PT-ratios and corresponding curves. It shows the quality of these curves by showing the ratios between the simulated values and the values calculated using these curves. In addition, Figure 6.3(c,d) shows the quality of the spectrum interpretations of terbium-160 and erbium-171 by showing the ratios between the interpreted number of disintegrations associated with each peak,  $N_E$ , and the true number,  $N_{true}$ .

### 6.4.2 Spectrum interpretation using the curves determined from the spectrum

Originally, the calibration method was introduced and tested using a lined well-type detector and using bromine-82 as a calibration radionuclide<sup>[4]</sup>. Furthermore, it used only two parameters for the PT-curve, disregarding the limitation parameter. Instead it applied a constraint in the fitting procedure to limit the PT-curve to physical values.

This section studies the characteristics of the calibration method for a non-lined well-type detector, using terbium-160 as a calibration nuclide and using parameterization (2.18) for the PT-curve. Thus, instead of having 92 keV as lowest energy, it tests the method using 46 keV (dysprosium-160  $K_{\alpha}$  X-ray) as lowest energy.

Two variants of the calibration method have been investigated. Variant I only needs one measurement of a radionuclide of known activity that shows considerable coincidence effects. It produces curves that are accurate for energy range limited by the lowest and highest full-energy peak energies in the spectrum. Variant I can be extended (Variant I+) by including the number of disintegrations in the fitting procedure. Thus, only an estimate of the activity of the source would have to be supplied.

Variant II allows for an extended energy range if the full-energy peak efficiency curve is obtained from a supplementary measurement. Now only the PT-parameters are to be varied in the fit.

Figure 6.4(a,b) and Figure 6.5(a,b) show the curves resulting from Variant I and II respectively and their relation to the individually calculated values. Additionally, the figures (c,d) show the fit results for each peak area of terbium-160 and the interpretation results for each peak area of erbium-171.

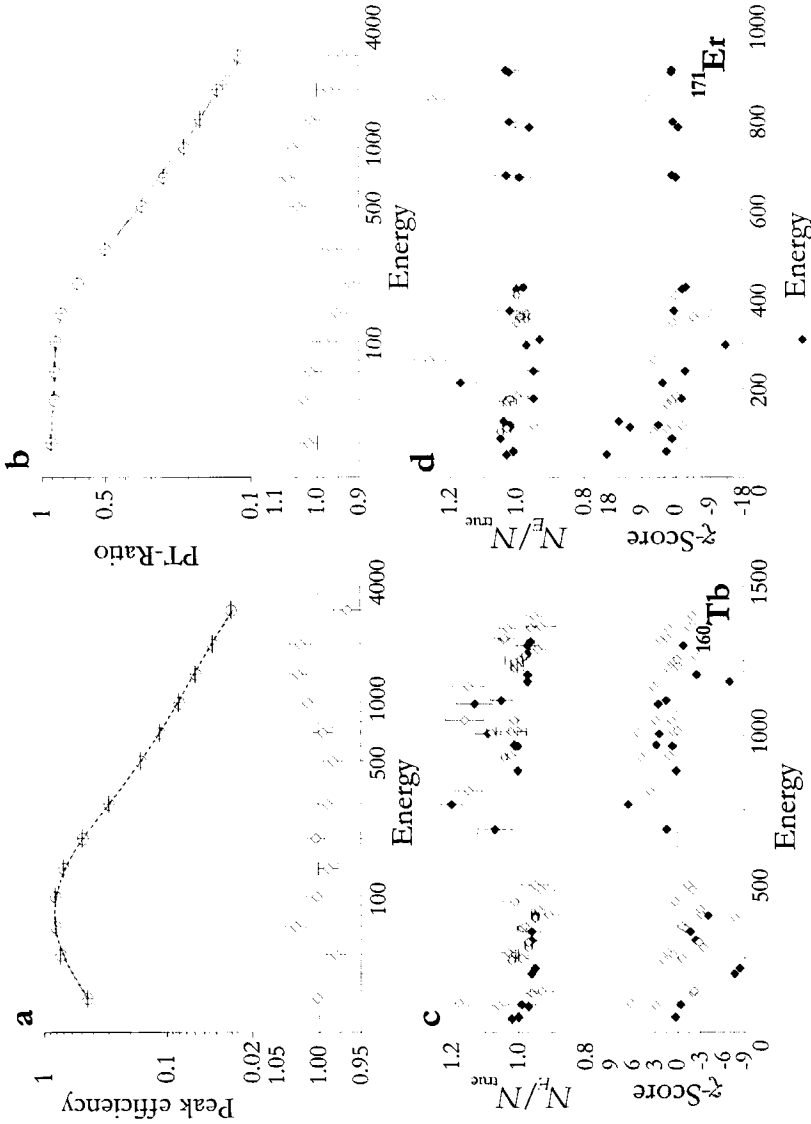


**Figure 6.3:** Reproduction of simulated terbium-160 and erbium-171 spectra from a point source, for the non-lined well-type geometry, using independently simulated full-energy peak efficiency and PT-values. **Upper plots (a, b):** Curves fitted (lines) to simulated efficiency, or PT-values (open circles) and quality of these fits described by the ratio fitted/simulated values. **Lower plots (c, d):** Spectrum reproduction using this set of curves in terms of  $N_E/N_{true}$ -ratios and  $\chi^2$ -scores; Filled diamonds indicate full-energy peaks, open diamonds indicate sum-peaks.

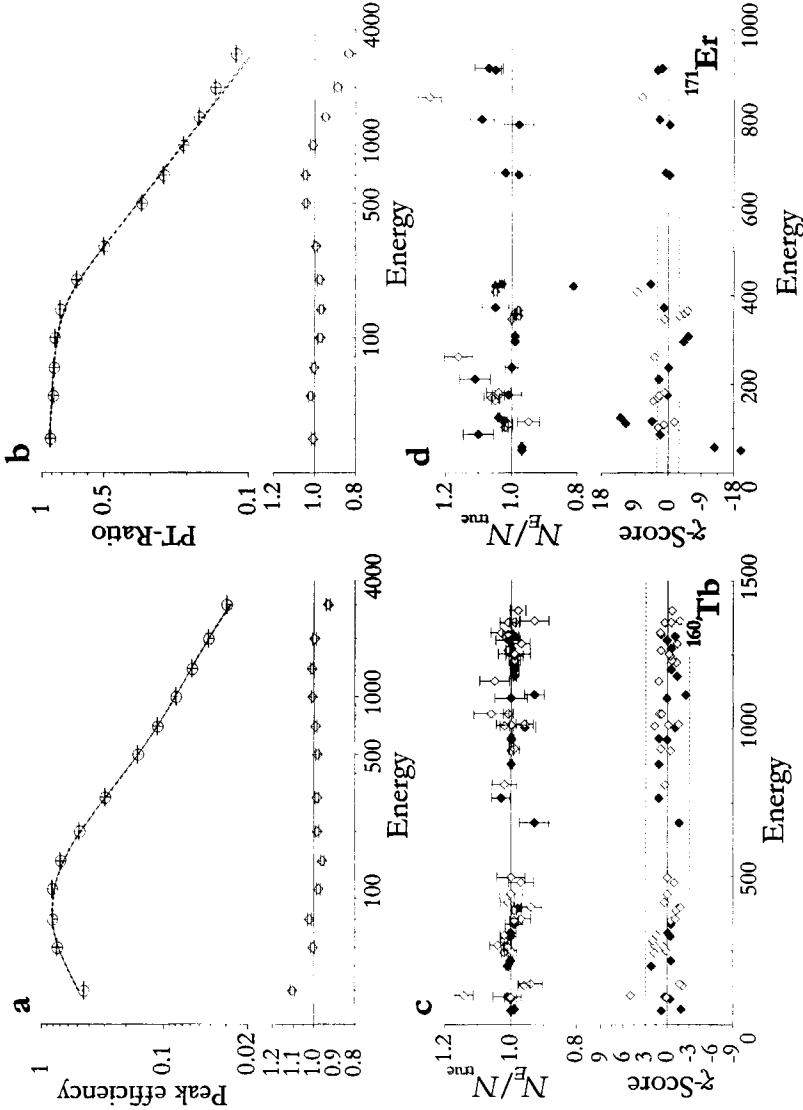
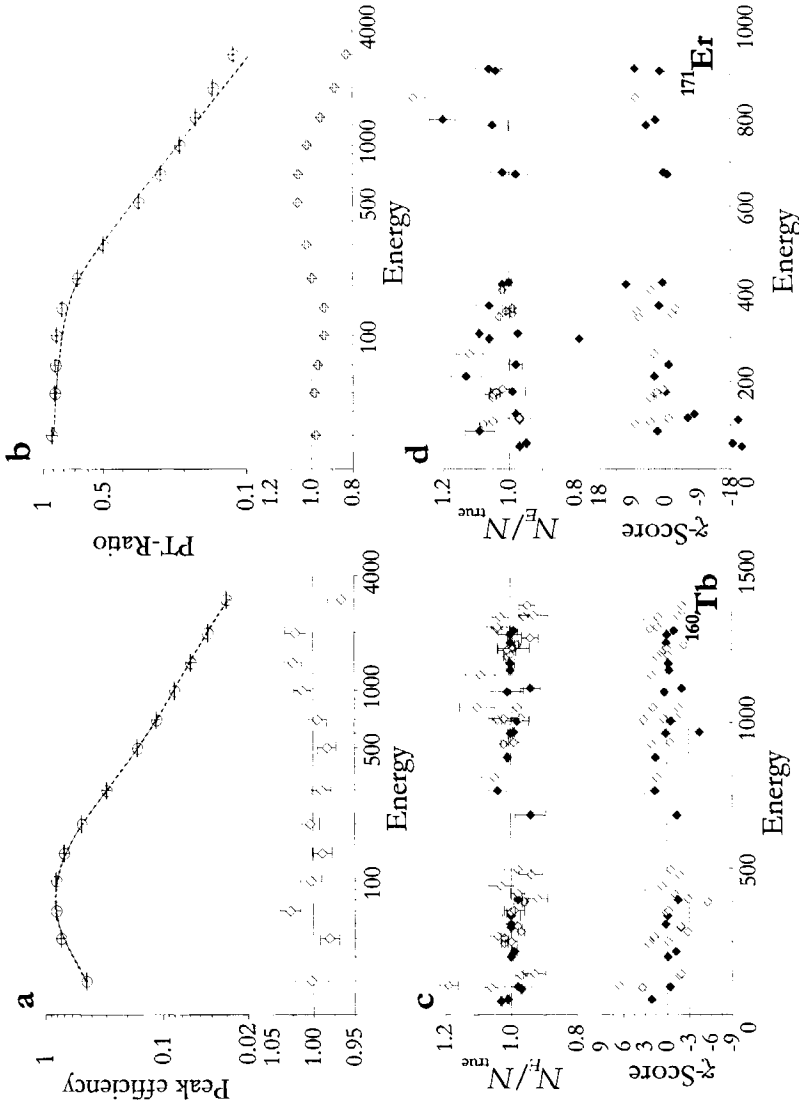


Figure 6.4: Reproduction of simulated terbium-160- and erbium-171-spectra from a point source, for the non-lined well-type geometry, using full-energy peak efficiency and PT-curves fitted from the terbium-160-spectrum. **Upper plots (a, b):** Fitted curves (lines) versus independently simulated efficiency and PT-ratios (open circles) and quality of these curves described by the ratio fitted/simulated values. **Lower plots (c, d):** Spectrum reproduction using this set of curves in terms of  $N^E/N_{\text{true}}$ -ratios and  $\chi^2$ -scores; Filled diamonds indicate full-energy peaks, open diamonds indicate sum peaks.





**Figure 6.5:** Reproduction of simulated terbium-160 and erbium-171 spectra from a point source, for the non-lined well-type geometry, using the efficiency curve obtained from independently simulated values. The PT-curve originates from a fit to the terbium-160 spectrum. **Upper plots (a, b):** Fitted curves (lines) versus simulated efficiency or PT-values (open circles) and quality of these curves described by the ratio fitted/calculated values. **Lower plots (c, d):** Spectrum reproduction using this set of curves in terms of  $N_F/N_{\text{true}}$ -ratios and  $\chi^2$ -scores; Filled diamonds indicate full-energy peaks, open diamonds indicate sum peaks.

**Table 6.1:** Fit results of the various procedures and interpretation results using fitted curves, in terms of: The ratio between the fitted/interpreted and the true number of disintegrations; The  $\chi^2$ -value for the comparison between the two.

Fit variant:	Fitting ( $^{160}\text{Tb}$ )		Interpretation			
	$N_{\text{fit}}/N_{\text{true}}$	$\chi^2$	$N/N_{\text{true}} (^{160}\text{Tb})$	$\chi^2$	$N/N_{\text{true}} (^{171}\text{Er})$	$\chi^2$
<b>MC:</b>	<b>n.a.</b>	<b>n.a.</b>	(0.989 ± 0.004)	18	(1.024 ± 0.005)	70
<b>I:</b> $\epsilon_{\text{F}}$ and PT	$N$ fixed	1.9	(1.000 ± 0.001)	1.7	(1.007 ± 0.005)	60
<b>I+:</b> $\epsilon_{\text{E}}$ , PT and $N$	(0.96 ± 0.04)	2.0	(0.961 ± 0.001)	1.7	(0.981 ± 0.005)	80
<b>II:</b> Only PT	$N$ fixed	12	(0.999 ± 0.003)	11	(1.001 ± 0.007)	120

### 6.4.3 Results

In addition to their graphical representation by Figure 6.3 through Figure 6.5, Table 6.1 shows the results of the various procedures numerically.

### 6.4.4 Discussion

The interpretation results obtained with the Monte Carlo curve-set show that the numbers of disintegrations of both the terbium-160 and the erbium-171 spectra are recovered within approx. 2%, however individual peak areas may vary a lot. This is illustrated by the lower plots of Figure 6.3, and explains the high  $\chi^2$ -values in Table 6.1.

The interpretation results are improved when using either (non-extended) variant of the fitting procedure. The number of disintegrations now is recovered within 1% when using Variant I and even within 0.1% when using Variant II. This improvement may be explained simply by a better determination of the curves. Whereas in the Monte Carlo case, the full-energy peak efficiency curve and the peak-to-total curve are determined by thirteen points each, in the fitting cases, they are determined by at least fifty points. Furthermore, in the fitting case they are determined simultaneously, implicitly taking into account covariances between efficiency and peak-to-total parameters.

Despite the better recovery of the numbers of disintegrations, the  $\chi$ -scores from individual peaks in the erbium-171 spectrum still are fairly large (Figure 6.4 and Figure 6.5). Although this is mainly owing to the high precision of the peak areas, the low energy area is somewhat suspect. This cannot be explained from inaccuracy of the decay schemes since the same decay schemes were employed throughout the spectrum simulations as well as throughout the interpretation procedures. Possibly, the terbium-160 spectrum does not yield enough information on the shape of the efficiency curve at low energies in conjunction with possibly inadequate parameterization of the full-energy efficiency curve in this energy region. Generally, however, peak areas of erbium-171-peaks with high  $\chi$ -scores are accounted for within 5%.

Finally, the results of Variant I+ indicate that the number of disintegrations is strongly correlated with some or all of the other parameters; the resulting value of the fitted number of disintegrations does not deviate significantly from the true value, however, the weighted averages of the numbers of disintegrations obtained from the

individual peaks through the use of the fitted efficiency curves strongly deviate from the truth in the statistical sense. Thus, the instability of the fit in Variant **I+** results in biased measured activities after calibrating this way. This implies that, in practice, it is preferable to calibrate with a source of known activity so  $N$  can be kept fixed in the fitting procedure.

## 6.5 Tantalum pentaoxide matrix calibration

Section 6.3.5 stated that in principle seventeen parameters are needed to predict a well-type spectrum. Since for point-sources self-attenuation effects are absent as described above, the parameters  $g_6 \dots g_9$  were excluded from the total set of parameters. Also, the LS-curve was set to 1.0 for all energies.

In the tantalum pentaoxide case, self-attenuation effects are present and parameters  $g_6 \dots g_9$  have to be determined. Also, the LS-curve is not necessarily unity for all energies. However, some a priori knowledge can be taken into account. First, the point source calibration provides information about external absorbers. Therefore, parameters  $g_4$  and  $g_5$ , representing external attenuation, can be kept fixed at their values obtained from the point source fit. This is necessary to avoid instability of the fit owing to indistinguishability between these parameters and the parameters representing internal attenuation. Second, parameter  $g_9$  representing the K-energy of the matrix material is kept fixed at its theoretical value of 67.42 keV. Thus, the total number of free parameters now is limited to fourteen, including the number of disintegrations.

### 6.5.1 Spectrum interpretation using simulated curves

Figure 6.6(abc) shows simulated full-energy peak efficiency values, PT- and LS-ratios and corresponding curves. It shows the quality of these curves by showing the ratios between simulated values and calculated values using these curves. In addition, Figure 6.6(d) shows the quality of the spectrum interpretations of terbium-160 by showing the ratios between interpreted number of disintegrations associated with each peak,  $N_E$ , and the true number,  $N_{\text{true}}$ .

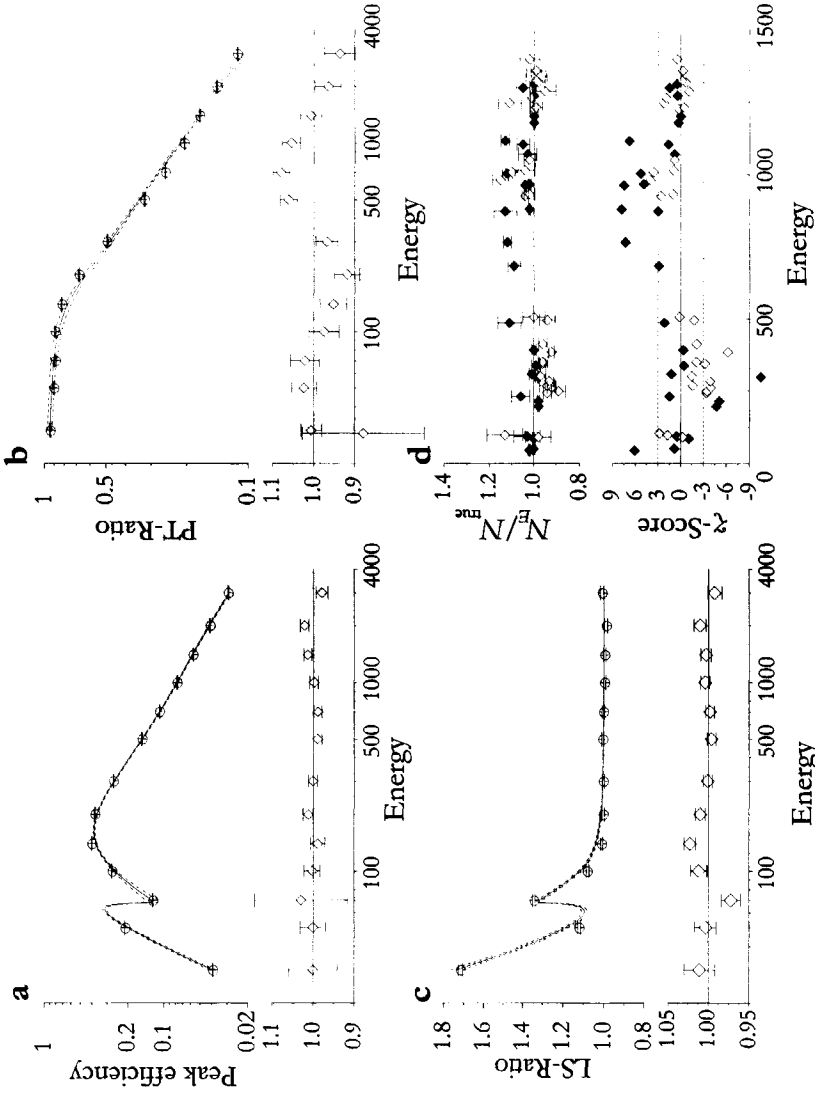


**Figure 6.6:** Reproduction of a simulated terbium-160- spectrum from a high-density source, for the non-lined well-type geometry, using independently simulated full-energy peak efficiency values, PT- and LS-ratios. (a, b, c): Curves fitted (lines) to simulated efficiency, PT- or LS-values (open circles) and quality of these fits described by the ratio fitted/simulated values. **Lower right plot (d):** Terbium-160-spectrum reproduction using this set of curves in terms of  $N_E/N_E^{sim}$ -ratios and  $\chi^2$ -scores; Filled diamonds indicate full-energy peaks, open diamonds indicate sum-peaks.

6.5.2 Spectrum interpretation using the curves determined from the spectrum

Two variants of the calibration method where the parameters characterizing the detector were fitted to the simulated terbium-160 spectrum were investigated. Table 6.2 shows the recipes for each variant. The value determined for  $\rho$  was  $0.94 \pm 0.06$ . Each variant could be extended (**I+** and **II+**) by including in the fit the number of disintegrations of the calibration radionuclide during the measurement.

Figure 6.7(abc) and Figure 6.8(abc) show the curves resulting from Variant **I** and **II** respectively and their relation to the individually calculated values. Additionally, the figures (d) show the fit results for each peak area of terbium-160. The curves resulting from the extended variants **I+** and **II+**, i.e. those that included the number of disintegrations in the fit, are not shown.

6.5.3 Results

Figure 6.9 shows the results of the interpretation of an erbium-171 spectrum using the Monte Carlo curves, as well as the curves obtained by Variants **I** and **II**. In addition to their graphical representation, Table 6.3 shows the results of all the various procedures numerically. The table includes results obtained by the extended variants **I+** and **II+**.

**Table 6.2:** Calibration recipes for the two variants **I** and **II**. The table shows the parameters that are varied in each step of the fit procedure.

Variant	<b>I</b>	<b>I+</b>	<b>II</b>	<b>II+</b>
First Estimate	Monte Carlo calculated curves			
Step 1	$\rho$ only ( $\rho = 0.94 \pm 0.06$ )			
Step 2	PT only		Efficiency curve ( $g_0, g_3, g_6, g_8$ )	
Step 3			$g_0, g_3, g_6, g_8$ and PT	
Step 4	PT and LS	PT, LS and $N$	$g_0, g_3, g_6, g_8$ , PT and LS	$g_0, g_3, g_6, g_8$ , PT, LS and $N$

**Table 6.3:** Results of the various fit procedures to a terbium-160 spectrum (fitting) and results of applying the fitted curves to the terbium-160 spectrum and to an erbium-171 spectrum (interpretation), in terms of: The ratio between the fitted/interpreted and the true number of disintegrations; The  $\chi^2$ -value for the comparison between the two.

Fit variant:	Fitting ( $^{160}\text{Tb}$ )		Interpretation			
	$N_{\text{fit}}/N_{\text{true}}$	$\chi^2$	$N/N_{\text{true}}$ ( $^{160}\text{Tb}$ )	$\chi^2$	$N/N_{\text{true}}$ ( $^{171}\text{Er}$ )	$\chi^2$
<b>MC</b>	<b>na</b>		(0.991 $\pm$ 0.003)	12	(1.025 $\pm$ 0.006)	56
<b>I</b>	$N$ fixed	1.8	(1.000 $\pm$ 0.001)	1.4	(0.996 $\pm$ 0.005)	36
<b>I+</b>	(0.96 $\pm$ 0.04)	2.1	(0.960 $\pm$ 0.001)	2.0	(0.971 $\pm$ 0.005)	36
<b>II</b>	$N$ fixed	3.0	(1.001 $\pm$ 0.002)	2.9	(1.005 $\pm$ 0.004)	22
<b>II+</b>	(0.995 $\pm$ 0.003)	2.1	(0.995 $\pm$ 0.001)	2.0	(0.999 $\pm$ 0.004)	22

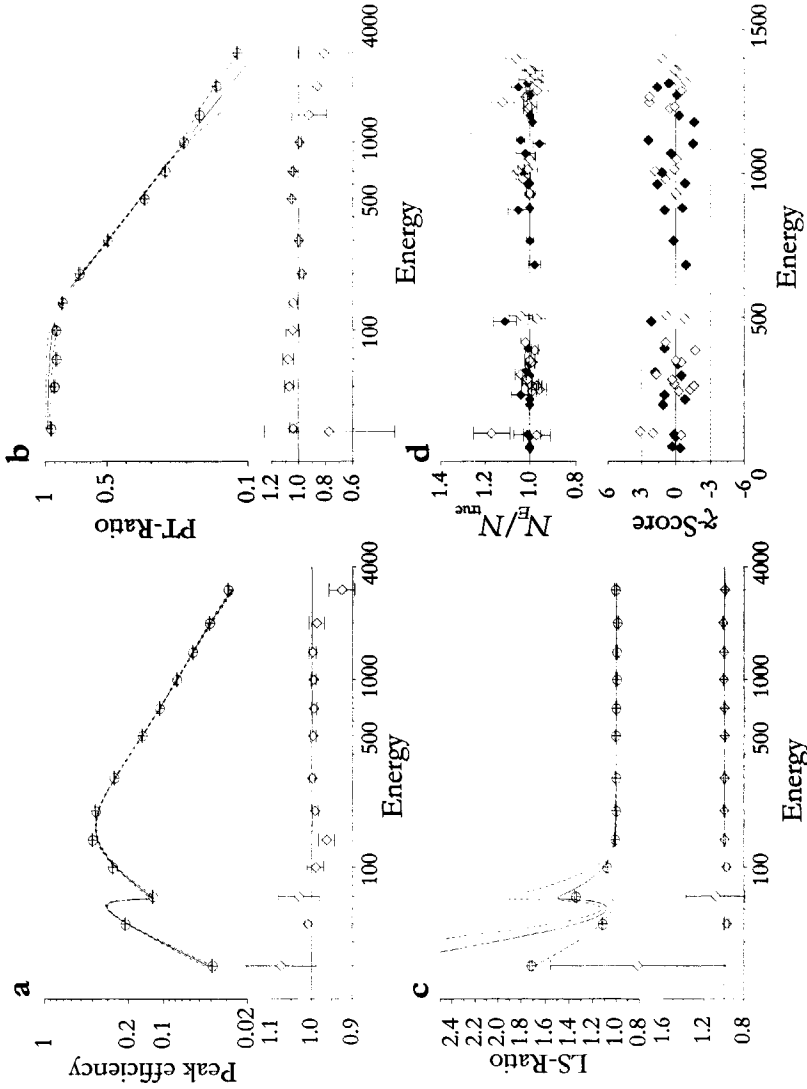


**Figure 6.7:** Reproduction of a simulated terbium-160-spectrum from a high-density source, for the non-lined well-type geometry, using efficiency-, PT- and LS-curves fitted from the terbium-160-spectrum. **a,b,c:** Fitted curves (lines) versus independently simulated efficiency, PT- or LS-values (open circles) and quality of these curves described by the ratio fitted/simulated values. **d (lower right):** Terbium-160-spectrum reproduction using this set of curves in terms of  $N_E/N_{Fit}$ -ratios and  $\chi^2$ -scores; Filled diamonds indicate full-energy peaks, open diamonds indicate sum-peaks.

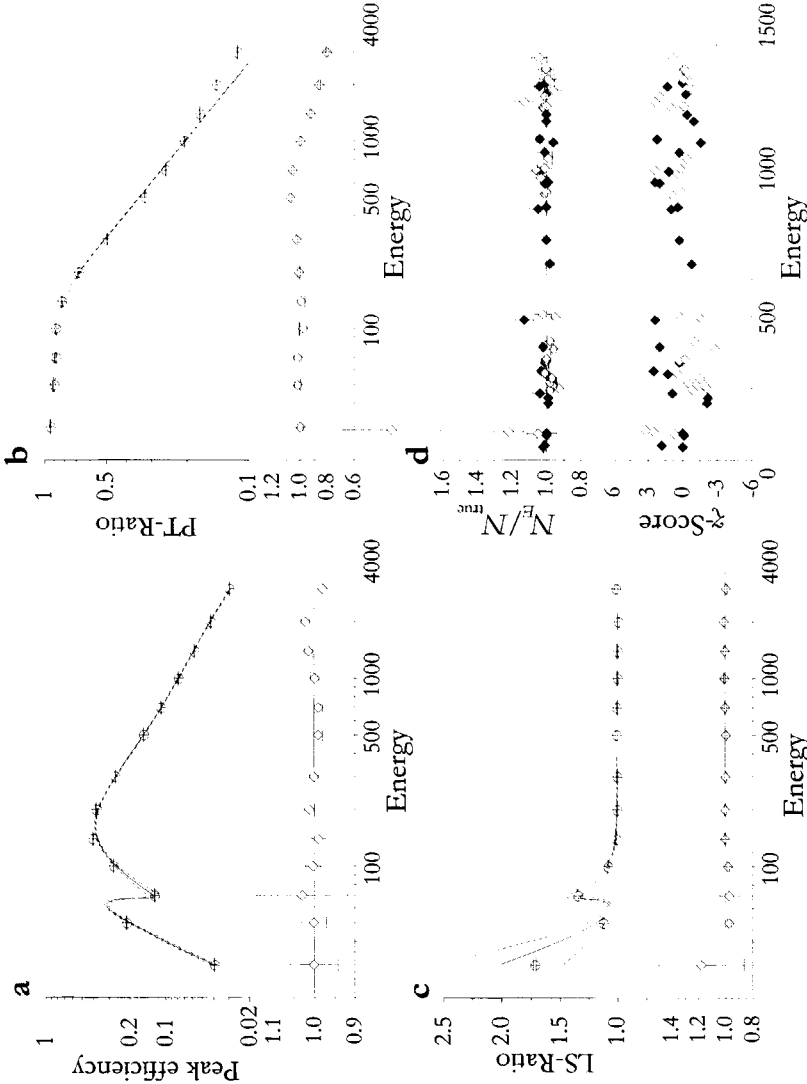


**Figure 6.8:** Reproduction of a simulated terbium-160-spectrum from a high-density source, for the non-lined well-type geometry, using an efficiency curve fitted to independently simulated efficiency-values and PT- and LS-curves fitted from the terbium-160-spectrum. **a,b,c:** Fitted curves (lines) versus simulated efficiency, PT- or LS-values (open circles) and quality of these curves described by the ratio fitted/simulated values. **d (lower right):** Terbium-160 spectrum reproduction using this set of curves in terms of  $N_E/N_{E_{fit}}$ -ratios and  $\chi^2$ -scores; Filled diamonds indicate full-energy peaks, open diamonds indicate sum-peaks.

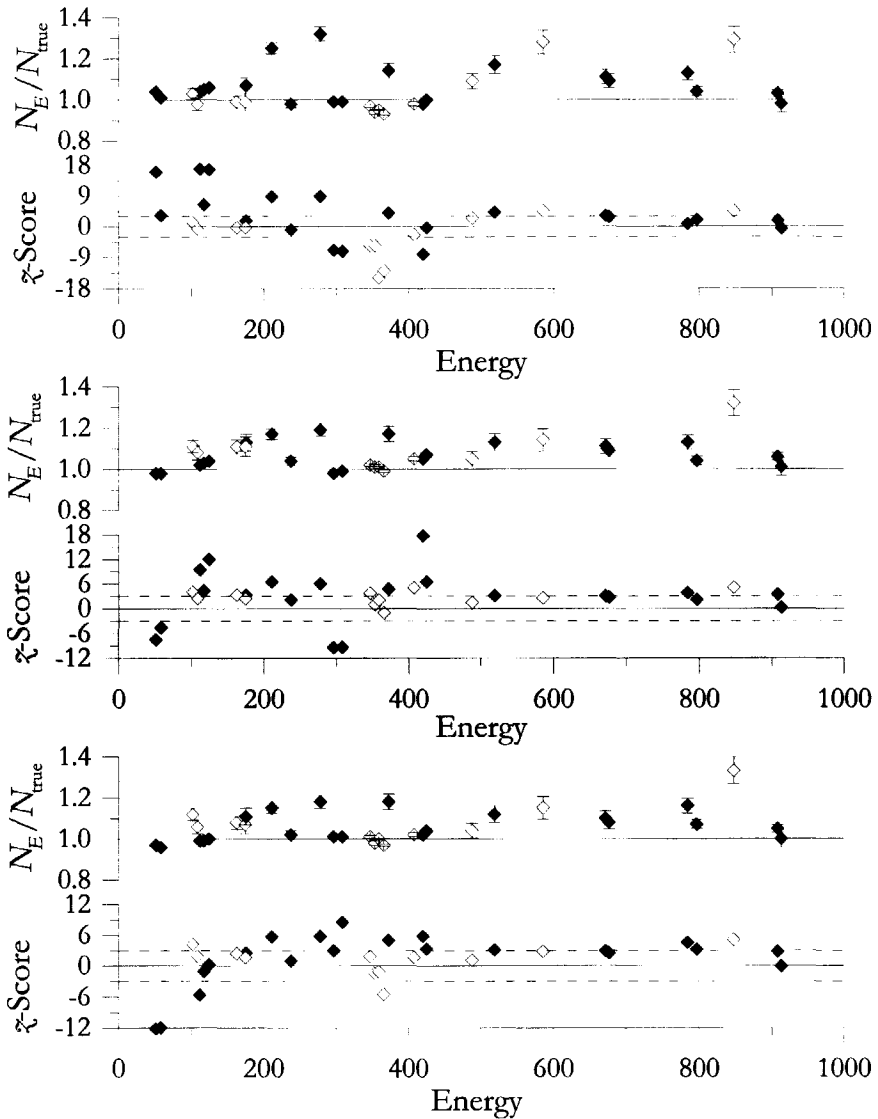


**Figure 6.9:** Interpretation results of erbium-171 spectra in terms of  $N_E/N_{\text{true}}$  ratios and  $\chi^2$ -scores for three curve sets: **upper plots:** using Monte Carlo calculated curves; **middle plots:** using Variant I curves; **lower plots:** using Variant II curves; Filled diamonds indicate full-energy peaks, open diamonds indicate sum-peaks.



#### 6.5.4 Discussion

The correlation parameter determined is statistically equal to unity. The results in the table show the same behaviour as the results obtained for the point source case: Usage of the Monte Carlo curve set results in relatively large  $\chi$ -scores on individual peak areas, even in the terbium-160 case. The number of disintegrations recovered with these curves again deviates approx. 2% for both terbium-160 and erbium-171.

The curves determined from the terbium-160 spectrum itself yield a perfect spectrum reproduction. Also the numbers of disintegrations do not deviate significantly from the true values. Varying the number of disintegrations in the fitting procedures (extended variants) is not an option in Variant I. However, if the full-energy peak efficiency curve is obtained from an auxiliary measurement like in Variant II, the terbium-160 spectrum can very well deliver the number of disintegrations.

The reproduction of the erbium-171 spectra is less satisfactory. Large  $\chi$ -scores on individual peaks are combined with high ratios (Figure 6.9). While the areas of most intense peaks are accounted for within 10%, some areas show deviations of over 20%. Especially Variant I results show large  $\chi$ -scores in the region near 100 keV.

### 6.6 General discussion and conclusion

The Monte Carlo based results in this chapter indicate that it is possible to determine the parameters required to characterize the sample-detector geometry from the measured spectrum of a calibration radionuclide like terbium-160, to the point where coincidence summing corrections with accuracies far better than the required 1% can be made for terbium-160 itself. The quality of the results will be optimal if the number of disintegrations in the calibration source is known and kept constant in the fitting procedure.

However, the simulated erbium-171 spectra were not satisfactorily explained from the curves obtained with terbium-160. Especially peaks in the low-energy region near 100 keV show large statistically significant deviations. Possibly, the full-energy peak efficiency curve is not well defined in this region. In this context, the reader is referred to section 2.2.1 which introduced an adapted version of the Gunnink parameterization. Originally, Gunnink divides the efficiency curve in three regions: <90 keV, 90 to 200 keV, and >200 keV. This work, however, uses only two regions, hereby combining the regions below 200 keV. This may very well explain the observed discrepancy in this region.

A second explanation for the observed discrepancy lies in the behaviour of the LS-curve as described in the last paragraph of section 6.2.1. Only very few terbium-160 photons in the low-energy region do coincide and therefore only marginally determine the curvature of the LS-curve. The determination in this region may simply be not accurate enough to fully explain low energy erbium-171 coincidences. This latter explanation, however, only explains discrepancies observed with the tantalum pentaoxide matrix source.

## References

- [1] R.F. Fleming, *Int. J. Appl. Radiat. Isot.*, **33** (1982) 1263.
- [2] R. Gunnink, *Nucl. Instr. and Meth.*, **A299**, (1990) 372
- [3] R. Gunnink, A.L. Prindle, *J. Radioanal. Nucl. Chem., Articles*, **160** (1992) 305
- [4] M. Blaauw, *Nucl. Instr. and Meth.*, **A332** (1993) 493

# Chapter Seven

## The missing curve for well-type detection geometries; Experimental verification

---

### Abstract

*This chapter verifies the calibration method described in the previous chapter. The method requires knowledge of the variation of the full-energy peak efficiency and the total efficiency over the source volume. Therefore, in addition to a peak-efficiency curve and a peak-to-total curve, it uses a third curve, the linear-to-squared curve, that accounts for this variation. This chapter describes two variants of the calibration method and their verification using experimental data. It is concluded that a calibration based on a combination of a measurement of a mixed radionuclide source and a measurement of a terbium-160 source provides the most accurate results. Compared to radionuclide-specific calibration, the method greatly reduces calibration efforts without compromising calibration quality too much.*

### 7.1 Introduction

Chapter Six explored the feasibility of the three efficiency curves approach in the case of well-type detectors developed in Chapter Two, using Monte Carlo simulations. For high- $Z$  sources it was necessary to introduce a parameterization for  $K$ -edges (section 6.2.1). This parameterization affected both the full-energy peak efficiency curve and the LS-curve. Chapter Six further argued that in well type detectors, the LS-curve and the correlation parameter play only a role in the case of summation of two low-energy photons. Therefore, depending on the decay scheme of the radionuclide of concern, it can be expected that the LS-curve, as well as the correlation parameter is of minor significance. On the other hand, only radionuclides emitting several low-energy photons

simultaneously are expected to provide enough information to estimate the LS-curve and the correlation parameter accurately.

Chapter Six observed discrepancies between spectra directly calculated via Monte Carlo methods and those predicted by the theory using Monte Carlo calculated efficiency curves. They were partly contributed to insufficient coverage of coincidence effects in the low-energy region by the terbium-160 decay, and partly to the simplified adaptation of Gunnink's efficiency curve in the energy region below 90 keV.

This Chapter explores the feasibility of the three efficiency curves approach in the case of well-type detectors using real measurements. Firstly, a measurement of a terbium-160 low-density source alone or combined with a measurement of a standard calibration source containing cadmium-109, cobalt-57, cerium-139, tin-113, caesium-137, cobalt-60, and yttrium-88 was used to determine the efficiency curves for a zirconium-lined well-type detector. The expected response of the detector for erbium-171 was calculated from these curves and compared to the measured response of a erbium-171 low-density source. Then, the same experiment was performed for the same detector after removal of the lining. Finally, the experiment was repeated with the activities in a tantalum pentoxide ( $Ta_2O_5$ ) sample matrix and the unlined detector to achieve high sample self-attenuation.

As a result of Blaauw's earlier work, low-Z bromine-82 sources are routinely used to calibrate commonly used counting geometries at IRI. Two such measurements were performed with the detector used in this chapter, once lined, once unlined. These measurements are incorporated in the analysis of the calibration method performance.

## 7.2 Experimental

### 7.2.1 Low-Z sources in lined detector

#### *Source preparation*

The low-Z source containing approximately 1 kBq of each of the standard calibration radionuclides cadmium-109, cobalt-57, cerium-139, tin-113, caesium-137, cobalt-60, and yttrium-88 (the "TM-source") was prepared by pipetting aliquots from a certified solution purchased from the Physikalisch-Technische Bundesanstalt (PTB) on a 4.5 mm thick layer of filter paper in a 1 cm high high-density polyethylene capsule. The source was dried in air for 16 hours.

Terbium peroxide ( $Tb_4O_7$ ) and erbium oxide ( $Er_2O_3$ ) were obtained from Aldrich at 99.999 % purity, containing less than ppm-levels of europium and gadolinium.

Terbium-160 was produced by dissolving 43 mg terbium peroxide in 16 ml 65 % nitric acid ( $HNO_3$ ) at 70 °C. An aliquot of 1 ml of the solution was irradiated in the HOR (Hoger Onderwijs Reactor) BP3 facility during 30 minutes at a neutron flux of approximately  $5 \times 10^{16} \text{ m}^{-2} \text{ s}^{-1}$ . After irradiation, the solution was diluted with 4 ml 65 %

nitric acid. Three low-Z sources were prepared by gravimetrically pipetting aliquots of 50  $\mu\ell$  in polyethylene capsules as described above for the PTB solution.

Erbium-171 was produced by dissolving 375 mg erbium oxide in 10 ml 6.5 % nitric acid at 70 °C. An aliquot of 1 ml of the solution was irradiated during 3 minutes in the same irradiation facility. After irradiation, the solution was diluted with 9 ml 6.5 % nitric acid. Three low-Z sources were prepared by gravimetrically pipetting aliquots of 50  $\mu\ell$  in polyethylene capsules as described above for the PTB solution.

The bromine-82-sources were prepared by pipetting aliquots of ammonium bromine ( $\text{NH}_4\text{Br}$ ) dissolved in water in polyethylene capsules as described above. The capsules were irradiated after drying during 30 minutes at a neutron flux of approximately  $5 \times 10^{16} \text{ m}^{-2}\text{s}^{-1}$ .

The radioactive lanthanides and bromine-82 sources were counted in independently calibrated counting geometries at large distances from coaxial detectors to establish the absolute activities.

### *Measurements*

All sources were counted in a well-type detector lined with approx. 0.8 mm zirconium. The exact geometry is the same as the one that has been modelled in the previous chapter and is depicted in Figure 6.2. This detector in its lined state has an absolute efficiency for the 1333 keV photons of 4.6 %. All counting times were long enough to achieve uncertainties in the main peak areas owing to counting statistics of better than 0.5 %. Peak areas were determined as described in ref.[1].

### *Fitting procedure*

Two sets of efficiency curves characterizing the counting geometry, sample included, were determined. A set of efficiency curves consists of the peak efficiency curve defined by parameters  $g_0$  through  $g_5$  as defined in Chapter Two, and a peak-to-total efficiency curve defined by parameters  $\eta_0$  through  $\eta_2$ . The LS-ratios were kept fixed at unity in these procedures. The first set was obtained from the terbium-160 spectrum alone (Variant I), and the second set from the terbium-160 and the TM-source together (Variant II). The latter variant was performed by fitting the full-energy peak efficiency curve to the spectrum of the TM-source and the peak-to-total curve to the spectrum of the terbium-160 source alternatingly until the quality of the result improved no further.

### *Verification procedure*

The two sets of efficiency curves obtained as described above were employed to compute the expected peak areas for erbium-171 and bromine-82, and these expected peak areas were compared to the experimental results in terms of  $\chi$ -scores and  $N/N_E$ -ratios, as well as in terms of erbium-171 and bromine-82 source activities, as described in

Appendix B. The set determined by Variant I was also verified in terms of source activities with the TM-source spectrum.

### 7.2.2 Low-Z sources in unlined detector

#### *Source preparation*

The sources used in this experiment were the same as those used in the experiment with the lined detector.

#### *Measurements*

All sources were counted in the same well-type detector after removal of the zirconium lining. All counting times were long enough to achieve uncertainties in the main peak areas owing to counting statistics of less than 0.5 %.

#### *Fitting procedure*

Two sets of efficiency curves characterizing the counting geometry, sample included, were determined by the same procedures (i.e. Variant I and II) as for the lined experiment described above. However, the energy region below 88 keV obtained in Variant I was preserved when fitting the peak efficiency curve to the TM source spectrum in Variant II.

#### *Verification procedure*

The two sets of efficiency curves obtained were again verified with the erbium-171, bromine-82 and TM-source spectra.

### 7.2.3 High-Z sources in unlined detector

#### *Source preparation*

The source containing approximately 1 kBq of each of the standard calibration radionuclides cadmium-109, cobalt-57, cerium-139, tin-133, caesium-137, cobalt-60, and yttrium-88 was prepared by pipetting aliquots from a certified solution purchased from PTB in a 1.5 cm high polyethylene capsule filled to 1 cm height with tantalum pentoxide ( $Ta_2O_5$ ). The source was dried in air for 16 hours, and shaken after sealing to homogenize the contents.

Three high-Z samples of the terbium-160 and erbium-171 solutions obtained as described for the previous experiments were prepared by gravimetrically pipetting aliquots of 50  $\mu\ell$  in polyethylene capsules as described above for the PTB solution. The activities of the sources were derived from the measured activities of the equivalent low-Z sources.

*Measurements*

All sources were counted in the same well-type detector after removal of the zirconium lining. All counting times were long enough to achieve uncertainties in the main peak areas owing to counting statistics of less than 0.5 %.

*Fitting procedure*

Two sets of efficiency curves characterizing the counting geometry, sample included, were determined by the same procedures (i.e. Variant I and II) as for the lined experiment described above for the unlined/low-Z experiment. However, the self-attenuation parameters were involved in the peak efficiency and the LS-curves this time as described and defined in Chapter Six. Parameters  $g_4$  and  $g_5$ , characterizing external attenuation, were kept fixed at the values obtained for the low-Z sources. Of the parameters  $g_6$  through  $g_8$ , only the optical density related parameter  $g_6$  was determined by fitting. The others were derived from the known matrix element properties. The correlation parameter,  $\rho$ , was kept fixed in this procedure at the same value of 0.94 used in the Monte Carlo exercise.

In the spectra, sum peaks were observed that were the result of simultaneous detection of tantalum X-rays and terbium-160  $\gamma$ -rays. Some of these interfered with pure terbium-160 peaks. These multiplets were disregarded in the fitting procedure. For example, the terbium-160  $\gamma$ -ray energy 355 keV also happens to be the sum of 298 keV and 57 keV, where 57 keV is the tantalum  $K_\alpha$  X-ray. The other cases were 486 ( $\approx 433 + 57$ ), 572 ( $= 506 + 66$ ) and 1338 ( $=1272 + 66$ ) keV.

*Verification procedure*

The two sets of efficiency curves obtained were again verified with the erbium-171 and TM-source spectra.

**7.3 Results**

The results are presented in Figure 7.1 through Figure 7.7 and in Table 7.1.

**Table 7.1:** Fit results of the various procedures and interpretation results using fitted curves, in terms of: The ratio between interpreted and the true number of disintegrations; The  $\chi^2$ -value for the comparison between the two.

Geometry	Variant	<sup>160</sup> Tb		<sup>137</sup> Cs	<sup>60</sup> Co		<sup>82</sup> Br	
		$N_{fit}/N_{true}$	$\chi^2$		$N/N_{true}$	$N/N_{true}$	$\chi^2$	$N/N_{true}$
Low-Z lined	I	1.000 ± 0.003	2.7	-	1.010 ± 0.005		0.91 ± 0.03	64
	II	1.001 ± 0.003	3.1	-	1.004 ± 0.005		0.90 ± 0.03	64
Low-Z unlined	I	1.000 ± 0.004	2.2	1.029 ± 0.013	0.976 ± 0.003	2.9	0.94 ± 0.04	113
	II	0.998 ± 0.004	2.3	1.025 ± 0.008	0.998 ± 0.003	3.0	1.00 ± 0.04	112
High-Z unlined	I	1.000 ± 0.003	1.2	1.033 ± 0.005	1.001 ± 0.004	4.1	1.00 ± 0.05	89
	II	1.000 ± 0.004	2.0	0.990 ± 0.005	1.026 ± 0.006	0.7	0.96 ± 0.05	92

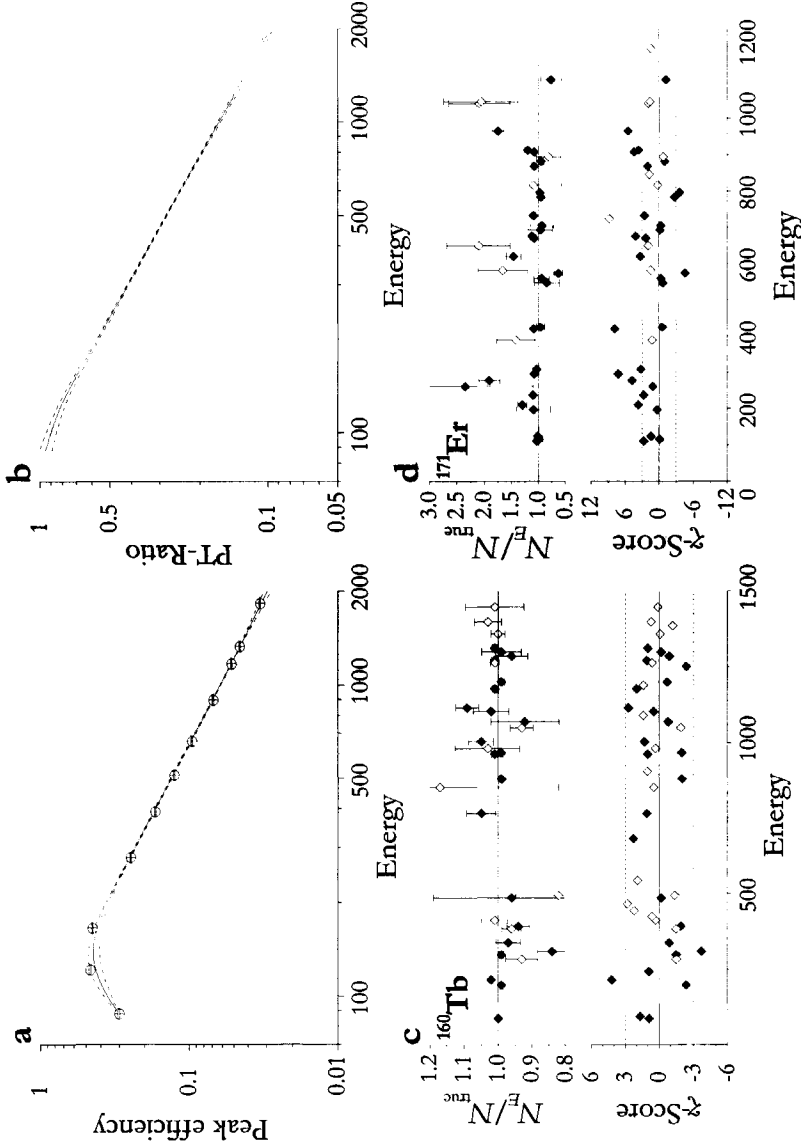


**Figure 7.1:** Reproduction of terbium-160 and erbium-171 spectra from a low-Z source for the lined well-type geometry using curves obtained with variant I of the fit procedure (see text) **Upper plots (a, b):** Curves fitted (solid lines) to terbium-160 spectrum and  $1\sigma$  confidence regions (dashed lines). Open circles and  $1\sigma$  error bars indicate full-energy peak efficiency values obtained from an independent calibration source. **Lower plots (c, d):** Terbium-160- and erbium-171-spectrum reproduction using this set of curves in terms of  $N_E/N_{unc}$ -ratios and  $\chi^2$ -scores; Filled diamonds indicate full-energy peaks, open diamonds indicate sum-peaks.



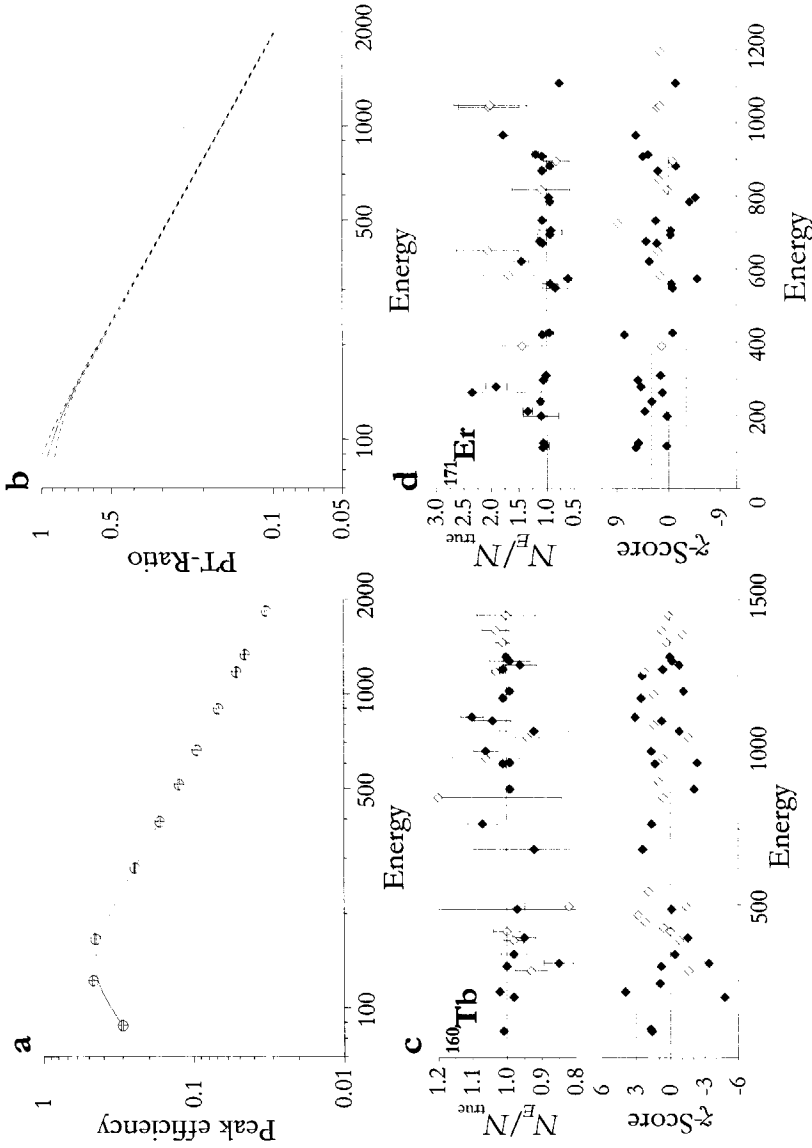


**Figure 7.2:** Reproduction of terbium-160 and erbium-171 spectra from a low-Z source for the lined well-type geometry using curves obtained with variant II of the fit procedure (see text) **Upper plots (a, b):** Curves fitted (solid lines) to terbium-160 spectrum and  $1\sigma$  confidence regions (dashed lines). **Lower plots (c, d):** Terbium-160- and erbium-171-spectrum reproduction using this set of curves in terms of  $N^E/N^E_{\text{fit}}$ -ratios and  $\chi^2$ -scores; Filled diamonds indicate full-energy peaks, open diamonds indicate sum-peaks.

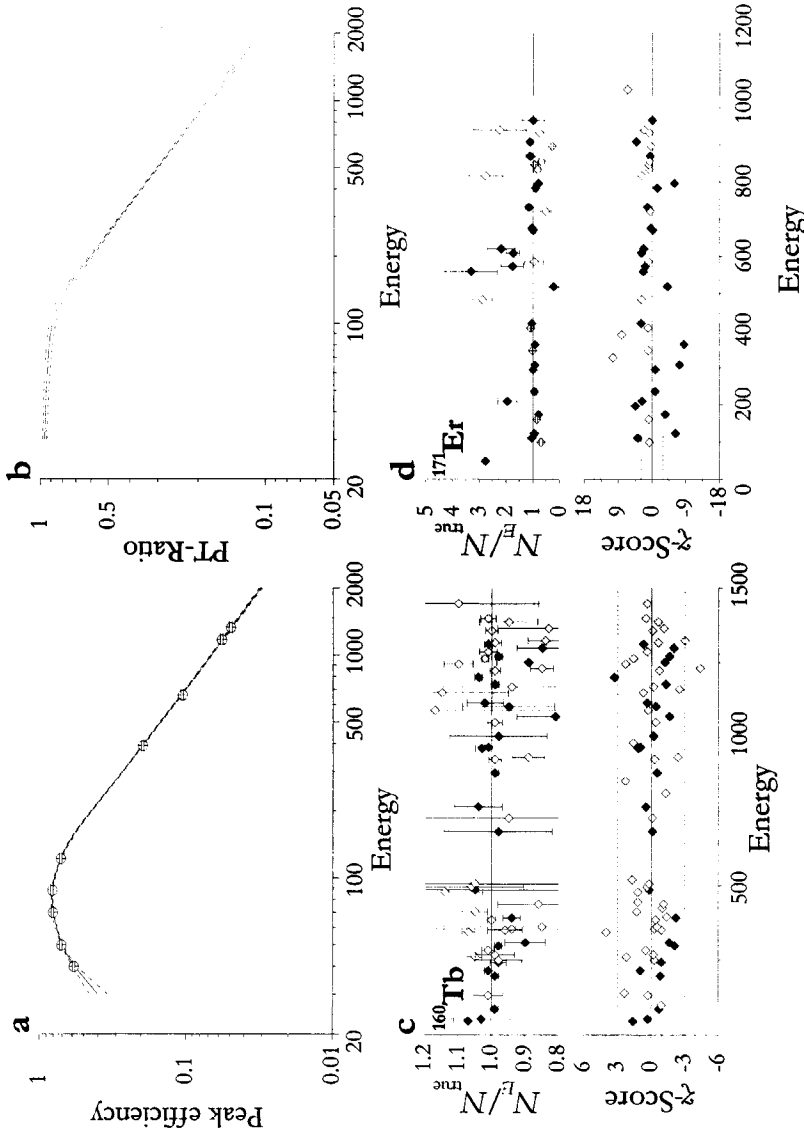


**Figure 7.3:** Reproduction of terbium-160 and erbium-171 spectra from a low-Z source for the non-lined well-type geometry using curves obtained with variant I of the fit procedure (see text) **Upper plots (a, b):** Curves fitted (solid lines) to terbium-160 spectrum and  $1\sigma$  confidence regions (dashed lines). Open circles and  $1\sigma$  error bars indicate full-energy peak efficiency values obtained from an independent calibration source. **Lower plots (c, d):** Terbium-160- and erbium-171-spectrum reproduction using this set of curves in terms of  $N_E/N_E^{\text{cal}}$ -ratios and  $\chi^2$ -scores; Filled diamonds indicate full-energy peaks, open diamonds indicate sum-peaks.

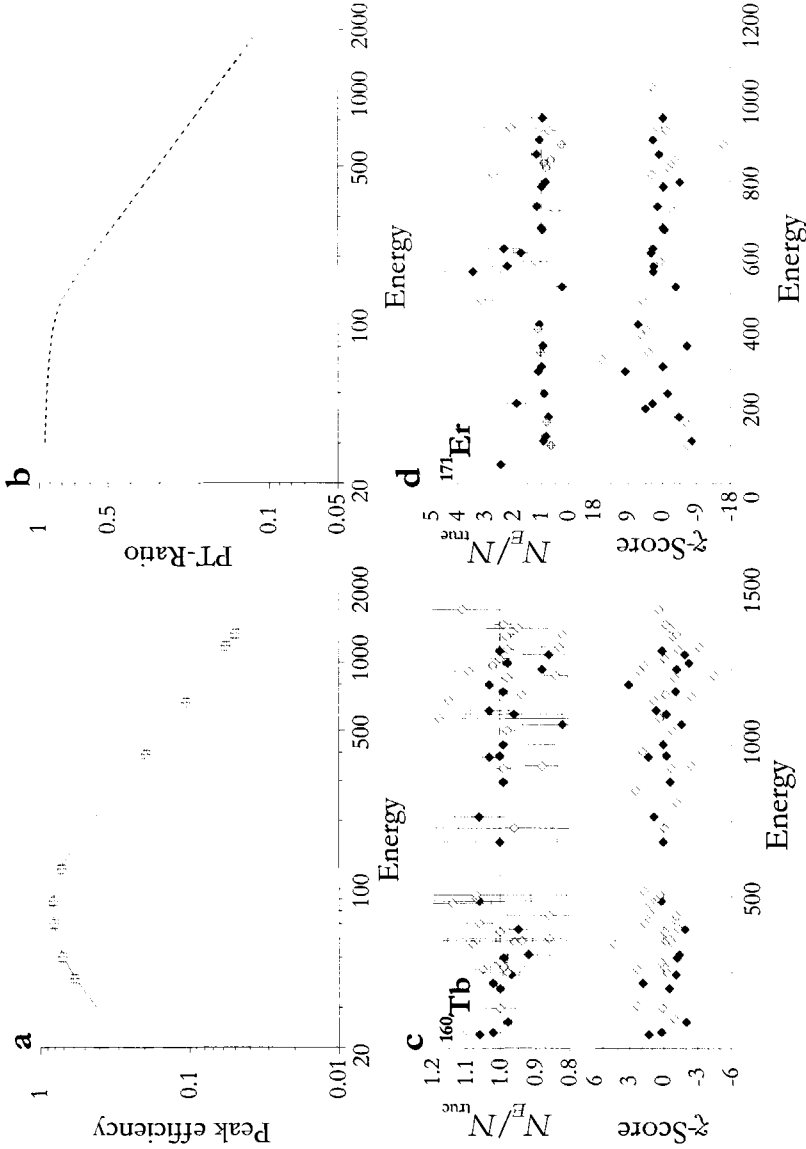


**Figure 7.4:** Reproduction of terbium-160 and erbium-171 spectra from a low-Z source for the non-lined well-type geometry using curves obtained with variant **II** of the fit procedure (see text) **Upper plots (a, b):** Curves fitted (solid lines) to terbium-160 spectrum and  $1\sigma$  confidence regions (dashed lines). Open squares and  $1\sigma$  error bars indicate full-energy peak efficiency values obtained from an independent calibration source. **Lower plots (c, d):** Terbium-160- and erbium-171-spectrum reproduction using this set of curves in terms of  $N_E/N_{Ec}$ -ratios and  $\chi^2$ -scores; Filled diamonds indicate full-energy peaks, open diamonds indicate sum-peaks.

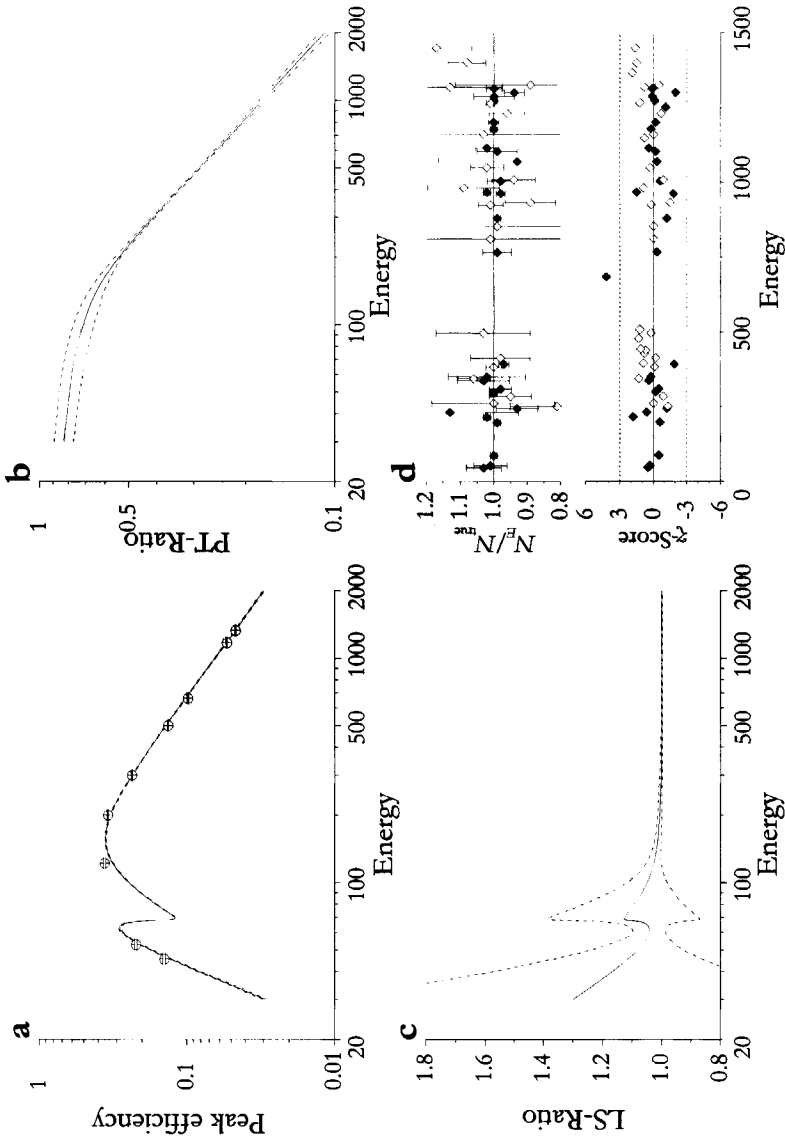


**Figure 7.5:** Reproduction of a terbium-160 spectrum from a high-Z source for the non-lined well-type geometry using curves obtained with variant I of the fit procedure (see text) (**a**, **b** and **c**): Curves fitted (solid lines) to terbium-160 spectrum and 1 $\sigma$  confidence regions (dashed lines). Open circles and 1 $\sigma$  error bars indicate full-energy peak efficiency values obtained from an independent calibration source. (**d**): Terbium-160 spectrum reproduction using this set of curves in terms of  $N^E/N^E$ -ratios and Z-scores; Filled diamonds indicate full-energy peaks, open diamonds indicate sum-peaks.

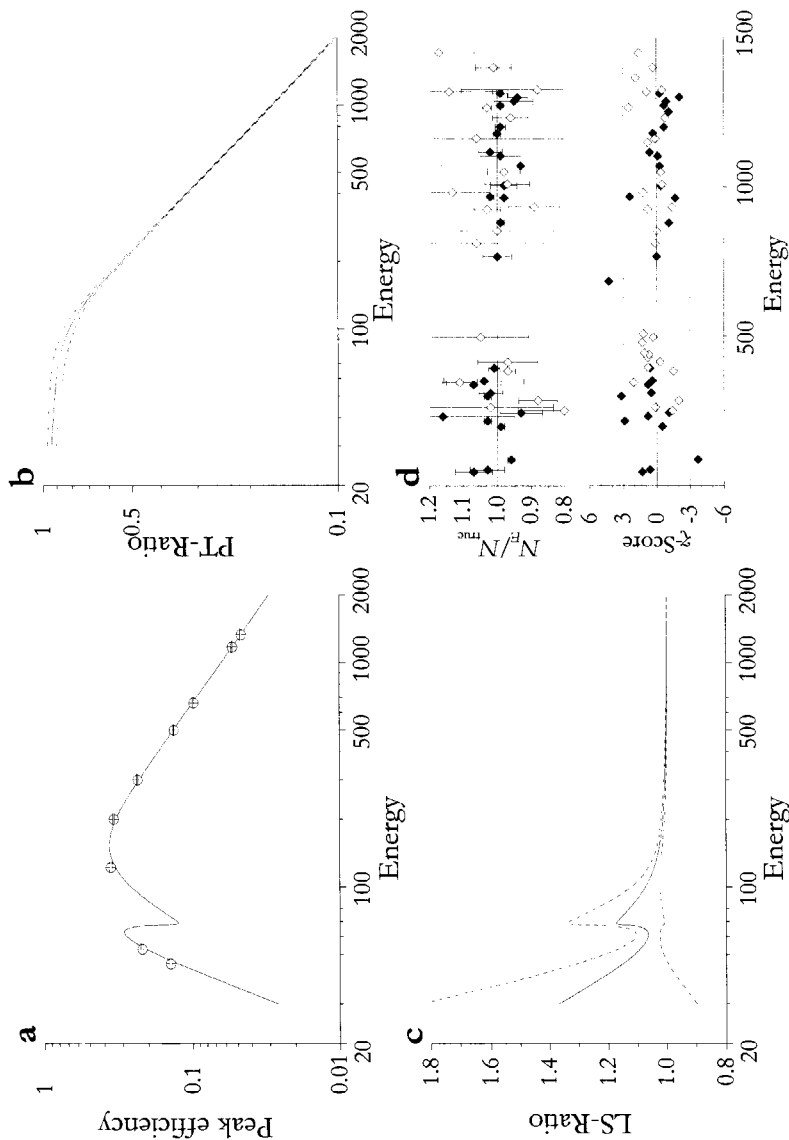


**Figure 7.6:** Reproduction of a terbium-160 spectrum from a high-Z source for the non-lined well-type geometry using curves obtained with variant II of the fit procedure (see text) (**a**, **b** and **c**): Curves fitted (solid lines) to terbium-160 spectrum and  $1\sigma$  confidence regions (dashed lines). Open circles and  $1\sigma$  error bars indicate full-energy peak efficiency values obtained from an independent calibration source. (**d**): Terbium-160 spectrum reproduction using this set of curves in terms of  $N_E/N_{true}$ -ratios and  $\chi^2$ -scores; Filled diamonds indicate full-energy peaks, open diamonds indicate sum-peaks.

#### 7.4 General discussion and conclusion

The results show that the problem of coincidence summing with X-rays, (in low-Z sources counted in a lined well-type, as well as in the other counting geometries), is extremely difficult to correct for theoretically. For the purpose of analysis, let's subsequently treat the three source-detector geometries used in this chapter in the order of increasing complexity.

The first well-type geometry under consideration is the lined one, using a standard low-Z, low-density source. This geometry is used routinely at IRI. The calibration results and the interpretation results obtained from this calibration are depicted in Figure 7.1 and Figure 7.2, in Table 7.1, and in the upper plot of Figure 7.7. Both variants of the calibration method succeed in reproducing the terbium-160 spectrum, as well as the

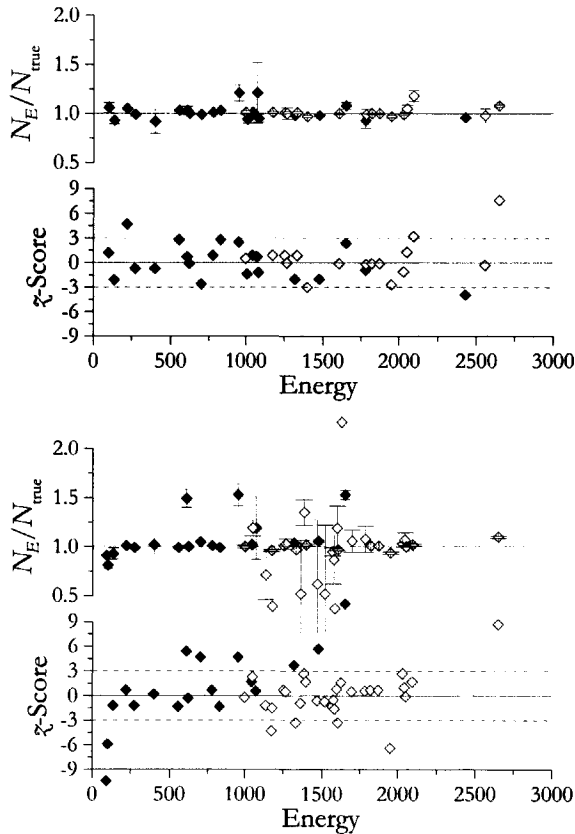


**Figure 7.7:** Interpretation results of bromine-82 spectra in terms of  $N_E/N_{true}$  ratios and  $\chi^2$ -scores using the curves obtained with Variant I for the low-density, low-Z source measured in either the lined geometry (**upper plot**) or in the unlined well-type geometry (**lower plot**)

caesium-137, cobalt-60 and bromine-82 spectra from this geometry. The erbium-171 spectra, however, are not satisfactorily reproduced. The erbium-171 discrepancy is strange if one realizes that the calibration method that was used for this geometry does not in any aspect differ from Blaauw's method, which is known to be accurate for a great many radionuclides by now<sup>[2]</sup>. Furthermore, Blaauw uses the same parameterization for the efficiency curves.

A plausible explanation for the erbium-171 discrepancy is hard to give. Possibly, the simplification of Gunnink's parameterization of the full-energy peak efficiency curve in the low energy region (see section 2.2.1) explains it, even though the lining prevents low-energy photons from being detected. The erbium-171 decay, however, might somehow be sensitive for said simplification. Another explanation might be deficient information on

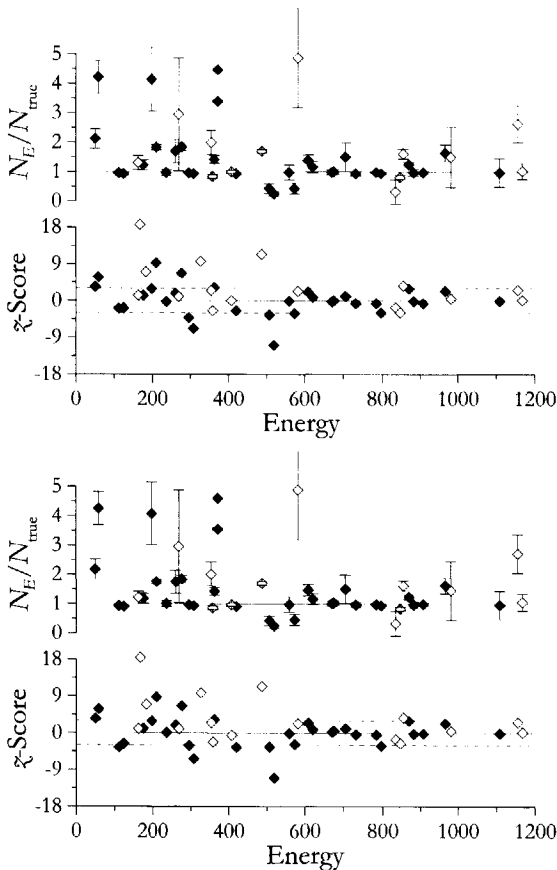


**Figure 7.8:** Interpretation results for erbium-171 spectrum from a high-Z Ta<sub>2</sub>O<sub>5</sub>-matrix source measured in the non-lined well-type geometry using either the curve set obtained with Variant I of the calibration method (**upper plot**) or the curve set obtained with Variant II (**lower plot**). Filled diamonds indicate full-energy peaks, open diamonds indicate sum-peaks.

the erbium-171 decay. From the agreement between terbium-160 and the simple radionuclides cobalt-60, caesium-137 and bromine-82, it appears that the decay scheme of erbium-171 is suspect. This suspicion is confirmed by interpretation of the erbium-171 spectrum using the efficiency curves that were obtained by Blaauw, showing similar discrepancies between theory and experiment. However, if a deficiency of the erbium-171 decay scheme exists, it would rather concern information on X-ray emission than on  $\gamma$ -ray emission. Erbium-171 X-rays, for that matter, are stopped by the lining very effectively.

The second well-type geometry under consideration is the non-lined one, using again a standard low-Z, low density source. The calibration results and the interpretation results are depicted in Figure 7.3 and Figure 7.4, in Table 7.1 and in the lower plot of Figure 7.7. Again, both variants of the method succeed in successfully reproducing the terbium-160 spectrum. Also they successfully reproduce the spectra of simple radionuclides cobalt-60, caesium-137 and bromine-82. They do not however explain the erbium-171 spectrum satisfactorily. Although variant II of the method (i.e. the one using an auxiliary full-energy peak efficiency curve) does recover the correct number of disintegrations, it does so at the cost of a very large  $\chi^2$  score.

Again, the same two explanations can be offered: An oversimplification of Gunnink's efficiency curve in the low-energy region, and a suspect decay scheme of erbium-171. Both are more plausible here than in the lined geometry since X-rays play a very important part in the non-lined erbium-171 spectrum mainly owing to coincidence effects (in this context the reader is referred to Chapter Four). Again, the suspicion of the erbium-171 decay scheme is confirmed by the interpretation of the erbium-171 spectrum using the efficiency curves that were obtained by Blaauw, showing similar discrepancies between theory and experiment. Thirdly, at the low energies involved in the unlined geometries, thickness variations in the glass sample holders may have played a part.

The final well-type detection geometry under consideration is the non-lined one, using a high-Z, tantalum pentoxide matrix source. The calibration results and the interpretation results are depicted in Figure 7.5, Figure 7.6 and Figure 7.8 and in Table 7.1. Again while the terbium-160, the cobalt-60 and the caesium-137 measurements are interpreted well, the erbium-171 measurement shows rather large discrepancies.

Next to the same three previous explanations, a fourth one can be offered: Physical phenomena such as the emission of X-rays by the lining and/or the source matrix should have been accounted for in the modelling, and/or the decay schemes of the radionuclides involved are not known well enough. The X-ray emissions by sample matrix and detector lining were assumed to be encompassed by the definition of total efficiency, but the resulting peaks in the spectrum may coincide with others - the more complex the spectrum becomes, the higher the likelihood of this happening.

The agreement between experiment and theory is, at least for the erbium-171 case rather unsatisfactory. However, employing the calibration methods described in this chapter would lead to systematic errors in reported activities of only 0 to 3 % for simple radionuclides such as caesium-137, depending on the counting geometry and the



radionuclide. It would lead to errors of 3 % for a complex case like bromine-82, and only up to 10 % for a complex radionuclide such as erbium-171. This latter value is an upper limit owing to the uncertainty in the true activity of the erbium-171 source, which was considerably larger than the uncertainties in the caesium-137 and cobalt-60 source activities; it may be that the systematic error made for erbium-171 in this work is in fact somewhat smaller than 10 %. The difference in the quality of the results for bromine-82 and erbium-171 may be owing to energies between 50 and 90 keV not playing a part for bromine-82.

In those cases where the radionuclide to be determined cannot be obtained in a known amount in the matrix of interest, and the use of well-type is deemed necessary, the procedures presented here currently are the only option for quantitative determination. One should realize that systematic errors caused by true coincidence summing in well-type counting geometries can easily amount to a factor of 2 to 3 for complex radionuclides (e.g. the magnitude of the coincidence summing effect for the 111 keV of erbium-171 is 0.40 in the lined geometry, 0.68 for the 879 keV of terbium-160) - in that respect, the methods presented here certainly are an improvement. However, the rather extreme variations between expected and measured peak areas of different peaks in the case of complex radionuclides emitting low-energy photons like erbium-171 make interference corrections by peak stripping rather hazardous.

## References

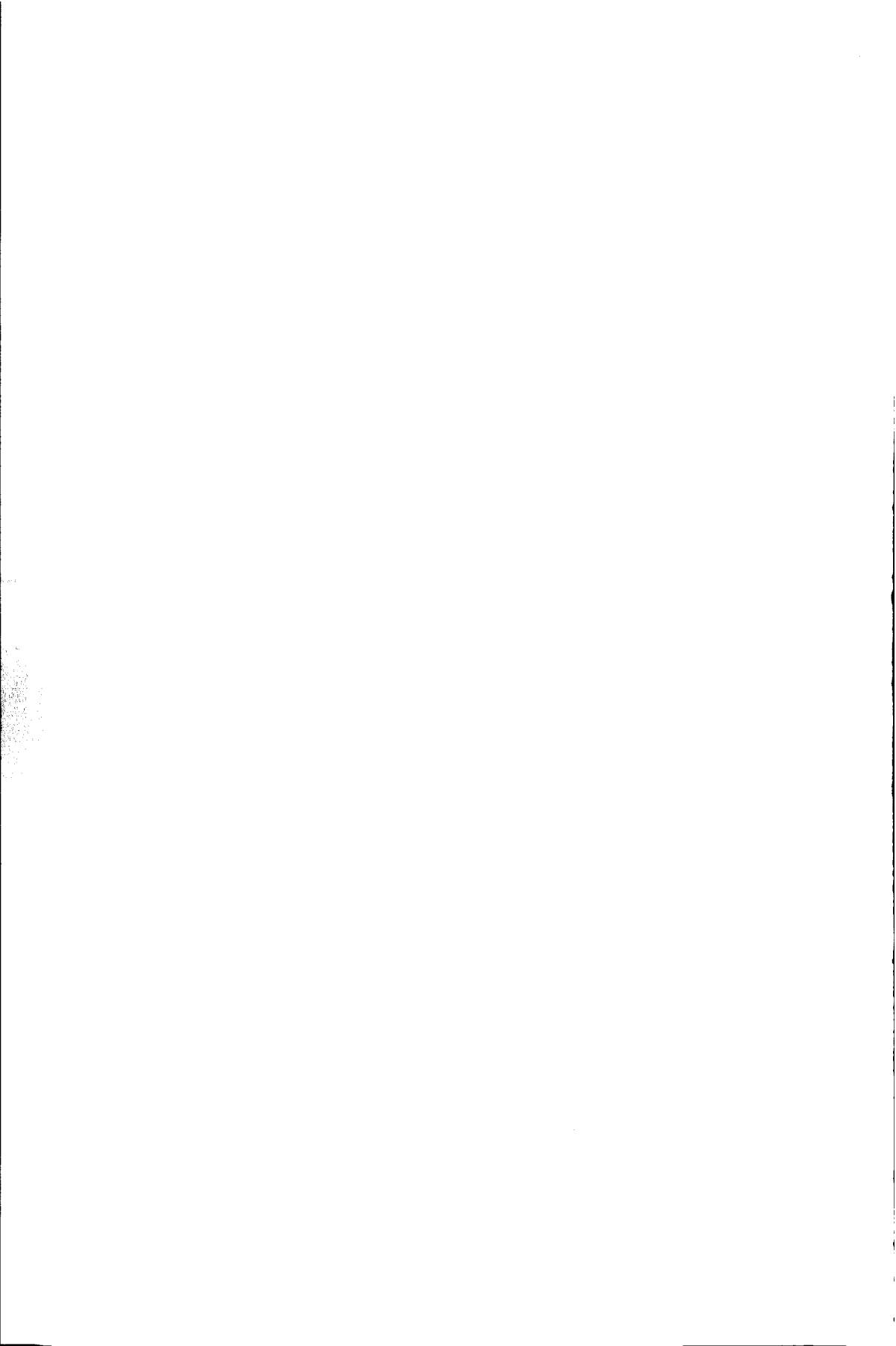
- [1] M. Blaauw, *The holistic analysis of gamma-ray spectra in INAA*, Ph.D. thesis, Delft University of Technology, Delft (1993)
- [2] M. Blaauw, *J. Radioanal. Nucl. Chem., Articles*, **245** (2000) 185



# **Part III**

## **Marinelli-beaker detection geometries**

---



# Chapter Eight

## The missing curve for voluminous source coincidence corrections; A Monte Carlo survey

---

### Abstract

*This chapter describes a calibration method that includes coincidence effect, as well as attenuation effect corrections for Marinelli-beaker type detection geometries. The method requires knowledge of the variation of the full-energy peak efficiency and the total efficiency over the source volume. Therefore, in addition to a peak efficiency curve and a peak-to-total curve, it uses a third curve that accounts for the variation. This chapter describes how the theory developed in Chapter Two provides the general shape of the curves. The actual calibration determines the curve parameters using a bromine-82 spectrum that shows severe coincidence effects. Although, in this chapter, the method is verified using computer simulations, the method itself does not require any simulation or volume integration calculations. Compared to other calibration methods for voluminous sources, the method greatly reduces calibration efforts. The next chapter will describe the use of the method in practice.*

### 8.1 Introduction

In  $\gamma$ -ray spectrometry, the quantitative measurement of radioactive samples with low specific activity such as environmental samples requires the use of a detection geometry that places a large volume of sample material as close to a radiation detector as possible. Marinelli beaker geometries are frequently used for this purpose. The large sample volume gives rise to  $\gamma$ -ray attenuation, which has to be accounted for. In addition, detection efficiencies are usually high enough to give considerable coincidence summing effects. Therefore, the calibration of a Marinelli beaker detection geometry deserves critical attention.

The most accurate method to calibrate the Marinelli geometry is by using a standard source containing all the radionuclides of interest and having exactly the same dimensions, atomic composition and density as the unknown sample. Furthermore, the distributions of the activity over the sample volume should be identical in both the standard source and in the unknown sample. This method, however, can be very laborious and time-consuming, especially when a large range of radionuclides or samples of different composition and/or densities are used. Moreover, standard sources are not always available.

This chapter describes a novel calibration method based on the mathematical model described in Chapter Two. It tests its feasibility using computer-simulated spectra (Chapter Three). It is organized as follows: Section 8.2 defines the geometries used, it describes the explicit determination by computer simulation of all curves and it introduces the simulated test spectra. Section 8.3 then validates the theory. Section 8.4 describes the use of the simulated spectrum of bromine-82 as a calibration spectrum. In addition, it describes the reproduction of the simulated spectra of barium-133 and caesium-134, now using the curves obtained by the calibration. The quality of the spectrum reproductions will show the quality of the method. Finally, Section 8.5 discusses the results from the previous sections and gives general conclusions.

At this point, it should be emphasized that although the tests of the method involve simulation techniques, the method itself does not need them, nor does it need dedicated programs to perform volume integrations. The next chapter will describe the application of the method in a real-life situation.

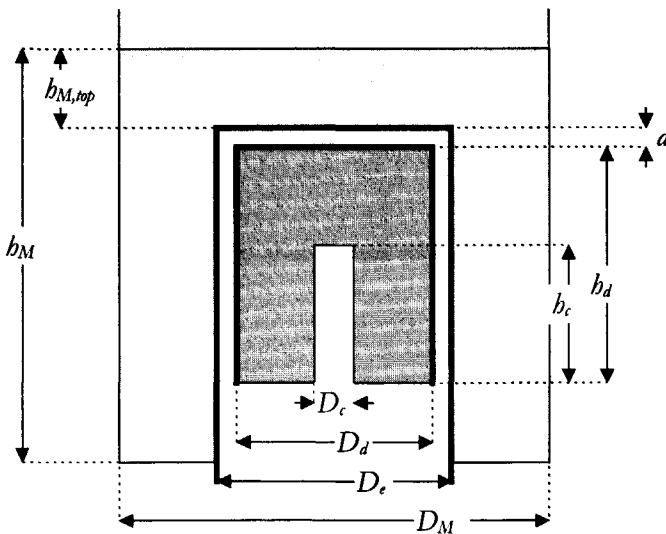


**Figure 8.1:** General Marinelli beaker detection geometry. Actual dimension are given by Table 8.1

## 8.2 Methods

The validation in Section 8.3 of the theory and the development in Section 8.4 of the calibration method require the calculation of both full-energy peak efficiency and total efficiency values, LS-ratios and the simulation of spectra. This section describes the geometries for which the calculation is performed and it describes the calculation itself in more detail. In addition it describes the use of z-scores and  $\chi^2$ -values when comparing spectra.

### 8.2.1 Detection geometries

The simulation programs use two Marinelli beaker type detection geometries. Each geometry bears close resemblance to actual measurement geometries. The first geometry consists of a 1 litre Marinelli beaker placed over a 18% relative efficiency Ge(Li) detector. This geometry will be referred to as "ORT". The other geometry consists of a 2 litre Marinelli beaker placed over a 98% HPGe detector. It will be referred to as "BIG". Figure 8.1 shows a general Marinelli beaker geometry. Table 8.1 shows the actual dimensions of both the ORT and the BIG geometry. For each geometry, two simulations have been performed. For the first simulated measurement, the beakers were modelled as being filled with pure water of density  $1.0 \cdot 10^3 \text{ kg} \cdot \text{m}^{-3}$ . For the other simulated measurements, the beakers were filled with sand, modelled as silicon dioxide of bulk density  $2.0 \cdot 10^3 \text{ kg} \cdot \text{m}^{-3}$ .

### 8.2.2 Determination of efficiency-, PT- and LS-curves, and correlation coefficients

Volume averaged full-energy peak efficiency curves, PT-curves, LS-curves and correlation coefficients for each of the four detection geometries were determined by

**Table 8.1:** Dimensions of detection geometries. Variables are defined by Figure 8.1

		ORT geometry	BIG Geometry
<b>Detector dimensions [mm]</b>			
Endcap diameter (Al):	$D_e$	70	95
Endcap thickness (Al) top		0.5	1
side		1	1.6
Crystal depth:	$d$	5	4
Dead layer thickness (Ge):		0.7	1
Crystal diameter (Ge):	$D_d$	48	76
Crystal height (Ge):	$h_d$	56	97
Core diameter:	$D_c$	15	11
Core height:	$h_c$	38	85
<b>Beaker dimensions [mm]</b>			
Inner wall thickness:		Material: Polyethylene 2	Material: Lucite 1.5
Diameter:	$D_M$	117	151
Total height:	$h_M$	130	173
Top height:	$h_{M,top}$	56	34

computer simulation as described in Chapter Three.

For the full-energy peak efficiency values  $\varepsilon$  used for the determination of the full-energy efficiency curves, the total number of photons was taken large enough to obtain an imprecision for  $\varepsilon$  lower than 0.5%. A full-energy peak efficiency curve  $\varepsilon(E)$  was then fitted to the twelve  $\varepsilon$ -values using Gunnink's efficiency curve<sup>[1]</sup> (see Section 2.2), with the supposed presence of an absorber. Thus, four parameters were used to describe the curve and an additional two parameters to allow for the presence of the absorber. Full-energy peak efficiency values and the results of the fits are shown by the upper plots of Figure 8.2

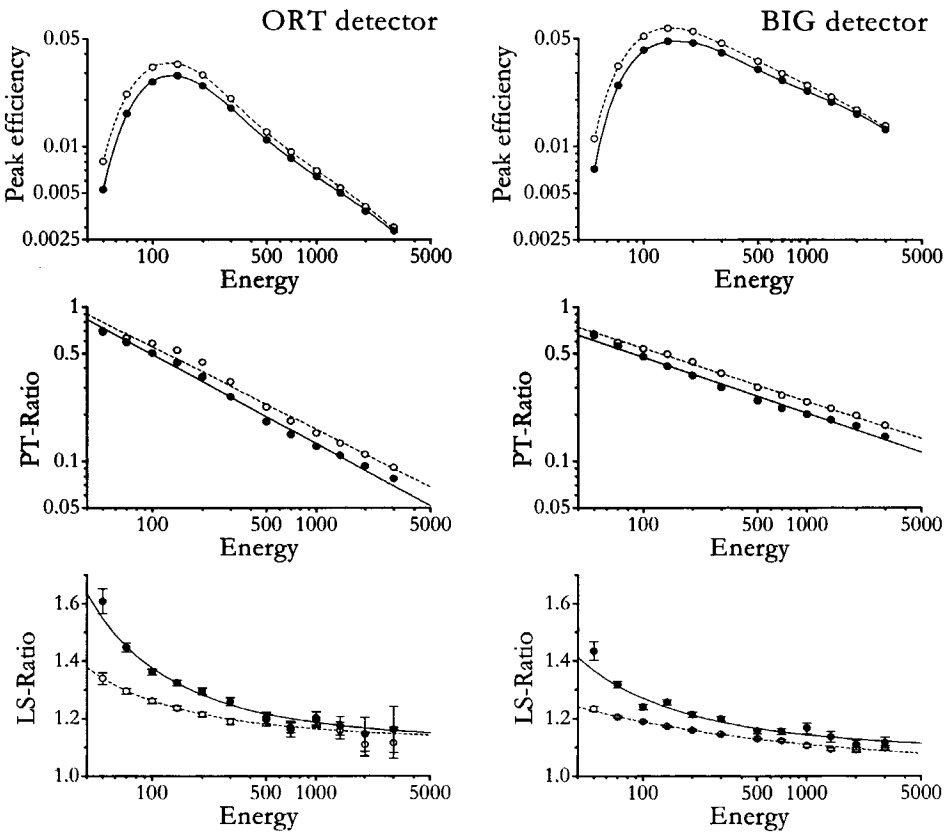


**Figure 8.2:** Simulation results for ORT (left) and BIG geometry (right). Open circles and dashed lines denote values and curves for water-filled beakers; Solid circles and solid lines denote values and curves for sand-filled beakers. **Upper plots:** Efficiency values and fitted Gunnink curves. **Middle plots:** PT-ratios and fitted PT-curves. **Lower plots:** LS-ratios and fitted LS-curves.



**Table 8.2:** Correlation parameter value results

	Water	Sand
ORT	$0.98 \pm 0.02$	$1.01 \pm 0.01$
BIG	$0.97 \pm 0.01$	$0.88 \pm 0.01$

The imprecision of the total efficiency values  $\varepsilon_i$  used for the determination of PT-curves was also lower than 0.5%. Peak-to-total ratios  $r$  were calculated from the  $\varepsilon$  and  $\varepsilon_i$ -values. The peak-to-total curve  $r(L)$  was then fitted to the twelve PT-ratios, using a straight line on double-log scale. Thus two parameters were used to describe the peak-to-total curve, and a third was used to limit the PT-curve to physically possible values. PT-ratios and PT-curves are shown by the middle plots of Figure 8.2.

The imprecision of the squared efficiency values  $\varepsilon^2$  used for the determination of LS-curves, was lower than 1% for energies between 70 and 700 keV and lower than 5% for all energies. Linear-to-squared values  $\sqrt{\eta^2+1}$  were calculated from these values using Equation (2.29). A Linear-to-squared curve was then fitted to the twelve LS-ratios using relation (2.30). Thus, three parameters were used to describe this curve. LS-ratios and LS-curves are shown by the lower plots of Figure 8.2.

Finally, the imprecision obtained for the  $\varepsilon_i \varepsilon_j$ -values used for the determination of correlation coefficients, was lower than 3% for combinations of energies between 100 and 700 keV and typically 5% for energies outside this range. Table 8.2 shows the values of the correlation coefficients for all four detection geometries.

### 8.2.3 Spectrum simulation

For all geometries, the spectra of bromine-82, barium-133 and caesium-134 were simulated by following a large number of batches of photons through the detection geometry. As described in Chapter Three, each batch contained the photons from a possible cascade from the decay-scheme of the daughter from a fed level to the ground state. The number of disintegrations, effectively the number of batches, was taken large enough to obtain an imprecision lower than 0.5% for the areas of the most important peaks in the spectra.

## 8.3 Validation.

This section presents the validation of the theory for both the water-filled and the sand-filled beakers on both detectors. Subsection 8.3.1 describes the interpretation of the simulated spectra of bromine-82, barium-133 and caesium-134 with respect to the number of disintegrations. This interpretation uses Equation (2.19) which is calculated using the stochastic approach described in Chapter Two. Thus, the interpretation validates the overall theory. Finally, subsection 8.3.2 discusses the results of the various validations.

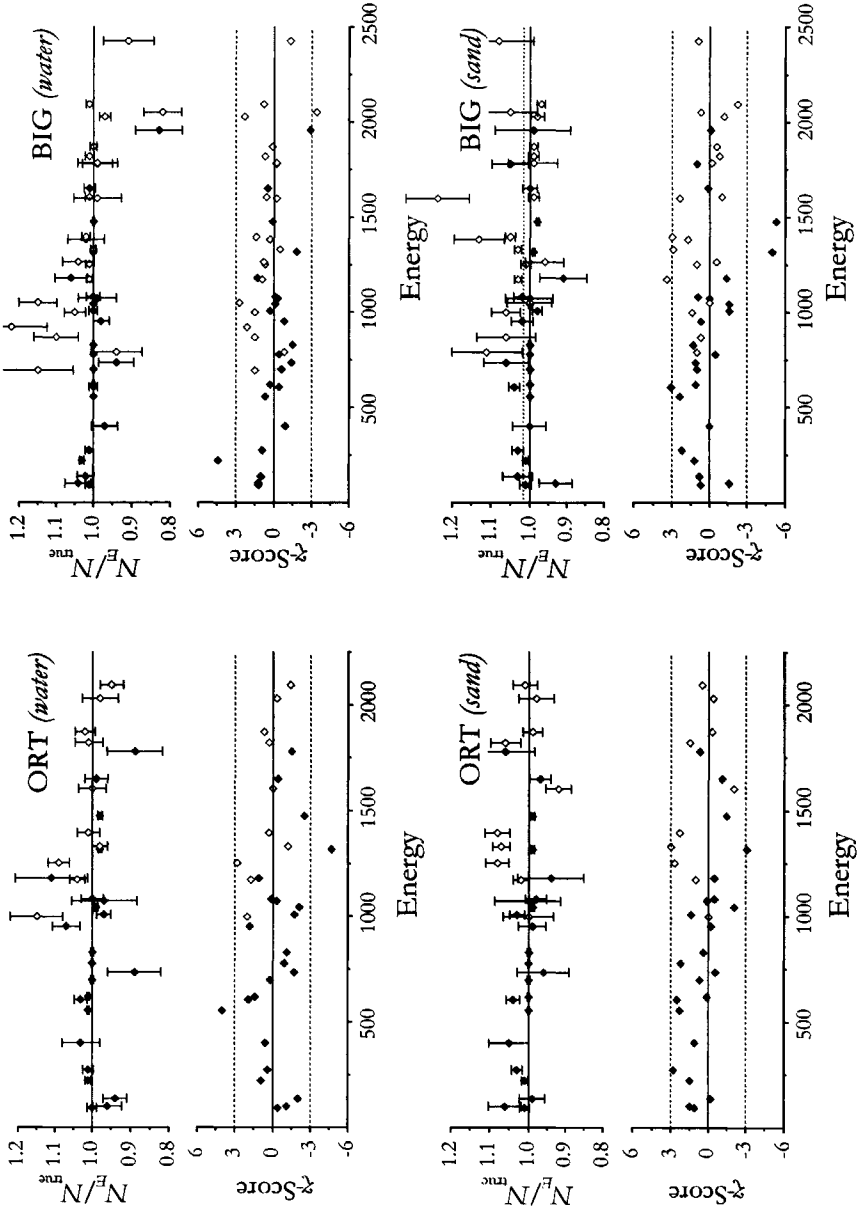


**Figure 8.3:** Interpretation results of bromine-82 spectra from the four geometries in terms of  $N_E/N_{true}$  ratios and  $\chi^2$  scores. Dotted lines in the ratio plots indicate interpreted  $N/N_{true}$  ratio; dashed lines in the  $\chi^2$  plots show  $-3..3$  interval. Filled diamonds indicate full-energy peaks, open diamonds indicate sum-peaks.

8.3.1 Validation of the overall theory

The theory was validated by interpreting the simulated spectra with respect to the number of disintegrations,  $N$ . This number was obtained by first calculating a separate number of disintegrations associated with each peak in the spectrum, i.e., by dividing peak areas by their corresponding  $P_{E-}$  values (Equation (2.19)). The reported number of disintegrations,  $N$ , is the weighted average of all the numbers of disintegrations associated with each peak. This calculation of  $N$  also produced a  $\chi^2$ -value. The number of disintegrations,  $N$ , was then compared to the real number,  $N_{\text{true}}$ , used in the simulation. The exact procedure is described in Appendix B.

For all geometries, Table 8.3 gives the results of the interpretation of the spectra in terms of the  $N/N_{\text{true}}$  ratios and  $\chi^2$ -values. In addition, Figure 8.3(a-d) shows the interpretation results for the bromine-82 spectra in more detail. For each peak in the spectra, their upper parts show the ratio between the true peak area and the interpreted peak area. Their lower parts show the corresponding  $z$ -scores.

To demonstrate the importance of the LS-curve, Table 8.4 shows the results of the interpretation when neglecting coincidence corrections or when neglecting the proper use of volume averages. For the latter interpretation, the warning expressed by Equation (2.20) is disregarded, effectively regarding the source as a point.

**Table 8.3:** Interpretation results of spectra regarding the source as voluminous in terms of  $N/N_{\text{true}}$  ratios and  $\chi^2$ -values.

	<sup>82</sup> Br		<sup>133</sup> Ba		<sup>134</sup> Cs	
	$N/N_{\text{true}}$	$\chi^2$	$N/N_{\text{true}}$	$\chi^2$	$N/N_{\text{true}}$	$\chi^2$
ORT (water)	(1.000 ± 0.002)	3.0	(1.011 ± 0.001)	0.9	(1.003 ± 0.002)	1.4
ORT (sand)	(0.999 ± 0.002)	2.2	(1.001 ± 0.003)	11	(1.000 ± 0.002)	2.0
BIG (water)	(1.000 ± 0.001)	2.0	(1.008 ± 0.002)	1.2	(0.996 ± 0.001)	0.8
BIG (sand)	(1.002 ± 0.002)	4.1	(0.994 ± 0.002)	2.3	(1.003 ± 0.002)	1.0

**Table 8.4:** Interpretation results of spectra when disregarding the LS-curve, effectively regarding the source as a point, and when excluding coincidence effect calculations. Reported values are  $N/N_{\text{true}}$  ratios and  $\chi^2$ -values.

	<sup>82</sup> Br		<sup>133</sup> Ba		<sup>134</sup> Cs	
	$N/N_{\text{true}}$	$\chi^2$	$N/N_{\text{true}}$	$\chi^2$	$N/N_{\text{true}}$	$\chi^2$
<b>Coincidence correction: Point source interpretation.</b>						
ORT (water)	(0.961 ± 0.005)	27	(0.996 ± 0.010)	47	(0.981 ± 0.007)	13
ORT (sand)	(0.947 ± 0.006)	37	(0.979 ± 0.012)	204	(0.962 ± 0.008)	46
BIG (water)	(0.943 ± 0.006)	91	(0.991 ± 0.010)	42	(0.970 ± 0.008)	52
BIG (sand)	(0.932 ± 0.007)	86	(0.973 ± 0.013)	129	(0.960 ± 0.011)	50
<b>No Coincidence corrections.</b>						
ORT (water)	(0.856 ± 0.004)	17	(0.960 ± 0.014)	114	(0.918 ± 0.008)	16
ORT (sand)	(0.832 ± 0.005)	29	(0.946 ± 0.014)	291	(0.902 ± 0.009)	67
BIG (water)	(0.719 ± 0.008)	294	(0.935 ± 0.023)	218	(0.825 ± 0.016)	248
BIG (sand)	(0.698 ± 0.007)	190	(0.921 ± 0.025)	462	(0.817 ± 0.017)	181

### 8.3.2 Discussion of results

Table 8.4 clearly shows the need for a coincidence correction method. Errors of over 25% can be made if coincidence corrections are omitted. Coincidence correction methods should take into account the voluminous nature of the source and not rely on correction for point source geometries. Else, errors of 5% can still be made. Our newly introduced LS-curve, combined with a correlation parameter  $\rho$ , does take into account the volume nature of the sources. If they are used in the coincidence calculations using the stochastic approach, errors are generally less than 0.5% and lie within the reported uncertainty. (Table 8.3)

The interpretation result with respect to the  $N$ -ratio for barium-133 in the ORT(*water*) case is slightly worse if the voluminous nature is accounted for, as compared to the point-source interpretation, viz. 1.011 vs 0.996, while the result with respect to the  $\chi^2$ -value is much better, viz. 0.9 vs 47. Apparently, the individual  $N_E$ -values defined by Equation (B 3) in Appendix B show less variation when using the LS-curve. Since barium-133 emits several gammas below 90 keV, a probable cause for the worse  $N$ -ratio may be the influence of the PT-curve and the LS-curve not accurately representing the actual values in this region, see also Figure 8.2.

Let us focus in detail on the bromine-82-spectrum reproduction results for the ORT beaker filled with water as presented by the upper left plot of Figure 8.3. According to the  $\chi$ -scores, the reproductions of the 554 keV peak ( $\chi=4.0$ ) and the 1318 keV peak ( $\chi=4.7$ ) are statistical outliers. However, the areas of these peaks are determined with a very low uncertainty of less than 0.4%. The corresponding ratios are 1.01 and 0.98 respectively. Since our interpretation routine uses all peaks to interpret the spectrum, these deviations are of very limited importance. In fact, the interpretation of this spectrum yields a number of disintegrations which is right on top of the true value.

The results for the bromine-82-spectrum reproduction for the other ORT beaker and for BIG beakers show similar effects (Figure 8.3 lower left, upper right and lower right respectively). For all main peaks that have  $\chi$ -scores outside the  $-3 \dots 3$  region, the ratios are off by a maximum of 3%. The reproduction of the 2051.4 keV sum peak in the BIG(*water*) spectrum however, shows not only a large negative  $\chi$ -scores of  $-3.4$ , but also a deviation of more than 5% ( $N$ -ratio=0.82). Still, the overall result of the spectrum interpretations for this geometry and for the other geometries as well, is very accurate and precise.

### Intermezzo

To apply the developed theory in a real-life situation, it is necessary to determine the three curves. Direct determination of the full-energy peak efficiency curve can still be done relatively easy by measuring a mixed radionuclide source containing radionuclides that emit coincidence free  $\gamma$ -rays. The direct determination of the peak-to-total curve requires yet more effort since a number of sources must be measured, each source

containing only one radionuclide that emits only one gamma. Finally, it is impossible to measure a linear-to-squared curve directly, since this would require a set of radionuclides that emit two gamma's with exactly the same energy in coincidence\*.

Although the curves can be determined using Monte Carlo or other volume integration techniques, this is undesirable because this would require accurate knowledge of all detector dimensions. This knowledge is often not readily available. Furthermore, as already mentioned in the introduction, the aim of the calibration method is to extract all information necessary to account for coincidence effects from measurements showing these effects.

The next section describes the principles of a calibration method that determines indirectly all three curves from a single bromine-82-spectrum. The calibration is an extension of a calibration method for point-source geometries, developed and described earlier by Blaauw<sup>[2]</sup>. Several variants of the method are tested and their properties are investigated using the simulated spectra from the water-filled beaker on the ORT geometry. The final variant is applied to the other geometries as well.

## 8.4 Calibration method

### 8.4.1 Principles of the calibration method

The theory developed in Chapter Two allows for the calculation of all peak areas of a bromine-82-spectrum if the full-energy peak efficiency curve, the PT-curve and the LS-curve are known. Six parameters are used to describe the full-energy peak efficiency curve, two parameters for the PT-curve and three for the LS-curve. Together with the correlation parameter and an additional parameter representing the number of disintegrations, the total number of parameters used to predict a spectrum is thirteen.

The calibration method described here inverts the problem of calculating peak areas from thirteen parameters: it calculates the parameters from measured peak areas. In the case of bromine-82, over thirty peaks can easily be observed with a Marinelli beaker detector set-up. This means that over thirty equations can be solved for these thirteen parameters. In principle, all parameters can be obtained by non-linear least squares methods, where the  $\chi^2$ -value of the measured full-energy peak areas as compared to the computed areas is minimized.

A computer program was written to perform the fitting. As all non-linear least squares fitting algorithms, the program requires a reasonable initial estimate of the parameter values. An estimate for the number of disintegrations is usually available and must be

---

\* For the direct measurement of a linear-to-squared curve, one would need a radionuclide that simultaneously emits two photons of the same energy in random, uncorrelated directions. Even the simultaneous emission of two 511 keV photons in position annihilation is of no avail because the two photons are emitted in opposite directions.

supplied to the program by the user. An initial estimate for the other parameters can either be supplied by the user or by the program itself. If the program is to supply a first estimate for the full-energy peak efficiency parameters, it calculates efficiency values for all main peaks in the spectrum disregarding all coincidence losses or gains. It then fits a Gunnink curve<sup>[1]</sup> to the individual values. As a first estimate for the PT-parameters, the LS-parameters and the correlation parameter, the program takes a predefined set for a typical Marinelli beaker detection geometry

Once the program has obtained estimated values for all parameters it can fit all parameters at once, or one or more sets at a time, three sets consisting of the parameters associated with a specific curve and the fourth consisting of the parameter used for the number of disintegrations. The correlation parameter in this respect is associated with the LS-curve parameter set.

#### 8.4.2 Demonstration of the calibration method

The characteristics of the calibration method have been studied using the Monte Carlo simulated bromine-82-spectrum of the water-filled beaker on the ORT geometry that was also used to test the validity of the theory (Section 8.3). The calibration method has been performed several times.

First, the calibration has been performed while not varying the number of disintegrations in the fit. Using the calibration method this way in real-life situations would require accurate knowledge of the source activity to calculate the number of disintegrations during the measurement. In our case the number of disintegrations is readily given by the program that simulated the bromine-82 spectrum. Two variants have been investigated. For Variant I, first estimates for the parameters have been used that were supplied by the program itself. This would be the way to use the calibration method in real-life situations. For Variant II, a first estimate was obtained via the independent computer simulations described in subsection 8.2.2. This was done to check the robustness of the fitting procedure. Then the calibration has been performed using the same variants, while allowing the number of disintegrations to vary in the fitting (Variant I+ and Variant II+). As a first estimate for the number of disintegrations the true value was used.

Table 8.5 shows the results of the various fitting procedures. In all cases, the procedure yields acceptable results with respect to the  $\chi^2$ -value of the comparison. However, if the number of disintegrations is allowed to vary in the fitting, the procedure does not accurately reproduce this number. Although in the case of Variant II, i.e. if the simulated curves are used as a first estimate, the ratio of the fitted to the real number is acceptable but the reported uncertainty for the fitted numbers is very large. Also, the covariance matrix of the fit results showed very large elements. This indicates that the number of disintegrations is interchangeable with the other parameters. Therefore, it is not recommended that the number of disintegrations is to be varied in the fitting procedure.

The two different uses of the fitting procedures in which the number of disintegrations was not varied, resulted in two sets of curves. To test the quality of these sets, they have been used to interpret the simulated spectra of barium-133 and caesium-134 that were also used to validate the theory. Table 8.6 summarizes the interpretation results for all nuclides.

For caesium-134, both sets of curves yield accurate results, indicated by a  $N/N_{true}$ -ratio close to 1.0, and reasonable low values for the  $\chi^2$ -values. Contrary to the caesium-134 spectrum, the barium-133 spectrum is not correctly interpreted with both sets: they combine a wrong interpretation result with high  $\chi^2$ -values, indicating a discrepancy between these sets and the true curve sets. The full-energy peak efficiency curve of these two sets is the result of a fit to the bromine-82 spectrum. Since bromine-82 does not emit photons with energies below 92 keV, the fit does not accurately determine the efficiency curve below this energy. Barium-133 however has several peaks below 92 keV. It is therefore understandable that set I and set II do not yield good interpretation results for barium-133. Notice however that the curve set from Section 8.3.1 does yield accurate results (Table 8.3). This set has been determined using 50 keV as the lowest energy.

**Table 8.5:** Results of the various fitting procedures in terms of: Ratio between fitted and true number of disintegrations.;  $\chi^2$ -value of the comparison between the two.

First estimate supplied by:		Fitting	ORT ( <i>water</i> )	
			$N_{fit}/N_{true}$	$\chi^2$
<b>I:</b>	Fitting Program	$N$ fixed	$N$ fixed	4.0
<b>II:</b>	Simulation	$N$ fixed	$N$ fixed	1.6
<b>IIb:</b>	Simulation	$N$ and $\epsilon$ fixed	$N$ fixed	3.4
<b>I+:</b>	Fitting Program		$(1.05 \pm 0.66)$	4.4
<b>II+:</b>	Simulation		$(0.99 \pm 0.63)$	1.6
<b>IIb:</b>	Simulation	$\epsilon$ fixed	$(0.96 \pm 0.01)$	2.3

**Table 8.6:** Interpretation results of spectra of bromine-82, barium-133 and caesium-134, using the sets of curves obtained from the fitting procedure (**Set I:** Using programs first estimate; **Set II:** Using simulated curves as first estimate; **Set IIb:** Using simulated curves as first estimate and keeping peak efficiency parameters fixed)

	<sup>82</sup> Br		ORT geometry ( <i>Water</i> )		<sup>134</sup> Cs	
	$N/N_{true}$	$\chi^2$	<sup>133</sup> Ba $N/N_{true}$	$\chi^2$	$N/N_{true}$	$\chi^2$
<b>Set I</b>	$(1.000 \pm 0.002)$	2.6	$(1.043 \pm 0.007)$	17	$(1.001 \pm 0.002)$	1.2
<b>Set II</b>	$(1.000 \pm 0.001)$	1.0	$(1.017 \pm 0.009)$	38	$(1.006 \pm 0.002)$	1.0
<b>Set IIb</b>	$(1.000 \pm 0.002)$	2.9	$(1.010 \pm 0.002)$	1.3	$(1.003 \pm 0.002)$	1.3

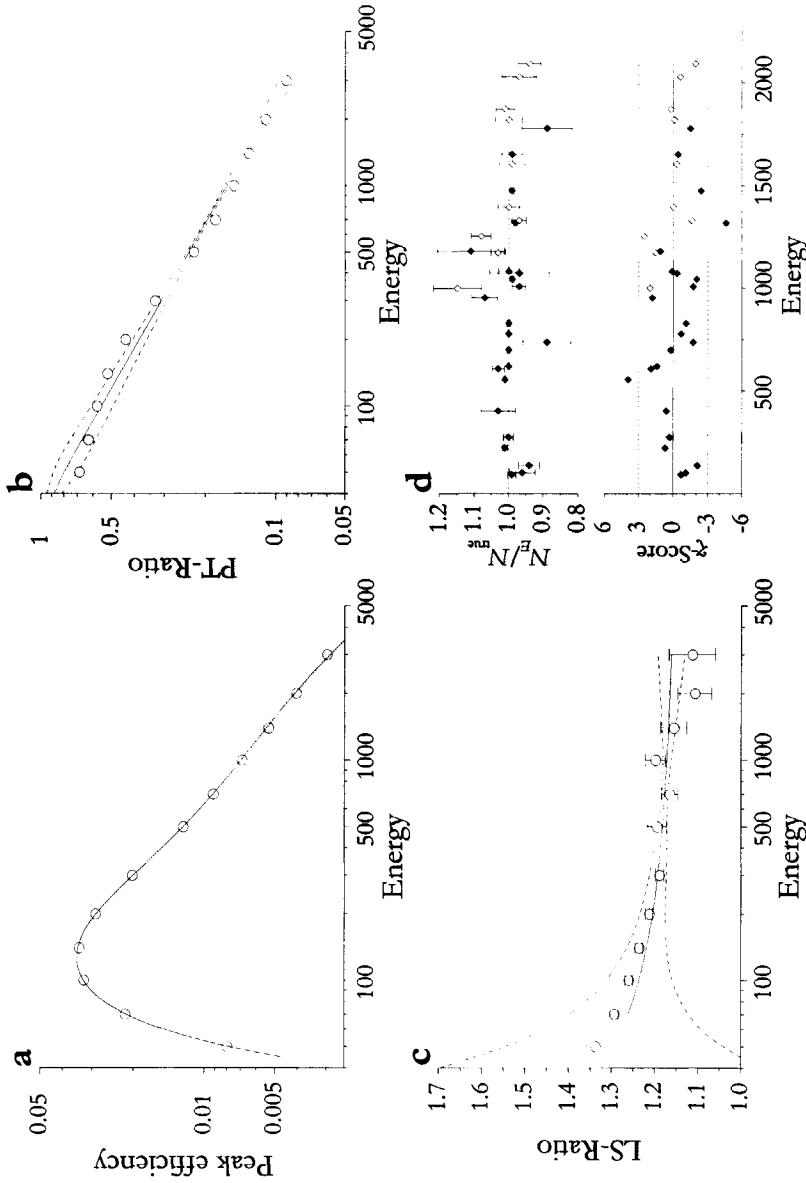


**Figure 8.4:** Reproduction of a bromine-82 spectrum from the ORT geometry using curves obtained with variant IIb (see text). (a,b and c): Curves fitted (solid lines) to the bromine spectrum and  $1\sigma$  confidence intervals (dashed lines) Open circles and  $1\sigma$  error bars indicate (a) simulated full-energy peak efficiency values, (b) simulated PT-values and (c) simulated LS-values. (d): Bromine spectrum reproduction using this set of curves in terms of  $N_E/N_{mc}$ -ratios and  $\chi^2$ -scores. Filled diamonds indicate full-energy peaks, open diamonds indicate sum-peaks.



At this point variant **II** of the calibration method to be investigated is redefined. Like before, this newly defined variant **IIb** uses as a first estimate the curves from section 8.3.1, but now only the parameters describing the PT-curve and the LS-curve are allowed to vary in the fitting. Thus, the full-energy peak efficiency curve is valid for energies down to 50 keV. In real-life situations, using the method this way would necessitate a preliminary measurement of a calibration source emitting non-coincident  $\gamma$ -rays to determine the parameters of the full-energy peak efficiency curve. This variant of the fitting procedure yielded a  $\chi^2$ -value of 3.4 if the number of disintegrations was kept fixed, and a  $\chi^2$ -value of 2.3 if this number was allowed to vary. The found number of disintegrations relative to the true value in the latter case was  $(0.96 \pm 0.01)$ . The interpretation results for the newly defined Variant **IIb** are added to Table 8.6. Using this set of curves, all spectra are interpreted well. Figure 8.4 shows the curves obtained with this variant and the resulting reproduction of the bromine-82 spectrum if the number of disintegrations is kept fixed at its true value.

#### 8.4.3 Discussion of the calibration results.

The results from the previous subsection show that in principle a bromine-82 spectrum can be used to determine a set of curves that describe a Marinelli beaker type detection geometry. However, if the method is to be used in real-life situations, some remarks must be made.

First, the number of disintegrations of bromine-82 during the calibration measurement should be accurately known. The apparent interchangeability between the number of disintegrations and other parameters, especially the LS-parameters, causes the fitting procedure to report inaccurate results. It is therefore not recommended that the number of disintegrations is varied in the fit.

Second, since bromine-82 does not emit  $\gamma$ -rays with energies below 92 keV, the validity of the curves below this energy is questionable. However, for energies lower than 92 keV, the method can very well provide accurate PT- and LS-curves if an accurate full-energy peak efficiency curves is obtained from another measurement. The parameters of this curve should then be used as first estimate and should not be varied in the fit.

Set **IIb** results from the method used as described above. The PT- and LS-curves from this set are compared to the PT- and LS-ratios obtained by the independent Monte Carlo calculation. Obviously, there is no need for comparison of the peak efficiency curve in set **IIb** since this curve is the result of a direct fit to the Monte Carlo efficiency values. Figure 8.4 shows the obtained curves from set **IIb** together with the values obtained by direct calculations (Section 8.3.1). Calculated values are plotted as open circles. In addition, it shows the bromine-82 spectrum reproduction. This figure shows that the PT-curves reproduce the calculated PT-ratios fairly well. Also the LS-curves reproduce the LS-ratios satisfactory.

The above shows that calibration procedure **IIb** provides the best curve set to interpret all three nuclides. This calibration procedure has been applied to the other

**Table 8.7:** Interpretation results of Monte Carlo simulated spectra of bromine-82, barium-133 and caesium-134, using the set of curves obtained from calibration procedure **I**ib****. (Using MC-curves as first estimate and keeping peak efficiency parameters fixed)

	<sup>82</sup> Br		<sup>133</sup> Ba		<sup>134</sup> Cs	
	$N/N_{\text{true}}$	$\chi^2$	$N/N_{\text{true}}$	$\chi^2$	$N/N_{\text{true}}$	$\chi^2$
ORT ( <i>water</i> )	$(0.999 \pm 0.002)$	2.9	$(1.010 \pm 0.002)$	1.8	$(1.003 \pm 0.003)$	1.6
ORT ( <i>sand</i> )	$(1.000 \pm 0.001)$	1.8	$(0.998 \pm 0.003)$	16	$(1.001 \pm 0.002)$	1.8
BIG ( <i>water</i> )	$(1.000 \pm 0.001)$	1.8	$(1.007 \pm 0.002)$	1.8	$(0.996 \pm 0.001)$	0.8
BIG ( <i>sand</i> )	$(1.000 \pm 0.001)$	2.1	$(0.999 \pm 0.001)$	1.1	$(1.002 \pm 0.001)$	0.4

geometries as well. Table 8.7 summarizes the results for all radionuclides and all geometries using calibration procedure **I**ib****. In addition, Figure 8.5 through Figure 8.7 show the interpretation results on individual peaks of the respective radionuclides, for all four geometries.

Let us compare these interpretation results with the interpretation results using the simulated curves (Table 8.3). In all cases, interpretation using set **I**ib**** is as accurate as using the simulated curves. Only barium-133 shows large  $\chi^2$ -values in the sand cases, indicating a large variation of the individual  $N_E$  values relative to their errors. However, the error in the final number of disintegrations, accounting also for the variation of the  $N_E$ -values, is still acceptably low. Moreover, the reported number of disintegrations is correct. The interpretation of bromine-82 in the BIG(*sand*) case is better with the use of set **I**ib**** than with the use of the simulated curves. Since set **I**ib**** is obtained from a spectrum showing coincidence effects, this illustrates our presumption stating that in order to accurately account for coincidence effects, the required information should be obtained from measurements that show these effects.

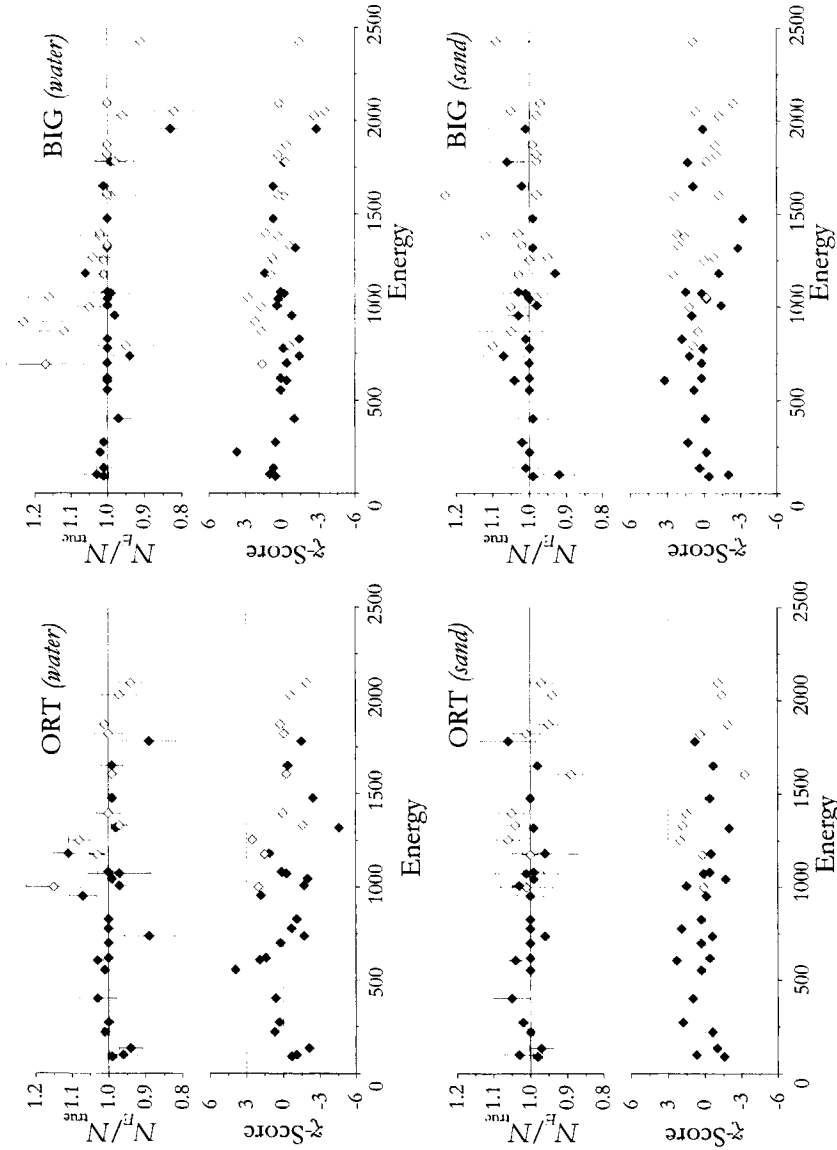


**Figure 8.5:** Interpretation results of the bromine-82 spectra from the four geometries in terms of  $N_i/N_{true}$  ratios and  $z$ -scores, using the curves obtained with Variant IIb, i.e. using simulated curves as a first estimate and keeping the peak to total parameters fixed. Filled diamonds indicate full-energy peaks, open diamonds indicate sum-peaks.

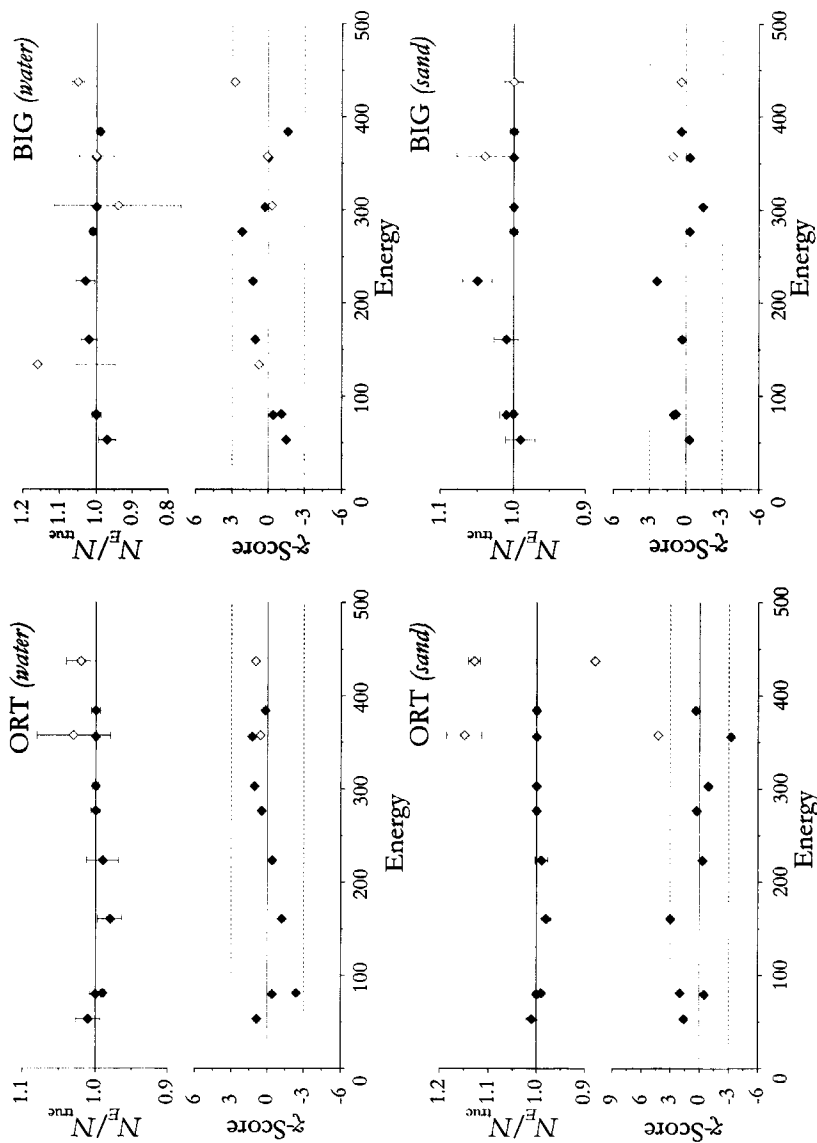


**Figure 8.6:** Interpretation results of the barium-133 spectra from the four geometries in terms of  $N_E/N_{\text{tot}}$  ratios and  $\chi^2$  scores, using the curves obtained with Variant IIb, i.e. using simulated curves as a first estimate and keeping the peak to total parameters fixed. Filled diamonds indicate full-energy peaks, open diamonds indicate sum-peaks.

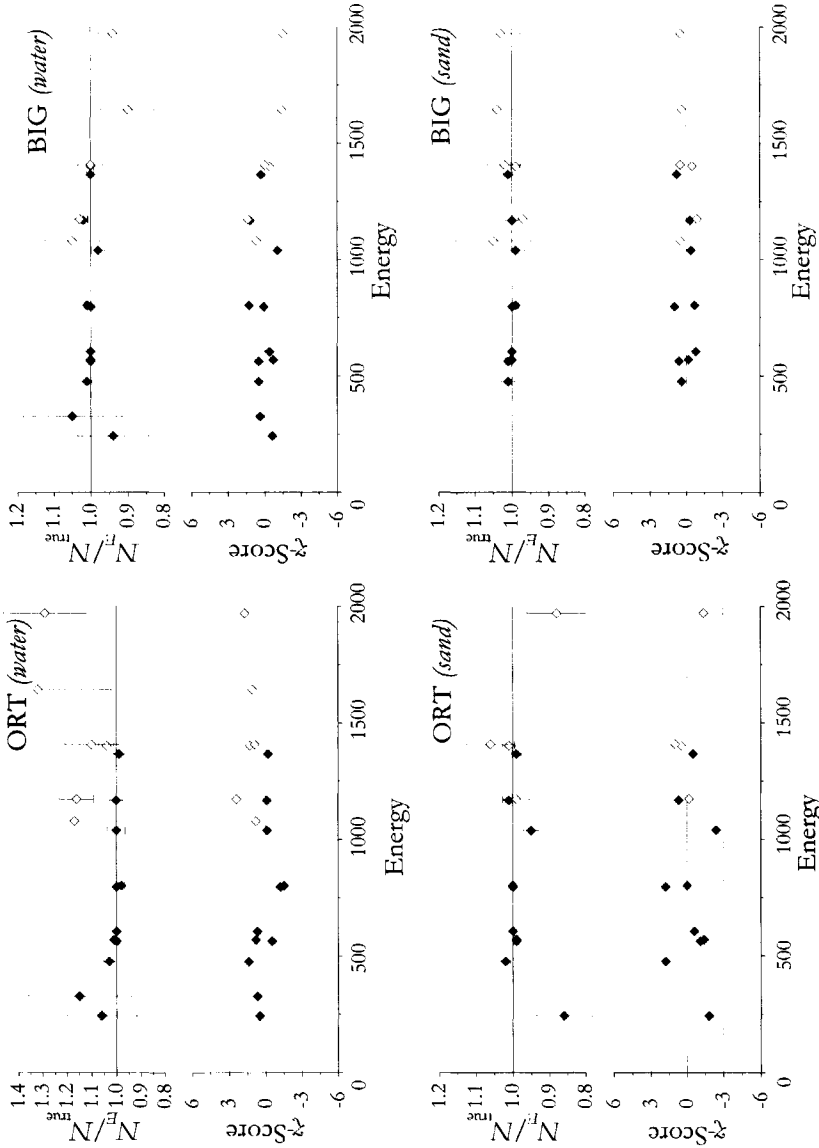


**Figure 8.7:** Interpretation results of the caesium-134 spectra from the four geometries in terms of  $N^F/N^E$  ratios and  $\chi^2$  scores, using the curves obtained with Variant IIb, i.e. using simulated curves as a first estimate and keeping the peak to total parameters fixed. Filled diamonds indicate full-energy peaks, open diamonds indicate sum-peaks.

## 8.5 General discussion and conclusion

This chapter described the development and test of a model that enables accurate calculation of peak areas obtained from the measurement of voluminous sources, specifically Marinelli beaker sources. For the test of the model we used computer simulation techniques.

To obtain accurate results for voluminous sources, the use of a full-energy peak efficiency curve in combination with a peak-to-total curve is not sufficient. In addition to these two curves, a third curve is needed that accounts for the variation of the efficiency over the source volume. In principle a bromine-82 spectrum can be used to determine all three curves that describe a Marinelli beaker type detection geometry. Moreover, the spectrum interpretation results are slightly better using curves obtained from a bromine-82 spectrum than using the curves obtained by direct calculation. This demonstrates the presumption expressed in the introduction that methods correcting for coincidence effects should obtain their information from these effects.

If the method is to be used in real-life situations, the number of disintegrations of the bromine-82 during the calibration measurement should be accurately known. The interchangeability between the number of disintegrations and the parameters describing the LS-curve causes the calibration method to produce inaccurate results. Furthermore, the validity of the curves based on a single bromine-82 measurement is questionable below 92 keV. However, for energies lower than 92 keV, the method can very well provide PT- and LS-curves if an accurate full-energy peak efficiency curve is obtained from a measurement of a source emitting non-coincident  $\gamma$ -rays covering the whole energy range of interest. Thus, the method would require at most two calibration measurements, or a single measurement of a suitable mixture of radionuclides. Typically, it allows for activity measurements results that are accurate within 1%.

These conclusions are drawn based upon Monte Carlo simulations of Marinelli beaker sources with volumes of 1  $\ell$  and 2  $\ell$  filled with low- $Z$  materials ( $Z \leq 14$ ) with densities of  $1 \cdot 10^3 \text{ kg} \cdot \text{m}^{-3}$  and  $2 \cdot 10^3 \text{ kg} \cdot \text{m}^{-3}$ . The limits on the source dimensions and composition translate into an upper limit on the attenuation coefficient  $\mu$ . This upper limit is given by the combination of highest  $Z$ , largest density and lowest energy of interest, i.e. 50 keV of barium-133. For these values,  $\mu$  is approximately  $1 \text{ cm}^{-1}$ . This limit is an experimental one, in the sense that the method has been verified (yet only by simulations) for sources with  $\mu < 1 \text{ cm}^{-1}$ . The method may very well perform for higher values of  $\mu$  as well. Recall that the theoretical limit is set by the LS-ratio being smaller than  $\sqrt{2}$ .

## References

- [1] R. Gunnink, *Nucl. Instr and Meth.*, **A299** (1990) 372
- [2] M. Blaauw, *Nucl. Instr and Meth.*, **A332** (1993) 493

# Chapter Nine

## The missing curve for voluminous source coincidence corrections; Experimental verification

---

### Abstract

*This chapter verifies the calibration method for Marinelli beaker type detection geometries of the previous chapter. The method requires knowledge of the variation of the full-energy peak efficiency and the total efficiency over the source volume. Therefore, in addition to a peak efficiency curve and a peak-to-total curve, it uses a third curve that accounts for this variation. This chapter verifies two variants of the calibration method using experimental data. It is concluded that a calibration based on a combination of a measurement of a commercially available mixed radionuclide source and a measurement of a bromine-82 source provides the most accurate results. Compared to radionuclide specific calibration, the method greatly reduces calibration efforts without compromising calibration quality.*

### 9.1 Introduction

Chapter Eight explored the feasibility of the three efficiency curves approach developed in Chapter Two for the Marinelli beaker case, using Monte Carlo simulations. It showed that the mathematical model from Chapter Two and a corresponding calibration method introduced in Chapter Eight, in principle allow for accurate activity measurements in Marinelli beaker if the attenuation coefficient,  $\mu$ , of the sample material is smaller than  $1 \text{ cm}^{-1}$ . In addition to a full-energy peak efficiency curve combined with a peak-to-total curve, the model uses a third curve, the linear-to-squared curve, and a correlation parameter that account for the variation of the efficiency over the source. The corresponding calibration method enables the simultaneous determination of all three curves. It is based on the philosophy that the curves, that are used to accurately describe

coincidence effects, should be obtained from coincidence effects observed in practice. In principle, it only needs one measurement of a radionuclide of known activity that shows considerable coincidence effects (Variant I). This way, it produces curves that are accurate for the energy range limited by the lowest and highest energy in the spectrum. A second variant of the method allows for an extended energy range if the full-energy peak efficiency curve is obtained from a supplementary measurement (Variant II).

This chapter describes the experimental verification of the mathematical model and the corresponding calibration method. It uses the proposed method both in the original variant (I), and in the extended variant (II) as described above. It then uses the resulting curves from the two variants to interpret a measurement of a Marinelli beaker verification source prepared and certified independently from the calibration sources. In addition, for those radionuclides present in both the calibration and the verification source, it interprets the verification measurement using radionuclide specific calibration.

The verification is performed for one Marinelli beaker geometry only. Based on the results of the computer simulation described in the previous chapter, the conclusion of this chapter can be extended to other Marinelli beaker geometries, as long as the upper limit of  $1.0 \text{ cm}^{-1}$  on the attenuation coefficient is not exceeded.

## 9.2 Experimental

### 9.2.1 Preparation of calibrated sources

#### *Mixed radionuclide calibration source*

A Marinelli beaker calibration source was prepared by taking  $(251.05 \pm 0.05)$  mg of a mixed radionuclide  $\gamma$ -ray reference solution from Amersham International plc. The exact amount was determined by weighing the solution in a small counting vial on a calibrated mechanical balance. After weighing, it was rinsed down with 0.5M hydrochloric acid in a 1 l volumetric flask. Finally the flask was filled up to 1 l with the same hydrochloric acid and poured out in a 1 l Marinelli beaker. The negligibly small amount of solution that was left behind was determined gravimetrically. The Marinelli calibration source thus prepared covers the energy range from 88.03 keV (cadmium-109) to 661.7 keV (caesium-137) with radionuclides that emit non-coincident  $\gamma$ -rays, and it covers the range up to 1836 keV with yttrium-88 and cobalt-60.

#### *Bromine-82 Marinelli beaker calibration source*

In order to obtain a bromine-82 solution of known activity, first a concentrated bromine stock solution was made by dissolving 0.5 g of sodium bromine in 10 ml of 0.5M hydrochloric acid. Thereafter, 1 ml of this solution was irradiated during 6 minutes at a



neutron flux of  $4 \cdot 10^{16} \text{ m}^{-2}\text{s}^{-1}$ . Then, weighed aliquots of this solution of respectively  $(8.6 \pm 0.1) \text{ mg}$ ,  $(9.4 \pm 0.1) \text{ mg}$  and  $(11.0 \pm 0.1) \text{ mg}$  were put into three polyethylene capsules. After weighing, the solvent in the capsules was evaporated and sodium-24/bromine-82 activity ratios were used to verify that no bromine was lost in the evaporation process.

The Marinelli beaker bromine-82 calibration source was based on the same stock solution. Thus, the activity of this source could be derived from the specific activity of the stock solution. From the stock a weighed amount of  $(14.9 \pm 0.1) \text{ mg}$  was added to 1 l of 0.5M hydrochloric acid in a Marinelli beaker.

#### *Mixed radionuclide verification source*

The Marinelli beaker verification source was prepared independently at the Kernfysisch Versneller Instituut in Groningen. It was part of a validation of a protocol for  $\gamma$ -ray measurements by means of an interlaboratory test programme among Dutch laboratories<sup>[2]</sup>. It was prepared by taking 47.000 g of a mixed radionuclide reference solution from the Physikalisch-Technische Bundesanstalt (PTB) Braunschweig in Germany. The exact amount was determined by weighing the solution in a 100 ml beaker on a three-digit balance. It was rinsed down with 0.5M hydrochloric acid in a 5 l polyethylene bottle. In addition, a weighed amount of 40.000 g of potassium chloride was added to the solution. Hereafter, the solution was filled up to 3500.0 g with the same hydrochloric acid and mixed for 1 hour on a magnetic stirrer. It was then shipped to Delft, where 1012.5 g was put in a 1 l Marinelli beaker. The verification source thus prepared contains certified amounts of cobalt-57, cobalt-60, barium-133, caesium-134 caesium-137, and a known amount of potassium-40.

Owing to the added potassium chloride the density and the atomic composition of this source is slightly different from the previously described sources. However, calculation showed that for 100 keV photons the resulting difference in the sample self-attenuation is less than 0.5%.

#### *9.2.2 Detection equipment*

The bromine-82 point sources were measured in a 120 cm<sup>3</sup> germanium well-type detector that was lined<sup>[3]</sup> with a thin layer of zirconium. Sources were placed in glass test tubes on the bottom of the cryostat well. The efficiency calibration of the detector<sup>[4]</sup> allows for activity measurements that are accurate to within 1% ( $1\sigma$ ), taking into account coincidence effects.

The various Marinelli beakers had inner core dimensions of ( $\varnothing 70 \times 74$ ) mm. and the outer dimensions of ( $\varnothing 117 \times 130$ ) mm. All beakers were counted on an 18% relative efficiency coaxial germanium (lithium doped) detector.

The counting times for all sources were chosen long enough to get uncertainties in the main full-energy peak areas of less than 1%. The counting time for the bromine-82

calibration source was chosen long enough to obtain the same uncertainty in the main sum peak areas. Peak areas were determined using in-house analysis software<sup>[5]</sup>. Dead time and pile-up were corrected for using the pulser method.

### 9.2.3 Data handling

As described in the introduction, two variants of the proposed method to calibrate the Marinelli beaker detection geometry have been investigated. For Variant **I**, all curves were determined from the bromine-82 Marinelli beaker measurement. First estimates for the curve parameters were supplied by the fit program.

For Variant **II**, ideally the measurement of the Marinelli beaker calibration source should provide the full-energy peak efficiency curve. Knowing this curve, the measurement of the bromine-82 should then provide the PT- and the LS-curve. However, next to radionuclides emitting non-coincident  $\gamma$ -rays, the source contains yttrium-88 and cobalt-60, both emitting two gamma photons in coincidence. To accurately determine the full-energy peak efficiency curve using this source, one should be able to calculate coincidence effect corrections, which cannot be done without the knowledge of the PT- and the LS-curve. However, in this variant, this knowledge can only be obtained if a full-energy peak efficiency curve is already known.

This circular problem was solved by iterative calibration: First, Variant **II** of the method was performed without correcting the yttrium-88 and cobalt-60 for coincidences. The resulting curve set was then used to calculate the corrections and Variant **II** was performed again. This was repeated until both the  $\chi^2$ -value for the fit of the peak-efficiency curve to the mixed radionuclide measurement and the  $\chi^2$ -value for the fit of the PT- and LS-curves to the bromine-82 measurement showed no further improvement.

The three final curves, resulting from either variant of the proposed calibration method, were used to calculate the activity of all radionuclides present in the PTB verification source. The areas of all peaks corresponding to one specific radionuclide were divided by their  $P_E$ -value using Equation (2.19). For each peak, this results in a corresponding number of disintegrations. The reported number of disintegrations,  $N$ , of the specific radionuclide is the weighted mean of the separate values associated with each peak. The imprecision of the reported number is obtained from the imprecision of the peak areas. The exact procedure is outlined in Appendix B.

In addition, for those radionuclides present in both the calibration and the verification source, the verification-source activity was determined using radionuclide specific calibration.

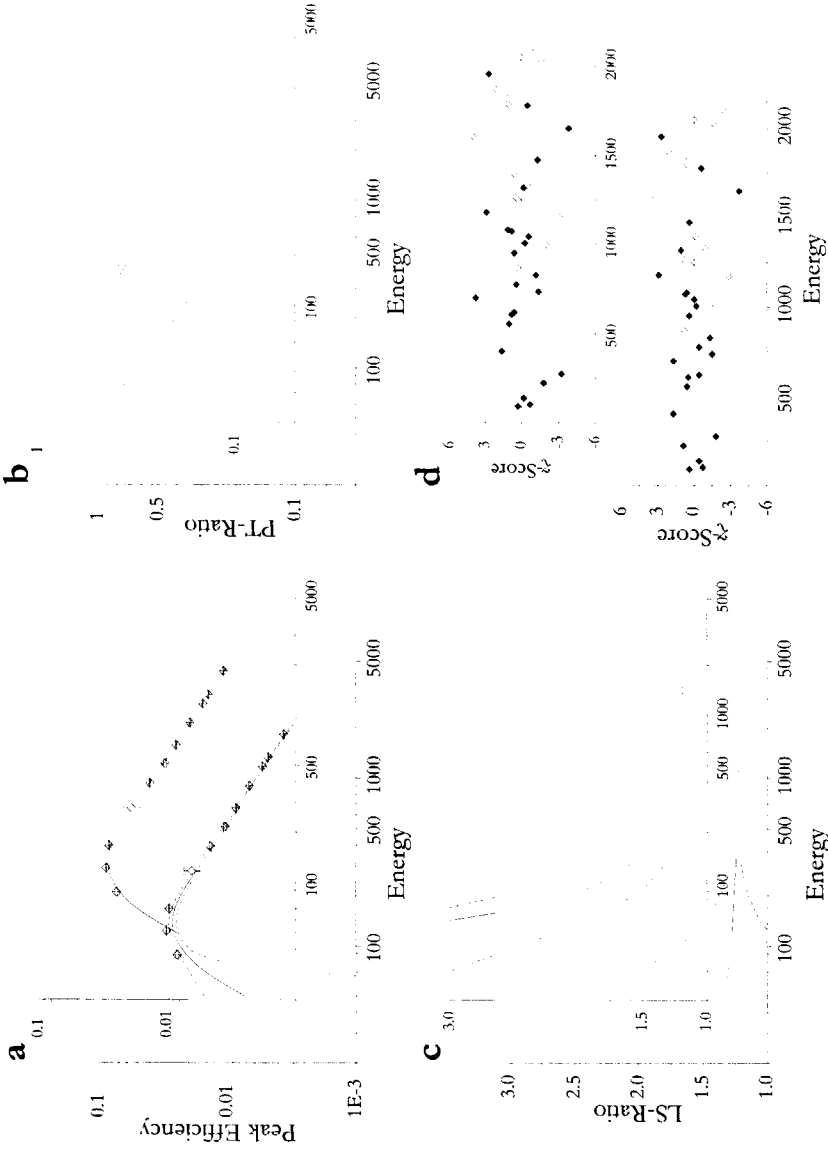


**Figure 9.1:** Reproduction of a bromine-82 spectrum using curves obtained with Variant I (Foreground plots) and Variant II (Background plots) of the calibration method. **a:** Full-energy peak efficiency curves (solid lines),  $1\sigma$  confidence regions (dashed lines) and efficiency values (diamonds and error bars) obtained from independent calibration. **b:** PT-curves; **c:** LS-curves; **d:** Bromine-82 spectrum interpretation in terms of  $\chi^2$ -scores. Solid points are associated with main peaks; open points with sum peaks.

### 9.3 Results

Figure 9.1(a-c) show the curves resulting from the two variants of the proposed calibration method. Full-energy peak efficiency values measured with the mixed radionuclide calibration source have been added to Figure 9.1a. The yttrium-88 and cobalt-60 values have been corrected for coincidence losses using the results from the iterative calibration. The correlation parameter determined with both variants did not deviate significantly from unity ( $\rho_{\text{variant I}} = 1.00 \pm 0.02$ ;  $\rho_{\text{variant II}} = 0.95 \pm 0.42$ ). Figure 9.1d shows the results of the fits to the bromine-82 spectrum in terms of  $\chi$ -scores.  $\chi^2$ -values yield respectively 2.2 for Variant I and 3.0 for Variant II. The first two columns of Table 9.1 show the interpretation results for the PTB verification source using the curves. The last column shows the interpretation results using radionuclide specific calibration. Figure 9.2 shows the results of the spectrum interpretations of those radionuclides in the PTB source that exhibit large coincidence effects, namely barium-133 and caesium-134.

### 9.4 Discussion

Variant I of the proposed calibration method uses only a bromine-82 spectrum to obtain all three curves. The full-energy efficiency curve from Variant I deviates considerably from the measured values at energies below 200 keV (see Figure 9.1a). The most intense peak of bromine-82 in this region, is the 92 keV peak which has an absolute intensity of only 0.75%. Also, the uncertainty of its intensity is relatively large. The determination of the full-energy efficiency curve in this region, however, is very critical owing to its strong curvature. The observed deviation of the efficiency curve can therefore be well understood. Variant II of the proposed method uses a supplementary

**Table 9.1:** Interpretation results of PTB verification source relative to reference for both variants of the proposed calibration method. In addition, interpretation results of PTB verification source when using radionuclide specific calibration. The standard deviation  $\sigma$  includes counting statistics and precision of reference values.

Radionuclide	Calibration method		Radionuclide specific $N/N_{\text{ref}} \pm 1\sigma$
	Variant I $N/N_{\text{ref}} \pm 1\sigma$	Variant II $N/N_{\text{ref}} \pm 1\sigma$	
<sup>57</sup> Co	$1.062 \pm 0.009$	$0.990 \pm 0.008$	$0.991 \pm 0.008$
<sup>133</sup> Ba	$1.032 \pm 0.008$	$0.983 \pm 0.010$	-
<sup>134</sup> Cs	$0.999 \pm 0.006$	$0.989 \pm 0.006$	-
<sup>137</sup> Cs	$1.003 \pm 0.008$	$0.978 \pm 0.008$	$0.974 \pm 0.009$
<sup>60</sup> Co	$1.015 \pm 0.007$	$0.998 \pm 0.007$	$1.000 \pm 0.007$
<sup>40</sup> K	$0.978 \pm 0.024$	$0.948 \pm 0.023$	-

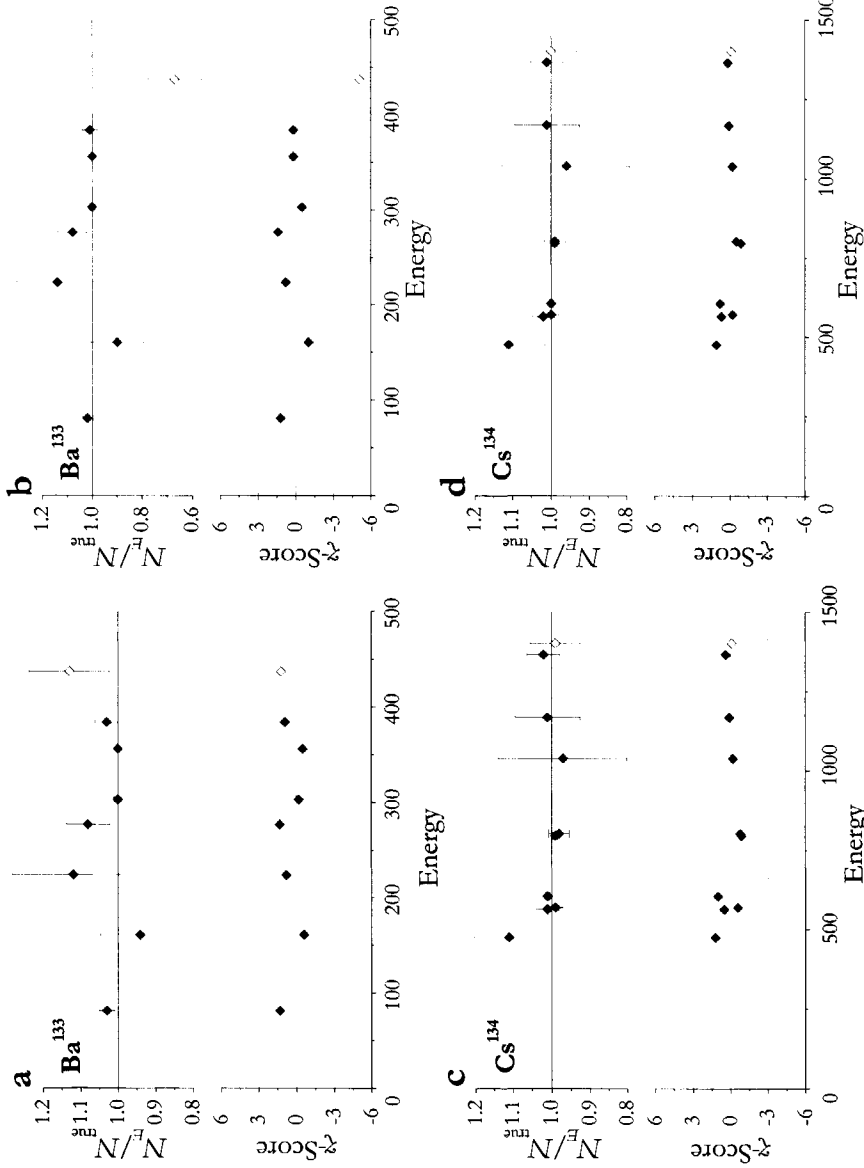


**Figure 9.2:** Interpretation results of the barium-133 and the caesium-134 spectra from the PTB source, using the curves obtained with both Variant I and Variant II. **a:** Barium-133 interpretation using Variant I; **b:** Barium-133 interpretation using Variant II; **c:** Caesium-134 interpretation using Variant I; **d:** Caesium-134 interpretation using Variant II;

measurement for the determination of the full-energy efficiency curve. It uses a calibration source that emits three photons in the critical region. With this variant, the curvature of the efficiency curve is well defined.

Comparing the other curves of the two variants with each other, the PT-curves show no significant difference. The observed difference between the two LS-curves has the same cause as the difference between the full energy efficiency curves. Like these curves, the LS-curve has a strong curvature, and therefore a degree of freedom, in the low energy region. Via coincidence effects, errors introduced by either the deviating full-energy efficiency curve or the uncertain 92 keV intensity are propagated to higher energy peaks, and are then corrected for by the deviating LS-curve in the low energy region.

The deviation of the efficiency curve of Variant I in the low energy region, is also shown by the results of the interpretation of the PTB verification source using this variant (Table 9.1). Since both  $^{57}\text{Co}$  and  $^{133}\text{Ba}$  emit photons below 200 keV, their activity is not well determined. The other radionuclides do not show significant deviations, taking into account the uncertainty of the used bromine-82 activity of 1%.

The interpretation results of the PTB verification source using Variant II show no inconsistencies. However, these results do show a slight bias of 1.5%. This bias may be owing to badly calibrated weighing equipment, certification errors, the additional KCl in the verification source, or owing to the proposed calibration method. To exclude the latter as a bias source, the PTB verification source measurement has been interpreted for those radionuclides also present in the calibration source, using radionuclide specific calibration. Since the results of this interpretation show a similar bias, it is concluded that the bias is not introduced by the calibration method. Moreover, the calibration method shows to be as accurate as radionuclide specific calibration.

## 9.5 Concluding remarks

The calibration method, presented in the previous chapter has been verified for one Marinelli beaker geometry. Based on the results of computer validations, there should be no fundamental limitation to extend the conclusions to other Marinelli beaker geometries, as long as the attenuation coefficient,  $\mu$ , of the sample material is smaller than  $1\text{ cm}^{-1}$ .

The model that has been developed enables accurate calculation of peak areas obtained from the measurement of voluminous sources, specifically Marinelli beaker sources. In addition the calibration method described can obtain all information necessary to apply this model. In principle the method allows for the determination of all information from one calibration measurement of a bromine-82 source with known activity. Although bromine-82 has been chosen for the calibration, other radionuclides may also be suited for this purpose. These radionuclides should have a decay scheme that is complex enough to show coincidence effects covering a large energy range, yet is simple enough to allow rapid fit sessions. Furthermore, it should allow easy homogenization with

different kinds of sample material. Caesium-134, for instance, would be a suitable candidate.

If bromine-82 is used as a calibration radionuclide, curves resulting from a single calibration measurement (Variant I) are questionable in the energy region approximately below 200 keV. If, on the other hand, an accurate full-energy peak efficiency curve is obtained from a supplementary measurement (Variant II), then the use of bromine-82 can very well provide accurate PT- and LS-curves. Thus, the method would require at most two calibration measurements, or a single measurement of a suitable mixture of radionuclides. It allows for calibrations that are as accurate as radionuclide specific calibrations and considerably less laborious.

### References

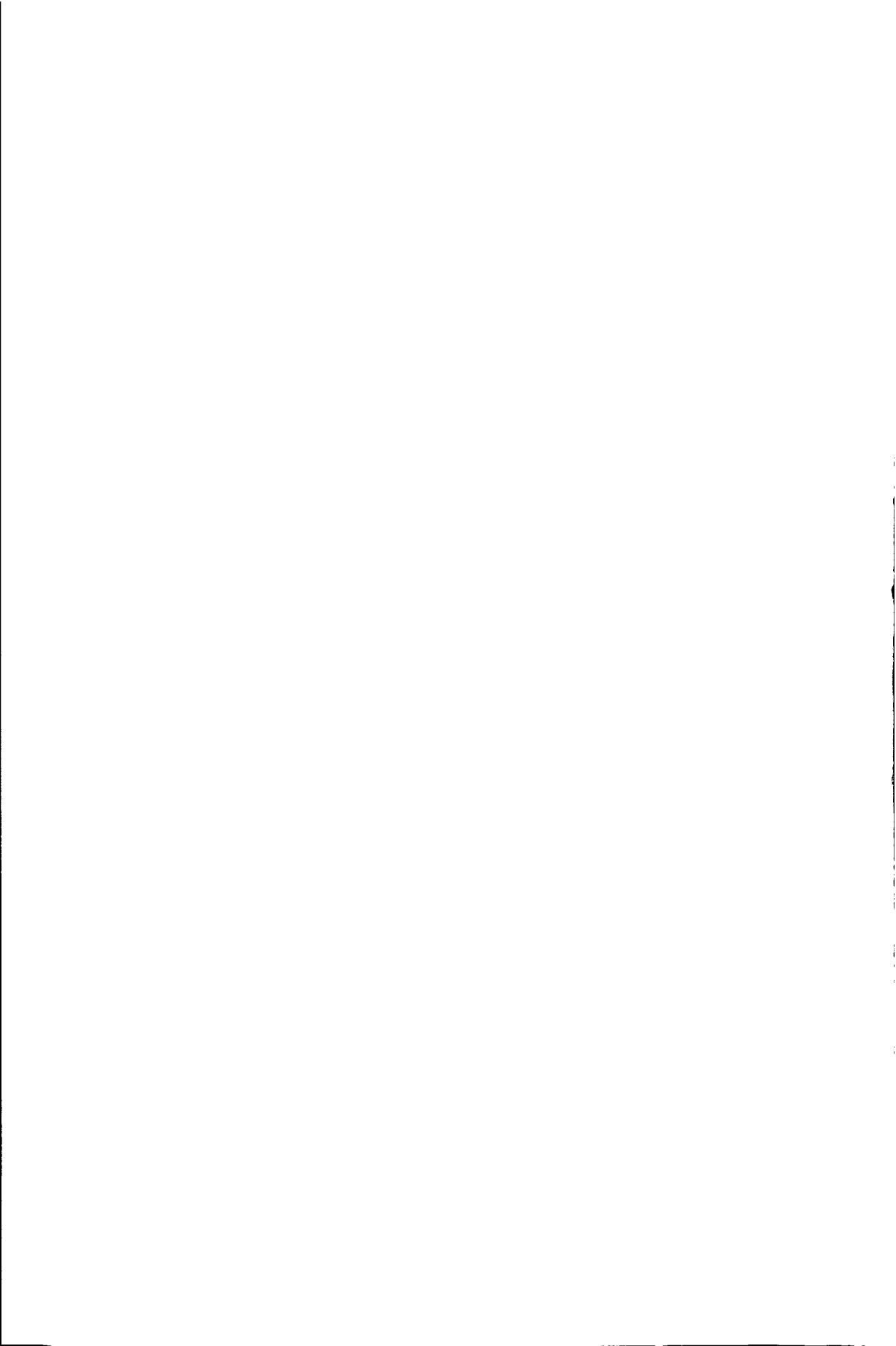
- [1] R. Gunnink, *Nucl. Instr. and Meth.*, **A299** (1990) 372
- [2] E.R. van der Graaf, L.B. Venema, L.W. Put, R.J. de Meijer, *KVI internal report S36*, December 1997. (in Dutch)
- [3] M. de Bruin, P.J.M. Korthoven, P. Bode, *Nucl. Instr. and Meth.*, **159** (1979) 410
- [4] M. Blaauw, *Nucl. Instr. and Meth.*, **A332** (1993) 493
- [5] M. Blaauw, *Nucl. Instr. and Meth.*, **A333** (1993) 548





# Epilogue

---



# Chapter Ten

## General discussion

---

### Abstract

*This chapter discusses the performance of the developed calibration method that includes coincidence effects in combination with sample self-attenuation effects. The method is based on three efficiency curves, the full-energy peak efficiency curve, the PT-curve and the LS-curve introduced in Chapter Two. While the previous chapters discuss its performance for well-type detection geometries and Marinelli beaker geometries separately, this chapter focuses on the overall performance.*

### 10.1 Introduction

It was at IRI in earlier years that first attempts were made to obtain both efficiency curves required for point-source coincidence computations from a single  $\gamma$ -ray spectrum. Still earlier methods required independent measurements to obtain a full-energy peak efficiency and a total efficiency (or peak-to-total) curve. The measurement of a full-energy peak efficiency curve is still relatively easy, but the measurement of a total efficiency curve requires yet more effort.

However, using an independently obtained peak-to-total curve for coincidence summing calculations addresses a more fundamental problem. Typically, total efficiency values obtained from direct measurements comply with the IUPAC definition, i.e. they are defined as a number of counts relative to the number of emitted photons, rather than as probabilities of detection. Total efficiency values to be used for coincidence summing calculations should be defined in terms of probabilities, which are a lot harder to measure, if at all. In Chapter Two, we saw that this thesis indeed uses the latter definition for the total efficiency as well as for the full-energy peak efficiency rather than the IUPAC one, despite the measurement problem.

To overcome the measurement problem, the IRI method (in this thesis previously referred to as Blaauw's method) discards the idea that an independent method must be

used to obtain the curves, and instead determines the curves from one single  $\gamma$ -ray spectrum, showing coincidence effects. This philosophy cleared the way for the definition of a curve that certainly could never be measured independently at all, i.e. the linear-to-squared curve\*. This linear-to-squared curve is the essence of this thesis. It was arrived at intuitively even before the theory of stochastic efficiencies described in Chapter Two was developed. The debugging of Monte Carlo software (Chapter Three) contributed greatly to the insight required to arrive at the linear-to-squared curve, as well as to the concept of stochastic efficiencies.

These aspects perhaps explain why nobody else arrived at the same idea earlier, even though the problem of coincidence summing in conjunction with self shielding had been noted and had even been worked on by others before. As compared to e.g. Tien-Ko Wang's form factors<sup>[1]</sup>, which also account for the difference between the product of two volume-averaged efficiencies and the volume average of the product of two efficiencies but must be computed for each peak and each radionuclide to fully characterize a detector, the linear-to-squared curve is compact and hardly slows down the computation of coincidence summing effects. Sima's approach<sup>[2]</sup>, where each radionuclide must be submitted to Monte Carlo algorithms to obtain full-energy peak detection probabilities, obviously is slower in the extreme.

## 10.2 Theory aspects

The aim of the work described in this thesis was to extend the existing theory of coincidence summing effects for point sources to voluminous source cases. Therefore, it was to take into account the variation of efficiency over the source volume. In addition, it was to introduce a calibration method that was based on this extended theory. Like Blaauw's method, it was to use the theory to provide the general form of efficiency curves. It was, however, to obtain the actual curve parameters from measurements showing coincidence effects. This way, the self-validating character of Blaauw's method was to be preserved, and moreover, this allowed for curves that could be determined implicitly only.

The newly introduced method would have to cover well-type geometries as well as Marinelli beaker detection geometries. For the method to be competitive, its inaccuracy and imprecision were to be as low as those of the most accurate and precise conventional methods, i.e. as low as those of radionuclide specific calibration methods. It was therefore to yield activities with an accuracy of better than 1%.

In order to properly account for coincidence summing effects in voluminous sources, Chapter Two developed the new concept of stochastic efficiencies. For voluminous

---

\* For the direct measurement of a linear-to-squared curve, one would need a radionuclide that simultaneously emits two photons of the same energy in random, uncorrelated directions. Even the simultaneous emission of two 511 keV photons in positron annihilation is of no avail because the two photons are emitted in two opposite directions.

sources, full-energy peak efficiencies and total efficiencies cannot be considered constant throughout the source volume. Instead, for every single decay, they depend upon the location of the decaying nucleus. Since this location is subject to probabilistic processes, it is natural to view efficiencies as stochastic variables having means, variances and cross-correlations. Having said that, Chapter Two introduced in a natural manner a third efficiency curve that accounts for the variation of the efficiency over the source volume by relating the variance of the efficiency distributions to their mean. It turned out that this third efficiency curve directly relates volume-averaged linear efficiencies to volume averaged quadratic ones. Therefore it is called the linear-to-squared (or LS-) curve.

The practical use of the newly introduced LS-curve was somewhat hampered by the appearance of cross-correlation coefficients in the applicable formulae. These coefficients express the correlation between, on the one hand, the efficiency for a certain energy, say,  $\varepsilon_1$  at a random position within the source volume and, on the other hand, the efficiency for a different energy, say  $\varepsilon_2$ , but for exactly that same position. Strictly, one would need a separate correlation parameter for every possible combination of energies. However, since the efficiency values are related by position, it is clear that the correlation between the two is large and positive. Therefore, all separate parameters are replaced by a single parameter  $\rho$  near 1. Using this approach however, care should be taken to first calculate summing-in effects and summing-out effects separately while using a large and positive correlation. Only as a last step, summing-in and summing-out effects can be combined, this time taking the correlation large and negative, i.e. near -1.

### 10.3 Monte Carlo aspects

Throughout this thesis it was explicitly stated several times that the applicability of the developed calibration methods should not rely on Monte Carlo calculations or on other volume integration routines, despite of their obvious advantage of the absence of need for calibration radionuclides. This approach is not owing to the computational demands of these methods. Although the time-aspect and possibly the complexity of these calculations might be a drawback when these methods are applied today, tomorrow there will be faster and user-friendlier computers that do the same computations in only one tenth of the time.

The motivation for the independence on Monte Carlo calculations is much more fundamental. To provide accurate calibration results, Monte Carlo based methods require accurate knowledge of the detector- and source geometry and of source-matrix composition. This knowledge includes the inner-dimensions of the detector such as those of the detectors active volume. This information is hardly ever available, at least not upto the accuracy needed. Therefore, Monte Carlo methods always must be calibrated themselves for every new detector via a calibration measurement. If one does need a calibration measurement after all, why not exploit this measurement to the fullest, like the method described in this thesis attempts to do.

Chapter Three, however, does deal completely with Monte Carlo techniques. The reason for the emphasis on these techniques lies not in their use in the application of the methods itself, but rather in their development. Monte Carlo techniques made it possible to test the internal consistency of the calibration methods. By using them, interfering sources of (systematic) error like for instance not sufficiently known decay schemes, could be completely eliminated, remaining only those introduced by the calibration methods. This advantage is well illustrated in Chapter Six and perhaps even better in Chapter Eight: As a first step, a set of efficiency curves and, independently, a bromine-82 spectrum are calculated. Both the geometry and the bromine-82 decay scheme used with these calculations are well defined. As a second step, the set of efficiency curves is used to reproduce the spectrum. Since the decay scheme is well defined, it is beyond suspicion as a source of error. Therefore, the second step gives great confidence in the consistency of the developed theory. As a third step, a curve set resulting from a fit to the spectrum is compared with the 'true' set. This step gives confidence in the quality of the fitting procedures. Moreover, it enabled a quest for the optimal fitting procedure.

A second advantage of the use of Monte Carlo techniques is the possibility to simulate events or calculate quantities that would never occur or be measured in real-life situations. An obvious example is the simulation of the detection of two simultaneously emitted gamma quanta of exactly the same energy, used to calculate LS-ratios. Another example is the calculation of PT-ratios that obey the definition of Chapter Two. (In this respect, the reader is also referred to the introductory section of this chapter.)

Perhaps the most important aspect of the use of Monte Carlo techniques is the insight it generated in complex scattering processes. The debugging of Monte Carlo software showed very well how often a photon can undergo Compton scattering in the source volume or in the detector volume before being totally absorbed by the photoelectric effect. As such, it contributed greatly to the insight required to arrive at the concept of stochastic efficiencies and to the definition of the LS-curve.

#### 10.4 Well-type detector aspects

To apply voluminous source coincidence summing corrections to well-type detectors might at first sight appear strange. After all, sources ordinarily counted in well-type detectors are small enough to behave as point sources. However, well-type detectors typically have no dead layer on the inside, and in some cases, the source matrix may absorb low-energy photons to a significant extent. For these photons, the detection probability depends on the exact location of the disintegrating nucleus within the source and therefore, the source is indeed voluminous, at least for these low-energy photons. Coincidence summing with their high-energy counterparts transfers the voluminous nature to the entire  $\gamma$ -spectrum.

Currently at IRI, well-type detectors are equipped with a high-Z lining that prevents low-energy photons from being detected. That way, the voluminous nature of high-Z

matrix sources is suppressed. This is, however, a rather unsatisfying solution since it degrades detector performance. Firstly, while unlined well-types have a large area of constant detection efficiency, lined well types show a geometry dependency of the detection efficiency on the source position in the well. This is demonstrated by experiments described in Chapter Four. Secondly, while well-types originally were introduced for their high (maximum) absolute detection efficiency of almost 1.0 for photons with energies around 100 keV, the lining considerably reduces maximum detection efficiencies to values near 0.5. Finally, the lining leads to a somewhat higher Compton continuum relative to the full-energy peak, that can obscure small peaks. This latter effect is revealed by the slightly worse PC- or PT-ratio for lined well-type detectors, as compared to non-lined ones in Chapter Five.

It is therefore that this thesis attempted to correct analytically for the voluminous nature of some of the well-type sources. It applied the strategy outlined in section 10.3 to develop such a method. First, the general theory from Chapter Two was expanded to include effects of K-edges in photoelectric absorption processes. Then, its internal consistency was verified by incorporating it in a calibration method which was applied to Monte Carlo generated spectra. Finally the method was applied to experimental data.

The Monte Carlo based results from Chapter Six were obtained with an unlined well-type geometry and two sources, a low-density, low-Z source and a high-Z tantalum pentaoxide matrix source. They indicate that that it is possible to determine the parameters required to characterize the sample-detector geometry from the measured spectrum of a calibration radionuclide like terbium-160, to the point where coincidence summing corrections with accuracies far better than the required 1 % can be made for terbium-160 itself. The quality of the results will be optimal if the number of disintegrations in the calibration source is known and kept constant in the fitting procedure. However, the simulated erbium-171 spectra were not satisfactorily explained from the curves obtained with terbium-160. Especially peaks in the low energy region near 100 keV show large statistically significant deviations.

The experimental results from Chapter Seven look very similar to the Monte Carlo based ones. They were obtained using not only a non-lined well-type geometry but also a lined one, using again both a low-density, low-Z source and a high-Z tantalum pentaoxide matrix source. The high-Z source was measured only in the non-lined geometry. Again, the terbium-160 spectra from all measurements were explained very well. Also spectra from additional radionuclides like cobalt-60, bromine-82 and caesium-137 proved to be no problem, but erbium-171 spectra did.

The failure of the method with erbium-171 occurs in all counting geometries, lined and non-lined, for both types of sources, low-Z and high-Z, and in the Monte Carlo world as well as in the real world. Chapter Six offers a first explanation for the observed discrepancy: It lies in the behaviour of the LS-curve as described in the last paragraph of section 6.2.1. Only very few terbium-160 photons in the low energy region do coincide and therefore only marginally determine the curvature of the LS-curve. The determination in this region may simply be not accurate enough to fully explain low energy erbium-171

coincidences. This explains, however, only discrepancies observed with the high-Z tantalum pentaoxide sources.

Chapter Seven offers several experimental explanations: Firstly, the decay scheme of erbium-171 may be suspect, which is confirmed by applying Blaauw's "proven-to-be-accurate" method to the erbium-171 showing similar discrepancies between theory and experiment. Secondly, at the low energies involved, thickness variations in the glass sample holders may have played a part. Finally, physical phenomena such as the emission of X-rays by the lining and/or the source matrix should have been accounted for in the modelling, and/or the decay schemes of the radionuclides involved are not known well enough. The X-ray emissions by sample matrix and detector lining were assumed to be encompassed by the definition of total efficiency, but the resulting peaks in the spectrum may coincide with others - the more complex the spectrum becomes, the higher the likelihood of this happening.

While all these explanations might be very plausible in themselves, they ignore the fact that the method fails with erbium-171 in all cases, including that uses the lined detector. The only explanation offered by both Chapter Six and Chapter Seven together that does account for the general nature of the problem is the following. The full-energy peak efficiency curve might not be well defined in the low-energy region. In this context, the reader is referred to section 2.2.1 which introduced an adapted version of the Gunnink parameterization. Originally, Gunnink divides the efficiency curve in three regions: <90 keV, 90 to 200 keV, and >200 keV. This work, however, uses only two regions, hereby combining the regions below 200 keV. This may very well explain the observed discrepancy in this region.

The obvious solution is to use Gunnink's original parameterization of the low-energy region of the full-energy efficiency curve. The researcher should, however, be aware that Gunnink did not incorporate well-type detectors in his investigation and that therefore his parameterization might not fulfil either. More research will still be required to establish which radionuclides behave according to the theory developed here and which do not. Unfortunately, more experiments in the counting geometry used in this thesis will be impossible since the detector's efficiencies changed drastically in a recent repair.

For the erbium-171 case, the agreement between experiment and theory is rather unsatisfactory. However, employing the calibration methods described in this chapter would lead to systematic errors in reported activities of only 0 to 3 % for simple radionuclides such as caesium-137, depending on the counting geometry and the radionuclide. It would lead to errors of 3 % for a complex case nuclides like bromine-82 and terbium-160, and up to 10 % only for complex radionuclides such as erbium-171.

In those cases where the radionuclide to be determined cannot be obtained in a known amount in the matrix of interest, and the use of well-type is deemed necessary, the procedures presented here currently are the only option for quantitative determination. One should realize that systematic errors caused by true coincidence summing in well-type counting geometries can easily amount to a factor of 2 to 3 for radionuclides with



complex decay schemes. In that respect, the methods presented here certainly are an improvement.

### 10.5 Marinelli beaker aspects

The value of developing voluminous source coincidence correction methods for Marinelli beaker detection geometries is obviously very high. Marinelli-beaker geometries are used much more often and in many more laboratories than well-type geometries, and the possible impact of a method in such applications is therefore much larger than it would have been for well-types even if I would have obtained the 1 % accuracy level. For Marinelli beaker geometries, the general theory provided by Chapter Two could be used without any modifications or expansions. The Monte Carlo based results obtained with four Marinelli beaker geometries from Chapter Eight show that, to obtain accurate results for voluminous sources, the use of a full-energy peak efficiency curve in combination with a peak-to-total curve is not sufficient. In addition to these two curves, indeed a third curve is needed that accounts for the variation of the efficiency over the source volume, i.e. the LS-curve. In principle a bromine-82 spectrum can be used to determine all three curves. Moreover, the spectrum interpretation results are slightly better using curves obtained from a bromine-82 spectrum than using the curves obtained by direct calculation. This demonstrates the presumption expressed in the introduction that methods correcting for coincidence effects should obtain their information from these effects.

If the method is to be used in real-life situations, the number of disintegrations of the bromine-82 during the calibration measurement should be accurately known. The interchangeability between the number of disintegrations and the parameters describing the LS-curve causes the calibration method to produce inaccurate results. Furthermore, the validity of the curves based on a single bromine-82 measurement is questionable below 92 keV. However, for energies lower than 92 keV, the method can very well provide PT- and LS-curves if an accurate full-energy peak efficiency curve is obtained from a measurement of a source emitting non-coincident  $\gamma$ -rays covering the whole energy range of interest. Thus, the method would require at most two calibration measurements, or a single measurement of a suitable mixture of radionuclides. Typically, it allows for activity measurements results that are accurate within 1%.

These conclusions are supported by the experimental results of Chapter Nine. Although the experiments were performed only for a 1ℓ, water-filled Marinelli beaker, there should be no fundamental limitation to extend the conclusions to other Marinelli beaker geometries, as long as the attenuation coefficient,  $\mu$ , of the sample material is smaller than  $1 \text{ cm}^{-1}$ .

The model that has been developed enables accurate calculation of peak areas obtained from the measurement of voluminous sources, specifically Marinelli beaker sources. In addition the calibration method described can obtain all information necessary

to apply this model. In principle the method allows for the determination of all information from one calibration measurement. Although bromine-82 has been chosen for the calibration, other radionuclides may also be suited for this purpose. Suitable radionuclides should have a decay scheme that is complex enough to show coincidence effects covering a large energy range, yet is simple enough to allow rapid fit sessions. Furthermore, it should allow easy homogenization with different kinds of sample material. Caesium-134 is an example of such a radionuclide.

If bromine-82 is used as a calibration radionuclide, curves resulting from a single calibration measurement are questionable in the energy region approx. below 200 keV. If, on the other hand, an accurate full-energy peak efficiency curve is obtained from a supplementary measurement, then the use of bromine-82 can very well provide accurate PT- and LS-curves. Thus, the method would require at most two calibration measurements, or a single measurement of a suitable mixture of radionuclides. It allows for calibrations that are as accurate as radionuclide specific calibrations and is considerably less laborious.

## 10.6 Conclusions

The approach developed in this thesis to analytically account for coincidence summing effects in combination with sample self-attenuation did meet the majority of criteria that Chapter One set for it. It certainly takes the variation of the efficiencies over the source volume into account. It provides a calibration method based on a parametric model while the actual parameters are obtained from measurements showing coincidence summing effects. It is applicable to point sources as well as voluminous sources. Furthermore, for Marinelli-beaker geometries, the accuracy of the method is indeed better than 1 %.

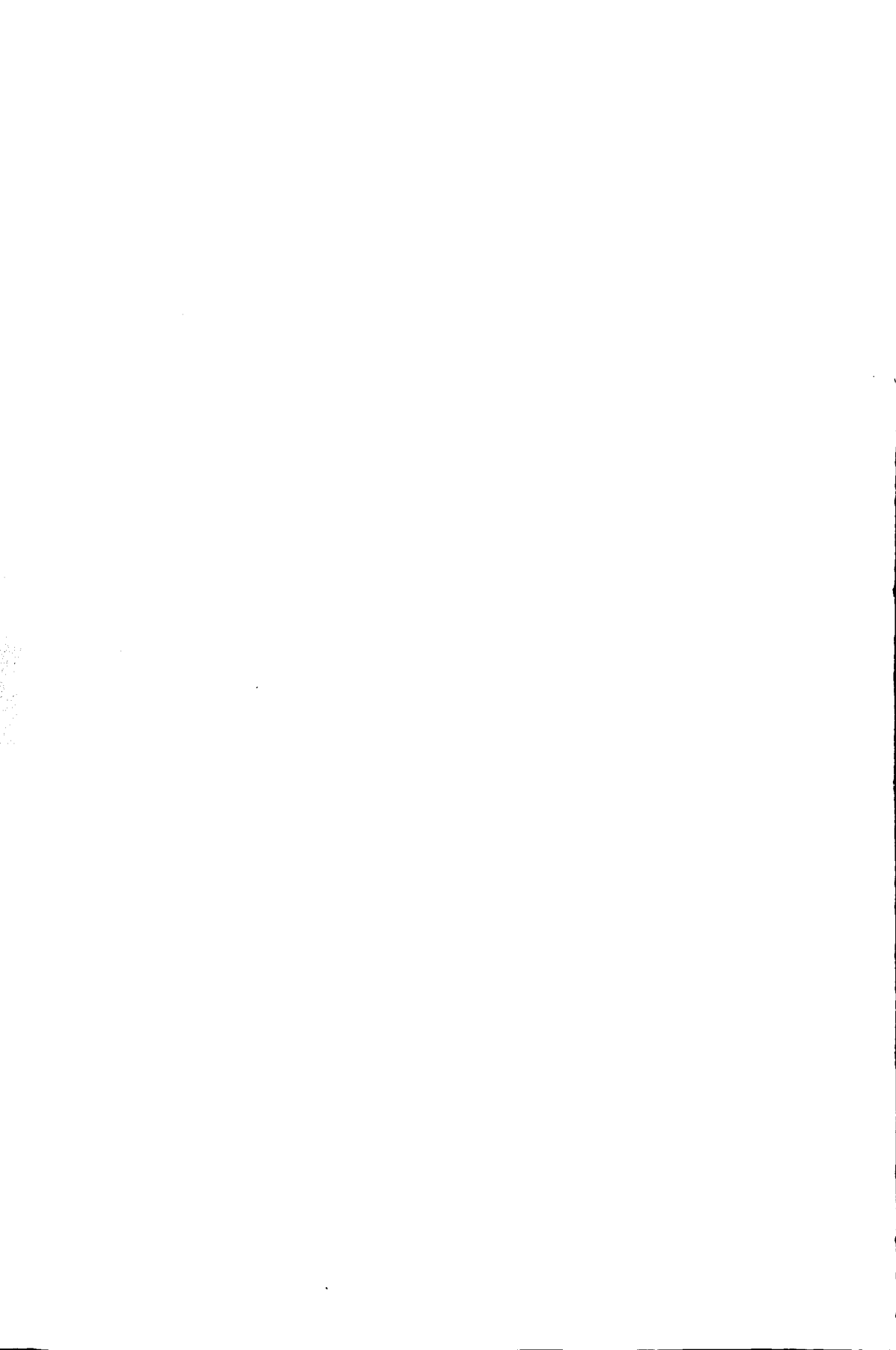
For well-type detection geometries however this aim is not met. While the majority of radionuclides, including terbium-160 and bromine-82 can be reproduced with accuracies better than 3 %, erbium-171 showed to be a problem. Further investigation should demonstrate if a more accurate parameterization of the full-energy peak efficiency curve below 200 keV might be a solution. Notice though that the lining did not solve the erbium-171 problem either.

On one hand, the worse performance of the method in the well-type case is a pity, because the work as a whole was started in order to be able to remove the lining from well-type detectors and dispense of its negative effects shown by Chapter Four and Chapter Five. On the other hand, Marinelli-beaker geometries are used much more often and in many more laboratories than well-type geometries, and the possible impact of the method in such applications might therefore be much larger than it would have been for well-types even at 1 % accuracy. In fact, this is already being demonstrated by the fact that PerkinElmer's ORTEC company incorporated the algorithms developed here in their popular  $\gamma$ -ray spectrometry program GammaVision version 5.2, released after Quality

Assurance testing in January 2001. Also as a consequence of this work, the company Analytics Inc. in Oak Ridge has begun the manufacturing process of voluminous calibration sources containing coincidence-rich cesium-134 as well as some of the well-known, coincidence-free calibration radionuclides, in October 2000.

### References

- [1] T.-K. Wang, T.-H. Ying, W.-Y. Mar, C.-L. Tseng, C.-H. Liao, M.-Y. Wang, *Nucl. Instr. and Meth.*, **A376** (1996) 192
- [2] O. Sima, C. Dovlete, *Appl. Radiat. Isot.*, **48** (1997) 59



# Appendix A

## A stochastic approach to $P_E$

---

### A.1 Introduction

The implementation of the stochastic approach introduced two specific assumptions. Firstly, efficiency terms ( $\varepsilon - \mu$ ) of higher order are neglected and secondly, the correlation between two factors  $\varepsilon_i$  and  $\varepsilon_j$  are taken close to 1 while the correlation between two factors  $\varepsilon_k$  and  $(1-\varepsilon_l)$  are taken close to -1. The implications of these assumptions for equation (2.19) are outlined in this appendix, yielding a simplified and workable expression for  $P_E$ . The original expression for  $P_E$  yields

$$P_E = \frac{1}{V} \int_V \sum_{\text{Cascades}} \left[ P_C \prod_{i=1}^{M_C} \varepsilon_i \prod_{j=1}^{N_C-M_C} (1-\varepsilon_j) \right] dV = \sum_{\text{Cascades}} \left[ P_C \prod_{i=1}^{M_C} \varepsilon_i \prod_{j=1}^{N_C-M_C} (1-\varepsilon_j) \right]. \quad (2.19)$$

The task this Appendix is facing with is to write the mean product on the left hand side of (2.19) as a product of its mean constituting factors, i.e. as a product of mean efficiencies. Therefore, we will first develop the necessary expressions for the mean value of a product of two stochastic variables.

The product of two stochastic variables,  $\varepsilon_1$  and  $\varepsilon_2$ , with mean  $\mu_1$  and  $\mu_2$  respectively and scaled variance  $\eta_1^2$  and  $\eta_2^2$  respectively, has mean  $\mu_{12}$  of

$$\mu_{12} = (1 + \rho \eta_1 \eta_2) \mu_1 \mu_2 \quad (2.25)$$

and scaled variance  $\eta_{12}^2$  of

$$\eta_{12}^2 \approx \eta_1^2 + \eta_2^2 + 2\rho \eta_1 \eta_2, \quad (2.27)$$

where the latter was found using a Taylor expansion (2.26) about the point  $(\mu_1, \mu_2)$  and using only linear terms. If, in the latter expression, we set  $\rho$  to 1, this expression transforms to

$$\eta_{12}^2 \approx (\eta_1 + \eta_2)^2,$$

or

$$\eta_{12} \approx \eta_1 + \eta_2.$$

We can now add a third stochastic variable,  $\varepsilon_3$ , to the product by treating the product of  $\varepsilon_1$  and  $\varepsilon_2$  as a single factor  $\varepsilon_{12}$  with mean and scaled variance  $\mu_{12}$  and  $\eta_{12}^2$ , respectively, and taking  $\mu_3$  and  $\eta_3$  as mean and scaled variance for  $\varepsilon_3$ . For  $\eta_1, \eta_2$  and  $\eta_3$  smaller than 1, this yields for the mean of the product of three stochastic variables,  $\mu_{123}$

$$\begin{aligned} \mu_{123} &= (1 + \rho\eta_{12}\eta_3)\mu_{12}\mu_3 = (1 + \rho\eta_1\eta_3 + \rho\eta_2\eta_3)(1 + \rho\eta_1\eta_2)\mu_1\mu_2\mu_3 \\ &= (1 + \rho\eta_1\eta_2 + \rho\eta_1\eta_3 + \rho\eta_2\eta_3)\mu_1\mu_2\mu_3 + \mathbf{O}(\eta^4) \end{aligned} \quad (\text{A } 1)$$

where the higher order  $\eta$ -terms are accounted for by the  $\mathbf{O}$ -operator. The (square root of the) scaled variance of the product can be derived in a similar manner as for the product of two variables:

$$\eta_{123} \approx \eta_1 + \eta_2 + \eta_3 \quad (\text{A } 2)$$

When neglecting the higher-order terms, for a product of  $n$  stochastic variables,  $\varepsilon_1 \dots \varepsilon_n$ , (A 1) generalizes to

$$\mu_{1\dots n} \approx \left(1 + \rho \sum_{i=1}^n \sum_{j=1}^n \eta_i \eta_j\right) \prod_{i=1}^n \mu_i, \quad (\text{A } 3)$$

and (A 2) generalizes to

$$\eta_{1\dots n} = \sum_{i=1}^n \eta_i. \quad (\text{A } 4)$$

## A.2 Summing-in factor

We can distinguish two main factors in the expression for  $P_E$ , (2.19), namely

$$\prod_{i=1}^{M_c} \varepsilon_i \quad (\text{A } 5)$$

and

$$\prod_{j=1}^{N_c-M_c} (1 - \varepsilon_{ij}). \quad (\text{A } 6)$$

of which (A 5) accounts for summing in effects. Using the general expressions (A 3) for the mean value of a product of efficiencies, the mean value of (A 5) can be written as

$$\overline{\prod_{i=1}^{M_c} \varepsilon_i} \approx \left( 1 + \rho \sum_{i=1}^{M_c} \sum_{j=i}^{M_c} \eta_i \eta_j \right) \prod_{i=1}^{M_c} \mu_{\varepsilon,i}. \quad (\text{A } 7)$$

The scaled variance of this product can be derived from (A 4). For this expression we had to approximate the correlation coefficient  $\rho$  to 1 in the scaled variance calculations. In section 2.3.2, it was argued that this is a valid approximation for the case of stochastic efficiency variables. Furthermore, we had to neglect  $\eta$ -terms of order 4 and higher, which is a simplification that is of the same order of the one used in the Taylor expansion (2.26).

### A.3 Summing-out factor

The mean value of the product (A 6), of factors  $(1 - \varepsilon_i)$  accounting for summing out effects owing to all photons in a specific cascade can be written in a similar manner as the product (A 5), using (A 3) and (A 4). Recalling that

$$\begin{aligned} \mathbf{E} [1 - \varepsilon_i] &= 1 - \mu_{\varepsilon,i}, & , \\ \text{var} [1 - \varepsilon_i] &= \sigma_{\varepsilon,i}^2 & \text{and thus} \\ \eta_{1-\varepsilon,i}^2 &= \eta_{\varepsilon,i}^2 \frac{\mu_{\varepsilon,i}^2}{1 - \mu_{\varepsilon,i}^2} & , \end{aligned} \quad (\text{2.24})$$

and again setting the correlation parameter  $\rho$  in the scaled variance calculations to 1 and neglecting  $\eta$ -terms of order 4 and higher, the mean of the product (A 6) is given by

$$\overline{\prod_{i=1}^{N_c-M_c} (1 - \varepsilon_{ii})} \approx \left( 1 + \rho \sum_{i=1}^{N_c-M_c} \sum_{j=i}^{N_c-M_c} \eta_i \eta_j \right) \prod_{i=1}^{N_c-M_c} (1 - \mu_{\varepsilon,i}), \quad (\text{A } 8)$$

while the scaled variance of this product, using (A 4) and (2.24), is given by

$$\eta_{\text{summing-out}} = \sum_{i=1}^{N_c-M_c} \eta_i \sqrt{\frac{\mu_{\varepsilon,i}^2}{1 - \mu_{\varepsilon,i}^2}}. \quad (\text{A } 9)$$

#### A.4 Combination

The final step in the derivation of a general simplified expression for  $P_E$  is combining the two factors that account for summing-in and summing-out effects, (A 5) and (A 6), respectively. We can use expression (2.25) in which for  $\mu_1$  we insert expression (A 3), for  $\mu_2$  we insert (A 8), for  $\eta_1$  we insert (A 4) and for  $\eta_2$  we insert (A 9). Following the approach outlined in section 2.3.2 we use  $-\rho$  as our correlation parameter. Thus expression (2.19) transforms to

$$\begin{aligned}
 P_E &= \frac{1}{V} \int_V \sum_{\text{Cascades}} \left[ P_C \prod_{i=1}^{M_C} \varepsilon_i \prod_{k=1}^{N_C-M_C} (1 - \varepsilon_{t,k}) \right] dV \\
 &\approx \sum_{\text{Cascades}} \left[ P_C \cdot \left\{ 1 - \rho \left( \sum_{i=1}^{M_C} \eta_i \right) \left( \sum_{k=1}^{N_C-M_C} \eta_k \sqrt{\frac{\mu_{\varepsilon,k}^2}{r_k^2 - \mu_{\varepsilon,k}^2}} \right) \right\} \cdot \right. \\
 &\quad \left. \left\{ 1 + \rho \sum_{i=1}^{M_C} \sum_{j=i}^{M_C} \eta_i \eta_j \right\} \cdot \left\{ 1 + \rho \sum_{k=1}^{N_C-M_C} \sum_{l=k}^{N_C-M_C} \eta_k \eta_l \right\} \cdot \prod_{i=1}^{M_C} \mu_{\varepsilon,i} \prod_{k=1}^{N_C-M_C} \left( 1 - \frac{\mu_{\varepsilon,k}}{r_k} \right) \right] \quad (2.28)
 \end{aligned}$$

In this expression the summations and products over index  $i$  (and  $j$ ) are taken over all photons in a specific cascade that constitute the full energy of the peak at energy  $E$ . Hence, they account for summing-in effects. The summation and product over index  $k$  (and  $l$ ) are taken over all other photons thus accounting for summing out effects.

The application of this expression requires knowledge of the mean peak efficiency values  $\mu_{\varepsilon}$  and the peak-to-total ratios  $r$ , which relate the mean peak efficiency values  $\mu_{\varepsilon}$  to the mean total efficiency values  $\mu_{\varepsilon,t}$ , both as a function of energy. Both the mean full-energy peak efficiency curve and the (mean)peak-to-(mean)total curve can be described using the same parameterizations as in the non-voluminous case. In fact, by defining them as mean curves, they are identically defined as the non-voluminous ones. The voluminous nature of the source is described by the scaled variance  $\eta$ , also as a function of energy, and by the constant  $\rho$ .  $\eta$  can be parameterized indirectly by the newly introduced *linear-to-squared* curve (2.23).

The validity of (2.28) is limited by the constraint on  $\eta$ ,  $\eta < 1$ , set by (A 1). Recalling the definition of  $\eta$  this means that the standard deviation of the distribution of efficiency over the source should not exceed the mean value. Since efficiencies are positive valued by definition, this constraint is met by the majority of sources.



# Appendix B

## Weighted mean, $\bar{x}$ -scores and $\chi_r^2$ -values

---

### B.1 Spectrum comparison

Much of the comparison results of this thesis are presented in terms of  $\bar{x}$ -scores and  $\chi_r^2$ -values. For two instances ( $A \pm \sigma_A$ ) and ( $B \pm \sigma_B$ ) of the same quantity, the  $\bar{x}$ -score can be written as

$$z_{AB} = \frac{A - B}{\sqrt{\sigma_A^2 + \sigma_B^2}}. \quad (\text{B } 1)$$

If the two instances are realizations of a normally distributed stochastic process, they are considered equal (on a 95% confidence level) if the  $\bar{x}$ -score lies between -2.0 and 2.0.

For the comparison of a range of instances (e.g. peak areas of a spectrum) the individual squared  $\bar{x}$ -scores can be summed and divided by their total number, yielding a  $\chi_r^2$ -value. For two series of instances ( $A_k \pm \sigma_{A,k}$ ) and ( $B_k \pm \sigma_{B,k}$ ) the previous can be written as

$$\chi_r^2 = \frac{\sum_{k=1}^K \bar{x}_{k,AB}^2}{K}. \quad (\text{B } 2)$$

If the series of instances stem from normal distributions, the expectation of the resulting  $\chi_r^2$ -value is unity. The variance of the  $\chi_r^2$ -distribution depends on the number  $K$  of squared  $\bar{x}$ -scores in the summation. Table B1 shows the cumulative  $\chi_r^2$ -distributions for different values of  $K$ .

Table B1:

$x$	$P(\chi^2 \leq x)$ $K = 5$	$P(\chi^2 \leq x)$ $K = 10$	$P(\chi^2 \leq x)$ $K = 20$	$P(\chi^2 \leq x)$ $K = 50$	$P(\chi^2 \leq x)$ $K = 100$
0.1	0.0079	0.0002	0.0000	0.0000	0.0000
0.2	0.0374	0.0037	0.0000	0.0000	0.0000
0.3	0.0869	0.0186	0.0011	0.0000	0.0000
0.4	0.1509	0.0527	0.0081	0.0000	0.0000
0.5	0.2235	0.1088	0.0318	0.0012	0.0000
0.6	0.3000	0.1847	0.0839	0.0112	0.0005
0.7	0.3766	0.2746	0.1695	0.0532	0.0098
0.8	0.4506	0.3712	0.2834	0.1568	0.0703
0.9	0.5201	0.4679	0.4126	0.3262	0.2468
1.0	0.5841	0.5595	0.5421	0.5266	0.5188
1.1	0.6421	0.6425	0.6595	0.7090	0.7678
1.2	0.6938	0.7149	0.7576	0.8428	0.9156
1.3	0.7394	0.7763	0.8342	0.9246	0.9765
1.4	0.7794	0.8270	0.8906	0.9676	0.9949
1.5	0.8140	0.8679	0.9301	0.9874	0.9991
1.6	0.8438	0.9004	0.9567	0.9955	0.9999
1.7	0.8693	0.9256	0.9739	0.9985	1.0000
1.8	0.8909	0.9450	0.9846	0.9996	1.0000
1.9	0.9093	0.9597	0.9911	0.9999	1.0000
2.0	0.9248	0.9707	0.9950	1.0000	1.0000
2.5	0.9715	0.9947	0.9998	1.0000	1.0000
3.0	0.9896	0.9991	1.0000	1.0000	1.0000
3.5	0.9964	0.9999	1.0000	1.0000	1.0000
4.0	0.9988	1.0000	1.0000	1.0000	1.0000
4.5	0.9996	1.0000	1.0000	1.0000	1.0000
5.0	0.9999	1.0000	1.0000	1.0000	1.0000

## B.2 Spectrum interpretation

The theory presented by Chapter Two of this thesis was validated repeatedly for different geometries by interpreting the simulated spectra with respect to the number of disintegrations  $N$ . This number was then compared to the real number  $N_{\text{true}}$  used in the simulation, or in the measurement. The calculation of  $N$  also produced a  $\chi^2$ -value.

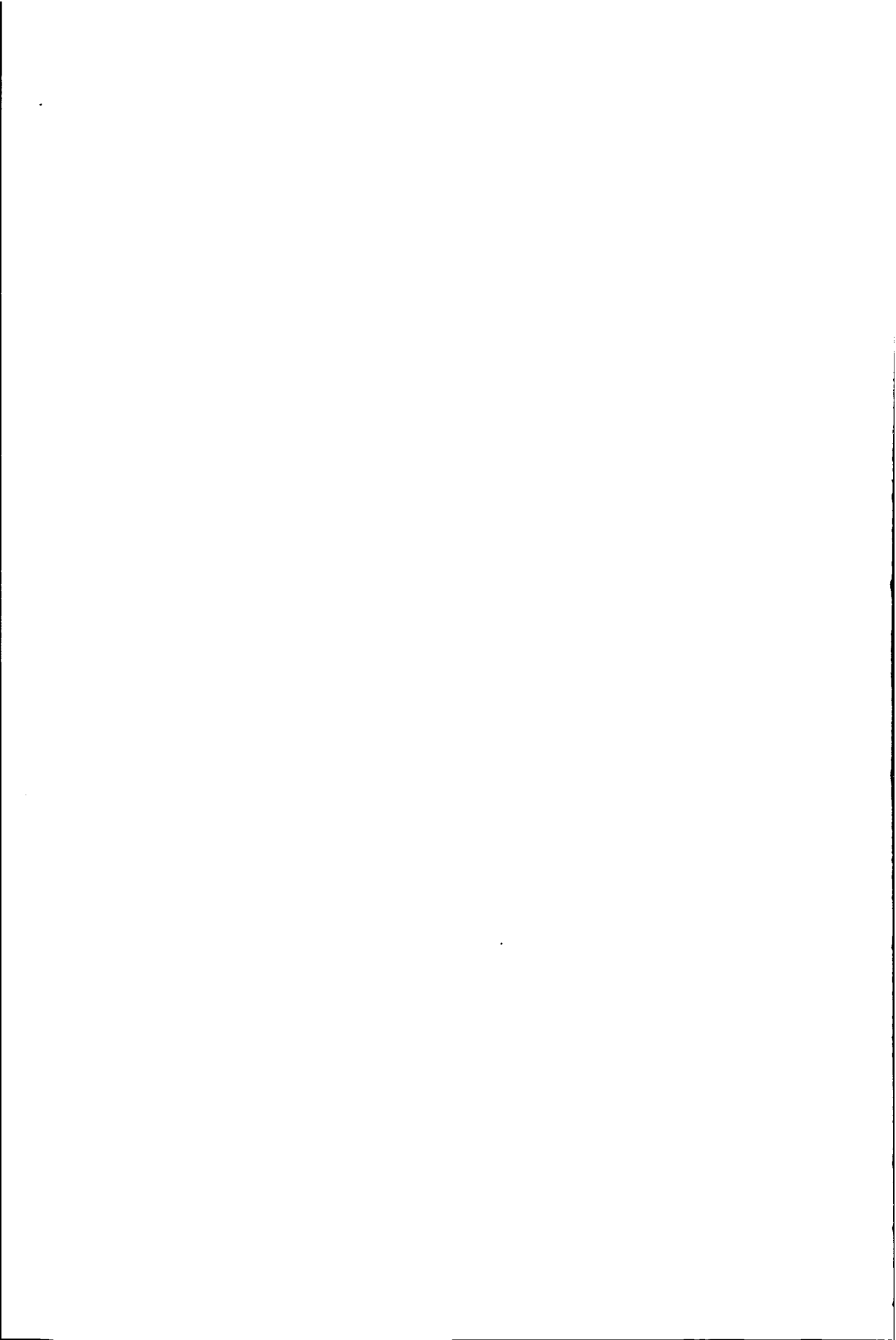
The number of disintegrations was calculated using the  $P_E$ -values from Equation (2.19) together with the curves to be validated. The areas  $A_E$  of the peaks in the spectrum were divided by their corresponding  $P_E$ -values. Thus, for each peak, a corresponding number of disintegrations  $N_E$  was obtained. The reported number of disintegrations  $N$  now is the weighted average of the number of disintegrations associated with each peak. The standard deviation of the reported number of disintegrations  $N$  is found from the variation of the individual  $N_E$ -values. Summarizing

$$N_E = \frac{A_E}{P_E}; \quad \delta N_E = \frac{\delta A_E}{P_E} \quad (\text{B 3})$$

and

$$N = \frac{\sum_E w_E N_E}{\sum_E w_E}; \quad \delta N = \sqrt{\frac{\left( \sum_E w_E N_E^2 \right) - \left( \frac{\sum_E w_E N_E}{\sum_E w_E} \right)^2}{n-1}}; \quad w_E = \frac{1}{\delta N_E}, \quad (\text{B 4})$$

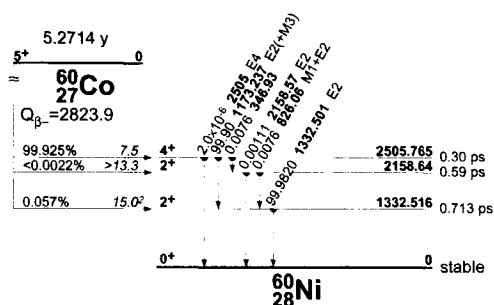
where the summations are taken over all peaks and  $K$  is the total number of peaks.



# Appendix C

## Decay schemes

The decay schemes presented in this appendix are extracted from [1]. The nuclear decay data listed in the tables is obtained from the IAEA Nuclear Data Centre<sup>[2]</sup>.



### Gammas for $^{60}\text{Ni}$ : $^{60}\text{Co}$ $\beta^-$ decay (5.2714 y)

$E_\gamma$	$E_{\text{level}}$	$I_\gamma^\dagger$	$I(\gamma+\text{ce})^\ddagger$	$T_{1/2}$	$\alpha$
346.93 7	2505.766 7	0.0076 5		0.30 ps 9	
826.28 9	2158.82 5	0.0076 8			
1173.237 4	2505.766 7	99.9736 7	99.9913 5	0.30 ps 9	$1.77 \cdot 10^{-4}$ 5
1332.501 5	1332.517 5	99.9856 4	99.9989 2	0.9 ps 3	$1.33 \cdot 10^{-4}$ 4
2158.77 9	2158.82 5	0.00111 18			
2505	2505.766 7	$2.0 \cdot 10^{-6}$ 4		0.30 ps 9	

$^\dagger$  For absolute intensities per 100 decays, multiply by 1

$^\ddagger$  Deduced from intensity balance

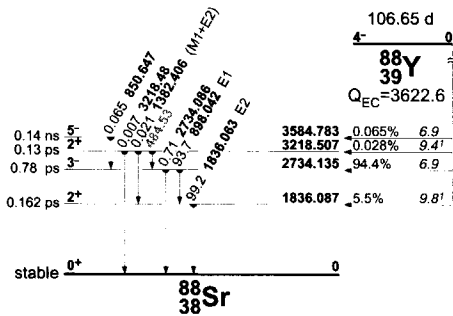


**Gammas for  $^{82}\text{Kr}$ :  $^{82}\text{Br}$   $\beta^-$  decay (35.30 h), cont.**

$E_\gamma$	$E_{\text{level}}$	$I_\gamma^\dagger$	$I(\gamma+\text{ce})^\ddagger$	$T_{1/2}$	$\alpha$
1044.002 5	1820.530 5	32.6 3			
1072.9 1	2547.60 7	0.095 15			
1081.29 5	2556.178 13	0.74 2			
1099.9 2	2920.44 20	0.007 3			
1174.0 4	2648.362 5	0.021 9			
1180.1 2	1956.65 5	0.103 9			
1317.473 10	2094.011 5	31.7 3			
1474.88 1	1474.899 5	19.53 20			
1650.37 4	2426.882 6	0.889 9			
1779.66 2	2556.178 13	0.136 2			
1871.6 2	2648.362 5	0.03 1			
1956.8 1	1956.65 5	0.0468 13			

$^\dagger$  For absolute intensities per 100 decays, multiply by 0.835

$^\ddagger$  Deduced from intensity balance

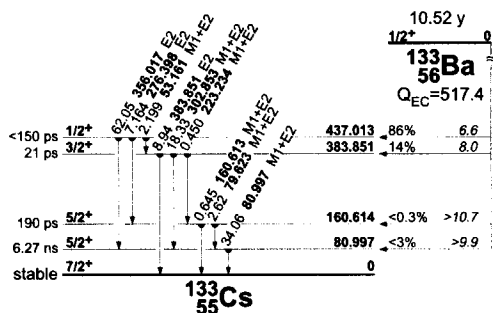


**Gammas for  $^{88}\text{Sr}$ :  $^{88}\text{Y}$   $\beta^+(\text{EC})$  decay (106.65 d)**

$E_\gamma$	$E_{\text{level}}$	$I_\gamma^\dagger$	$I(\gamma+\text{ce})^\ddagger$	$T_{1/2}$	$\alpha$
850.6 8	3584.7 8	0.066 13			
898.042 3	2734.130 13	94.4 3			0.00031
1382.2 10	3218.6 9	0.021 6			0.00035
1836.063 12	1836.084 12	100.0 3			
2734.0 5	2734.130 13	0.72 7			
3219.7 20	3218.6 9	0.0071 20			

$^\dagger$  For absolute intensities per 100 decays, multiply by 0.9924

$^\ddagger$  Deduced from intensity balance



**Gammas for  $^{133}\text{Cs}$ :  $^{133}\text{Ba}$   $\epsilon$  decay (10.52 y)**

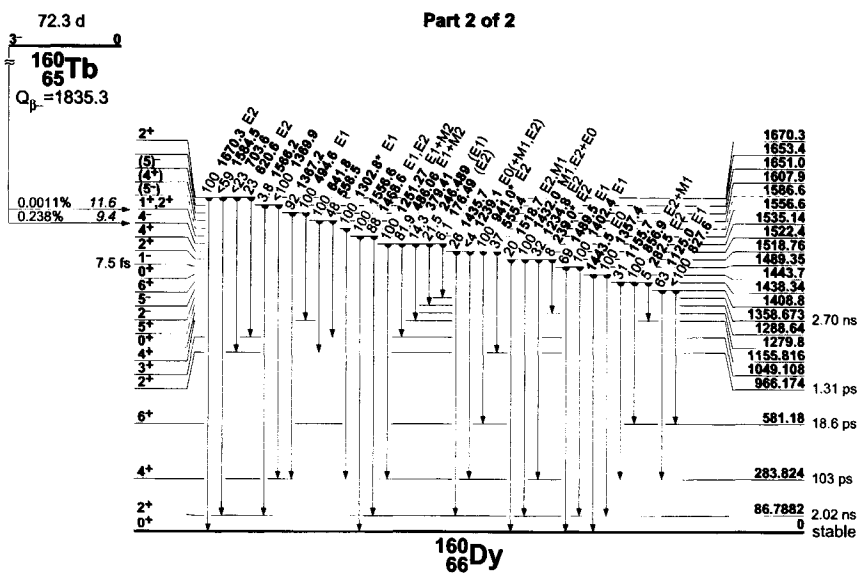
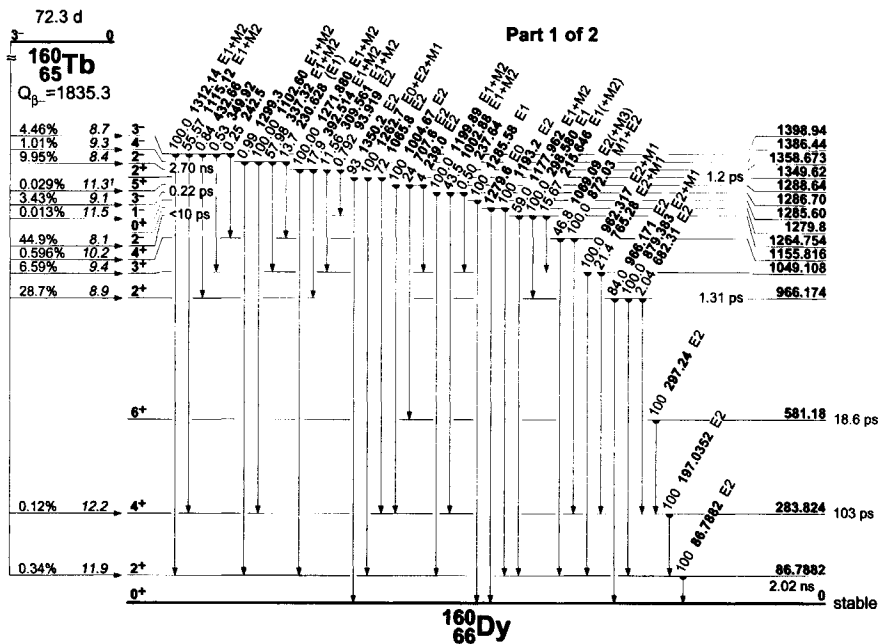
$E_\gamma$	$E_{\text{level}}$	$I_\gamma^\dagger$	$I(\gamma+ce)^\ddagger$	$T_{1/2}$	$\alpha$
53.1625 6	437.0111 9	2.199 22		$\leq 150$ ps	6.0 3
79.6139 13	160.6113 10	2.62 6		172 ps 4	1.70 6
80.9971 12	80.9972 8	34.06 27		6.28 ns 2	1.72
160.6109 17	160.6113 10	0.645 8		172 ps 4	0.296 3
223.2373 14	383.8487 8	0.450 4		42 ps 11	0.098
276.3997 13	437.0111 9	7.164 22		$\leq 150$ ps	0.0569
302.8510 6	383.8487 8	18.33 6		42 ps 11	0.0438
356.0134 6	437.0111 9	62.05 19		$\leq 150$ ps	0.0255
383.8480 12	383.8487 8	8.94 3		42 ps 11	0.0203

$^\dagger$  For absolute intensities per 100 decays, multiply by 1

$^\ddagger$  Deduced from intensity balance







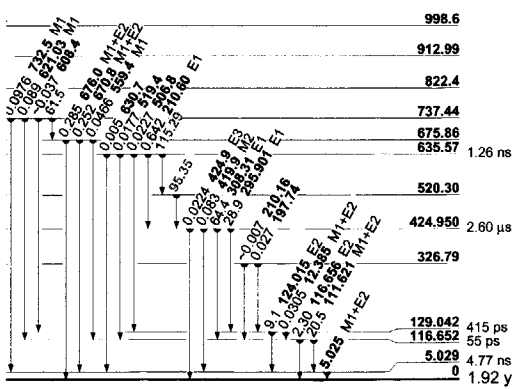
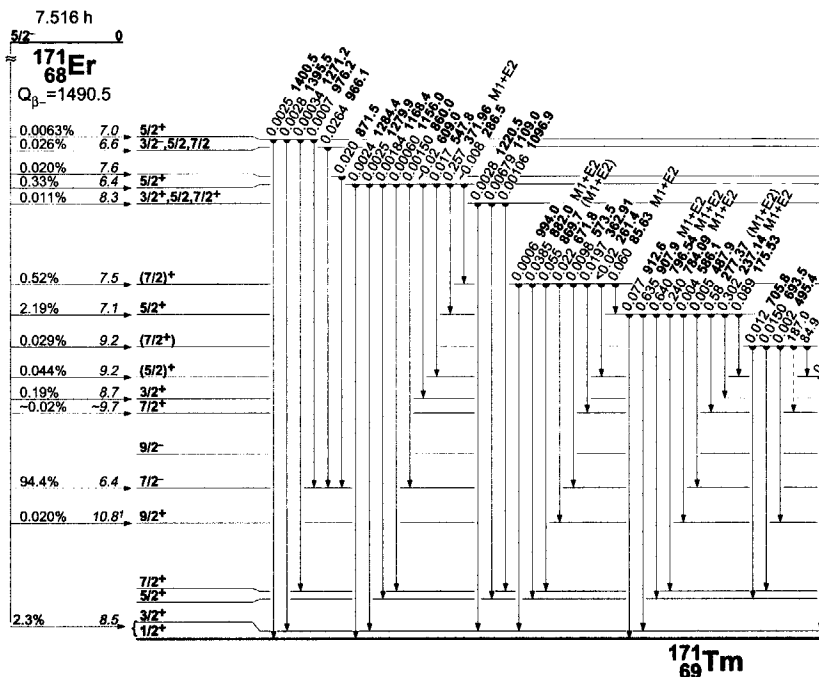
**Gammas for  $^{160}\text{Dy}$ :  $^{160}\text{Tb}$   $\beta^-$  decay (72.3 d)**

$E_\gamma$	$E_{\text{level}}$	$I_\gamma^\dagger$	$I(\gamma+\text{ce})^\dagger$	$T_{1/2}$	$\alpha$
86.7882 4	86.7882 4	43.7 4		2.026 ns 12	4.69
93.919 6	1358.673 5	0.188 6		2.70 ns 14	3.47
176.49 3	1535.157 23	0.0205 11			0.364
197.0352 11	283.8236 12	17.22 9		103 ps 5	0.250
215.6464 12	1264.7543 20	13.35 5		$\leq 10$ ps	0.0400
230.628 13	1386.439 19	0.268 3			0.0336
237.64 9	1286.695 24	0.020 7			
239.7 6	1288.67 3	0.007 3			0.131
242.5 8	1398.942 23	0.025 3			
246.489 16	1535.157 23	0.069 3			0.0283
297.3 <sup>b</sup>	581.1 7	0.031 16			0.0667
298.5800 19	1264.7543 20	86.8 6		$\leq 10$ ps	0.0174
309.561 15	1358.673 5	2.867 12		2.70 ns 14	0.0160 1
337.32 3	1386.439 19	1.127 9			0.0132 3
349.92 11	1398.942 23	0.048 3			
379.41 8	1535.157 23	0.047 2			
392.514 26	1358.673 5	4.44 3		2.70 ns 14	
432.66 12	1398.942 23	0.077 3			
486.06 5	1535.157 23	0.281 5			
682.31 4	966.1738 18	1.98 3			
707.6 10	1288.67 3	0.033 17			
765.28 4	1049.1079 22	7.11 4			
872.03 6	1155.815 21	0.723 12			
879.383 3	966.1738 18	100.0 2			
962.317 4	1049.1079 22	32.6 3			
966.171 3	966.1738 18	83.4 4			
1002.88 4	1286.695 24	3.45 2 $\S$			
1005.0 10	1288.67 3	0.13 3 $\S$			
1069.09 5	1155.815 21	0.332 5			
1102.60 3	1386.439 19	1.932 11			
1115.12 3	1398.942 23	5.20 5			
1177.962 4	1264.7543 20	49.4 2		$\leq 10$ ps	
1199.89 3	1286.695 24	7.92 4			
1251.27 5	1535.157 23	0.352 3			
1271.880 8	1358.673 5	24.73 7		2.70 ns 14	
1285.58 10	1285.59 10	0.051 4			
1299.3 3	1386.439 19	0.0181 18			
1312.14 4	1398.942 23	9.51 12			
1468.6 3	1555.8 2	0.0019 5			
1556.6 4	1555.8 2	0.0016 2			

$^\dagger$  For absolute intensities per 100 decays, multiply by 0.335

$^\ddagger$  Deduced from intensity balance

$^b$  Placement of transition in this level scheme is uncertain



**Gammas for  $^{171}\text{Tm}$ :  $^{171}\text{Er}$   $\beta$ - decay (7.516 h)**

$E_\gamma$	$E_{\text{level}}$	$I_\gamma^\dagger$	$I(\gamma+\text{ce})^\ddagger$	$T_{1/2}$	$\alpha$
5.025 6	5.028 5		907 31	4.77 ns 8	1408 55
12.385 8	129.044 6	0.305 18	82 4	415 ps 20	268
85.6 1	998.6 1	0.60 4			5.01
111.621 4	116.653 5	205 8		55 ps 13	2.31
116.656 6	116.653 5	23.0 6		55 ps 13	1.74
124.017 4	129.044 6	91 3		415 ps 20	1.39
166.4 3	Unplaced				
175.63 4	913.01 4	0.89 9			0.643
197.7 2	326.88 10	0.27 5			0.463
210.1 2	326.88 10	$\approx 0.07$ 0.223			
210.60 3	635.56 3	6.42 19		1.26 ns 6	0.0472
237.14 4	913.01 4	3.02 10			0.278
261.4 2	998.6 1	<0.2			
277.43 5	913.01 4	5.8 2			0.175
286.5 2	1285.0 1	$\approx 0.08$			0.167
295.901 14	424.948 12	289 8		2.60 $\mu\text{s}$ 2	0.0199
308.291 18	424.948 12	644 16		2.60 $\mu\text{s}$ 2	0.0180
362.91 14	998.6 1	0.197 11			0.0893
371.96 9	1285.0 1	2.57 10			0.0804
419.9 3	424.948 12	0.83 4		2.60 $\mu\text{s}$ 2	0.207
424.9 5	424.948 12	0.224 23		2.60 $\mu\text{s}$ 2	0.0864
455.6 2	Unplaced	0.06 2			
487.9 2	913.01 4	0.05 2			
495.4 2	822.4 2	0.02 1			
506.9 6	635.56 3	0.227 20		1.26 ns 6	0.0376
519.2 6	635.56 3	0.177 16		1.26 ns 6	0.0353
547.8 5	1285.0 1	0.17 4			
559.5 4	675.87 6	0.466 19			0.0292
573.5 2	998.6 1	0.098 15			
586.0 2	913.01 4	0.04 2			
608.6 2	737.39 5	$\approx 0.37$			
609.0 2	1285.0 1	$\approx 0.2$			
621.03 23	737.39 5	0.89 3			0.0224
630.7 2	635.56 3	0.05 1		1.26 ns 6	
670.7 2	675.87 6	2.52 5			0.0183
671.7 2	998.6 1	0.22 5			
676.1 3	675.87 6	2.85 6			0.0180
693.9 5	822.4 2	0.150 16			
705.8 2	822.4 2	0.12 4			
732.5 3	737.39 5	0.976 24			0.0148
745.0 5	Unplaced	0.066 8			
767.8 2	Unplaced	0.045 5			
784.09 17	913.01 4	2.40 5			0.0118 4

$^\dagger$  For absolute intensities per 100 decays, multiply by 0.100

$^\ddagger$  Deduced from intensity balance

Gammas for  $^{171}\text{Tm}$ :  $^{171}\text{Er}$   $\beta^-$  decay (7.516 h), cont.

$E_\gamma$	$E_{\text{level}}$	$I_\gamma$ †	$I(\gamma+\text{ce})$	$T_{1/2}$	$\alpha$
796.55 13	913.01 4	6.40 13			0.0105 6
860.0 2	1285.0 1	0.0150 24			0.00191
869.7 3	998.6 1	0.55 5			0.00940
871.5 2	1296.4 2	0.20 5			
882.0 4	998.6 1	0.385 19			0.00929
907.7 4	913.01 4	6.35 13			0.00828
912.6 5	913.01 4	0.77 5			
966.1 4	1391.1 4	0.264 8			
976.2 5	1400.6 3	0.007 3			
994.0 5	998.6 1	0.006 3			
1051.0 5	Unplaced	0.004 2			
1096.9 8	1225.7 4	0.0106 19			
1109.0 5	1225.7 4	0.0679 21			
1156.0 5	1285.0 1	0.0060 15			
1168.4 5	1285.0 1	0.0184 15			
1172.9 5	Unplaced	0.008 3			
1182.0 5	Unplaced	0.003 2			
1220.5 8	1225.7 4	0.028 2			
1271.2 5	1400.6 3	0.0034 15			
1279.9 5	1285.0 1	0.025 2			
1284.4 5	1285.0 1	0.024 2			
1395.5 5	1400.6 3	0.028 8			
1400.5 5	1400.6 3	0.025 1			

† For absolute intensities per 100 decays, multiply by 0.100

‡ Deduced from intensity balance

## References

- [1] R.B. Firestone, V.S. Shirley, C.M. Baylin, S.Y.F. Chu, J. Zipkin,, "Table of Isotopes", CD-ROM Edition 1.0, John Wiley & Sons inc., New York (1996)
- [2] IAEA Nuclear Data Centre, <http://www-nds.iaea.or.at/>

# Summary

---

## Advanced $\gamma$ -ray spectrometry dealing with coincidences and attenuation effects

In  $\gamma$ -ray spectrometry, the use of highly efficient detectors and detection geometries introduces *coincidence summing* effects: Two or more  $\gamma$ -quanta emitted from the same nucleus can both interact with the detector within a very short time frame, not allowing the detector to distinguish between them. As a result, the detector treats them as a single interaction, the energy transfer being the sum of the transfers of the individual interactions. Such count-rate independent coincidence effects can seriously affect a  $\gamma$ -ray spectrum.

Coincidence effects are most prominent when using well-type detectors. They can be accurately modelled if the source can be considered as a point, i.e. if the detection efficiency does not vary over the source volume. However, in 1978, de Bruin *et al.* [*Nucl. Instr. and Meth.*, **159** (1979) 301] found that owing to coincidence effects, the areas of high-energy peaks in a  $\gamma$ -ray spectrum were influenced by the attenuation of low-energy photons in the sample, and therefore were sample-matrix dependent. As a consequence, the source cannot be considered as a point, and the mathematical modelling of coincidence summing is seriously hampered. Coincidence effects therefore necessitate time-consuming radionuclide specific calibrations.

Also when using Marinelli beakers, detection efficiencies generally are high enough to give rise to coincidence summing. Evidently, Marinelli beaker sources cannot be considered as point sources either. Therefore, coincidence summing modelling for Marinelli beaker detection geometries is not trivial. Like well-type geometries, Marinelli beaker geometries are usually calibrated specifically for each combination of radionuclide and sample-matrix composition of interest.

In the  $\gamma$ -ray spectrometry community, coincidence summing effects generally are considered as a problem that preferably should be avoided, or else should be '*corrected for*'. Blaauw [*Nucl. Instr. and Meth.*, **A332** (1993) 493], however, does not regard them as disturbing but exploits them as a source of information used for the calibration of point-source detection geometries. Indeed, instead of being hampered by coincidence effects, Blaauw's method actually relies on coincidence effects to occur. Specifically, his method uses a general parametric model that describes the formation of a  $\gamma$ -ray spectrum, accounting for coincidence summing effects. Then it determines the actual parameters by fitting them to a calibration spectrum that shows coincidence effects. In this way, his method can be considered self-validating, meaning that possible errors or simplifications made in the model are either automatically corrected for, or show up by bad fit results.

However, Blaauws method fails when applied to voluminous source geometries [Nucl. Instr. and Meth., **A385** (1997) 330]. The work described in this thesis therefore develops a similar method that does include voluminous-source coincidence summing effects. Like Blaauws method, it uses a general parametric model that describes the formation of  $\gamma$ -ray spectra, taking into account the combination of coincidence effects and sample self-attenuation effects. The actual calibration of a voluminous source detection geometry is performed by fitting the model parameters to a calibration measurement.

After Chapter One of this thesis elaborates more on the history of the problem and it specifies the aims of the work described in this thesis, Chapter Two develops the general parametric model. It provides a parameterisation of the full-energy efficiency curve, based on the one by Gunnink [J. Radioanal. Nucl. Chem., *Articles*, **160** (1992) 305], and of the peak-to-total ratio, based on the one commonly used. For voluminous sources, these curves describe the mean full-energy peak efficiency and the mean peak-to-total ratio over the source volume as a function of energy. However, Chapter Two argues that, if the full-energy peak efficiency varies over the source volume, coincidence summing calculations should not only make use of mean efficiencies, but should take into account their variation as well. In the general parametric model, this variation is described by third newly introduced curve: the *linear-to-squared* curve.

The derivation of this linear-to-squared curve is based upon the following philosophy. For voluminous sources, detection efficiencies cannot be considered constant throughout the source volume. Instead, for every single decay, they depend upon the location of the decaying nucleus. Since this location is subject to probabilistic processes, it is natural to view them as stochastic variables. In this context, the distribution over the source volume of the full-energy peak efficiency as a function of energy can be described by its moments, of which the first and the second are its mean and its variance. Further development of this philosophy in Chapter Two shows that it is more convenient to use a scaled variance of the efficiency, instead of the variance itself, hence the name *linear-to-squared* ratio.

Chapter Three of this thesis emphasizes Monte-Carlo techniques. Monte-Carlo techniques made it possible to test the internal consistency of the proposed method. By using these techniques, interfering sources of (systematic) error, e.g. insufficiently accurately known decay schemes, could be completely eliminated, remaining only those introduced by the calibration method itself. This advantage is well illustrated in Chapter Six and perhaps even better in Chapter Eight: As a first step, a set of efficiency curves and, independently, a calibration spectrum are calculated. Both the geometry and the decay scheme of the calibration radionuclide used with these calculations are well defined. As a second step, the set of efficiency curves is used to reproduce the spectrum. Since the decay scheme is well defined, it is beyond suspicion as a source of error. Therefore, the second step gives great confidence in the consistency of the developed theory. As a third step, a curve set resulting from a fit to the spectrum is compared with the 'true' set. This step gives confidence in the quality of the fitting procedures. Moreover, it enabled a quest for the optimal fitting procedure.



Chapter Four and Chapter Five provide a justification for the work on well-type detectors. Currently at IRI, well-type detectors are equipped with a high-Z lining that prevents low-energy photons from being detected. That way, the voluminous nature of high-Z matrix sources is suppressed. This is however a rather unsatisfying solution since it degrades detector performance. Firstly, while unlined well-types have a large area of constant detection efficiency, lined well-types show a geometry dependency of the detection efficiency on the source position in the well. This is demonstrated by experiments described in Chapter Four. Secondly, while well-types originally were introduced for their high (maximum) absolute detection efficiency of almost 1.0 for photons with energies around 100 keV, the lining considerably reduces maximum detection efficiencies to values near 0.5. Finally, the lining leads to a higher Compton continuum relative to the full-energy peak, which can obscure small peaks. This latter effect is revealed by the slightly worse PC- or PT-ratio for lined well-type detectors, as compared to non-lined ones in Chapter Five.

Chapter Six and Chapter Seven describe the performance of the calibration method for a well-type detection geometry, to Monte-Carlo simulated spectra and real spectra, respectively. The Monte Carlo based results from Chapter Six were obtained with an unlined well-type geometry and two sources, a low-density, low-Z source and a high-Z Ta<sub>2</sub>O<sub>5</sub> matrix source. They indicate that it is possible to determine the parameters required to characterize the sample-detector geometry from the measured spectrum of a calibration radionuclide like terbium-160, to the point where coincidence summing corrections with accuracies far better than the required 1 % can be made for terbium-160 itself. However, the simulated erbium-171 spectra were not satisfactorily explained from the curves obtained with terbium-160. Especially peaks in the low energy region near 100 keV show large statistically significant deviations.

The experimental results from Chapter Seven are very similar to the Monte Carlo based ones. They were obtained using not only a non-lined well-type geometry but also a lined one, using again both a low-density, low-Z source and a high-Z Ta<sub>2</sub>O<sub>5</sub>-matrix source. The high-Z source was measured only in the non-lined geometry. Again, the terbium-160 spectra from all measurements were explained very well. Also spectra from additional radionuclides like cobalt-60, bromine-82 and caesium-137 proved to be no problem, but erbium-171 spectra did.

The failure of the method with erbium-171 occurs in all counting geometries, lined and non-lined, for both types of sources, low-Z and high-Z, and in the Monte Carlo world as well as in the real world. Both Chapter Six and Chapter Seven offer several explanations. While all these explanations might be very plausible in themselves, they ignore the fact that the method fails with erbium-171 in all cases, including the one that uses the lined detector. The only explanation offered by both Chapter Six and Chapter Seven together that does account for the general nature of the problem is the following. The full-energy peak efficiency curve might not be well defined in the low-energy region. Originally, Gunnink divides the efficiency curve in three regions: <90 keV, 90 to 200 keV, and >200 keV. This work however uses only two regions, hereby

combining the regions below 200 keV. This may very well explain the observed discrepancy in this region.

For the erbium-171 case, the agreement between experiment and theory is rather unsatisfactory. However, employing the calibration methods described in this thesis would lead to systematic errors in reported activities of only 0 to 3 % for simple radionuclides such as caesium-137, depending on the counting geometry and the radionuclide. It would lead to errors of 3 % for complex case nuclides like bromine-82 and terbium-160, and up to 10 % only for complex radionuclides such as erbium-171.

Chapter Eight and Chapter Nine describe the performance of the method to Monte-Carlo simulated spectra and real spectra, respectively, for Marinelli beaker detection geometries. Chapter Eight described the Monte-Carlo based results obtained with four Marinelli beaker geometries filled with either water or silicon dioxide, with dimensions ranging from 1ℓ to 2ℓ and densities ranging from  $1 \cdot 10^3 \text{ kg} \cdot \text{m}^{-3}$  to  $2 \cdot 10^3 \text{ kg} \cdot \text{m}^{-3}$ . The limits on the Marinelli beaker geometry translate into an upper limit on the attenuation coefficient of the sample material:  $\mu < 1 \text{ cm}^{-1}$ . Both chapters showed that, to obtain accurate results for voluminous sources, indeed a third curve is needed that accounts for the variation of the efficiency over the source volume, i.e. the linear-to-squared curve. A bromine-82 spectrum was used to determine all three curves. Spectrum interpretations of barium-133 and caesium-134 spectra using these curves were under complete statistical control, i.e. within 1% imprecision owing to counting statistics. The experimental results of Chapter Nine supported these conclusions. Although the experiments were performed only for a 1ℓ, water-filled Marinelli beaker, the conclusions extend to other Marinelli beaker geometries, as long as the attenuation coefficient,  $\mu$ , of the sample material is smaller than  $1 \text{ cm}^{-1}$ .

The approach developed in this thesis to analytically account for coincidence summing effects in combination with sample self-attenuation meets the majority of criteria set for it beforehand. It certainly takes the variation of the efficiencies over the source volume into account. It provides a calibration method based on a parametric model while the actual parameters are obtained from measurements showing coincidence effects. It is applicable to point sources as well as voluminous sources. Furthermore, for Marinelli-beaker geometries, the accuracy of the method is indeed better than 1 %.

For well-type detection geometries however this aim is not met. While the majority of radionuclides, including terbium-160 and bromine-82 can be reproduced with accuracies better than 3 %, erbium-171 showed to be a problem. On one hand, the worse performance of the method in the well-type case is a pity, because the work as a whole was started in order to be able to remove the lining from well-type detectors and dispense of its negative effects shown by Chapter Four and Chapter Five. On the other hand, Marinelli-beaker geometries are used much more often and in many more laboratories than well-type geometries, and the possible impact of the method in such applications might therefore be much larger than it would have been for well-types even at 1 % accuracy. In fact, this is already being demonstrated by the fact that PerkinElmer's

ORTEC company incorporated the algorithms developed here in their popular  $\gamma$ -ray spectrometry program GammaVision version 5.2, released after Quality Assurance testing in January 2001. Also as a consequence of this work, the company Analytics Inc. in Oak Ridge has begun the manufacturing process of voluminous calibration sources containing coincidence-rich caesium-134 as well as some of the well-known, coincidence-free calibration radionuclides, in October 2000.

Sjoerd Gelsema  
October 2001



# Samenvatting

---

## Over hoe om te gaan met effecten van cascadesommatie en bronverzwakking in $\gamma$ -spectrometrie.

(Advanced  $\gamma$ -ray spectrometry dealing with coincidence and attenuation effects)

Radioactief verval van een radionuclide is een proces waarbij de kern van het nuclide van energietoestand, en in het algemeen ook van samenstelling verandert en waarbij straling vrijkomt. Dit gebeurt vaak in twee stappen. De eerste stap omvat meestal één van de volgende gebeurtenissen: Het afsplitsen van een helium kern ( $\alpha$ -straling), een elektron of een positron ( $\beta^-$ - of  $\beta^+$ -straling), of uit het opnemen van een elektron uit de omringende schil (Elektronvangst gevolgd door emissie van Röntgenstraling). Na deze eerste stap is de kern al van samenstelling veranderd, maar bevat vaak nog een overmaat aan energie. Deze nieuwe kern bevindt zich zogezegd *in een aangeslagen toestand*. De tweede stap omvat het verval van de aangeslagen toestand naar de *grondtoestand*, waarbij de overmaat aan energie in de vorm van  $\gamma$ -straling wordt uitgezonden.  $\gamma$ -Straling en ook Röntgenstraling bestaat uit fotonen met discrete energieën. De precieze energieën van de uitgezonden fotonen liggen vast voor ieder radionuclide. Ook de relatieve aantallen fotonen per fotonenergie liggen vast. Deze informatie kan worden samengevat in een vervalschema zoals daarvan bijvoorbeeld in Appendix C een aantal is gegeven.

$\gamma$ -Spectrometrie behelst het meten van zowel de energie van de fotonen, alsook van het aantal fotonen per energie, of beter, per energiegebied. De meting laat zich weergeven in de vorm van een  $\gamma$ -spectrum zoals bijvoorbeeld in figuur 2.1. Het spectrum toont pieken op die plaatsen die overeenkomen met de energie van de uitgezonden fotonen. Anders dan de naam doet vermoeden bevat een  $\gamma$ -spectrum overigens ook Röntgenpieken.  $\gamma$ -Spectrometrie is tegenwoordig een volwassen techniek, in die zin dat alle valkuilen bekend zijn en dat voor het merendeel daarvan een oplossing bestaat. Dit proefschrift levert een oplossing voor misschien wel de laatste open eindjes die de techniek nog kent.

Bij het gebruik van efficiënte detectoren in  $\gamma$ -spectrometrie spelen cascade-sommatieeffecten een rol: twee of meer fotonen die zijn ontstaan bij het verval van één enkele kern worden gelijktijdig gedetecteerd door de detector. Als gevolg hiervan ziet de detector slechts één foton waarvan de energie gelijk is aan de som van de afzonderlijke fotonen. In een  $\gamma$ -spectrum ontstaat op die manier een piek op de 'verkeerde' plaats. Deze cascade-sommatieeffecten, of kortweg sommatieeffecten kunnen een  $\gamma$ -spectrum dus

behoorlijk beïnvloeden. Reden waarom men in het algemeen sommatieeffecten als storend ervaart.

Het optreden van sommatieeffecten biedt echter ook voordelen. Een voorbeeld is het kalibreren van de efficiëntie van een detectieopstelling. In dit geval wordt de foton-detectiekans als functie van de fotonenergie voor de betreffende opstelling bepaald. Het is handig een  $\gamma$ -spectrum te beschouwen als een stelsel vergelijkingen, waarbij iedere vergelijking de inhoud geeft van één van de pieken in het spectrum. Iedere vergelijking heeft de detectiekans van het betreffende foton als onbekende parameter. Aangezien ook de bronactiviteit nog een onbekende parameter in het stelsel is, is het stelsel niet oplosbaar. Alleen indien de bronactiviteit bekend is kan het stelsel opgelost worden en kunnen de detectiekansen van de fotonen, of met andere woorden, kan de efficiëntie van de detectieopstelling als functie van fotonenergie bepaald worden.

Indien sommatieeffecten optreden wordt het stelsel uitgebreid met vergelijkingen die de inhoud van de sompieken geven. De kans op een gesommeerde detectie is gelijk aan het product van de detectiekansen van de fotonen die met elkaar sommeren. De extra vergelijkingen kosten dus geen extra onbekende parameters. Ze leveren zodoende extra informatie die gebruikt kan worden om bijvoorbeeld de bronactiviteit, in combinatie met de detectieefficiëntie te bepalen. Een andere mogelijkheid is om andere detectorparameters te bepalen dan de detectieefficiëntie.

Een voorwaarde voor het gebruik van sommatieeffecten op deze manier is een goed begrip van de manier waarop fotonen in de detector worden gedetecteerd. Voor bronnen die als een punt kunnen worden beschouwd wordt het detectieproces inderdaad goed begrepen. Voor het kalibreren van puntbronopstellingen gebruikt Blaauw [*Nucl. Instr. and Meth.*, **A332** (1993) 493] een parametrisch model dat de opbouw van een  $\gamma$ -spectrum beschrijft en dat rekening houdt met sommatieeffecten. De parameters van het model zijn de onbekenden in het stelsel vergelijkingen dat wordt gegeven door het kalibratiespectrum. Zoals hierboven beschreven maken sommatieeffecten het stelsel oplosbaar.

Blaauws methode blijkt echter te falen voor volumineuze bronnen [*Nucl. Instr. and Meth.*, **A385** (1997) 330]. In dit proefschrift wordt daarom de ontwikkeling beschreven van een analoge methode die wel rekening houdt met sommatieeffecten in volumineuze bronnen. Net als die van Blaauw maakt deze methode gebruik van een parametrisch model om de opbouw van een  $\gamma$ -spectrum te beschrijven, waarbij nu ook sommatie in verzwakkende monsters mathematisch wordt beschreven. De daadwerkelijke kalibratie van een detectieopstelling vindt weer plaats door de parameters van het model aan te passen aan een kalibratiemeting.

Hoofdstuk 2 van dit proefschrift beschrijft het parametrisch model. Daarbij wordt gebruik gemaakt van Gunninks parametrisatie van de piek-efficiëntiecurve [*J. Radioanal. Nucl. Chem., Articles*, **160** (1992) 305] en van een zeer gangbare parametrisatie van de totale-efficiëntiecurve, die beide nodig zijn om sommatieeffecten goed te beschrijven. Deze curven beschrijven de gemiddelde waarden van de twee grootheden over het

bronvolume, als functie van de fotonenergie. Het blijkt echter dat deze twee gemiddelde curven niet voldoende informatie omtrent de bron bevatten om sommatieberekeningen goed te kunnen uitvoeren. Niet alleen zijn de gemiddelde piek- en totale-efficiëntie belangrijk, ook de variaties van de efficiënties over het bronvolume moeten in rekening worden genomen. In het parametrische model wordt deze informatie geleverd door een derde, nieuw geïntroduceerde curve. Deze curve relateert de gemiddelde piekefficiëntie aan het gemiddelde kwadraat van de piekefficiëntie. Vandaar de naam '*linear-to-squared curve*' of '*LS-curve*'.

De afleiding van deze LS-curve is gebaseerd op het volgende idee. Voor een volumineuze bron is de detectieefficiëntie niet constant over het bronvolume, maar hangt onder andere af van de precieze positie van de vervallende kern. Omdat de positie onderhevig is aan stochastische processen, is het logisch om ook de detectieefficiëntie als een stochastische grootheid te beschouwen. De verdelingsdichtheid van de efficiëntie over het bronvolume kan in benadering worden beschreven door een gemiddelde en een variantie. De LS-curve is direct gerelateerd aan de variantie van de verdeling.

De rest van het proefschrift beschrijft de validatie van de nieuwe methode. Daartoe maak ik gebruik van twee typen detectieopstellingen waarbij de bron niet als een punt kan worden beschouwd. Het eerste type opstelling is de putdetector. Hierbij wordt een kleine bron omringd door de detector. Omdat de afstand van de bron tot de detector erg klein is, en omdat de detector de bron min of meer volledig omringt, is de detector erg efficiënt. Sommatieeffecten spelen hier een grote rol. Als het bronmateriaal zodanig van samenstelling is dat laagenergetische fotonen al in de bron geabsorbeerd kunnen worden, dan kan de bron niet meer als een punt worden beschouwd. Een oplossing hiervoor is het verlagen van de detectieefficiëntie voor laagenergetische fotonen door het aanbrengen van een voering van absorberend materiaal in de put. Dit is echter weinig elegant, en kent bovendien enige ongewenste bijwerkingen. Deel II van het proefschrift gaat geheel over putdetectoren.

Het tweede type detectieopstelling dat ik beschouw is de Marinellibeker. Dit is een emmer met een extra, aan de bovenkant gesloten cilinder middenin, die over een detector heen geschoven kan worden. Op die manier omringt het bronmateriaal de detector en zo kan een grote hoeveelheid bronmateriaal dicht bij een detector worden geplaatst. Ook hier is, door de kleine afstand tussen bron en detector, de opstelling erg efficiënt en ook hier spelen sommatieeffecten een rol. Bovendien is het duidelijk dat, vanwege zijn afmetingen, de bron niet als een punt kan worden beschouwd. Deel III van het proefschrift gaat over Marinellibeker opstellingen.

Een belangrijk onderdeel van de validatie is gedaan met Monte Carlo technieken voor spectrum berekeningen. Het gebruik van Monte Carlo technieken maakt het mogelijk de interne consistentie van de ontwikkelde methode te testen. De Monte Carlo exercitie heeft namelijk geen last van systematische fouten zoals bijvoorbeeld het onvoldoende bekend zijn van vervalschema's. De enige fouten die een rol spelen zijn die fouten of vereenvoudigingen die door de methode zelf veroorzaakt worden. Zowel Hoofdstuk 6 als Hoofdstuk 8 illustreren dit. Hierin bereken ik eerst een volledige set van efficiëntiecurven

en daarnaast, onafhankelijk, een kalibratiespectrum. Zowel de bron-detector geometrie en het vervalschema zijn goed bekend. Daarna gebruik ik de theorie ontwikkeld in Hoofdstuk 2 om met behulp van de curven het spectrum te reproduceren. Juist omdat het vervalschema foutloos is, zijn de afwijkingen tussen het gesimuleerde en gereproduceerde spectrum uitsluitend het gevolg van de gebruikte reproductie methode. Tenslotte pas ik een set efficiëntie curven aan het gesimuleerde spectrum aan en vergelijk deze met de vooraf berekende set. Deze vergelijking geeft vertrouwen in de gebruikte aanpassingsmethode.

De validatie met zowel Monte Carlo simulaties alsook met werkelijke metingen laat zien dat de onnauwkeurigheid van de methode, in het geval van Marinellibeker opstellingen beter is dan 1%. Voor putdetectoren is de methode minder nauwkeurig. Hoewel de activiteit van het merendeel van de radionucliden in de bronnen gereproduceerd kan worden met een onnauwkeurigheid van beter dan 3%, blijkt vooral het nuclide erbium-171 een probleem te vormen.

Aan de ene kant is het jammer dat de methode zich bij putdetectoren niet perfect gedraagt, want de hele exercitie was eigenlijk begonnen om de voering uit de put te krijgen. Aan de andere kant worden wereldwijd putdetectoren lang niet zoveel gebruikt als Marinellibeker opstellingen. De relevantie van de ontwikkelde methode is dus veel hoger voor de laatste, zelfs al zou de nauwkeurigheid van de methode voor putdetectoren vergelijkbaar zijn. Deze stelling wordt ondersteund door het feit dat het Amerikaanse bedrijf 'PerkinElmer – ORTEC' de hier ontwikkelde algoritmes gebruikt in hun populaire  $\gamma$ -spectrometrieapplicatie 'GammaVision'. Bovendien is het bedrijf 'Analytics Inc.' uit Oak Ridge in oktober 2000 begonnen met de fabricage van een kalibratiebron waarin ook coincidenties een rol spelen.

Sjoerd Gelsema  
Oktober 2001



# Dankwoord

---

Beste Menno,

dit boekje zou er niet hebben gelegen zonder jouw begeleiding en inzet. Niet alleen vak-inhoudelijk maar ook bijvoorbeeld qua programmeerstijl, presentatietechniek, en engelse taal heb ik veel van je geleerd. Echter, verreweg de meeste dank ben ik je verschuldigd voor je inspanningen vanaf 1998, toen mijn dienstverband bij het IRI er reeds op zat. Door nieuwe inzichten was ik genoodzaakt grote delen van het proefschrift te herschrijven en dat te doen naast de drukte van een reguliere baan en een jong gezin. Jij overtuigde mij –en Nicole– van de noodzaak om door te zetten en offerde menig vrije avond op om samen de grote lijnen op papier te zetten. Jouw betrokkenheid ging verder dan men redelijkerwijs van een mentor mag verwachten.

Beste Jeroen,

als promotor kreeg jij mijn werk vaak pas onder ogen als het al de vorm van een manuscript had. De discussies erover heb ik altijd als erg plezierig ervaren. Je had een scherp oog voor slordigheden in mijn schrijfstijl en in mijn formuleringen. Dankzij jouw commentaar heeft het proefschrift zeker aan duidelijkheid gewonnen.

Beste Aad, Kees en Koos,

jullie wil ik zeer hartelijk bedanken voor de praktische hulp die jullie boden bij het vervaardigen van, en het manipuleren met respectievelijk de Amersham- bronnen, de broombronnen en de erbium- en terbiumbronnen.

Beste collega promovendi,

dank jullie voor de goede sfeer tijdens koffiepauzes, die soms naadloos overgingen in lunchpauzes, die op hun beurt soms naadloos overgingen in theepauzes.

Lieve papa,

dank je wel voor je vaste vertrouwen in mijn capaciteiten. Het spijt mij dat het je niet was gegund om dit werk te bewonderen. Je wist echter wel dat het er zou komen en ik weet dat je trots op me zou zijn geweest.

Lieve mama,

dank je wel voor je aanmoediging en ondersteuning en voor je hulp bij de zorg voor Romy en Jurre. Je was en bent onmisbaar in een gezin waarvan beide ouders werken.

Lieve Nicole, Romy en Jurre,

jullie maken thuis daadwerkelijk een Thuis, waar alle dagelijkse wetenschappelijke besognes in het perspectief worden geplaatst van de zaken die er werkelijk toe doen.



## Curriculum vitae

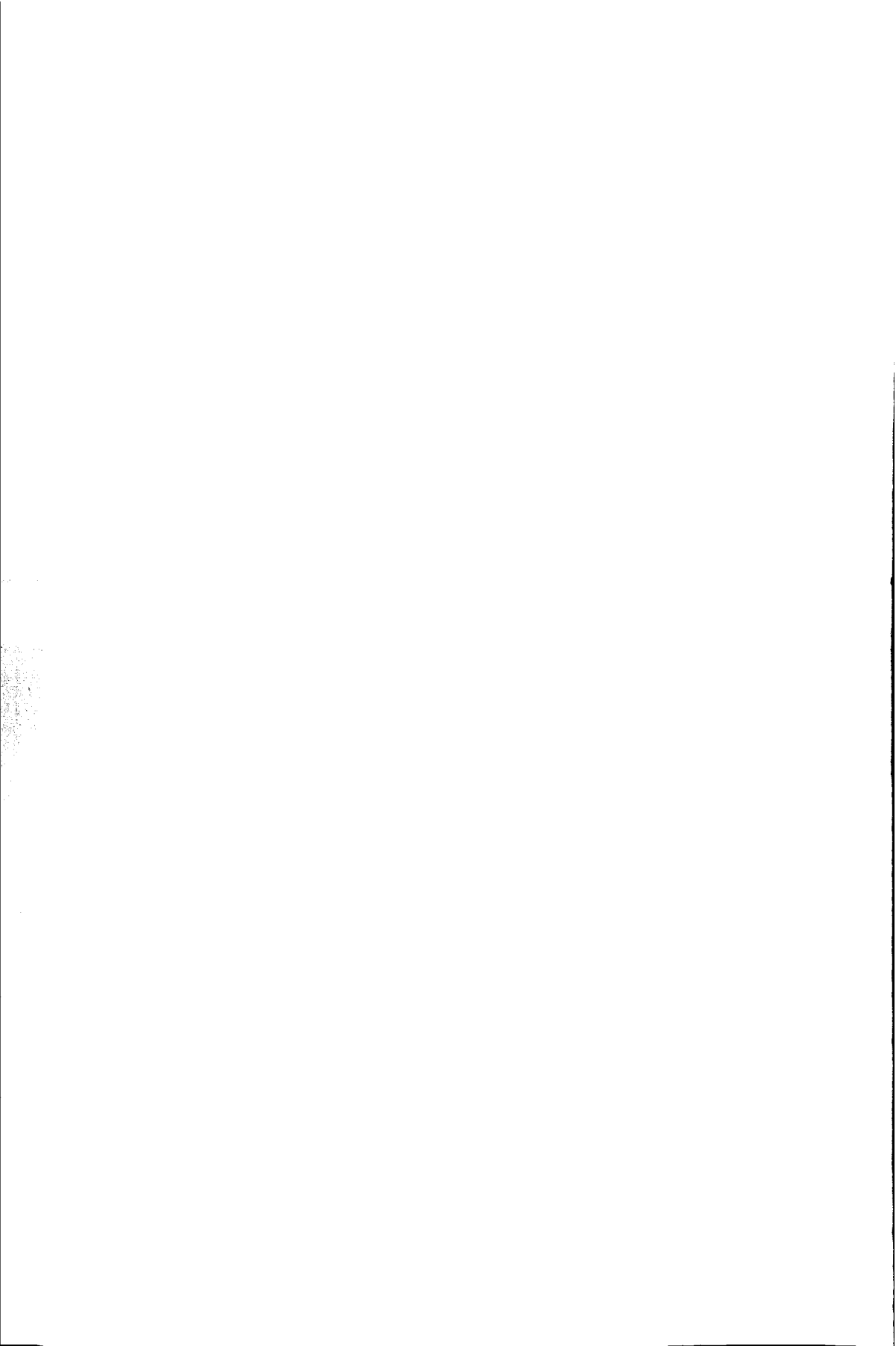
---

Sjoerd Gelsema was born in Middelburg, on September 16, 1968. He obtained his VWO diploma at the Rijnlands Lyceum in Sassenheim in 1986. Directly afterwards he started his studies at the Delft University of Technology (TUD). He obtained his Masters degree in Physics in 1993 for his work on silicon strip detectors for DNA sequencing in the Radiation Technology group of the Interfaculty Reactor Institute (IRI), under supervision of Prof. Dr. Ir. C.W.E. van Eijk. From 1993 until 1994, he fulfilled his military obligations with the Engineering Corps of the Royal Netherlands Army in Vught and Ermelo.

From 1994 until 1998, Sjoerd worked as a Ph.D. student at the IRI, in the Physical and Mathematical Radioanalysis groep of the Department of Radiochemistry. The work described in this thesis was conducted during this period, under close supervision of Dr. Menno Blaauw and Prof. Dr. Ir. J.J.M. de Goeij.

In 1998, Sjoerd accepted his current position with the TNO Physics and Electronics Laboratory (TNO-FEL) where he works in the Radar Signal Processing and Concepts group. His work at TNO-FEL focuses on the recognition of aircraft using radar reflections.

Sjoerd is married to Nicole and has two children: Romy (1996) and Jurre (1998).



# List of publications

---

## Publications directly related to this thesis

### Chapter Four:

S.J. Gelsema, M. Blaauw, "Geometry effects in Ge well-type detectors due to the introduction of high-Z linings", *Nucl. Instr. and Meth.*, **A368** (1996) 410

### Chapter Five:

S.J. Gelsema, M. Blaauw, P. Bode, "The influence of counting geometry and lining on the Compton continuum in well-type detectors", *Nucl. Instr. and Meth.*, **A379** (1996) 289

### Chapter Six and Chapter Seven

S.J. Gelsema, M. Blaauw; "True-coincidence summing corrections in gamma-ray spectrometry with Well-type Germanium detectors in the presence of significant gamma-ray self attenuation", *Final Program & Book of Abstracts*. Tenth International Conference on Modern Trends in Activation Analysis (Bethesda, Maryland, USA, 19-apr-1999), p. 83-83

### Chapter Eight and Chapter Nine

S.J. Gelsema, M. Blaauw, J.J.M. de Goeij, "True-coincidence summing corrections in gamma-ray spectrometry with Marinelli beaker detection geometries" *Nucl. Instr. and Meth.*, (in preparation)

## Publications on related topics

V.P. Kolotov, V.V. Atrashkevich, S.J. Gelsema, "Estimation of true coincidence corrections for voluminous sources", *J. Radioanal. Nucl. Chem.*, **210**(1996) 183

M. Blaauw, M.J.J. Ammerlaan, S.J. Gelsema, "The use of sources emitting coincident gamma-rays for the determination of photopeak and total efficiencies in non-point-source counting geometries", *Nucl. Instr. and Meth.*, **A385** (1997) 330

M. Blaauw, S.J. Gelsema, "The influence of peak area determination bias in quantitative gamma-ray spectrometry", *Nucl. Instr. and Meth.*, **A422** (1998) 417







ISBN: 90-107-2255-6

DUP Science